Title

Turbulence and cross-slope transport off Antarctica and California

Author

Palóczy Filho, André

Publication Date

2020

UNIVERSITY OF CALIFORNIA SAN DIEGO

Turbulence and cross-slope transport off Antarctica and California

A dissertation submitted in partial satisfaction of the
requirements for the degree
Doctor of Philosophy

in

Oceanography

by

André Palóczy Filho

Committee in charge:

Sarah Gille, Co-Chair
Jennifer MacKinnon, Co-Chair
Julie McClean, Co-Chair
Falk Feddersen
Eugene Pawlak
Fiammetta Straneo
Amy Waterhouse

2020

The dissertation of André Palóczy Filho is approved, and it is acceptable in quality and form for publication on microfilm and electronically:

Co-Chair

Co-Chair

Co-Chair

University of California San Diego

2020

TABLE OF CONTENTS

LIST OF FIGURES

LIST OF TABLES

ACKNOWLEDGEMENTS

Throughout my scientific training, I have had the privilege of only having outstanding mentors. I am indebted to my advisors, Jennifer MacKinnon, Sarah Gille and Julie McClean, for several years of guidance, encouragement and inspiring mentoring. Many thanks also to Amy Waterhouse for unofficially advising me in the last two chapters of this dissertation.

I am also indebted to the other members of my committee. Thanks to Falk Feddersen, Fiamma Straneo and Geno Pawlak for their independent criticism and helpful guidance in refining my thesis work.

Thanks to my friends, my cohort and the entire SIO and UCSD community, for nurturing such a welcoming environment. Thanks also to CASPO and MPL administrative staff, in particular Tomomi Ushii and Eva Friedlander.

Being part of the Inner Shelf DRI community has been very inspiring and instructive. In that regard, I also thank the UC Ship Funds Program for providing me with the unique opportunity to develop my own field experiment.

Finally, there are several people without whom I would have been unable to complete my entire education, and for whose existence I am most grateful. Many thanks to my parents, Cristiane and André, to my aunt Cristina, to my uncle Toni, to my grandparents, Maria Domingas and José Bráulio, and to Catarina, for their unconditional love and support along the way.

My training, education and research at SIO/UCSD were funded by the Department of Energy, the Office of Naval Research and the UC Ship Funds Program.

Chapter 2, in full, reprints material as it appears in Palóczy, A., Gille, S. T., & McClean, J. L. (2018). Oceanic Heat Delivery to the Antarctic Continental Shelf: Large-Scale, Low-Frequency Variability. Journal of Geophysical Research: Oceans, 123(11), 7678–7701. DOI: 10.1029/2018JC014345. The dissertation's author was the primary investigator and author of this paper.

Chapter 3, in full, reprints material as it appears in Palóczy, A., McClean, J. L., Gille, S. T. & Wang, H. (2020). The large-scale vorticity balance of the Antarctic continental margin in a fine-resolution global simulation. Journal of Physical Oceanography, 50(8), 2173-2188. DOI: 10.1175/JPO-D-19-0307.1 . The dissertation's author was the primary investigator and author of this paper.

Chapter 4, in full, consists of material that has been submitted for publication in the Journal of Physical Oceanography: Palóczy, A., MacKinnon, J. A. & Waterhouse, A. F. Subtidal to supertidal variability of Reynolds stresses in a mid-latitude stratified inner-shelf. The dissertation's author was the primary investigator and author of this paper.

Chapter 5, in full, consists of material that is being prepared for submission for publication in Geophysical Research Letters: Palóczy, A., MacKinnon, J. A. & Waterhouse, A. F. Balanced to unbalanced transition in the coastal ocean: Insights from simulations and an along-isobath survey. The dissertation's author was the primary investigator and author of this paper.

VITA

EDUCATION

2013	B. S. in Oceanography, University of São Paulo, Brazil
2015	M. S. in Oceanography, University of São Paulo, Brazil
2020	Ph. D. in Oceanography, University of California San Diego

PUBLICATIONS

A. Palóczy, MacKinnon, J., Waterhouse, A. F. Balanced to unbalanced transition in the coastal ocean: Insights from simulations and an along-isobath survey. In preparation for *Geophys. Res. Lett.*

N. Kumar, Lerczak, J., Xu, T., Waterhouse, A., Thomson, J., Terrill, E., Swann, C., Suanda, S., Spydell, M., Smit, P., Simpson, A., Romeiser, R., Pierce, S., de Paolo, T., **Palóczy, A.,** *et al.* The Inner-Shelf Dynamics Experiment. Submitted to *Bull. Am. Met. Soc.*

A. Palóczy, MacKinnon, J., Waterhouse, A. F. Subtidal to supertidal variability of Reynolds stresses in a mid-latitude stratified inner-shelf. Submitted to *J. Phys. Oceanogr.*

A. Palóczy, McClean, J. L., Gille, S. T., Wang, H. (2020). The large-scale vorticity balance of the Antarctic continental margin in a fine-resolution global simulation. *J. Phys. Oceanogr.*, 50(8), 2173-2188, DOI: 10.1175/JPO-D-19-0307.1.

A. Palóczy, Gille, S. T., McClean, J. L. (2018). Oceanic heat delivery to the Antarctic continental shelf: Large-scale, low-frequency variability. *J. Geophys. Res. Oceans*. DOI: 10.1029/2018JC014345.

A. Palóczy, Brink K.H., da Silveira, I.C.A., Arruda, W.Z., Martins, R.P. (2016). Pathways and mechanisms of offshore water intrusions on the Espírito Santo Basin shelf (18°–22°S, Brazil). *J. Geophys. Res. Oceans*. DOI: 10.1002/2015JC011468.

C. Yamashita, Nagai, R.N., Martins, M.V.A., Vicente, T.M., Sousa, S.H.M., Frontalini, F., **Palóczy, A.** *et al*. (2016). On the interplay between hydrodynamics, bottom morphology, sedimentary processes and benthic foraminifera assemblages in the São Paulo Bight (Brazil, SW Atlantic). *Journal of Sedimentary Environments*. DOI: 10.12957/jse.2016.25990.

A. Palóczy, da Silveira, I.C.A., Castro, B.M., Calado, L. (2014), Coastal upwelling off Cape São Tomé (22°S, Brazil): The supporting role of deep ocean processes. *Cont. Shelf Res.* DOI: 10.1016/j.csr.2013.09.005.

ABSTRACT OF THE DISSERTATION

Turbulence and cross-slope transport off Antarctica and California

by

André Palóczy Filho

Doctor of Philosophy in Oceanography

University of California San Diego, 2020

Sarah Gille, Co-Chair
Jennifer MacKinnon, Co-Chair
Julie McClean, Co-Chair

Onshore penetration of oceanic water across the Antarctic continental slope (ACS) plays a major role in global sea level rise by delivering heat to the Antarctic marginal seas, thus contributing to the basal melting of ice shelves. We show that the time-mean and eddy components of the onshore Heat Transport (HT) around the Antarctic Continental Margin (ACM) in a global 0.1°coupled ocean-sea ice model add up to O(20 TW) in the annual average. The contributions from eddy advection, eddy stirring, and mean flow advection to the total onshore HT vary regionally. The time-mean component governs the seasonal variability of the total HT and largely cancels the eddy component. We examine the depth-integrated vorticity balance of this simulation to gain further insight into the dynamics of these processes. Maps of the time-averaged depth-integrated vorticity budget terms and time series of the spatially-averaged, depth-integrated vorticity budget terms reveal that the flow in the Amundsen, Bellingshausen and Weddell Seas and in the western portion of East Antarctica, is closer to an approximate Topographic Sverdrup Balance compared to other segments of the ACM. This suggests that the surface-stress curl, imparted by the wind and the sea ice, has the potential to contribute to the meridional, approximately cross-slope, transport to a greater extent in some segments of the ACM than others.

In the second part of this thesis, we describe the observed spatio-temporal variability and vertical structure of turbulent Reynolds stresses in a stratified mid-latitude inner-shelf with an energetic internal wave climate. We link the Reynolds stresses to different physical processes, namely internal bores, mid-water shear instabilities within vertical shear events related to wind-driven subtidal along-shelf currents; and non-turbulent stresses related to incoming Nonlinear Internal Wave (NLIW) trains. Among other conclusions, the results highlight that internal bores and shoaling NLIWs may also be important dynamical players in other inner-shelves with energetic internal waves. In the mesoscale, simulations and an along-isobath survey suggest that the balanced-to-unbalanced transition along the 50 m isobath is at 12-22 km, and that baroclinic instability of the subtidal along-shelf flow is a plausible explanation for the cross-shelf structure of the transition scale.

Chapter 1

Introduction

1.1 Background and motivation

Transport and stirring of properties in the coastal ocean happens across a range of scales. Barotropic/baroclinic tides, mesoscale/submesoscale eddies, and buoyancy-, wind-, and wave-driven subtidal currents are important in waters over different types of continental shelves, coastline geometries and cross-shelf locations. These motions may also drive turbulent mixing through various processes, from the edge of the continental shelf to the surfzone. In the coastal ocean, large cross-shelf property gradients imply that even weak cross-shelf currents often dominate the transport of heat, salt, nutrients, biota and pollutants across the edge of the continental shelf and further inshore (*e.g.*, Brink, 2016a). This dissertation investigates some aspects of cross-isobath transport processes and turbulence – both in the mesoscale and in the microscale – along the Antarctic continental margin and along California's central coast.

A sub-field of coastal oceanography that has seen substantial breakthroughs over the past ten years is the study of cross-slope exchange processes in the Antarctic continental margin, with improved understanding of processes brought about by the combination of increasingly fine-resolution idealized and realistic numerical models and large observational programs such as

SO GLOBEC, Palmer LTER, SASSI and MEOP[1]. Models and observations both suggest that mesoscale eddies are the prime mediators of ocean-to-shelf heat transport in some regions of the Antarctic continental margin (*e.g.*, Stewart and Thompson, 2015b; Stewart et al., 2018; Foppert et al., 2019). In some studies (including Chapter 2 of this thesis), eddies do emerge as one of the leading-order contributors to the net on-shelf heat transport, but non-eddying, large-scale motions are also found to be important at seasonal and interannual time scales (see Chapters 2 and 3). What breaks the Taylor-Proudman constraint (hence causing cross-isobath transport) at these scales? Answering this question will likely be an important step in understanding the effects of climate-scale atmospheric forcings and feedbacks on the heat budget of the Antarctic continental shelf, and therefore on continental ice loss and sea level rise.

Over the past 50 years, remarkable progress has been made in the measurement of small-scale turbulent motions by the ocean mixing community, enabling the discovery of new classes of processes and causing paradigm shifts in our theoretical understanding of ocean circulation and energetics (reviewed by *e.g.*, Thorpe, 2004). The field of coastal physical oceanography has found several dynamical insights from novel theories, observations and numerical simulations. The short spatial and temporal scales of turbulence challenge observational efforts, while the dynamically-oriented coastal oceanography studies have focused mostly on subtidal dynamics (reviewed by Lentz and Fewings, 2012). The Inner Shelf Dynamics Departmental Research Initiative (ISDRI, Lerczak et al., 2019) was a recent effort funded by the Office of Naval Research (ONR) that combined several groups and observing platforms to study physical processes in the region inshore of the 50 m isobath and the coupling with the surfzone and the mid-/outer-shelf, seeking to fill some of the existing knowledge gaps in inner-shelf dynamics. Chapters 4 and 5 of this thesis were carried out in the context of this project.

A major motivation for solving the problems mentioned above is that their direct and

---

[1] SO GLOBEC: Southern Ocean Global Ecosystem Dynamics; Palmer LTER: Palmer Long Term Ecological Research; SASSI: Synoptic Antarctic Shelf-Slope Interactions. MEOP: Marine mammals Exploring the Oceans Pole-to-pole.

indirect societal implications, both in Antarctica and in mid-latitude shelves, are far-reaching. Sea level rise-induced migration is projected to affect 600 million to 1.4 billion people by 2100 (Hauer et al., 2019). In addition, the lower limb of the Global Overturning Circulation is directly influenced by heat transport across the Antarctic Slope Current and by the properties of Antarctic Bottom Water and its formation rates, indirectly influencing the entire climate system (Thompson et al., 2018). Regarding mid-latitude shelves, the understanding of cross-shelf exchange and mixing is directly related to the health and resilience of coastal ecosystems, maintenance of fisheries, search and rescue operations and pollutant dispersal, among other activities and livelihoods.

The goal of this thesis is to make specific contributions to the solution of these two problems, by studying the physical mechanisms of cross-slope heat exchange around Antarctica and the turbulence in a mid-latitude continental shelf. To achieve the former, I examine the large-scale pathways of heat transport from the Southern Ocean onto the Antarctic continental margin (Chapter 2) and some aspects of their dynamics (Chapter 3). To achieve the latter, I investigate the observed variability of Reynolds stresses and their potential connection with the momentum balance and inner-shelf circulation at different time scales (Chapter 4) and the transition from geostrophically-balanced to unbalanced motion in the coastal ocean (Chapter 5).

1.2 Outline of the thesis

This thesis is written in manuscript form. Chapters 2 through 5 are self-contained studies on cross-slope exchange and turbulence in the coastal ocean. Chapter 2 quantifies cross-slope transport of heat around the Antarctic Continental Margin (ACM) and examines the associated physical processes in a global eddy-permitting coupled ocean-sea ice model. The contributions to total onshore heat transport from eddy advection, eddy stirring, and mean flow advection vary regionally around the ACM. The time-mean component governs the seasonal variability of the total heat transport and largely cancels the eddy component. Chapter 3 examines the depth-integrated vorticity balance of the same simulation to gain further insight into the dynamics of some of the heat transport processes in the ACM. We find that an approximate balance between the net vertical stress (the surface minus the bottom stress) curl, the planetary vorticity advection and the relative vorticity tendency holds in some marginal seas of the ACM to a higher degree than in others.

Chapters 4 and 5 address questions related to turbulence (both in the microscale and in the mesoscale) in the mid-latitude stratified continental shelf waters off central California. Specifically, Chapter 4 examines the observed variability of Reynolds stresses using moored observations and shows that several physical processes have associated Reynolds stress signatures, including internal bores, shoaling Nonlinear Internal Waves and wind-driven subtidal along-shelf currents. An important implication of Chapter 4's results is that internal waves (both in bore and unbroken forms) may be important drivers of inner-shelf circulation. Turning to the ocean macroturbulence problem, Chapter 5 examines the transition from geostrophically-balanced to unbalanced motion on the continental shelf and shows that the scale of this transition is approximately 12-22 km at the 50 m isobath off California, significantly less than the transition scale found in the deep-ocean part of the California Current System.

Chapter 2

Oceanic heat delivery to the Antarctic continental shelf: Large-scale, low-frequency variability

2.1 Introduction

Basal melting of ice shelves has emerged as the primary driver of continental ice mass loss in Antarctica (*e.g.*, Rignot et al., 2013; Liu et al., 2015). This process has major societal ramifications, as it modulates global sea level rise and its possible acceleration (Nerem et al., 2018; Shepherd et al., 2018). All of the water masses occupying the continental shelf may provide heat to drive melting, including fresh and cold (but seasonally warming) Antarctic Surface Water (AASW) and cold Antarctic Shelf Bottom Water (ASBW) (*e.g.*, Dinniman et al., 2016). However, the warmest shelf water mass is modified Circumpolar Deep Water (mCDW, 2-4°C above the *in situ* freezing point), which is formed when offshore water with higher CDW content enters the continental shelf and is stirred and mixed by the coastal circulation. mCDW is thought to dominate basal melt at seasonal through decadal (Thoma et al., 2008; Jenkins et al., 2016; Cook et al., 2016) time scales. Melting induced by mCDW occurs in regions where it has access to the subglacial cavities of ice shelves, such as in the Amundsen and Bellingshausen Seas (*e.g.*, Jenkins et al., 2016). This view is further supported by the similarities between the spatial structure of the observed trends in ice-shelf thickness (Paolo et al., 2015) and water mass properties in the Weddell and Ross Seas and in West Antarctica: where ice shelves are thinning, both CDW and ASBW are warming, and the CDW core on the adjacent continental slope is shoaling (Schmidtko et al., 2014). Further, recent observations in East Antarctica reveal that mCDW also reaches the Totten (Greenbaum et al., 2015; Rintoul et al., 2016; Silvano et al., 2016) and Moscow University (Silvano et al., 2017) ice shelves through deep cross-shelf troughs, with sufficient heat content to induce melt rates comparable to those found in West Antarctica (Rignot et al., 2013; Greenbaum et al., 2015).

At meso- and sub-mesoscales, evidence has shown that eddies of O(1-5 km) are prime contributors to the onshore mass and heat transports across the continental slope (*e.g.*, Nøst et al., 2011; Stewart and Thompson, 2013, 2015b, 2016; Graham et al., 2016; Stewart et al., 2018, hereafter SKM18), likely via eddy stirring of temperature along isopycnals (Stewart and Thompson, 2016, SKM18). The background Antarctic Slope Current/Undercurrent (ASC/ASUC) flow also plays an important role (Chavanne et al., 2010; Walker et al., 2013; Peña-Molino et al., 2016). In particular, the ASUC vertical structure has been observed to lift the pycnocline above the sill depth of some cross-slope troughs in the southeastern Weddell Sea through thermal wind shear (Chavanne et al., 2010), suggesting that it could play a similar role in other marginal seas. Bottom Ekman transport (Wåhlin et al., 2012; Peña-Molino et al., 2016) and inertial penetration of the Antarctic Circumpolar Current (ACC) onto the shelf (Dinniman and Klinck, 2004; Dinniman et al., 2011) may also be important on the continental slope and shelf break.

Part of the heat delivered to the shelf break by eddies and the background mean flow is channeled farther onshore by cross-shelf troughs, pathways that have been most extensively observed in West Antarctica (*e.g.*, Walker et al., 2007, 2013; Moffat et al., 2009; Nakayama et al., 2013; Wåhlin et al., 2013, 2016; Zhang et al., 2016; Couto et al., 2017; Gunn et al., 2018). Onshore heat transports within these troughs are estimated to be of O(1-10 TW) based on *in situ* observations (Walker et al., 2007; Martinson and McKee, 2012; Wåhlin et al., 2013; Assmann et al., 2013; Ha et al., 2014; Kalén et al., 2015) and idealized or regional numerical simulations (*e.g.*, St-Laurent et al., 2013; Graham et al., 2016). At the circumpolar scale, numerical models have simulated on-shelf transports in the 20-50 TW range across the 1000 m isobath (Dinniman et al., 2015; Goddard et al., 2017, SKM18, Table 2.1).

Although progress regarding the importance of heat transport pathways at meso- and submesoscales has been encouraging, observed long-term trends in shelf temperature (Schmidtko et al., 2014; Jenkins et al., 2016; Cook et al., 2016) suggest that cross-shelf edge heat transport may occur over a range of spatiotemporal scales. Enhanced warming on the Antarctic continental shelf has recently been simulated in global high-resolution climate models (Spence et al., 2014, 2017; Goddard et al., 2017), and results suggest that large-scale atmospheric modes such as the Southern Annular Mode (SAM) may be important drivers of interannual coastal variability at the circumpolar scale. Indeed, Armitage et al. (2018) show that the joint effects of the SAM and the El Niño/Southern Oscillation (ENSO) modulate coastal sea level and the strength of the Antarctic Slope Current (ASC) at seasonal and interannual time scales, which likely influences cross-isobath heat transport. Some of the fastest-melting ice shelves in West Antarctica (those located between the East Ross and West Amundsen Seas) appear to be particularly sensitive to strong El Niños (Paolo et al., 2018). In contrast, farther north in the West Antarctic Peninsula, Martinson et al. (2008) observed a much higher volume of mCDW on the shelf in 1999 (strong La Niña and strong SAM+) relative to 1998 (strong El Niño and moderate SAM+). While a strong La Niña combined with SAM+ events maximizes the response of the Amundsen Sea Low's strength (ASL, Fogt et al., 2011, their Figure 5e), the effects of each El Niño/La Niña on the ASL are different, and this has been suggested to modulate the basal melt of ice shelves (Paolo et al., 2018). This fragmented picture indicates gaps in our understanding of the possible links between climate modes and the oceanic heat transports around the Antarctic margin.

To our knowledge, previous work on this problem using eddy-permitting ocean models has only examined short-duration simulations (SKM18), decadal averages (Spence et al., 2014), or the statistically steady state of the system under a semi-idealized atmospheric forcing (Spence et al., 2014; Dinniman et al., 2015; Goddard et al., 2017). SKM18 found that over most of the Antarctic margin, the tidal and mean onshore heat transports roughly cancel at the shelf break, and the net onshore heat transfer is accomplished by the eddy component in an eddy-resolving model. However, the short duration of their simulation (13 months) precluded an analysis of interannual variability. Investigating the response of the time-varying, large-scale flow to realistic forcing has the potential to improve our understanding and projections of sea level rise and the global overturning circulation (Stewart and Thompson, 2013; Thompson et al., 2014; Ruan et al., 2017).

The central aim of this paper is to quantify the contribution of large-scale pathways to the heat budget of the Antarctic continental margin and the mechanisms associated with its low-frequency variability (seasonal through multidecadal). To achieve this, we perform a circumpolar heat budget analysis along the Antarctic continental margin in a global simulation with realistic atmospheric forcing and coupled ocean and sea ice models. We first describe the model (Section 2.2) and observational tools (Section 2.3). Next, we evaluate model biases by comparing the simulated fields to *in situ* observations in Section 2.4. We then examine the time-averaged along-isobath (Section 2.5.1) and cross-isobath (Section 2.5.1) structure of the cross-isobath heat transport, followed by its seasonal (Section 2.5.2) and interannual (Section 2.5.3) variability and its potential drivers. Finally, in Section 2.6 we summarize our results, discuss some of their implications and present our main conclusions.

Table 2.1: Recent model estimates of time-averaged, circumpolarly-integrated heat transport across the 1000 m isobath (Φ^{circ}, positive onshelf). All ocean models were coupled to associated sea ice models. The two values on the Goddard et al. (2017) study refer to their control and doubled atmospheric CO_2 experiments, respectively. The value for Dinniman et al. (2015) is an average of the last five years of their simulation, where the atmospheric forcing was based on 2010 fields, applied cyclically every model year. The value for the present study is also a five-year average, but is over 2005-2009, as our simulation was forced with the interannually-varying CORE-II atmospheric product.

Study	Φ^{circ}	Resolution	Atmospheric forcing	Ice shelves	Tides	Freshwater
Dinniman et al. (2015)	$\sim$50 TW	10 km	2010 reanalysis (cyclic)	yes	no	yes
Goddard et al. (2017)	$\sim$25-33 TW	4-6 km	Coupled atmosphere	no	no	yes
Stewart et al. (2018)	$\sim$27 TW	<1 km	2011-2012 reanalysis	no	yes	yes
This study	22.2 TW	3.8-4.7 km	Time-varying CORE-II	no	no	no

2.2 The global 0.1°POP simulation

We analyze model fields derived from a global coupled ocean/sea ice simulation based on the Los Alamos Parallel Ocean Program 2 (POP2, *e.g.*, Smith et al., 2010) and Community Ice CodE 4 (CICE4, *e.g.*, Hunke et al., 2010) in the Community Earth System Model (CESM) framework (McClean et al., 2018). The simulation is configured on a global nominal 0.1° tripole grid with 3.8 km-4.7 km horizontal resolution on the Antarctic shelf and 42 vertical levels, with vertical spacing varying from 10 m near the surface to 500 m near the bottom. Partial bottom cells (Pacanowski and Gnanadesikan, 1998) are used to improve the discretization of the bottom topography. The simulation spanned the period 1948-2009, and was forced with the corrected interannually-varying air-sea fluxes from the Coordinated Ocean-ice Reference Experiment version 2 (CORE-II, Large and Yeager, 2009). We analyze the model output only after 1958, allowing for a eleven-year spin-up period. Vertical mixing of temperature and salinity by non-local convection (when the mixed layer is gravitationally unstable) and local diabatic processes was implemented with the K-Profile Parameterization (KPP, Large et al., 1994). Sub-grid scale horizontal mixing is parameterized using biharmonic operators, whose associated coefficients for momentum and tracers vary spatially with the cube of the grid cell size. At the equator, the horizontal mixing coefficients for momentum and tracers have values of -2.7×10^{10}

$m^4\ s^{-1}$ and $-3.0 \times 10^9\ m^4\ s^{-1}$, respectively.

In order to perform regional analyses of the water mass structure and heat transports, we divide the circumpolar Antarctic continental slope (ACS) into ten segments: Ross Sea, Byrd Coast, Amundsen and Bellingshausen Seas, south and north portions of the Western Antarctic Peninsula, Weddell Sea and West, Central and East portions of East Antarctica (Figure 2.1a). Following Goddard et al. (2017), we choose the 1000 m isobath as a proxy for the Antarctic Slope Front (ASF, Figure 2.1b-f). We define the ACS as the closed control volume bounded by the 800 m and 2500 m isobaths (Figure 2.1a). The ACS volume was used to calculate spatial averages of the *in situ* observations and to ensure that the discrete cross-ASF heat transport calculations are consistent with a numerically closed heat budget (See supporting information, Figure S1).

Realistic representation of mesoscale and submesoscale eddies is made difficult by the small internal deformation radius, which typically decreases from 10 km to 4 km across the Antarctic continental slope (*e.g.*, Moffat et al., 2009; Stewart and Thompson, 2013). A horizontal resolution of ∼1 km is needed to fully resolve eddies on the continental slope and shelf (St-Laurent et al., 2013; Stewart and Thompson, 2015b; Graham et al., 2016, SKM18). Our simulation's resolution is therefore eddy-permitting, and we limit ourselves to analyzing the low-frequency (multiannual to multidecadal, spanning 1959-2009) variability of the large-scale, O(100-1000 km) cross-isobath transports.

Evidently, the circumpolar integral of the total cross-isobath heat transport is constrained by the area integral of the surface heat flux within the closed isobath, which will necessarily account for the similarities and differences of the circumpolar heat transport among independent simulations (Table 2.1). The segment-averaged eddy component of the heat transport is O(1 MW/m) in our simulation (Figure S6), as is SKM18's (their Figure 2), even though our eddy kinetic energy levels are typically a factor of 10 smaller along the 1000 m isobath (Figures 2.1d and 2.7e) and our model has no tidal circulation.

Two other important limitations to point out are the absence of tides and ice shelves.

Regarding tides, SKM18 find that although the eddy heat transport is more important along the continental slope, tides contribute a larger onshore heat transport than eddies at the shelf break in their eddy-resolving simulation. Ice shelves play a role in the heat budget of the system both directly as a boundary sink, and indirectly as a source of potential energy for the coastal circulation, which may in turn modify the advective heat transports across the shelf break and their convergences/divergences within the continental shelf. We find that a heat transport of 14 TW into the circumpolar system is required to account for Rignot et al. (2013)'s estimate of 1325 Gt/year of ice shelf meltwater production, using a latent heat of melt of $L_f = 334$ kJ/kg (*e.g.*, Jourdain et al., 2017). This amounts to 71% of the 19.7 TW we find for the time-averaged (1959-2009) circumpolar onshore heat transport, and this heat must be released to the atmosphere in the absence of thermodynamically active ice shelves (the heat tendency term averages to a small number in the long-term mean). Also, the missing density gradients due to the absence of ice shelves and freshwater imply that some of the heat that is available on the continental slope but is not brought onto the shelf in this simulation might be if ice shelves are introduced, since their effect on the circulation can be substantial (*e.g.*, St-Laurent et al., 2013; Dinniman et al., 2015; Jourdain et al., 2017). In a future contribution, we will compare our present results with a global eddy-resolving POP/CICE simulation (1-2 km resolution on the Antarctic continental margin) with climatological freshwater fluxes of ice-shelf melting and iceberg calving derived from observations (Hammond and Jones, 2016).

2.3 The MEoP CTD observations

We evaluate the realism of the model fields using Conservative Temperature (Θ) and Absolute Salinity (S_A) profiles derived from the Marine Mammals Exploring the Oceans Pole to Pole (MEoP) dataset (*e.g.*, Roquet et al., 2014, Figure 2.1a). Each tagged animal carries a Conductivity, Temperature and Depth Satellite Relay Data Logger (CTD-SRDL), and records

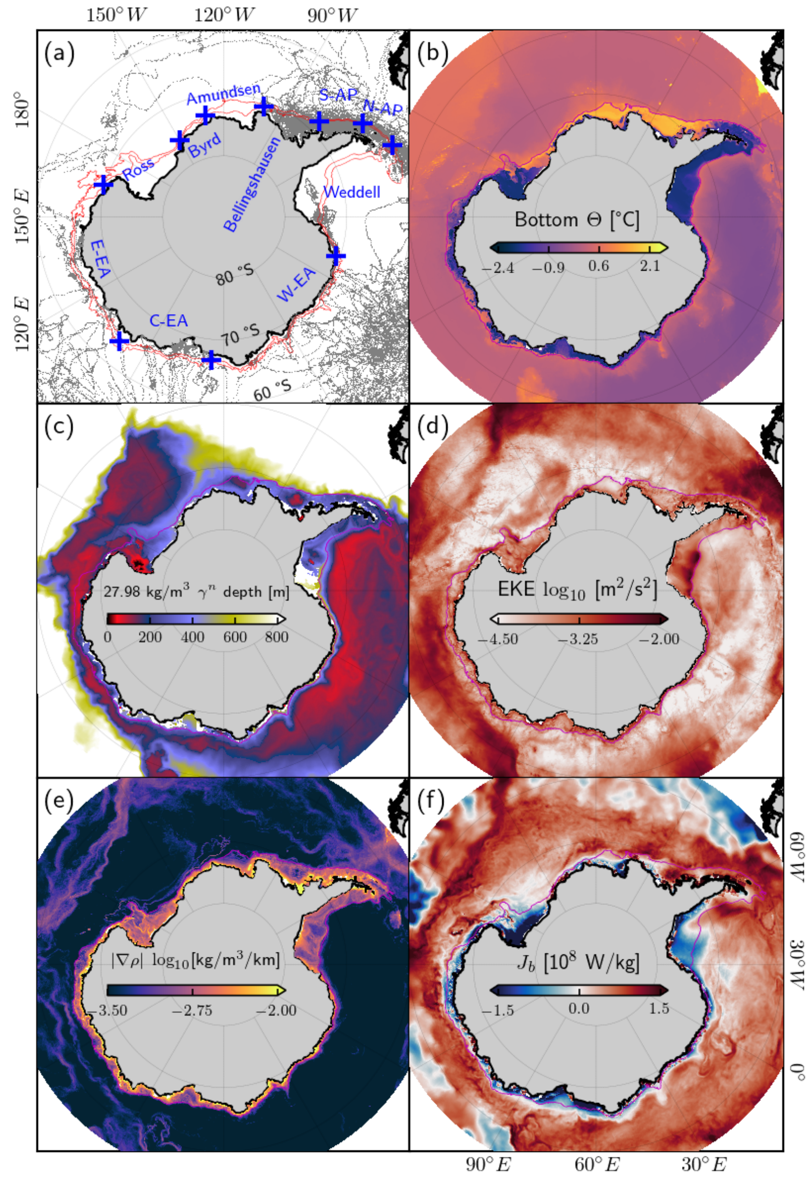

Figure 2.1: Definition of the sub-regions analyzed, distribution of *in situ* data and model horizontal variability in the Antarctic continental slope (ACS). **(a):** Segments chosen to partition the ACS. The red contours are the 800 m and 2500 m isobaths, and blue crosses demarcate boundaries between segments. Gray dots indicate the locations of the *in situ* hydrographic profiles (MEoP dataset). S-AP and N-AP: South and North Antarctic Peninsula. E-EA, C-EA and W-EA: East, Central and West portions of East Antarctica. **(b-f):** Time-averaged (2005-2009) horizontal model fields. **(b):** Bottom Conservative Temperature (Θ). **(c):** Depth of the 1027.98 kg m^{-3} neutral density surface. **(d):** Logarithm of depth-averaged Eddy Kinetic Energy (EKE). **(e):** Logarithm of depth-averaged lateral density gradient magnitude ($|\nabla\rho|$). **(f):** Surface buoyancy flux (J_b), positive where the ocean becomes more buoyant. The magenta contour in (b-f) is the 1000 m isobath.

data during the ascent of each dive. Only the deepest dive in a six-hour interval is transmitted, with 10 to 25 data points per profile (Roquet et al., 2014). The accuracy of the ARGOS geopositioning system is $\sim$5 km. Different calibration procedures are applied to the post-processed data depending on the availability of nearby shipboard observations and the water masses sampled in the profile (Roquet et al., 2011), therefore error estimates for individual deployments have not been attempted (Roquet et al., 2014). As a result, the post-processed *in situ* profiles have variable instrumental errors and calibration uncertainties. Profiles measured in 2007 or more recently are estimated to be accurate to ± 0.03°C for *in situ* temperature (T) and ± 0.05 psu for practical salinity (S_p), while pre-2007 profiles have accuracies of 0.1°C and 0.1 psu (Roquet et al., 2014). Although only 10% of the profiles used in our analyses were measured before 2007, we estimate uncertainties in results derived from the observed profiles by making the most conservative assumptions, namely ± 0.1°C for T and ± 0.1 for S_p (Roquet et al., 2014).

2.4 The circumpolar water mass structure

Intrusions of modified Circumpolar Deep Water (mCDW) are ultimately regulated by the availability of CDW on the continental slope. Therefore, prior to calculating the circumpolar heat budget it is desirable to evaluate the realism of the simulated water mass structure along the Antarctic continental slope, especially the depth and temperature of the CDW. To achieve this, we compare simulated and observed Θ and S_A profiles along the Antarctic continental slope (ACS) to evaluate the model representation of the water mass structure across individual segments of the ACS. The observed profiles are interpolated onto the model vertical grid, and then simulated and observed profiles are both time-averaged for the 2005-2009 period and spatially-averaged within the segments that have a higher density of MEoP profiles (Bellingshausen, S-AP, N-AP, W-EA, C-EA and E-EA, see Figure 2.1a). This approach enables the spatial averaging of the *in situ* profiles necessary to obtain statistically meaningful comparisons with the model fields.

The section of model Conservative Temperature above the freezing point ($\Theta - \Theta_f$, Figure 2.2a) reveals warm CDW (up to 4°C above the freezing point), and overlying cold Antarctic Surface Water (AASW). The model 1027.98 kg m^{-3} isoneutral surface (a surface of same neutral density γ^n), which is a proxy for the model CDW layer is 0-200 m deeper than observed (red and blue dots in Figure 2.2a). In the CDW layer, the model overestimates Θ by $\sim$0.5°C in the Bellingshausen Sea and in East Antarctica (Figure 2.2b,c,e,g).

This near-ubiquitous warm bias in model CDW is comparable to that found in the Amundsen Sea shelf by Jourdain et al. (2017) in their regional implementation of the Nucleus for European Modelling of the Ocean (NEMO) ocean/sea ice model with static ice shelves. They attributed the warm bias of $\sim$0.5-1.1°C to a more stratified thermocline caused by an overestimated amplitude of the sea ice formation/melting seasonal cycle. This intensified sea ice seasonal cycle is also found in the present simulation (Figure S2), and is a known bias of global simulations under CORE-II IAF forcing (Downes et al., 2015). The biases in the cold and fresh end of the $\Theta - S_A$ curve (the AASW layer) are less consistent. The thermocline stratification is well represented in most segments, with simulated and observed Θ-S_A curves often being statistically indistinguishable away from the CDW and AASW layers (Figure 2.2b-g).

Although this model-observation comparison is encouraging, the AASW and CDW layers are the dominant sources of oceanic heat. We thus expect the model biases in the vertical water mass structure to impact our estimates of cross-isobath heat transport. The depth-averaged difference between the simulated and observed temperatures ($\overline{\Theta_{\text{mod}} - \Theta_{\text{obs}}}^z$) is up to 0.3°C, or 11% of $\overline{\Theta_{\text{obs}} - \Theta_f}^z$, where $\overline{\bullet}^z$ indicates a depth average. With the circulation unchanged, a 10% warm bias translates into a 10% heat transport bias (Equation 2.1), *e.g.*, a $\sim$2 TW error for a 20 TW model circumpolar heat transport. However, the model cross-slope velocity bias is unknown, and it is therefore unclear whether the real on-shelf heat transport is being over- or under-estimated.

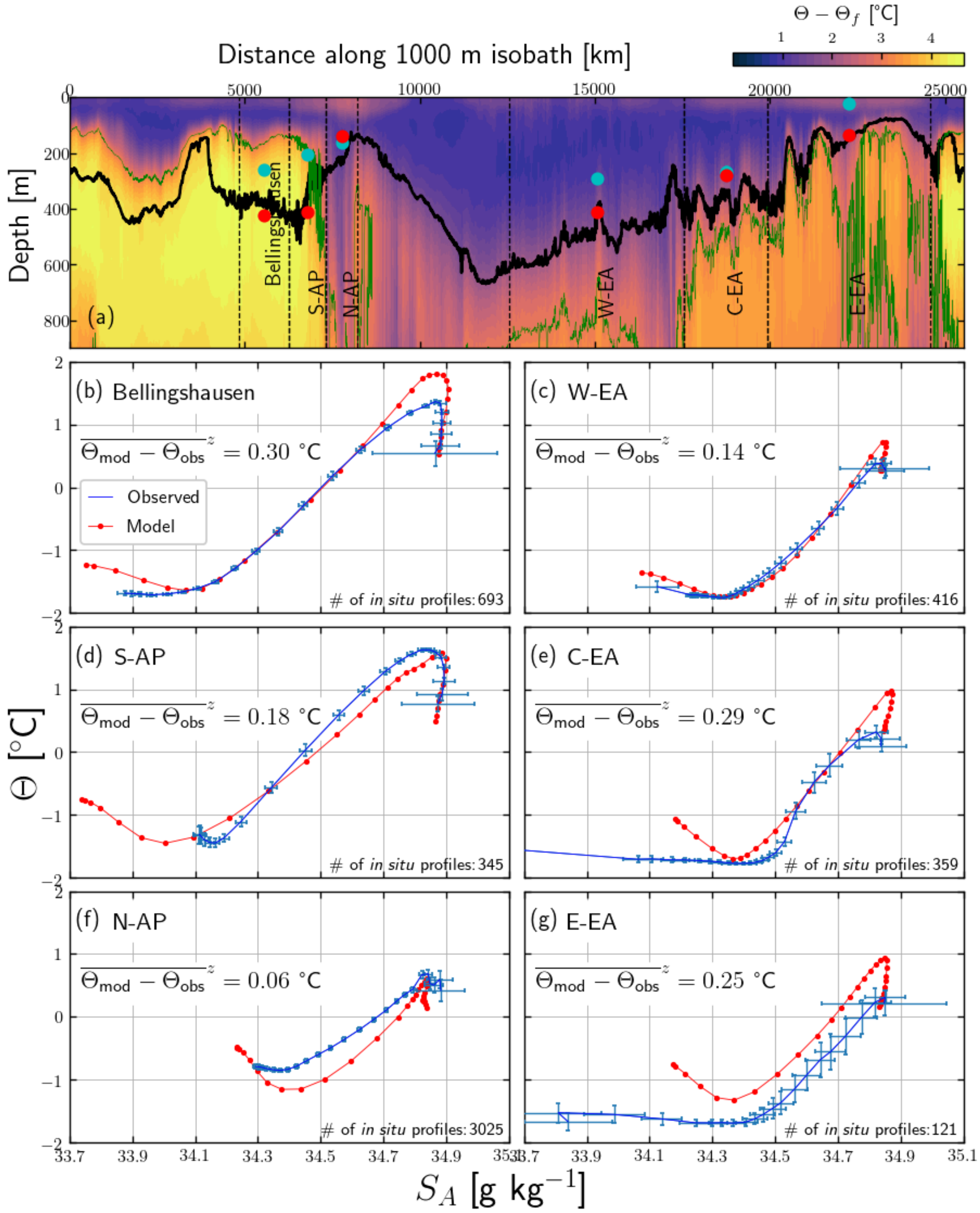

Figure 2.2: Model-data comparison of the time-averaged (2005-2009) water mass structure along the Antarctic continental slope (ACS). **(a)** Section of model Conservative Temperature above the freezing point ($\Theta - \Theta_f$) along the 1000 m isobath. The green contour is the $\Theta - \Theta_f =$ 3°C isoline. The black contour is the 1027.98 kg m^{-3} model isoneutral, whose spatially-averaged depth within each segment is indicated by the red (model) and blue (observed) dots. The only segment where the model and observed isoneutral depths are statistically indistinguishable is C-EA. **(b-g)** Conservative Temperature-Absolute Salinity (Θ-S_A) diagrams. The blue errorbars indicate the 95% confidence intervals about the observed Θ and S_A mean profiles. The number of observed profiles on each segment and the depth-averaged difference between model and observed temperatures ($\overline{\Theta_{\text{mod}} - \Theta_{\text{obs}}}^z$) are also shown on each panel. Spatial averages are calculated only for six of the segments of the ACS defined in Figure 2.1a.

2.5 The cross-shelf break heat transport along the Antarctic continental margin

We define the total heat transport relative to the freezing point as

$$\Phi(y) \overset{\text{def}}{=} \rho C_p \int_{-h}^{0} u(y,z')[\theta(y,z') - \theta_f]\, dz', \tag{2.1}$$

where y and z are the along-isobath and vertical coordinates, respectively, and z' is a dummy integration variable parallel to z; $u(y,z)$ is the cross-isobath velocity (positive onshore); C_p is the heat capacity of seawater; ρ is the potential density referenced to 0 dbar; $\theta(y,z)$ is the potential temperature referenced to 0 dbar; and θ_f is the θ at which seawater freezes. In the presentation of the model results, we replace Θ with θ, because θ is the model temperature variable. The density ρ is set to 1026 kg m^{-3} and C_p is set to 3996 J $\text{kg}^{-1}{}^{\circ}\text{C}^{-1}$ to be consistent with the simulation. The product $u(y,z,t)\theta(y,z,t)$ is accumulated at each model time step. However, since neither the quantity $\theta(y,z,t) - \theta_f(y,z,t)$ nor the product $u(y,z,t)\theta_f(y,z,t)$ were saved, we follow Goddard et al. (2017) and set θ_f to the minimum freezing temperature found along the 1000 m isobath in the simulation ($\theta_f = -2.64$°C). This means that the quantity $\rho C_p[\theta(y,z) - \theta_f]$ must be interpreted as an upper bound (*i.e.*, warmest value) for the melting potential of the intruding water masses. Setting θ_f to its minimum value also ensures that the volume and heat transports are in the same direction, facilitating the interpretation of our results.

We break Φ into eddy (Φ^{eddy}) and time-mean (Φ^{mean}) components, *i.e.*, $\Phi^{\text{eddy}} \overset{\text{def}}{=} \Phi - \Phi^{\text{mean}}$, where Φ^{mean} is calculated offline using the monthly-averaged velocity and temperature fields. This decomposition separates the eddying variability (any motion with period shorter than 30 days) from the lower-frequency variability. Motions such as barotropic Kelvin waves (Kusahara and Ohshima, 2014; Spence et al., 2017) and partially resolved mesoscale eddies project onto Φ^{eddy}, while Φ^{mean} captures very low-frequency continental shelf wave modes (Kusahara and Ohshima, 2009), Ekman transports and seasonal variability, including its interannual changes over the analyzed period (1959-2009). We point out that since the outputs for the full time span of the simulation are available in monthly-averaged fields, any averaging period that is a multiple of a month is possible. The choice of 1 month (as opposed to *e.g.*, 1 year or 1959-2009) is made in order to avoid including the seasonal variability in Φ^{eddy}. Seasonality is instead projected on Φ^{mean}.

In order to examine possible physical mechanisms associated with Φ^{eddy}, we follow Stewart and Thompson (2016, hereafter ST16) and further split Φ^{eddy} into contributions from eddy advection ($\Phi^{\text{eddy}}_{\text{adv}}$) and eddy stirring ($\Phi^{\text{eddy}}_{\text{stir}}$), with

$$\Phi^{\text{eddy}}_{\text{adv}} \overset{\text{def}}{=} \rho C_p \int_{-h}^{0} \overline{u^{\text{eddy}}}(z') \left[\overline{\theta}(z') - \theta_f\right] dz', \tag{2.2}$$

where $u^{\text{eddy}} = -\partial_z \psi^{\text{eddy}}$ and ψ^{eddy} is the Neutral Density Transformed Eulerian Mean (NDTEM) overturning streamfunction (Stewart and Thompson, 2015a), defined as

$$\psi^{\text{eddy}} \overset{\text{def}}{=} \frac{\overline{\beta}\,\overline{u'S_p'} - \overline{\alpha}\,\overline{u'\theta'}}{\overline{\beta}\,\partial_z \overline{S_p} - \overline{\alpha}\,\partial_z \overline{\theta}}, \tag{2.3}$$

where $\overline{\alpha} = \alpha(\overline{S_p}, \overline{\theta}, p)$ is the thermal expansion coefficient, $\overline{\beta} = \beta(\overline{S_p}, \overline{\theta}, p)$ is the haline contraction coefficient, u is the cross-isobath transport, S_p is practical salinity and θ is potential temperature. Overbars ($\overline{\bullet}$) indicate averaging in the along-isobath direction (along the length of the segment considered) and in time (over each month). Primes ($\bullet'$) indicate departures from this average.

Equation 2.3 is analogous to the eddy thickness fluxes of the Gent-McWilliams parameterization (Gent and McWilliams, 1990) in models that do not resolve eddies. Motivated by this analogy, we follow ST16 and define $\Phi^{\text{eddy}}_{\text{stir}}$ as the difference $\Phi^{\text{eddy}} - \Phi^{\text{eddy}}_{\text{adv}}$. In this decomposition, the quantity $\Phi^{\text{eddy}}_{\text{adv}}$ is the heat carried by eddy motions via advection of warmer or colder water masses across the isobath (*i.e.*, the eddy overturning circulation) and is associated with a nonzero thickness (hence volume) flux. In contrast, $\Phi^{\text{eddy}}_{\text{stir}}$ is not linked to any net volume transport, and therefore measures the heat transport due to stirring of potential temperature along isoneutral surfaces (ST16).

2.5.1 The time-mean (1959-2009) circumpolar structure

Along-isobath distribution of on-shelf heat transports

We now search for persistent on-shelf heat penetration pathways on the Antarctic continental margin by examining the time-averaged (1959-2009) spatial structure of the mean (Φ^{mean}) and eddy (Φ^{eddy}) components of the total (Φ) heat transport across the 1000 m isobath. Both Φ^{mean} and Φ^{eddy} have rich spatial structures that generally mirror one another (Figure 2.3a,b). The net circumpolar transports Φ^{mean} and Φ^{eddy} (averaged over 1959-2009) are 4.6 TW and 15.1 TW, respectively, for a total of 19.7 TW. The total heat transport averaged over the 2005-2009 period is 22.2 TW, comparable to other recent model estimates (Table 2.1).

Figure 2.3a-c shows the time-averaged Φ^{mean}, Φ^{eddy} and Φ as functions of distance along the 1000 m isobath. The widespread cancellation between onshore and offshore heat transport in along-isobath bands is evident, especially in East Antarctica. There is also consistent cancellation between Φ^{mean} and Φ^{eddy}, which leaves small onshore or offshore Φ residuals, sometimes along O(100-1000 km) segments (Figure 3b). For example, in the Bellingshausen, East Amundsen and east end of E-EA (later called the Oates sub-segment), Φ is onshore (gray stripes and black line in Figure 3b). These hotspots of enhanced heat transport are often collocated with abrupt topographic features (Figure 2.3f), as previously found in model studies (Graham et al., 2016; Goddard et al., 2017, SKM18) and observations (*e.g.*, Ha et al., 2014; Kalén et al., 2015).

In addition to these sites of preferred cross-isobath heat transport, the along-shelf divergence of the heat transport across adjacent segments of the Antarctic continental shelf (Figure 2.3d) appears to be an important pathway for heat delivery (where there is convergence) or sequestration (where there is divergence). The along-shelf divergence of the heat transport partly or almost completely compensates for the incoming offshore heat in some segments (Ross, Byrd, S-AP, N-AP and W-EA), while in other segments along-shelf convergence adds to the oceanic on-shelf heat input (Amundsen, Bellingshausen, C-EA and E-EA, Figure 2.3d). For instance, an average of 2.76 TW enters the Amundsen segment from the Byrd segment, but only 2.08 TW exit the Amundsen segment across its boundary with the Bellingshausen segment. Combined with the incoming 0.96 TW crossing the 1000 m isobath, there is a total 1.64 TW of advective heat convergence within the Amundsen Sea segment (in the 1959-2009 mean). Rodriguez et al. (2016) find a 2005-2009 average total heat transport convergence of 1.15 TW in the Amundsen segment (their Table 2) in the coarser (1/6°) Southern Ocean State Estimate (SOSE). This is comparable to the 1.78 TW in the 2005-2009 POP average (not shown).

The time-averaged on-shelf volume transport U_{onshelf} within each segment is typically less than 1 Sv, and does not appear to follow the time averages of Φ^{mean}, Φ^{eddy} or Φ in a regular fashion across segments (Figure 2.3d,e). In time, however, U_{onshelf} turns out to be very strongly anti-correlated with Φ^{eddy} in all segments at 10 months lag, and moderately correlated with Φ^{mean} in most segments at 10 months lag (Table S1). While the mechanism involved in the strong control of Φ^{eddy} by U_{onshelf} is unclear, the small net U_{onshelf} is consistent with an isobath-following mean geostrophic flow, and suggests that eddy momentum flux convergence is playing an important part in the cross-isobath overturning circulation, as noted by SKM18 in the East Antarctic sector of their simulation.

Except for the Ross, C-EA and E-EA segments, the segment-averaged Φ^{mean} and Φ^{eddy} are in opposite directions. Breaking down the vertically-integrated transport in surface (0 - 100 m), bottom (700 m - 1000 m) and interior (100 m - 700 m) layers reveals that Φ^{mean} and Φ^{eddy} partially cancel each other throughout most of the system, especially in the top and bottom layers (Figure 2.3c). SKM18 find a similar cancellation between the net onshore tidal and offshore mean heat fluxes in their eddy- and tide-resolving simulation. The contribution of the surface Ekman transport to the onshore circumpolar heat transport can be estimated as

$$\Phi_{\mathrm{Ek}}^{\mathrm{mean}} = -L_{\mathrm{circ}} C_p (\Theta - \Theta_f) \frac{\tau_{\mathrm{circ}}^{y}}{f}, \tag{2.4}$$

where $\Theta - \Theta_f$ = 1.43°C is the Conservative Temperature above the freezing point averaged in the top 25 m (Figure 2.2a), $f = -1.36 \times 10^{-4}$ s^{-1} is the inertial frequency and τ_{circ}^{y} = -0.036 Pa is the along-isobath wind stress. These values are along-isobath circumpolar averages, $C_p = 3996$ J kg^{-1}°C^{-1} is the specific heat capacity of seawater and $L_{\mathrm{circ}} = 25520$ km is the total length of the 1000 m isobath. This yields an estimate of $\Phi_{\mathrm{Ek}}^{\mathrm{mean}} = 33.7$ TW. This suggests that the time-mean heat transport in the upper 100 m (Figure 2.3c) is mostly due to Ekman transport, as SKM18 find in their simulation.

Cross-slope overturning circulation and heat transport structure

In contrast with an idealized, along-shelf-uniform continental shelf/slope model (*e.g.*, ST16), flow properties in POP around the Antarctic continental margin are very noisy and sensitive to the along-shelf location being examined. We therefore present cross-shelf profiles and sections of along-shelf averaged quantities (within sub-regions of the segments in Figure 2.1a), rather than at specific along-shelf locations. In this section we discuss three representative sub-segments as case studies (Figure 2.4), occasionally referring to the other sub-segments (Figures S9 and S10). The cross-slope heat transport components and the mean (ψ^{mean}) and eddy (ψ^{eddy}) streamfunctions are plotted as functions of the pseudo-cross-isobath coordinate $x^{\star}$, defined by SKM18 as

$$x^{\star}(h_0) \overset{\mathrm{def}}{=} \frac{1}{L_y} \iint_{h<h_0} 1\, dA, \tag{2.5}$$

where $h(x,y)$ is the bottom depth, $z = -h_0$ is a specific isobath and dx, dy and $dA = dx\,dy$ are cross-isobath, along-isobath and horizontal area elements, respectively. Ultimately, $x^{\star}$ is the distance along the profile of $h(x)$ averaged within each sub-segment's length L_y. As such, it

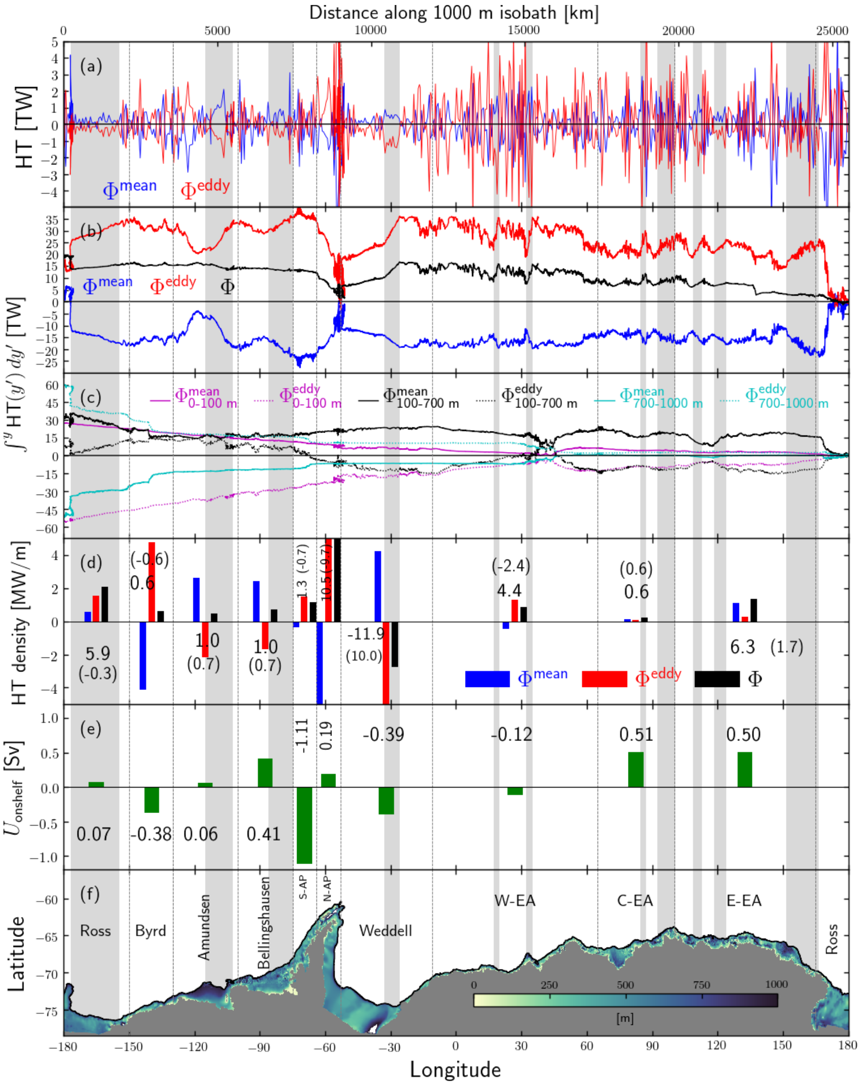

Figure 2.3: Time-averaged (1959-2009) cross-isobath heat transport (HT, positive on-shelf) along the Antarctic continental slope (1000 m isobath). **(a)** Vertically-integrated (0-1000 m) mean (Φ^{mean}) and eddy (Φ^{eddy}) components of the total cross-1000 m heat transport, Φ. **(b)** Along-isobath cumulative sums (from east to west) of Φ^{mean}, Φ^{eddy} and Φ. **(c)** Mean and eddy contributions to the heat transport integrated within the top (0-100 m), middle (100-700 m) and bottom (700-1000 m) layers, also cumulatively summed from east to west. **(d)** Along-isobath averages of Φ, Φ^{mean} and Φ^{eddy} for each segment (vertical bars); Φ integrated over the segment (non-bracketed numbers); and along-shelf convergence of the along-shelf heat transport within the segment (bracketed numbers). **(e)** Total cross-isobath volume transport within each segment ($U_{onshelf}$, positive on-shelf). **(f)** Bottom topography inshore of the 1000 m isobath (black line). The vertical dashed lines demarcate the segments defined in Figure 2.1a. The gray shaded areas mark some of the heat intrusion pathways that are O(100 km) or larger. The cumulative sums in (b) and (c) are calculated westward starting from 180°E in order to follow the prevailing direction of the shelf and slope currents.

captures the mean cross-slope topography for each segment. We examine the along-shelf averages of the mean streamfunction

$$\psi^{\mathrm{mean}}(x^{\star}, z) \overset{\mathrm{def}}{=} \int_{z}^{0} \overline{u}(x^{\star}, z')\, dz', \tag{2.6}$$

where again $\overline{\bullet}$ indicates an along-isobath and time average and u is the cross-slope velocity. For the eddy streamfunction ψ^{eddy}, we take the along-shelf median instead of the mean because ψ^{eddy} is a noisy variable, as it is inversely proportional to (often large) vertical gradients of salinity and temperature (Equation 2.3).

Both components of the cross-slope overturning circulation (ψ^{mean} and ψ^{eddy}) tend to reinforce one another (as ST16 find in their idealized model) instead of cancelling out (Figures 2.4, S9, S10), with the exceptions of the deeper half of the slope on the East Amundsen (Figure 2.4), Amery and Central Weddell (Figures S9, S10) segments. This result stands in contrast with the prevalent cancellation of Φ^{mean} and Φ^{eddy} both locally (Pearson's correlation coefficient r = -0.97 significant at the α = 99% confidence level, Figure 2.3a,b) and in the segment-averaged sense (Table S1), which implies that there is some cancellation between the eddy advection ($\Phi^{\mathrm{eddy}}_{\mathrm{adv}}$, Equation 2.2) and eddy stirring ($\Phi^{\mathrm{eddy}}_{\mathrm{stir}}$) contributions to Φ^{eddy} along the 1000 m isobath. The mean overturning circulation occupies the entire water column in all sub-segments, and as a result, its sense determines the direction of Φ^{mean}: where ψ^{mean} is clockwise (negative, red shading in Figure 2.4f), warmer waters at depth (with higher CDW content) move up-slope towards the shelf, while the cooler overlying waters (with higher AASW/WW content) move offshore (Figure 2.4j,k,l). Conversely, when the circulation is counter-clockwise (positive, blue shading in Figure 2.4d,e), the opposite happens, and the net heat flux is offshore.

We now examine the advective ($\Phi^{\mathrm{eddy}}_{\mathrm{adv}}$) and stirring ($\Phi^{\mathrm{eddy}}_{\mathrm{stir}}$) contributions to Φ^{eddy} (Figure 2.4a,b,c) in order to seek further insight into the processes responsible for eddy heat transfer and how they differ around the Antarctic continental margin. In the Oates sub-segment, we find that onshore eddy thickness fluxes (positive $\Phi^{\mathrm{eddy}}_{\mathrm{adv}}$ and counter-clockwise ψ^{eddy}, Figure

2.4a,g) transport heat from the CDW core at mid-depth away from the continental slope up to the $\sim$2000 m isobath, where isoneutral eddy stirring becomes dominant (positive $\Phi^{\text{eddy}}_{\text{stir}}$, Figure 2.4a), transferring heat all the way to the shelf edge ($\sim$500-1000 m isobath), qualitatively consistent with ST16's along-shelf uniform simulation. In the East Ross, $\Phi^{\text{eddy}}_{\text{stir}}$ dominates the onshore Φ^{eddy} over the entire continental slope (Figure 2.4b), possibly as a result of the enhanced mid-depth cross-slope temperature gradient produced by the thin counter-clockwise eddy overturning cell at the level of the CDW core ($\sim$500 m, Figure 2.4h,k). In the East Amundsen sub-segment, the warm CDW tongue that penetrates far onto the shelf has a complicated overturning pattern (possibly because of its comparatively short along-shelf averaging length), and the on-shelf heat transport is accomplished mainly by a clockwise ψ^{mean}, with some reinforcement from the weakly clockwise ψ^{eddy} at the CDW level over the upper slope and outer shelf (Figure 2.4c,f,i,l).

The remaining sub-segments (Maud, Amery, West Ross, West Byrd, East Bellingshausen and Central Weddell, Figures S9-10) feature both similarities and differences compared to the ones in Figure 2.4. The main similarities are that the direction of Φ^{mean} closely follows the sense of ψ^{mean} across the slope, that most of Φ^{eddy} and Φ^{mean} cancel out at all across-slope locations and the presence of intense clockwise ψ^{eddy} cells in the upper $\sim$100 m (possibly the response of the mixed layer to the weather-band variability of the air-ice-ocean fluxes). However, note that Equation 2.2 gives only an estimate of $\Phi^{\text{eddy}}_{\text{adv}}$ (and hence $\Phi^{\text{eddy}}_{\text{stir}}$), as Equation 2.3 itself is an asymptotic approximation to the eddy streamfunction in the Boussinesq case (see Stewart and Thompson, 2015a).

The full-depth character of ψ^{mean} is evident in all sub-segments analyzed (panels d-f of Figures 2.4, S9-10). Combined with the approximate cancellation of the cross-slope mean heat transports within the near-surface and near-bottom layers (solid magenta and cyan lines in Figure 2.3c), this pattern indicates an approximately two-dimensional wind-driven mean circulation, with opposing Ekman transports within the top and bottom boundary layers, while the net heat transport is carried out by the eddies in the CDW layer within the geostrophic interior. This dynamical model is similar to that suggested by observational evidence from the Northwestern Weddell Sea (Thompson et al., 2014) and by ST16's numerical results, although our simulation's lower eddy kinetic energy levels under-estimates ψ^{eddy} and Φ^{eddy}.

2.5.2 The 1959-2009 mean seasonal cycle

The seasonal cycles of the wind stress and the surface heat and buoyancy fluxes suggest that the lateral heat advection across and along isobaths may be coupled to these forcings. Indeed, the water mass structure has been observed to have strong seasonal variability in several segments of the ACS, including the regions off the Adélie Coast in East Antartica (Snow et al., 2016) and the Central Amundsen (Wåhlin et al., 2013), East Amundsen (Mallett et al., 2018), Ross (Castagno et al., 2017) and East Weddell (*e.g.*, Ryan et al., 2017) Seas. With the exception of the Adélie Coast, these regions show a greater presence of warm CDW-influenced water on the shelf during summer and early fall. Can this variability be related to a seasonality in the circumpolarly-integrated on-shelf heat transport? We approach this question by examining the climatological eddy ($\overline{\Phi^{\mathrm{eddy}}}$), mean ($\overline{\Phi^{\mathrm{mean}}}$), and total ($\overline{\Phi}$) heat transport components (Figure 2.5a), and their anomalies relative to the annual mean (Figure 2.5b). Hereafter, all overbars ($\overline{\bullet}$) indicate circumpolarly-integrated or averaged variables. Clearly, $\overline{\Phi^{\mathrm{mean}}}$ (not $\overline{\Phi^{\mathrm{eddy}}}$) dominates the seasonal variability of $\overline{\Phi}$ in the 1959-2009 mean seasonal cycle. This disparity is not as evident regarding the seasonality of the along-isobath averages of Φ^{mean} and Φ^{eddy} within each segment (Figure S3). $\overline{\Phi}$ ranges from -17 TW in May to 48 TW in February, which is approximately the same timing found by Dinniman et al. (2015, their Figure 12). At zero lag, $\overline{\Phi^{\mathrm{mean}}}$ is positively correlated both with the circumpolar Ekman transport divergence ($\overline{W_{\mathrm{ek}}}$, r = 0.82 significant at $\alpha = 99.9\%$) and surface buoyancy flux ($\overline{J_b}$, r = 0.68 at $\alpha = 99.9\%$). In contrast, $\overline{\Phi^{\mathrm{eddy}}}$ correlates weakly with both variables at zero lag (r = 0.03 with $\overline{W_{\mathrm{ek}}}$, not significant at $\alpha = 50\%$ and r = 0.26 with $\overline{J_b}$, significant at $\alpha = 99.9\%$). However, $\overline{\Phi^{\mathrm{eddy}}}$ has maximum correlation at 5 months lag with $\overline{W_{\mathrm{ek}}}$ (r = -0.40 significant at $\alpha = 99.9\%$) and at 7 months lag with $\overline{J_b}$ (r = -0.61 significant at

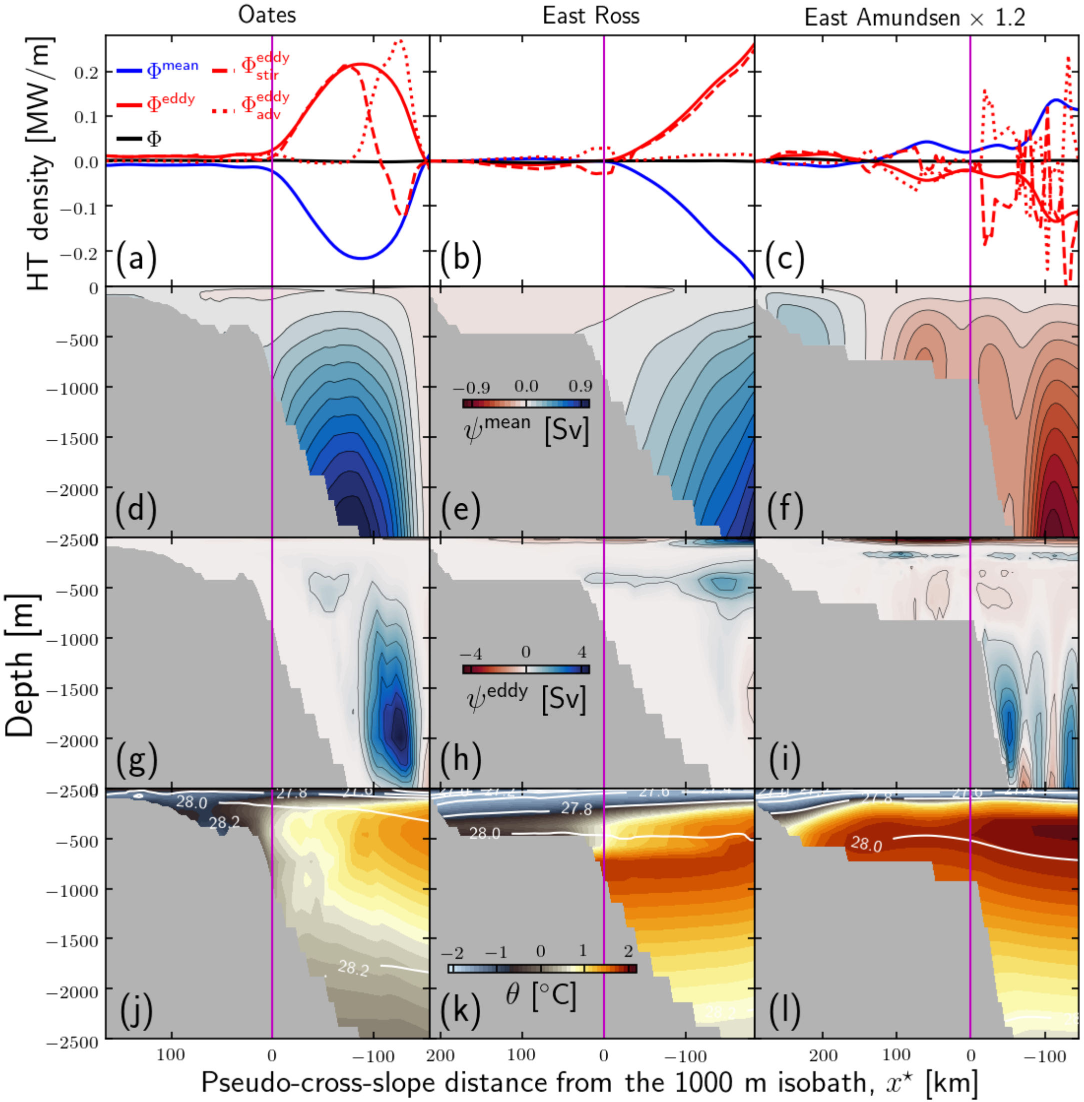

Figure 2.4: Time-averaged (1959-2009) and along-shelf-averaged sections of the components of the heat transport (HT, positive onshore), mean and eddy overturning stream functions and potential temperature (θ) at sub-segments Oates (135°E to 150°E), East Ross (180°W to 155°W) and East Amundsen (115°W to 110.5°W), see Figure 2.1a. **(a,b,c):** Time-mean (Φ^{mean}), eddy advection $\Phi^{\text{eddy}}_{\text{adv}}$, eddy stirring $\Phi^{\text{eddy}}_{\text{stir}}$ and total eddy ($\Phi^{\text{eddy}} = \Phi^{\text{eddy}}_{\text{adv}} + \Phi^{\text{eddy}}_{\text{stir}}$) contributions to the total pseudo-onshore heat transport per unit along-shelf length, Φ. To facilitate comparison, the heat transport components for the East Amundsen (c) sub-segment are multiplied by 1.2. **(d,e,f):** Mean overturning stream function, $\psi^{\text{mean}}(x^{\star}, z)$. **(g,h,i):** Eddy overturning stream function, $\psi^{\text{eddy}}(x^{\star}, z)$. The abscissa on all panels is a pseudo-cross-isobath coordinate, $x^{\star}$ (see Section 2.5.1). Red indicates clockwise circulation, which tends to be linked to positive (onshore) heat transport. Note that the existence of open streamfunction contours is a result of the along-shelf averaging. **(j,k,l):** Cross-slope potential temperature, θ with the γ^n - 1000 isoneutrals overlaid (white contours). The vertical magenta lines across the panels indicates the along-shelf mean position of the 1000 m isobath.

$\alpha = 99.9\%$).

Although it is difficult to interpret the differences in the lags of maximum correlation between these quantities, the analyses above shows that both wind and buoyancy forcing may have a causal link with $\overline{\Phi}$, and that $\overline{\Phi^{\mathrm{mean}}}$ accounts for most of the variance in $\overline{\Phi}$. Is there a dominant forcing mechanism? Breaking $\overline{J_b}$ into its heat ($\overline{J_{\mathrm{SHF}}}$) and freshwater ($\overline{J_{\mathrm{SFWF}}}$) components reveals that $\overline{J_{\mathrm{SFWF}}}$ is $\sim$2-10 times larger than $\overline{J_{\mathrm{SHF}}}$ (Figure 2.5c). During the sea ice formation season (March-September, Figure S2c), brine rejection and heat loss to the atmosphere (Figure 2.5c) diabatically decrease $\overline{|\nabla\rho|}$ and facilitate onshore heat transport. Conversely, when the sea ice is melting most rapidly (November-February, Figure S2c), $\overline{J_{\mathrm{SFWF}}}$ and $\overline{J_b}$ (and to a lesser extent, $\overline{J_{\mathrm{SHF}}}$) are most positive, helping increase $\overline{|\nabla\rho|}$ and hinder onshore $\overline{\Phi}$.

While the buoyancy forcing's contribution changes sign seasonally, $\overline{W_{\mathrm{ek}}}$ is negative (*i.e.*, convergent/downwelling-favorable) year-round (mean of -5.8 Sv), and therefore acts to block onshore $\overline{\Phi}$ on average. Over the summer (February-April), $\overline{W_{\mathrm{ek}}}$ becomes incrementally more downwelling-favorable, and that coincides with an increase in $\overline{|\nabla\rho|}$ and a decrease in $\overline{\Phi}$. The gradual increase in $\overline{\Phi}$ that follows ($\sim$May-February) correlates with the slackening of the downwelling-favorable $\overline{W_{\mathrm{ek}}}$ and a decrease in both $\overline{|\nabla\rho|}$ and $\overline{\mathrm{EKE}}$ (Figure 2.5).

These results suggest that the persistently downwelling-favorable mechanical forcing of the convergent Ekman transport overwhelms the steric contribution of the surface buoyancy fluxes controlled by the ocean-atmospere-sea ice interactions, therefore controlling the seasonal variability of $\overline{|\nabla\rho|}$, and hence $\overline{\Phi^{\mathrm{mean}}}$ and $\overline{\Phi}$. This interpretation is supported by the climatological wind stress fields. From June through December/January, the easterlies weaken (especially in East Antarctica, red patches in Figure 2.6f-l,a), while $\overline{\Phi}$ gradually increases onshore (Figure 2.5a,b). Later in the summer and into the fall (February-May), the easterlies quickly build up, increasing the onshore Ekman transport and strengthening the ASF (blue patches in Figure 2.6b-e and Figure 2.5b,c). This matches with the abrupt drop in $\overline{\Phi}$, which turns offshore in the fall (April-June). This interpretation is quantitatively supported by the stronger correlation of $\overline{\Phi^{\mathrm{mean}}}$

with $\overline{W_{\mathrm{ek}}}$ (r = 0.82, $\alpha = 99.9\%$) than with $\overline{J_b}$ (r = 0.68, $\alpha = 99.9\%$).

In accordance with the heat transport blocking paradigm (Spence et al., 2014), $\overline{\mathrm{EKE}}$ and $\overline{|\nabla\rho|}$ are both 180° out of phase with $\overline{\Phi^{\mathrm{mean}}}$ (Figure 2.5a,b,d). However, $\overline{\Phi^{\mathrm{eddy}}}$ has a very small seasonal amplitude (Figure 2.5b). This is perhaps surprising, since $\overline{\mathrm{EKE}}$ has a well-defined seasonal signal, in phase with $\overline{|\nabla\rho|}$ (r = 0.76, significant at $\alpha = 99.9\%$, Figure 2.5b,d) as intuitively expected. Further, $\overline{\Phi^{\mathrm{eddy}}}$ is very weakly correlated with $\overline{\mathrm{EKE}}$ at zero lag (r = 0.08, significant at $\alpha = 85\%$). In order to satisfy the hypothesis that the circumpolar eddy heat transport responds to varying eddy activity of the ASC jet at monthly time scales, $\overline{\mathrm{EKE}}$ and $\overline{\Phi^{\mathrm{eddy}}}$ would need to be in phase and more strongly correlated. Still, $\overline{\Phi^{\mathrm{eddy}}}$ has its maximum correlation with $\overline{\mathrm{EKE}}$ at 5 months lag (r = 0.46, significant at $\alpha = 99.9\%$). Perhaps the local uplifting of isotherms associated with the arrival of remotely-generated fast barotropic Kelvin waves (Spence et al., 2017) and/or slower continental shelf wave modes (Kusahara and Ohshima, 2009) can help explain this non-intuitive result. However, these processes are not identifiable in the present circumpolarly-integrated, monthly-averaged analysis.

2.5.3 Interannual variability

Annually-averaged circumpolar heat transport time series

In addition to seasonal changes in the continental shelf hydrography and circulation, the climate-scale wind forcing is known to drive significant variability in the transport of the Antarctic Slope Current (ASC, *e.g.*, Stewart and Thompson, 2013; Armitage et al., 2018). This can be expected to affect cross-isobath transports through the changes in the along-isobath pressure gradient force associated with the path of the ASC as it follows the continental slope, and the more remote response of the shelf pressure field. The interannual variability of the time-mean and eddy components of the circumpolarly-integrated heat transport across the 1000 m isobath ($\overline{\Phi^{\mathrm{mean}}}$ and $\overline{\Phi^{\mathrm{eddy}}}$, respectively) is shown in Figure 2.7a,b,c. Clearly, $\overline{\Phi^{\mathrm{mean}}}$ is the major contributor to

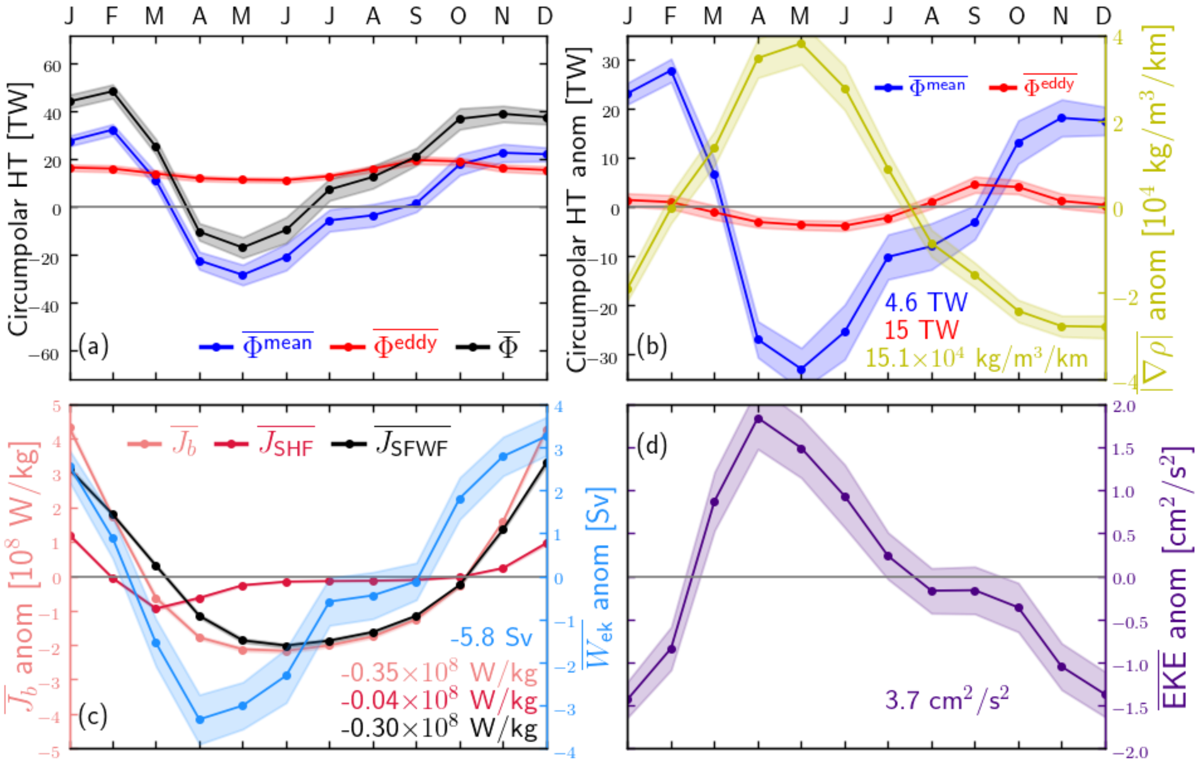

Figure 2.5: Climatological (1959-2009) seasonal cycle of circumpolarly-integrated or averaged variables along the 1000 m isobath (or area-averaged in case of the buoyancy fluxes). Quantities in panels (b,c,d) are monthly anomalies relative to the annual mean. **(a)** Monthly-averaged total ($\overline{\Phi}$), mean ($\overline{\Phi^{\mathrm{mean}}}$) and eddy ($\overline{\Phi^{\mathrm{eddy}}}$) circumpolar heat transports across the 1000 m isobath (magenta contour on the maps). **(b)** Circumpolarly- and depth-averaged lateral density gradient magnitude ($\overline{|\nabla\rho|}$) and $\overline{\Phi^{\mathrm{mean}}}$ and $\overline{\Phi^{\mathrm{eddy}}}$. **(c)** Circumpolarly-averaged Ekman transport divergence ($\overline{W_{\mathrm{ek}}}$, positive when the net Ekman transport is more strongly offshore than in the climatological mean) and shelf-averaged net surface buoyancy flux ($\overline{J_b}$) and its surface heat ($\overline{J_{\mathrm{SHF}}}$) and freshwater ($\overline{J_{\mathrm{SFWF}}}$) flux components. The anomalies of the buoyancy fluxes are positive when the ocean gains more buoyancy than in the climatological mean). **(d)** Circumpolarly- and depth-averaged Eddy Kinetic Energy ($\overline{\mathrm{EKE}}$). The shaded envelopes indicate the 95% confidence intervals about each 1959-2009 climatology. The numbers on the lower-right corners are the mean values that were subtracted to produce the anomaly time series in panels (b,c,d). Note the amplitude of each variable's anomaly compared with its mean value (*e.g.*, $\overline{J_b}$, $\overline{J_{\mathrm{SHF}}}$ and $\overline{J_{\mathrm{SFWF}}}$ change signs while $\overline{W_{\mathrm{ek}}}$ is negative year-round).

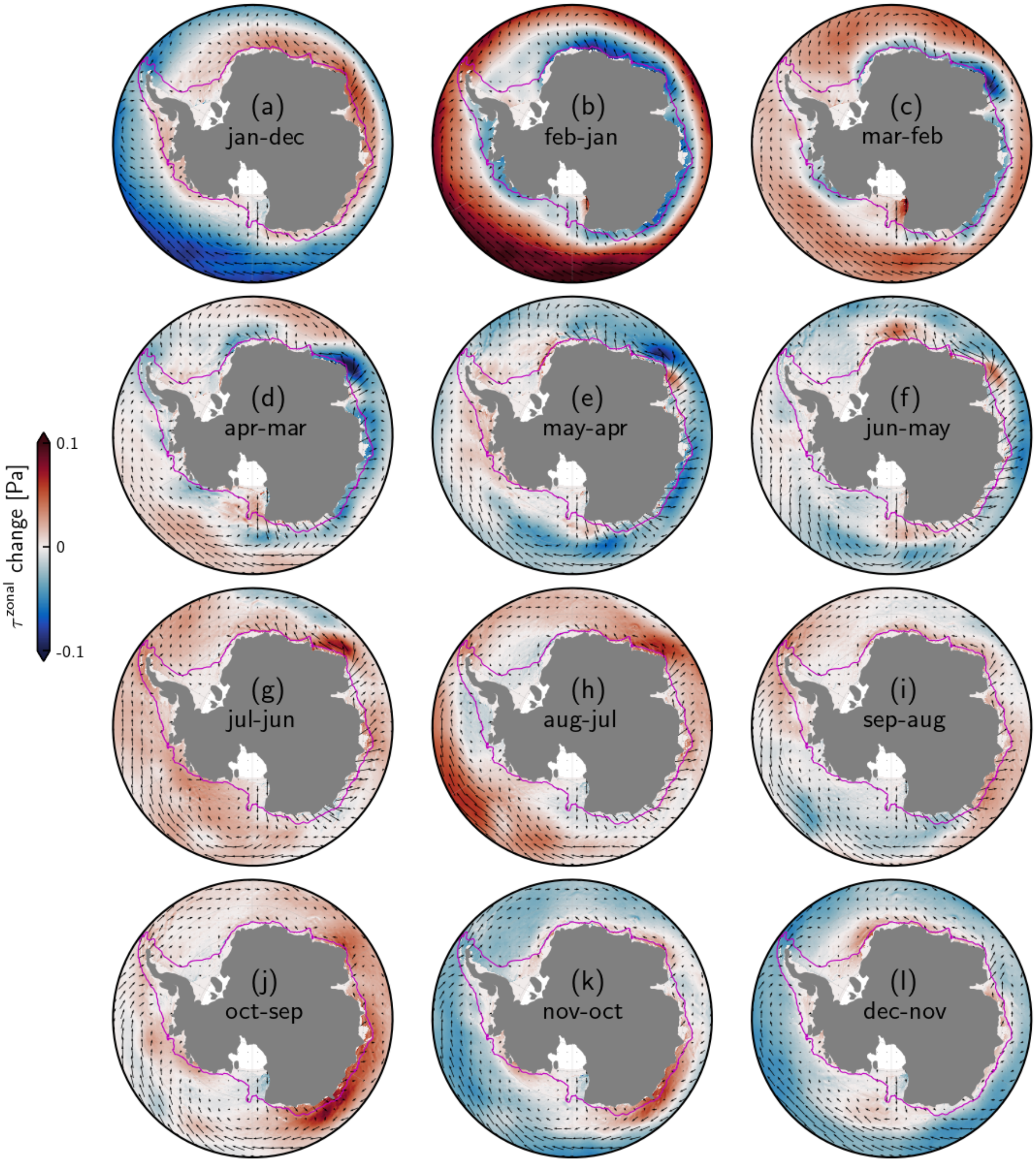

Figure 2.6: Climatological (1959-2009) seasonal cycle of the wind stress patterns over the Antarctic continental margin. Arrows are the monthly means of the wind stress vector, and the color shading is the difference in its zonal component relative to the previous month. Blue indicates strengthening of the easterlies and blocking of the onshore heat transport. Red indicates weakening of the easterlies and facilitation of the onshore heat transport. The magenta contour is the 1000 m isobath.

the variability of $\overline{\Phi}$, from monthly through interannual time scales. The monthly-averaged $\overline{\Phi^{\text{mean}}}$ ranges from -75 TW to 62 TW, while $\overline{\Phi^{\text{eddy}}}$ ranges from 4 TW to 35 TW (Figure 2.7a). The annually-averaged $\overline{\Phi^{\text{mean}}}$ ranges from -10 TW to 17 TW, while $\overline{\Phi^{\text{eddy}}}$ ranges from 9 TW to 24 TW. At time scales of 2-3 years, $\overline{\Phi^{\text{mean}}}$ varies more abruptly than $\overline{\Phi^{\text{eddy}}}$, which is seen also in the time series of $\overline{W_{\text{ek}}}$, $\overline{|\nabla\rho|}$ and $\overline{\text{EKE}}$ (Figure 2.7d,e). In some years, $\overline{\Phi^{\text{mean}}}$ even turns offshore, but $\overline{\Phi^{\text{eddy}}}$ is persistently onshore, and therefore keeps the annually-averaged $\overline{\Phi}$ positive (Figure 2.7b). The cumulative contribution of $\overline{\Phi^{\text{eddy}}}$ to the heat budget of the system in the 1959-2009 period is more than three times that of $\overline{\Phi^{\text{mean}}}$ (24 YJ versus 7.2 YJ, not shown). Removing the individual 1959-2009 means from $\overline{\Phi^{\text{mean}}}$ and $\overline{\Phi^{\text{eddy}}}$ confirms that the time-mean background state plays a key role in the maintenance of a net on-shelf heat transport (Figure 2.7c).

It is worth emphasizing that $\overline{\Phi^{\text{eddy}}}$ keeps $\overline{\Phi}$ positive both seasonally (Figure 2.5a) and interannually (Figure 2.7a). This result also holds regionally, as Φ^{mean} is either persistently offshore or turns offshore for several years in some segments, such as in E-EA and C-EA (containing Totten, Moscow University and Amery Ice Shelves, Figure S5), while Φ^{eddy} is consistently onshore (albeit 5-10 times weaker in the segment-averaged sense, Figure S6). This reversal may cut off some ice shelves from or expose new ones to deep-ocean heat sources and thereby modulate their melt rates in segments where the along-shelf flow convergence does not compensate this heat deficit (Figure 2.3d). The common and sometimes persistent sign changes of Φ across segments supports this conjecture (Figure S4). Interestingly, almost all of the along-shelf transport is due to the mean flow (not shown), in accord with SKM18's eddy-resolving model results. This suggests that eddies are not as important for along-shelf heat transport are they are for cross-shelf heat transport.

The relatively low intra-annual variance of $\overline{\Phi^{\text{eddy}}}$ compared to its mean counterpart (Figure S7) may be due to underestimated eddy kinetic energy in the present simulation (see Section 2.2 and Figure 2.1d). Both the spatial distribution and the magnitude of $\overline{\Phi^{\text{eddy}}}$ are known to be sensitive to model grid resolution (Stewart and Thompson, 2015b; Graham et al., 2016, SKM18).

Hence we expect a finer-resolution POP/CICE simulation (currently in production) to have different magnitudes and patterns of EKE and Φ^{eddy}. Like in SKM18, the time-mean EKE in our simulation is evenly distributed over most of the continental slope and shelf, and is elevated only at a few locations such as the central Weddell and Ross Seas (Figure 2.1d).

Relation to climate modes

Wind perturbations in East Antarctica are known to produce both local and remote changes in the heat content at the edge of the continental shelf through modulation of the Antarctic Slope Front (ASF), often linked to the Southern Annular Mode (SAM, Stewart and Thompson, 2013; Spence et al., 2017). Likewise, El Niño events have been shown to impact the mass balance of ice shelves in West Antarctica through the competition between increased snowfall (thickening) being offset by enhanced basal melt rates (thinning, Paolo et al., 2018). We now examine a possible causal relationship between these climate modes and the interannual variability of the heat transports described in the previous section.

Figure 2.8a shows the difference in potential temperature at 1000 m or the bottom (whichever is shallower locally) between a conditionally-averaged high-SAM scenario (average of years when the SAM index exceeds the 90th percentile) and a low-SAM scenario (average of years when the SAM index is below the 10th percentile). Warming of typically 0.5°C-1°C is found in the East Ross, East Amundsen, West Bellingshausen Seas and in the C-EA segment (off the Amery Ice Shelf location, $\sim$75°E), while cooling of a similar magnitude is found in the W-EA segment, in parts of the E-EA segment and in the East Weddell Sea (Filchner Trough, $\sim$30°W). Figure 2.8b plots the same type of potential temperature difference, but for the Niño 3.4 index. The warming relative to low-Niño 3.4 years covers a similar but slightly larger area than the SAM case, although the magnitudes of the difference are smaller in the Niño 3.4 case. The regions where there is a higher warming than in the SAM case are off of Amery Ice Shelf and Filchner Trough.

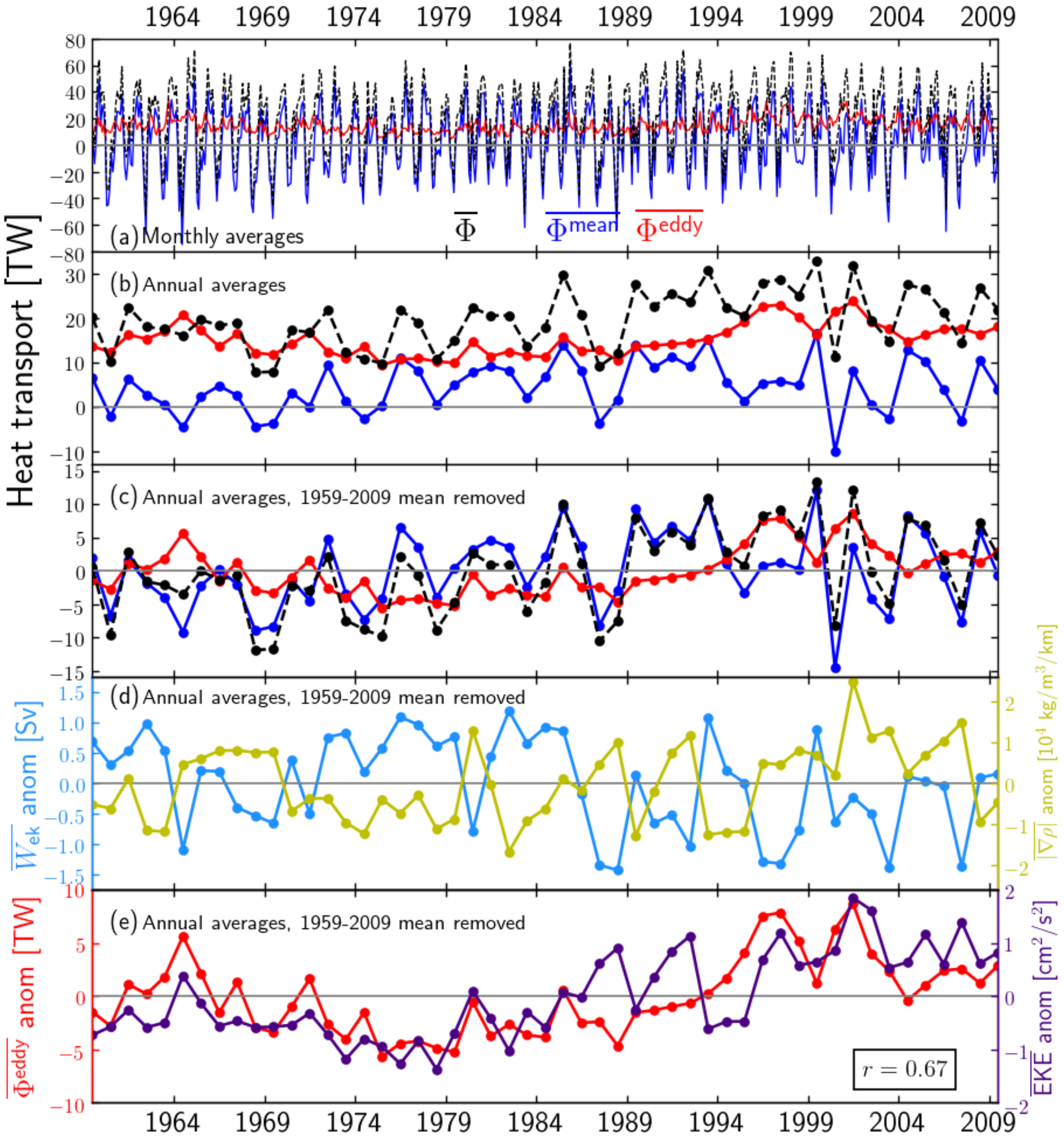

Figure 2.7: Interannual variability of the circumpolarly-integrated heat transport across the 1000 m isobath (positive onshore). **(a)** Time series of monthly-averaged total ($\overline{\Phi}$), mean ($\overline{\Phi^{\mathrm{mean}}}$) and eddy ($\overline{\Phi^{\mathrm{eddy}}}$) heat transport. **(b)** Same as (a), but annually-averaged. **(c)** Same as (b), but as anomalies relative to the long-term (1959-2009) mean. **(d)** Time series of annually-averaged $\overline{W_{\mathrm{ek}}}$ (blue) and $\overline{|\nabla\rho|}$ (yellow) as anomalies relative to the long-term (1959-2009) mean. **(e)** Time series of annually-averaged $\overline{\Phi^{\mathrm{eddy}}}$ and $\overline{\mathrm{EKE}}$ as anomalies relative to the long-term (1959-2009) mean. The zero-lag correlation of 0.67 in panel (e) is significant at the 99.9% confidence level.

This spatially (*i.e.*, along-isobath) heterogeneous temperature response to the SAM-related poleward shift of the easterlies is consistent with the spatial structure of the zero-lag correlation between Φ and the SAM index. The SAM and Niño 3.4 indices have maximum correlation with $\overline{\Phi}$ at zero lag and 7-9 months lag, respectively (not shown), and we therefore examine the along-isobath structure of the correlations at these lags in Figure 2.9. The SAM-Φ correlations change over short along-isobath distances, but are generally positive over most of East Antarctica, West Amundsen and East Bellingshausen Seas (Figure 2.9a). The Niño 3.4-Φ correlations are generally weaker, but more consistently positive in West Antarctica than the SAM-Φ correlations (Figure 2.9b). Also, Figures 2.9c-e show that the local cancellation patterns between Φ^{mean} and Φ^{eddy} found in Figure 2.3a,b,d are persistent throughout the 1959-2009 span of the simulation over virtually the entire Antarctic continental margin, as a result of the ubiquitous recirculation along the shelf edge.

Despite the mean/eddy cancellation, the heat content of the Antarctic continental shelf, Q_V (defined as the volume enclosed by the 1000 m isobath, magenta line on Figure 2.8), is positively correlated with the SAM index in the annually-averaged sense (r = 0.68 significant at α = 99.9%), while the Niño 3.4 index is not (Figure 2.10a). The circumpolar integrals of the on-shelf heat transport components ($\overline{\Phi^{\mathrm{mean}}}$ and $\overline{\Phi^{\mathrm{eddy}}}$) are weakly, but significantly correlated with the SAM index at zero lag ($r \sim 0.2$ and $r \sim -0.2$, respectively, both significant at α = 95%, Figure 2.10b). Within individual segments, the along-isobath averages of Φ are also significantly correlated with SAM at zero lag at the Byrd, Amundsen and Bellingshausen segments in West Antarctica (Figure 2.10c), and across all of East Antarctica (segments W-EA, C-EA and E-EA, Figure 2.10e). These results suggest that the SAM, possibly via its modulation of the ASF structure (Armitage et al., 2018), is more important than ENSO as a climate driver of onshore heat transport at the circumpolar scale.

What are the physical mechanisms linking the simulated SAM variability to the cross-isobath heat transport? In Sections 2.5.2 and 2.5.3 we used the conceptual model of Spence et al.

(2014) to explain the seasonal and interannual variability of $\overline{\Phi}$ as a response to the cross-shelf downwelling circulation forced by circumpolar Ekman transport convergence. The markedly circumpolarly-symmetric pattern of negative correlation between the SAM index and the coastal sea level anomaly at zero lag, combined with the lack of correlation at larger lags (Armitage et al., 2018, their Figure S7) supports this interpretation. We find the highest correlation between the circumpolar Ekman transport divergence ($\overline{W_{\mathrm{ek}}}$) and SAM at zero lag, while the highest correlation between $\overline{W_{\mathrm{ek}}}$ and Niño 3.4 is at 10 months lag (not shown). This implies that stronger model SAM events are indeed related to weakened easterlies (or strengthened westerlies) and decreased onshore Ekman transport and downwelling (or enhanced offshore Ekman transport and upwelling) at the circumpolar scale. This would produce a negative correlation between the SAM index and the coastal sea level anomaly, which is consistent with observations (Armitage et al., 2018). Since the observed SAM index typically decorrelates in less than 6 months (Armitage et al., 2018, their Figure S8) as well as in CORE-II (integral timescale of 1.1 months, not shown), it is not surprising that higher correlations are not found at lags larger than about a year.

The Niño 3.4 index contrasts with the SAM, in that it has no strong correlation with any of the circumpolar variables (Q_V, $\overline{\Phi^{\mathrm{mean}}}$ or $\overline{\Phi^{\mathrm{eddy}}}$) at zero lag (Figure 2.10a,b). Weak correlations ($r \sim 0.1$, significant at $\alpha = 80\%$) with $\overline{\Phi^{\mathrm{mean}}}$ and $\overline{\Phi^{\mathrm{eddy}}}$ exist at 10-12 months lag (Figure 2.10b), which can be traced to significant correlations with the segment-averaged Φ in the Amundsen and Bellingshausen segments (Figure 2.10d), supporting the causal link between ENSO and ocean variability in West Antarctica found in previous studies (*e.g.*, Steig et al., 2012; Paolo et al., 2018). These correlations are consistent with the hypothesis that the SAM is a more significant climate driver for on-shelf transport of warm CDW than ENSO, particularly in East Antarctica (Figure 2.10a).

In West Antarctica, episodic warm intrusions found in global simulations have been connected to the arrival of fast, barotropic Kelvin waves originating from wind perturbations in East Antarctica (Spence et al., 2017). Our findings suggest that a similar mechanism may be operating in POP: Monthly-timescale changes in the zonal wind along East Antarctica (exemplified by the localized seasonal patches in Figure 2.6) serve as an ancillary mechanism for warm intrusions along the shelf edge in West Antarctica. However, it is unclear whether the feedbacks of this increased onshore heat transport with other regional changes induced by climate modes (*e.g.*, circulation and/or heat content changes due to modified meltwater input or surface heat flux) would result in a net increase or decrease of heat actually reaching the ice shelves.

2.6 Summary and conclusions

In this study, we have analyzed some of the large-scale, low-frequency physical processes involved in the onshore transport of heat across the Antarctic continental slope (ACS), based on fields from a 0.1°-resolution global coupled ocean-sea ice model (POP2/CICE4) forced by realistic, interannually-varying atmospheric forcing. This 50-year (1959-2009) subset of the model output has enabled us to analyze the cross-ACS heat transport throughout all Antarctic marginal seas over time scales ranging from seasonal to multidecadal. We examined the vertical water mass structure along the model ACS by comparing temporally- and spatially-averaged model Conservative Temperature (Θ) and Absolute Salinity (S_A) profiles with observations from the Marine Mammals Exploring the Oceans Pole to Pole (MEoP) dataset (Figure 2.2), which indicated good representation of the time-averaged ACS stratification by the model. Agreement of the model heat transport magnitudes and along-isobath scales with those reported in independent studies (Rodriguez et al., 2016; Graham et al., 2016, Table 2.1) is also found. The 50-year (1959-2009) averages of the vertically-integrated mean (Φ^{mean}) and eddy (Φ^{eddy}) cross-slope heat transports along the 1000 m isobath show important areas of convergence of the along-shelf heat transport and the existence of O(100-1000 km) segments of persistent cross-isobath heat transport (Figure 2.3). Analysis of the cross-shelf structure of the mean and eddy overturning circulations in different segments of the ACS (Figures 2.4, S9-10) revealed that advection due to

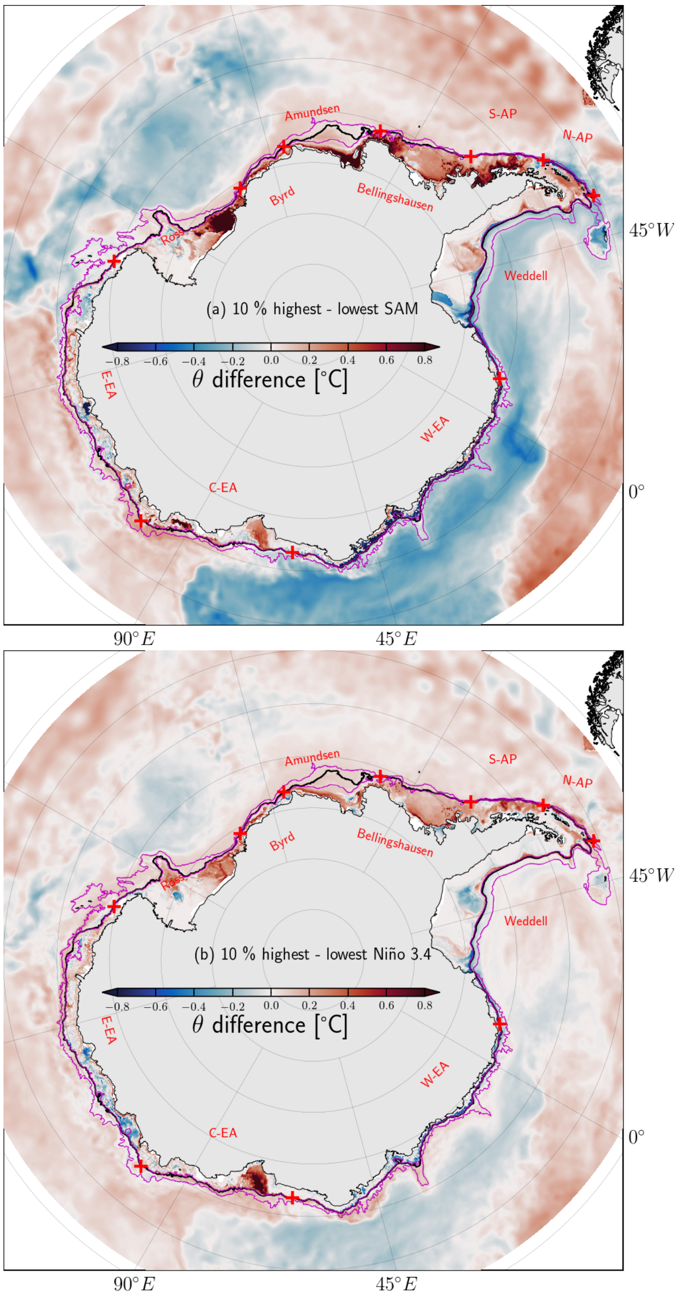

Figure 2.8: Spatial structure of the difference in the model potential temperature at 1000 m or the bottom (whichever is shallower), conditionally-averaged in high- and low-SAM years (a) and high- and low-Niño 3.4 years. The high-index and low-index composites are the averages of the years when either index is below its 10th percentile and above its 90th percentile, respectively. Red areas are warmer in high-SAM/high Niño 3.4 years compared to low-SAM/low Niño 3.4 years, while blue areas are colder. The magenta lines are the 800 m and 2500 m isobaths, and the black line is the 1000 m isobath. Note the relative warming from the East Ross Sea to the tip of the Antarctic Peninsula, as well as some areas of East Antarctica for both SAM and Niño 3.4, although the differences associated with SAM are generally larger.

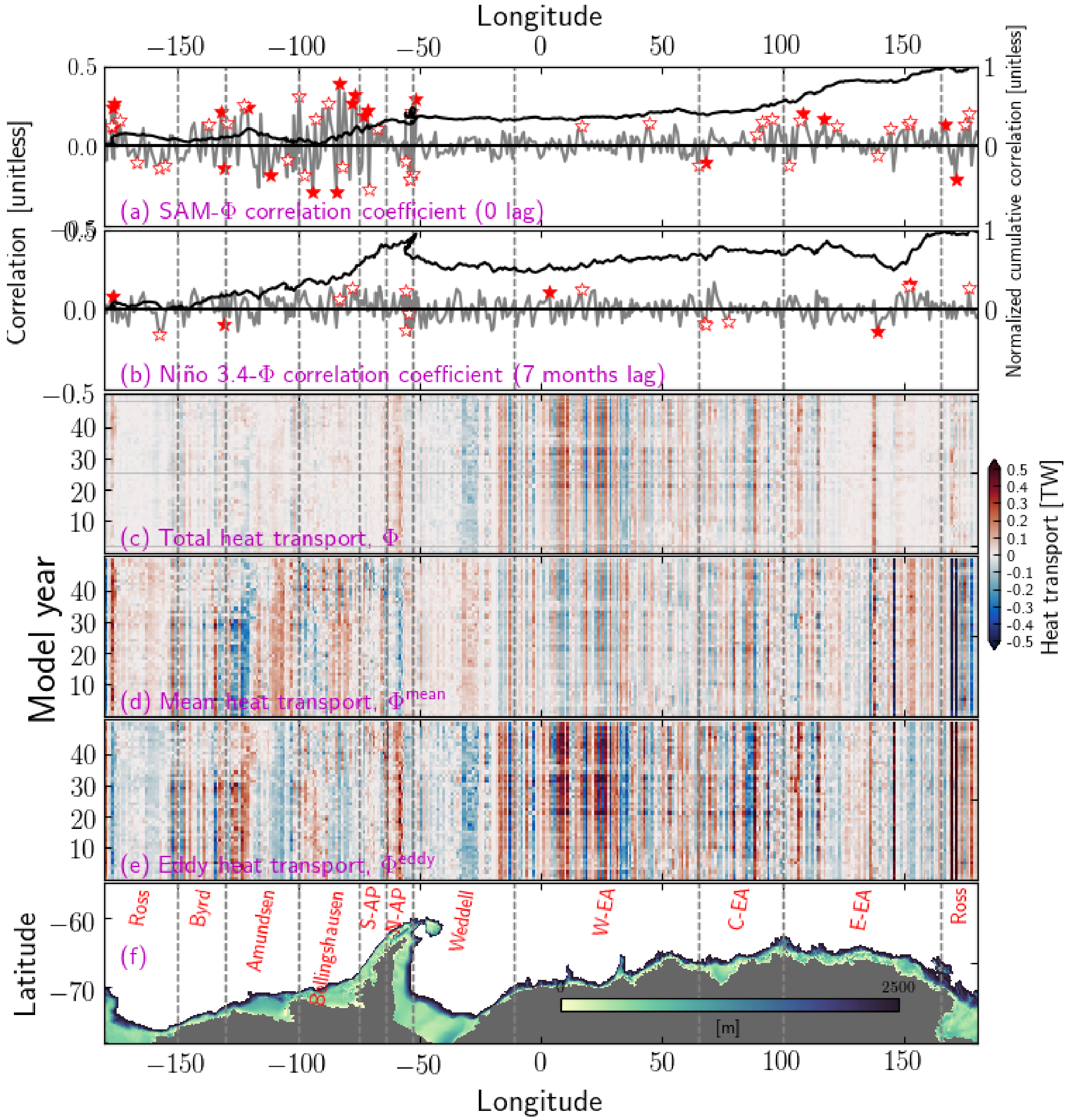

Figure 2.9: Temporal and spatial variability of the total (Φ), mean (Φ^{mean}) and eddy (Φ^{eddy}) cross-isobath heat transport. **(a)**: Correlation coefficient at zero lag (gray line) and its along-isobath cumulative sum (black line) between Φ and the Southern Annular Mode (SAM) index as functions of distance along the 1000 m isobath. **(b)**: Same as (a), but for the Niño 3.4 index at 7 months lag. The filled and open stars in panels a and b indicate, respectively, points where the correlation is significant at the 95% and 80% confidence levels, accounting for the varying number of degrees of freedom at different along-isobath locations. **(c,d,e)**: Annually-averaged heat transports as functions of along-isobath distance and model year, averaged in 50 km-long along-isobath bins. **(f)**: Reprise of Figure 2.3f.

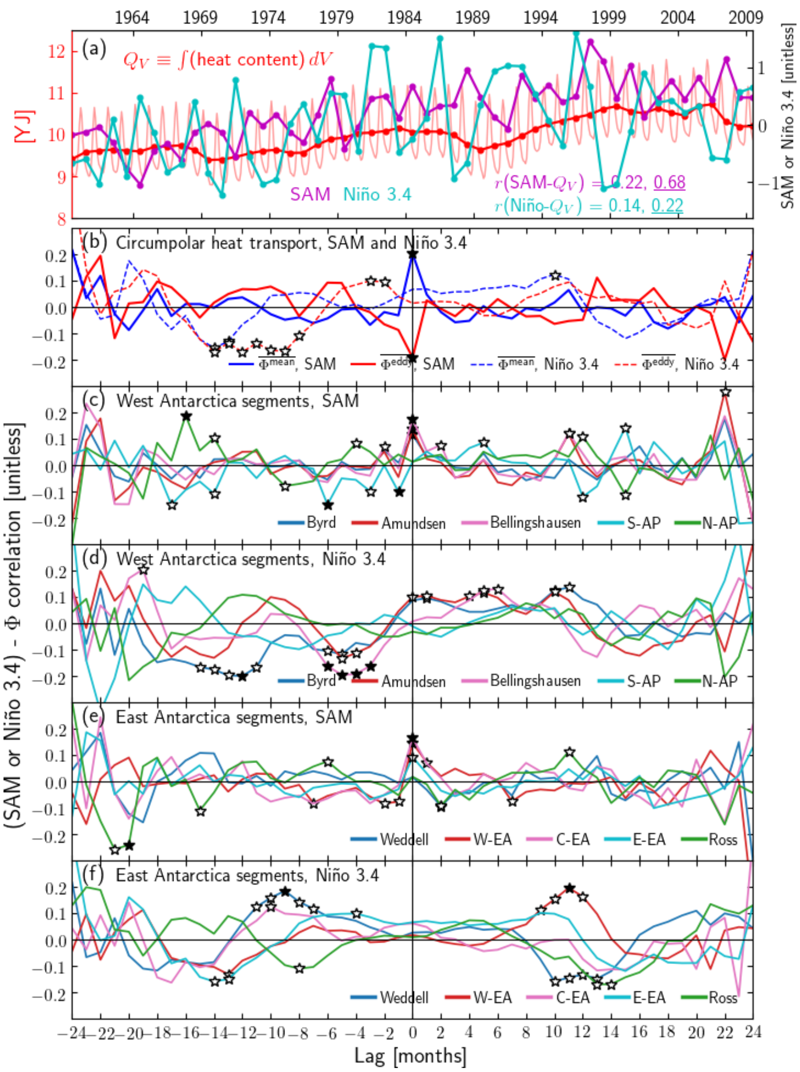

Figure 2.10: Circumpolar on-shelf heat transport and the Southern Annular Mode (SAM). **(a)** Circumpolar heat content Q_V (of the volume bounded by the 1000 m isobath, Figure 2.1b), overlain with annual averages of SAM and Niño 3.4 indices. The faint red line is the monthly-averaged Q_V, while the heavy red line is the annually-averaged Q_V. The Q_V-SAM and Q_V-Niño 3.4 zero-lag correlation coefficients are shown both for the monthly- and annually-averaged time series, with the annually-averaged values underlined. For SAM, the monthly mean and the annual mean correlations with Q_V are both significant at the 99.9% confidence level, while the Q_V-Niño 3.4 correlations are significant at the 99.0% (monthly) and 80% (annual) confidence levels. **(b)** Lagged correlation coefficient between either SAM or Niño 3.4 and the circumpolarly-integrated mean ($\overline{\Phi^{\text{mean}}}$) and eddy ($\overline{\Phi^{\text{eddy}}}$) on-shelf heat transports. **(c,d)** Lagged correlation coefficient between either SAM (c) or Niño 3.4 (d) and the along-isobath averages of Φ for the Western segments. **(e,f)** Same as (c,d), but for the Eastern segments. The filled and open stars in panels b-f indicate, respectively, correlations that are significant at the 95% and 80% confidence levels, accounting for the varying number of degrees of freedom for different segments and at different lags.

the mean flow or eddies and stirring of potential temperature along density surfaces by eddies can operate in different combinations depending on the isobath and the along-shelf location. In the climatological annual cycle, Φ^{mean} (representing monthly mean heat transport) dominates, while Φ^{eddy} (representing effects due to anomalies relative to the monthly mean) is relatively constant throughout the year (Figure 2.5). November-February peaks and April-June troughs in heat transport are consistent with a response to seasonal wind variability in the Southern Ocean (Figure 2.6). On longer time scales (Figure 2.7), some of the variability of the heat transport correlates with changes in the Southern Annular Mode and the El Niño/Southern Oscillation (Figures 2.8, 2.9 and 2.10). In brief, our main conclusions are:

- The 0.1° POP2/CICE4 simulation has a realistic time-mean stratification in the pycnocline layer along the Antarctic margin, but has biases at the core depth of O(10-100 m) and the core temperature (typically 0.1-0.5°C) of the Circumpolar Deep Water (CDW);
- The ranges of annually-averaged circumpolar integrals of the mean ($\overline{\Phi^{\text{mean}}}$), eddy ($\overline{\Phi^{\text{eddy}}}$) and total ($\overline{\Phi}$) on-shelf heat transport are -10 TW–17 TW, 9 TW–24 TW and 8 TW–33 TW, respectively;
- As functions of the along-isobath distance y, both the time-mean $\Phi^{\text{mean}}(y)$ and the eddy $\Phi^{\text{eddy}}(y)$ components of the heat transport have coherent spatial structures at scales of O(100-1000 km), and they partially cancel locally;
- Eddy stirring of potential temperature along isoneutral surfaces ($\Phi^{\text{eddy}}_{\text{stir}}$) seems to be the dominant form of eddy heat transport (both onshore and offshore) in most segments, supporting previous findings (ST16, SKM18);
- Where Φ^{eddy} is offshore, Φ^{mean} is onshore, associated with a full-depth, clockwise cross-isobath overturning circulation moving warm CDW-influenced water onshore and overlying AASW/WW offshore;

- Seasonal variability of $\overline{\Phi}$ is dominated by $\overline{\Phi^{\text{mean}}}$;
- The variability of the total circumpolar convergence of the cross-isobath surface Ekman transport is a stronger driver of $\overline{\Phi^{\text{mean}}}$ (and hence $\overline{\Phi}$) than the circumpolar surface buoyancy flux;
- Interannual and longer-period variability of $\overline{\Phi}$ can be interpreted as a response to the zonally-symmetric wind stress variability linked to the Southern Annular Mode (SAM) and a smaller contribution from El Niño events, whose influence is more prevalent in West Antarctica;

This study has some limitations and caveats. Our 0.1° POP2/CICE4 simulation's resolution only partially resolves eddies on the Antarctic continental slope and shelf, has no ice shelves or continental freshwater release, and no tidal forcing. Recent results demonstrate the important roles of these forcings in the cross-ACS heat transport. We also expect the choice of a fixed isobath as the boundary of the coastal control volume to introduce some bias in the heat transport calculations, because it does not always record the heat transport across the moving Antarctic Slope Front axis (as discussed by Goddard et al., 2017, for their simulation).

For most of the Antarctic margin, the emerging picture for the coastal circulation seems to confirm the paradigm proposed by Dinniman and Klinck (2004): the cross-slope heat transport is driven partially by flow-topography interaction processes such as inertial overshooting of the Antarctic Slope Current, but the shelf circulation must conspire to enable the heat originating from the ACC to actually reach the ice shelves instead of recirculating back offshore. In this regard, an encouraging aspect of our time-averaged analyses is the existence of O(1 TW) heat transports locked to sharp topographic features (Figure 2.3a,b,c,f), as found in eddy-permitting (4 km) and eddy-resolving (1.5 km) simulations (St-Laurent et al., 2013; Graham et al., 2016, Figure 7 in the latter) and observations (*e.g.*, Walker et al., 2007; Wåhlin et al., 2013). Despite the under-representation of eddies, our model results suggest that barotropic mean flow-topography interaction processes may be locally important, as found by Goddard et al. (2017) in their simulation and by Kalén et al. (2015) in their observations of flow in the Dotson Trough in the Amundsen Sea.

Considering the interannual and decadal trends in Θ and S_A estimated by Schmidtko et al. (2014), the deep ocean is likely to be a major driver of changes in the cross-ACS heat transport at the circumpolar scale, although there does not seem to be a single process or even a relatively broadly applicable combination of processes able to account for all of the oceanic heat entering the Antarctic shelf. The cross-ACS heat transport may be modified by changes in the stratification of the ASC/ASUC system or the ACC (through thermal wind shear, *e.g.*, Walker et al., 2007, 2013; Chavanne et al., 2010; Martinson and McKee, 2012) by a poleward migration of the Southern ACC front, or by an increase in the cross-ACC eddy heat transport. At present, a robust change in the zonally-averaged latitude of the ACC has not been observed (Gille et al., 2016), although a more localized incursion of its southern front (*e.g.*, Figure S8) could also be capable of delivering heat to previously sheltered ice shelves in key regions. The large-scale shoaling and deepening trends in the CDW core along the ACS and their correlation with the temperature trends at the bottom of the adjacent shelf (Schmidtko et al., 2014, their Figure 2) can perhaps be explained by a combination of these processes.

In conclusion, response to large-scale differences in surface buoyancy and wind forcing, bottom topography and the continental shelf circulation are probably important in different combinations in each marginal sea, although the availability of warm CDW at the shelf edge (modulated by the ASC/ASUC and ACC) is ultimately necessary to support the simulated and observed heat transports at very low frequencies. Locally, the amount of oceanic heat actually reaching the subglacial cavities is likely to be more strongly constrained by a complex combination of bottom topography, surface buoyancy fluxes and the convergence/divergence of along-shelf temperature advection, rather than the cross-isobath heat transport alone. Examination of the combined effects of these forcings and their interactions with the low-frequency cross-shelf heat transports examined in this study awaits longer eddy-resolving model simulations with tides, freshwater fluxes and thermodynamically active ice-shelf cavities.

Acknowledgments

The authors gratefully acknowledge support from the US Department of Energy (DOE, grant # DE–SC0014440) in the scope of the "Ocean and Sea Ice and their Interactions around Greenland and the West Antarctic Peninsula in Forced Fine–Resolution Global Simulations" project and high-performance computing support from Yellowstone (ark:/85065/d7wd3xhc) provided by NCAR's Climate Simulation Laboratory (CSL), sponsored by the National Science Foundation (NSF) and other agencies. JLM was supported by an earlier U.S. DOE Office of Science grant entitled "Ultra-High Resolution Global Climate Simulation" via a Los Alamos National Laboratory subcontract to carry out the POP/CICE simulation; both Caroline Papadopoulos (SIO/UCSD) and Elena Yulaeva (UCSD) participated in its production. The analyses of the model output performed in this study were enabled by computing resources provided by Oak Ridge Leadership Computing Facility (OLCF).

The marine mammal data were collected and made freely available by the International MEoP Consortium and the national programs that contribute to it (http://www.meop.net). All code and reduced datasets necessary to reproduce the results are available online at https://github.com/apaloczy/Antarctica
We are grateful to two anonymous reviewers, whose thorough work substantially improved the quality of the manuscript.

Chapter 2, in full, reprints material as it appears in Palóczy, A., Gille, S. T., & McClean, J. L. (2018). Oceanic Heat Delivery to the Antarctic Continental Shelf: Large-Scale, Low-Frequency Variability. Journal of Geophysical Research: Oceans, 123(11), 7678–7701. DOI: 10.1029/2018JC014345. The dissertation's author was the primary investigator and author of this paper.

Table 2.2: Maximum values of the lagged cross-correlation function between monthly-averaged on-shelf volume transport (U) and the (monthly-averaged) along-isobath mean (Φ^{mean}), eddy (Φ^{eddy}) and total (Φ) on-shelf heat transports averaged within each segment, and also between Φ^{mean} and Φ^{eddy} (right-most column). The number of lags reported here (in months) is associated with the maximum absolute value of the cross-correlation, which is reported in its signed form in the r_{max} columns. The cross-correlation functions were averaged from 51 one-year chunks. Values that are not significant at the 95% confidence level are marked with an asterisk.

	$\text{corr}(U, \Phi^{\text{mean}})$		$\text{corr}(U, \Phi^{\text{eddy}})$		$\text{corr}(U, \Phi)$		$\text{corr}(\Phi^{\text{mean}}, \Phi^{\text{eddy}})$	
	r_{max}	lags	r_{max}	lags	r_{max}	lags	r_{max}	lags
Ross	0.814	10	-0.948	10	0.348*	4	-0.753	10
Byrd	0.874	10	-0.997	10	0.374*	10	-0.867	10
Amundsen	0.768	10	-0.998	10	-0.392*	10	-0.758	10
Bellingshausen	0.796	10	-0.995	10	0.418*	10	-0.774	10
S-AP	0.753	10	-0.991	10	-0.418*	10	-0.731	10
N-AP	0.617	10	-0.999	10	-0.799	10	-0.618	10
Weddell	0.746	10	-0.992	10	-0.879	10	-0.743	10
W-EA	-0.451	20	-0.958	10	0.523	18	-0.258*	10
C-EA	0.740	10	-0.992	10	-0.614	13	-0.717	10
E-EA	0.750	13	-0.979	10	0.842	15	-0.769	7

2.7 Supporting information

Figure S1's caption details the procedure used to define the control volume encircling the Antarctic continental margin in the model grid.

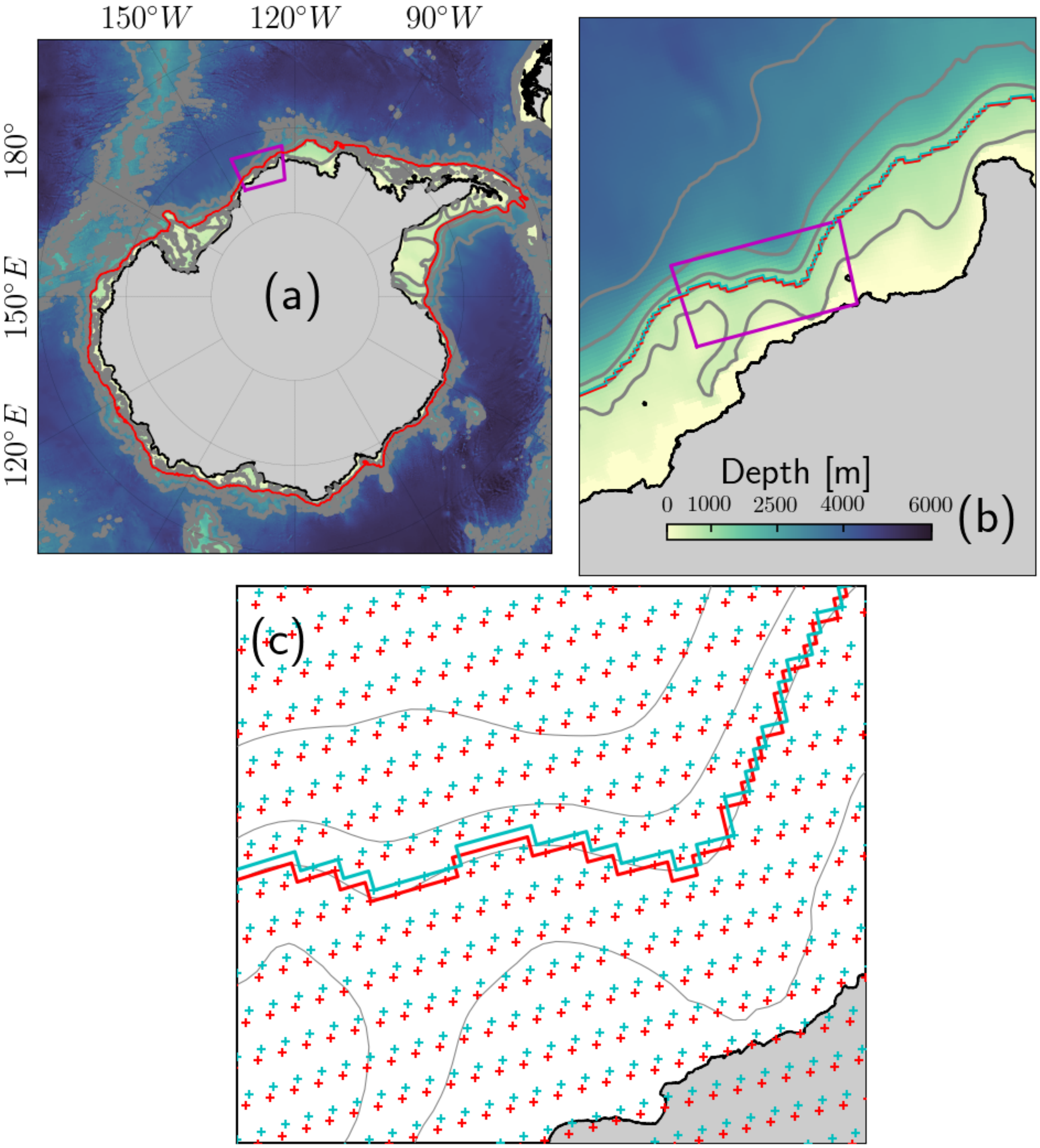

Figure 2.11: Control line (1000 m isobath, red/cyan contours) used for the cross-isobath heat transport calculations and model bottom topography (color shading). **(a)** Large-scale view of the model bottom topography and the control line. The line is calculated by first contouring the model topography, and then performing a nearest-neighbor interpolation of the points lying on the 1000 m contour to the actual model grid points, while ensuring that the interpolated line always follows adjacent cells. **(b)** Expanded view of the box in panel (a). **(c)** Expanded view of the box in panel (b) showing every second T-point (red crosses) and U-point (cyan crosses) of the Arakawa B-grid used by POP. The physical location of the control line (cyan line) is at U-points, *i.e.*, following the faces of T-cells. The red line connects the associated T-points. The gray lines are the 500 m, 1000 m, 1500 m, 2500 m and 3500 m model isobaths contoured with linear interpolation.

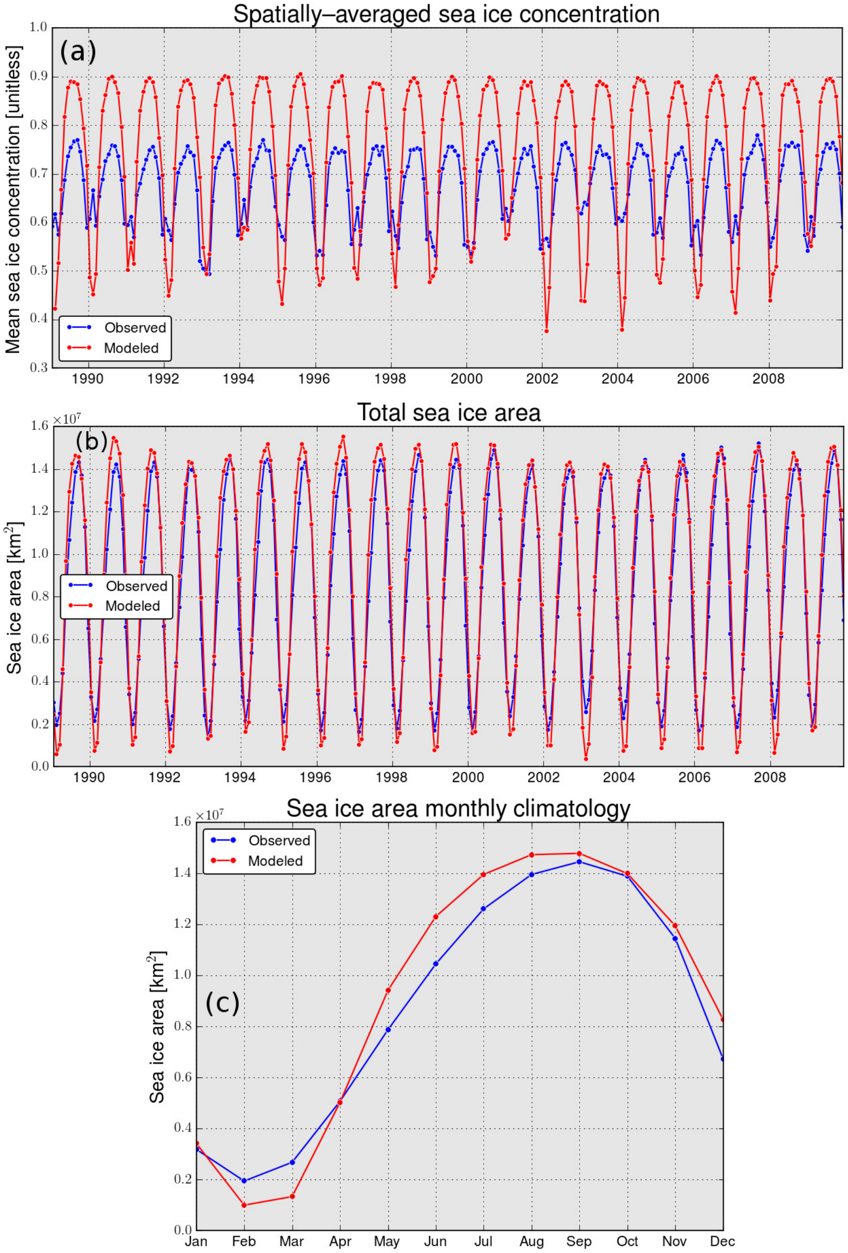

Figure 2.12: Comparison of simulated and observed circumpolarly-averaged sea ice concentrations **(a)** and total sea ice extents **(b)**. **(c):** 1989-2009 climatologies of simulated and observed sea ice extent. Only grid cells with sea ice concentration of 15% or greater are considered for the mean sea ice concentration and sea ice extent (*i.e.*, total area with sea ice present) calculations. The observed sea ice concentrations are derived from Special Sensor Microwave/Imager (SSM/I) processed with the NASA Team Sea Ice Algorithm (Cavalieri et al., 1997).

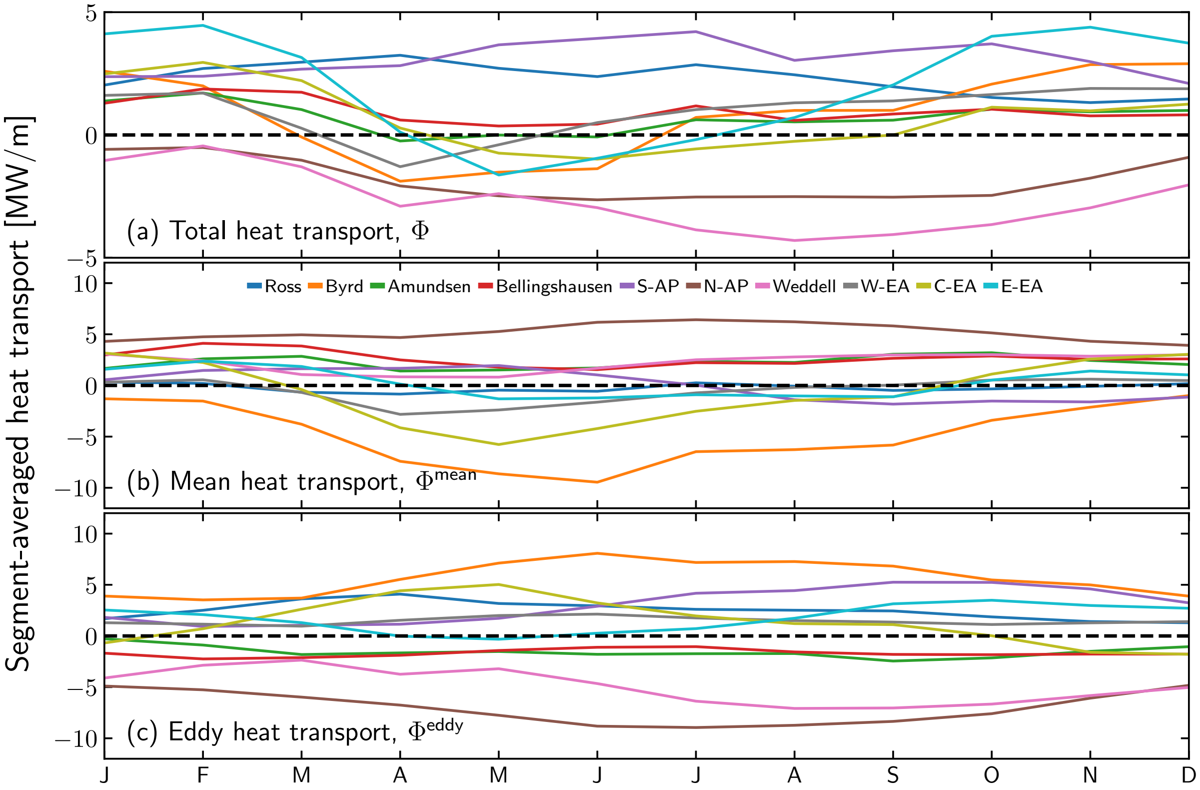

Figure 2.13: Climatological seasonal cycle (1959-2009 means) of heat transport across the 1000 m isobath averaged within each of the segments defined for the analyses (see Figure 1a in the manuscript).

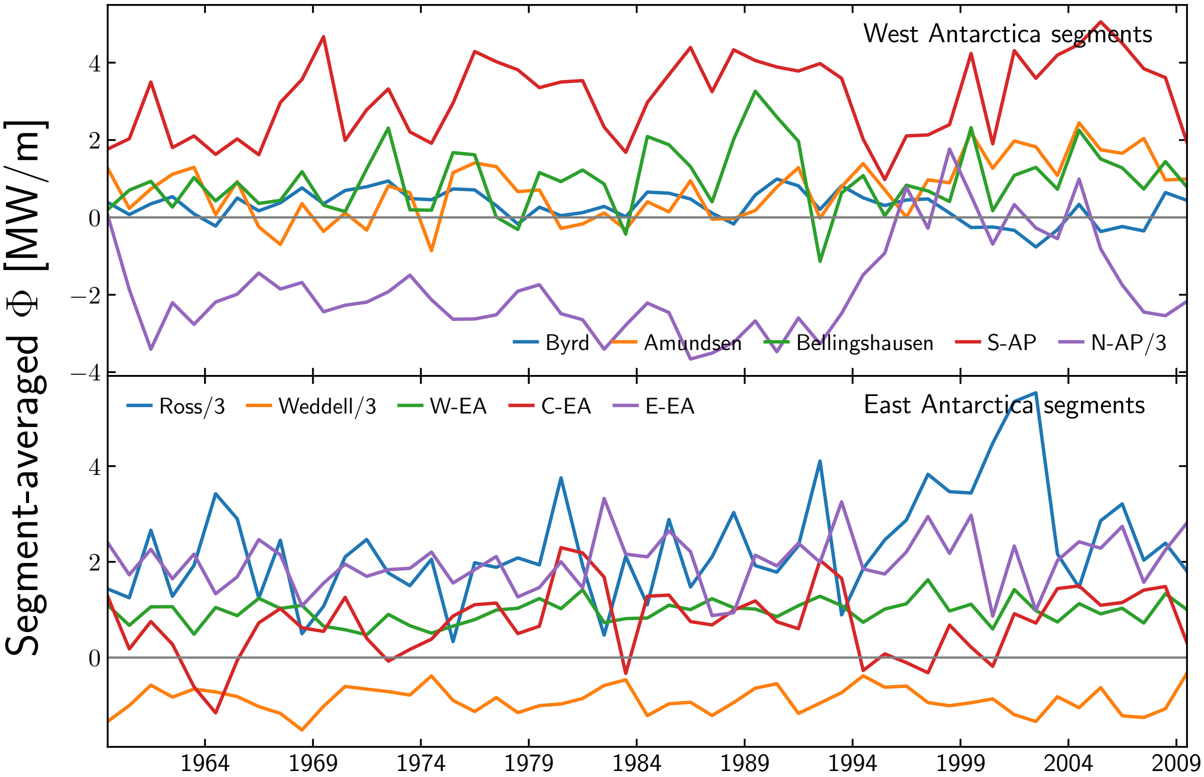

Figure 2.14: Time series of yearly-averaged total heat transport (Φ) across the 1000 m isobath averaged within each of the segments defined for the analyses (see Figure 1a in the manuscript). To facilitate comparison, the Φ time series for the Weddell, Ross and N-AP segments have been divided by 3.

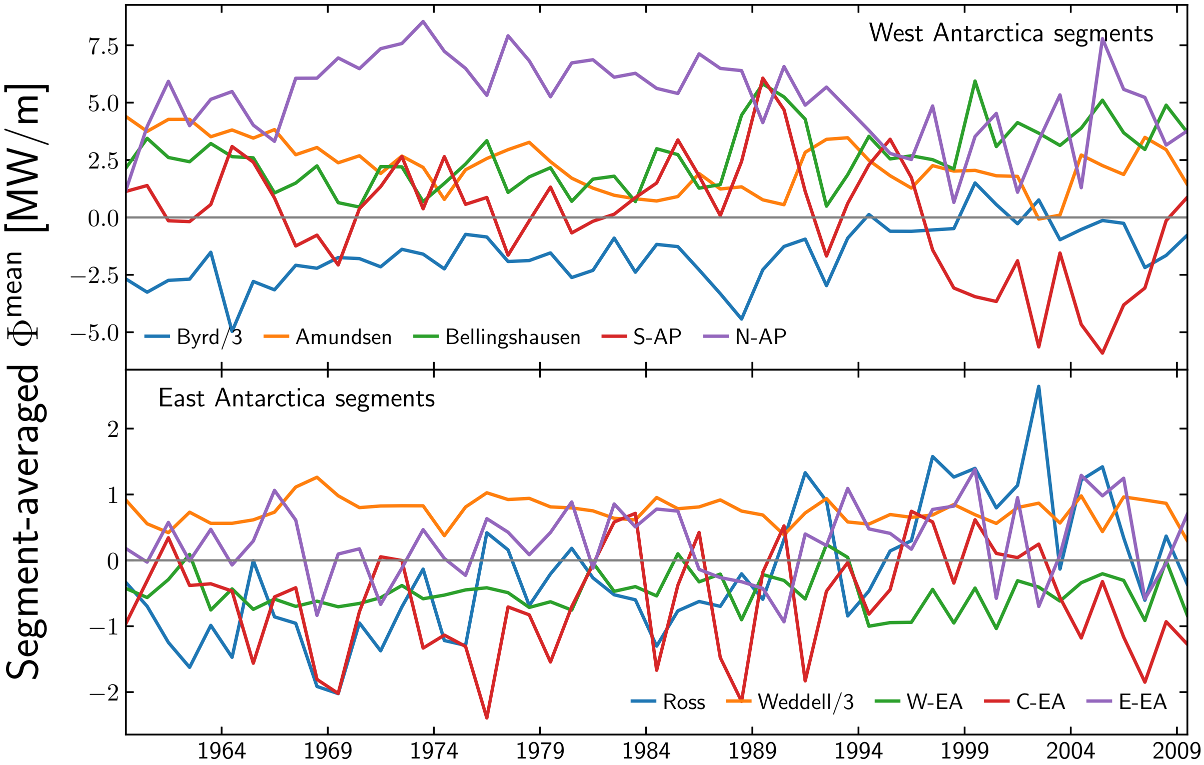

Figure 2.15: Same as Figure S4, but for the mean (Φ^{mean}) component of the total cross-isobath heat transport. To facilitate comparison, the Φ^{mean} time series for the Weddell and Byrd segments have been divided by 3.

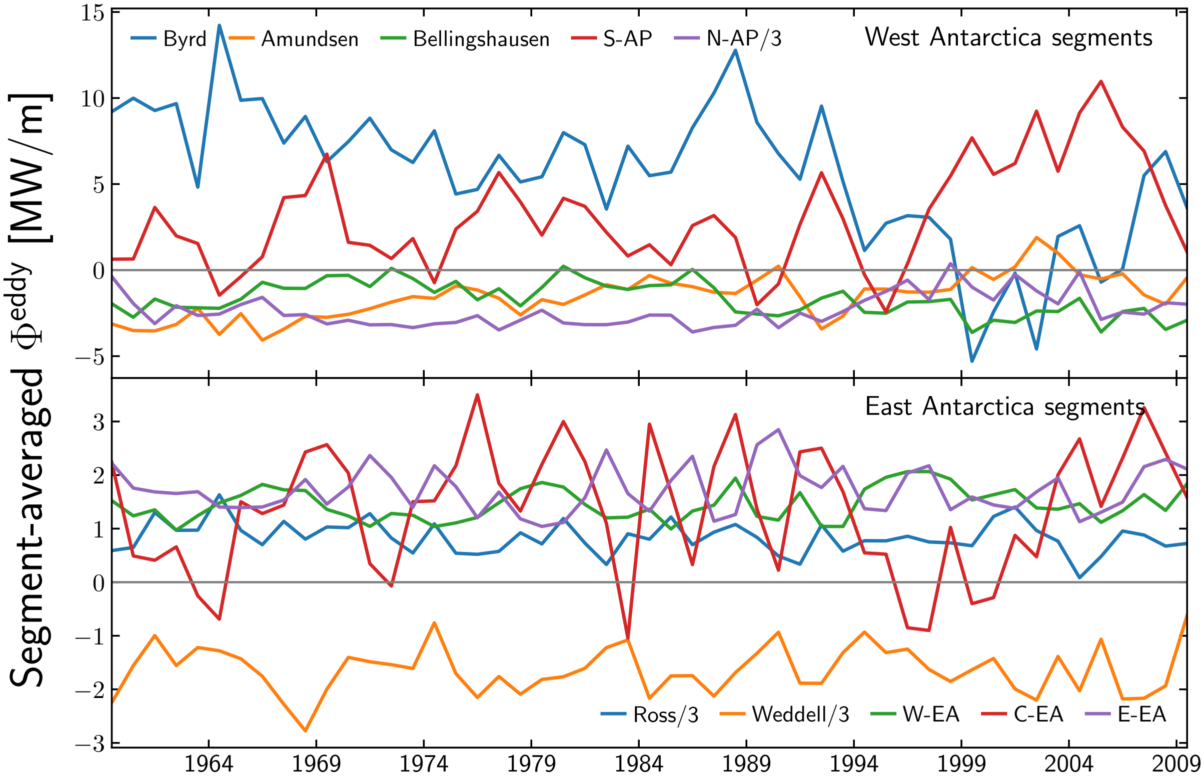

Figure 2.16: Same as Figure S4, but for the eddy (Φ^{eddy}) component of the total cross-isobath heat transport. To facilitate comparison, the Φ^{eddy} time series for the Weddell, Ross and N-AP segments have been divided by 3.

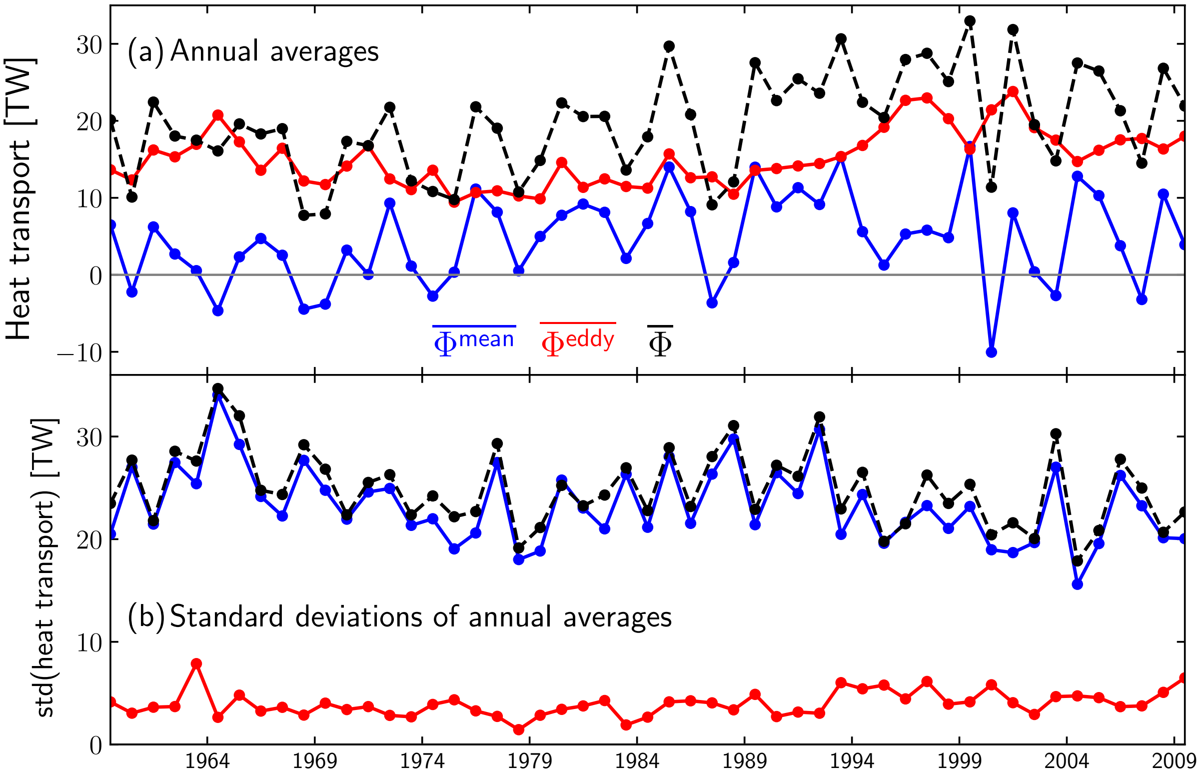

Figure 2.17: **(a)** Time series of annual averages of circumpolarly-integrated heat transport across the 1000 m isobath ($\overline{\Phi}$) and its mean ($\overline{\Phi^{\text{mean}}}$) and eddy ($\overline{\Phi^{\text{eddy}}}$) components (reprise of Figure 7b in the manuscript), calculated from monthly-averaged model fields. **(b)** Time series of the standard deviations associated with the annual averages in panel (a).

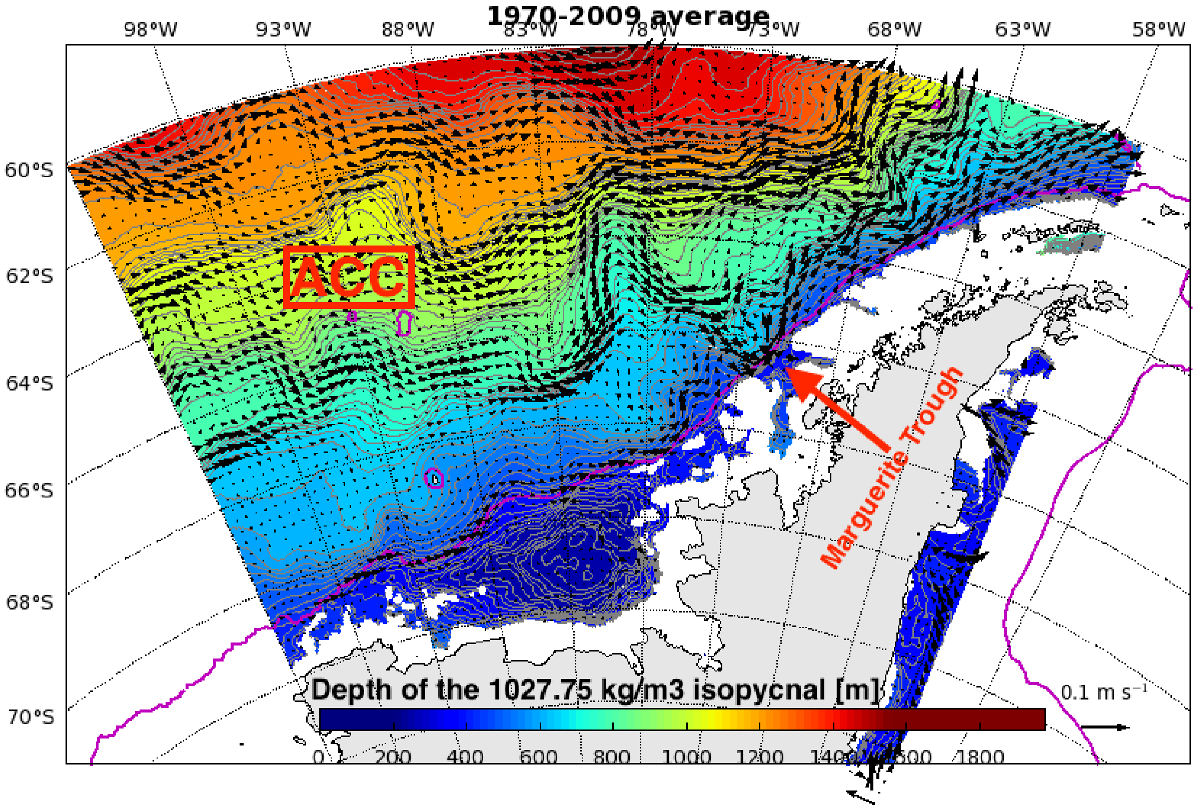

Figure 2.18: Model time-averaged (1970-2009) depth of the 1027.75 kg m^{-3} isopycnal surface referenced to 0 dbar (color shading and gray contours) and horizontal velocity vectors at the same depth (arrows) in the Bellingshausen Sea and West Antarctic Peninsula sectors. The magenta line is the 1000 m isobath. The multiple jets of the Antarctic Circumpolar Current (ACC) and the location of Marguerite Trough are indicated.

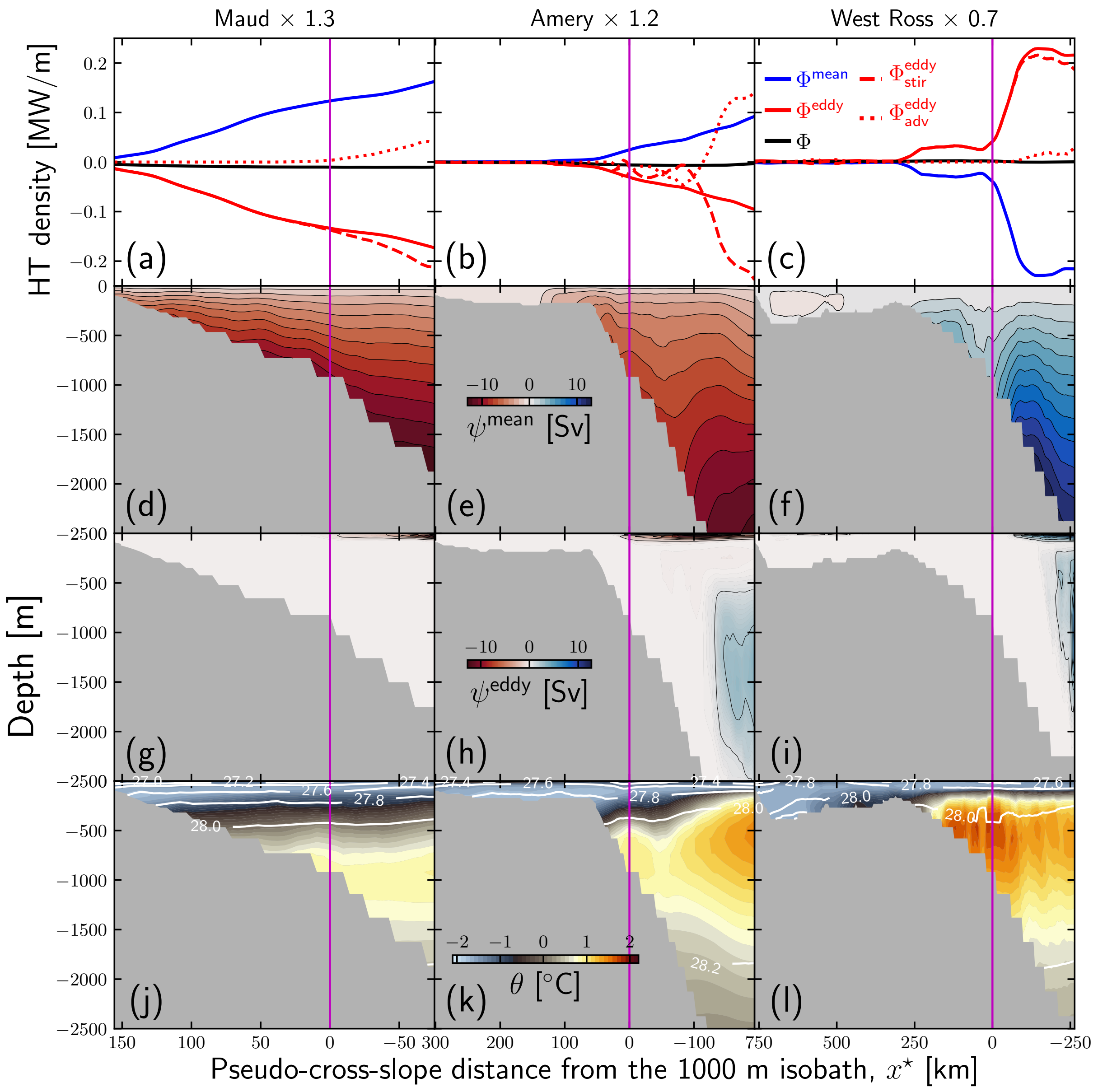

Figure 2.19: Same as Figure 4 in the manuscript, but for sub-segments Maud (25°E to 50°E), Amery (70°E to 95°E) and West Ross (155°E to 180°E), see Figure 1a in the manuscript. To facilitate comparison, the heat transport components for the (a) Maud, (b) Amery and (c) West Ross sub-segments are multiplied by 1.3, 1.2 and 0.7, respectively.

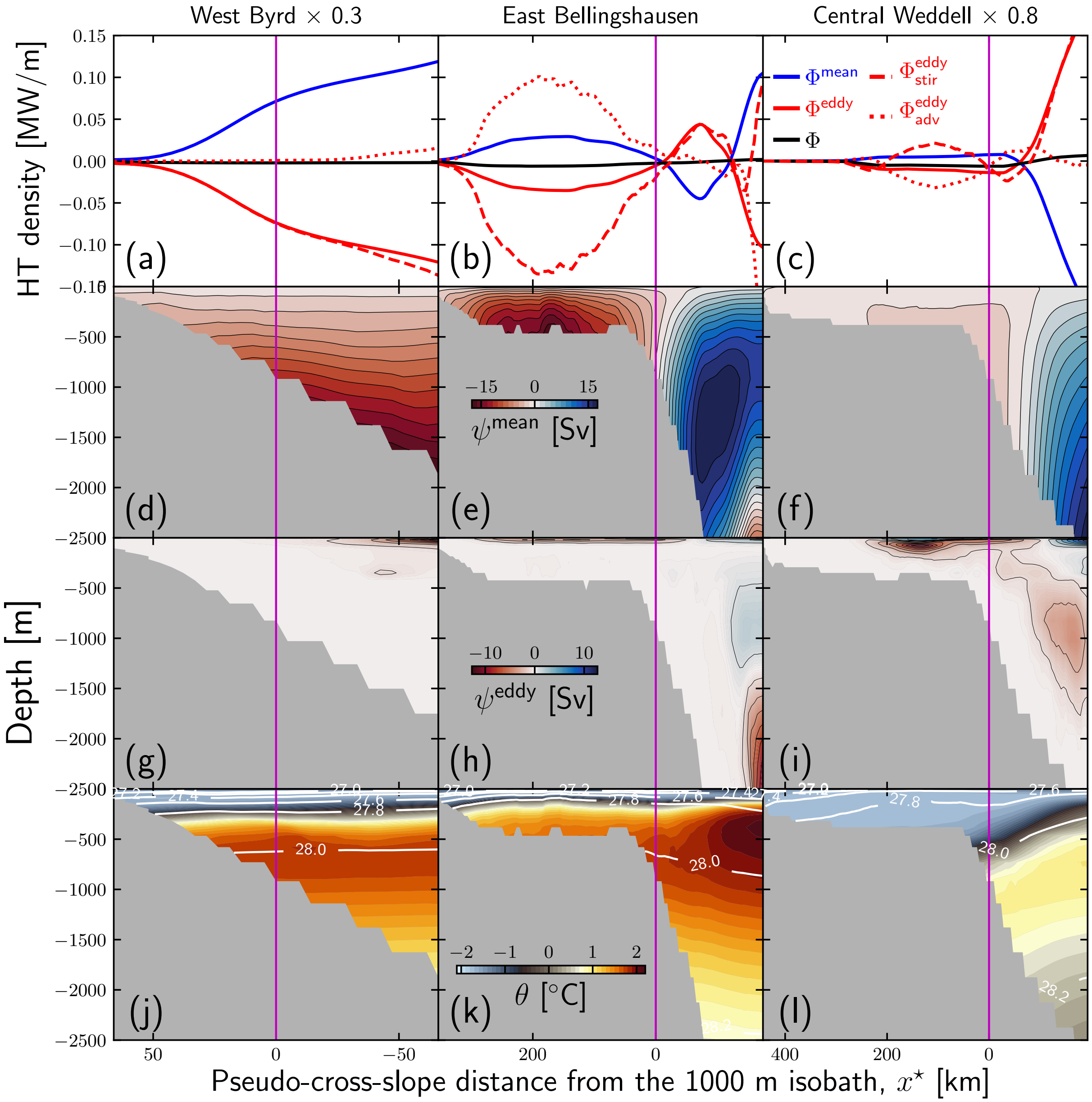

Figure 2.20: Same as Figure 4 in the manuscript and Figure S9, but for sub-segments West Byrd (150°W to 135°W), East Bellingshausen (85°W to 75°W) and Central Weddell (50°W to 25°W), see Figure 1a in the manuscript. To facilitate comparison, the heat transport components for the (a) West Byrd and (c) Central Weddell sub-segments are multiplied by 0.3 and 0.8, respectively.

Chapter 3

The large-scale vorticity balance of the Antarctic continental margin in a fine-resolution global simulation

3.1 Introduction

The circulation over the Antarctic Continental Margin (ACM) mediates the exchange of mass and heat between the Southern Ocean and the coast, particularly where the Antarctic Slope Front (ASF) occurs. It is thus a key player in the ocean's global overturning circulation and in Earth's climate system (*e.g.*, Thompson et al., 2018). The processes responsible for this exchange are also relevant for understanding and predicting global sea level change. Heat brought from offshore by relatively warm Circumpolar Deep Water (CDW) intrudes onto the continental shelf and underneath the ice shelves' subglacial cavities (*e.g.*, Jacobs et al., 2011; Nøst et al., 2011; Rintoul et al., 2016; Silvano et al., 2016, 2017; Castagno et al., 2017; Mallett et al., 2018) and is the major contributor to the observed mass loss rates of the ice shelves that buttress the Antarctic Ice Sheet (Rignot et al., 2013; Depoorter et al., 2013). Understanding the large-scale dynamics driving these processes and how they manifest themselves in climate and Earth System models is thus of primary societal importance.

Dynamically, the problem is to identify the processes responsible for breaking the Taylor-Proudman constraint, which posits that purely geostrophic flow on an f-plane must follow isobaths (*e.g.*, Brink, 2016a), or in the case of variable f, contours of f/h, where f is the Coriolis parameter and h is the ocean depth (*e.g.*, Holland, 1973; Mertz and Wright, 1992; Holloway, 2008). The vorticity balance offers a useful dynamical framework for studying cross-f/h transport processes for two reasons: First, it filters out large horizontal pressure gradients associated with the geostrophic balance, which are not physically insightful by themselves because they can be caused by several different mechanisms, and second, it is insensitive to the choice of rotation angle, unlike the cross-isobath velocity in the along-isobath momentum balance (Brink, 2016a). The insensitivity to rotation angle is particularly important in complicated geometries such as that of the ACM (Stewart et al., 2018, 2019). In regions where the ACM is predominantly zonally-oriented, the planetary vorticity advection term (βV, where β is the planetary vorticity gradient and V is the vertically-integrated meridional velocity) in the depth-integrated vorticity equation is an approximate metric for cross-slope transport. This was exploited by Rodriguez et al. (2016), who found a net transport of $\sim$1 Sv into the Amundsen Sea embayment associated with the 2005-2010 time-mean cyclonic wind stress curl in the Southern Ocean State Estimate (SOSE).

Some previous diagnostic studies of the large-scale vorticity budget in coarse (Lu and Stammer, 2004; Yeager, 2013, 2015) and eddy-permitting (Hughes and de Cuevas, 2001) models have examined the role of bottom pressure torques or bottom vortex stretching in driving the depth-integrated circulation patterns in the vicinity of sloping topography, as first discussed for a stratified square basin with sloping sidewalls by Holland (1973). A common thread in these studies is that regions with relatively flat topography are diagnosed to be closer to Sverdrup balance as predicted by classical idealized theories (see also Wunsch, 2011), while depth-integrated flow close to steep topography is found to be strongly influenced by bottom pressure torques (Hughes and de Cuevas, 2001; Lu and Stammer, 2004; Yeager, 2013, 2015). At shorter time scales, one may also expect the relative vorticity tendency term to be important, further complicating the vorticity balance. Examination of the validity and localization of these simplified dynamical balances in the ACM is the central goal of this study.

A major circulation feature of the ACM is the Antarctic Slope Current (ASC), an extensive current encircling most of Antarctica, associated with the ASF and thought to act as a mediator of cross-slope transport (*e.g.*, Thompson et al., 2018). Recent modeling work suggests that the ASC's jet is mostly driven by tidal momentum flux convergences at the shelf break in the Weddell-Scotia confluence (*e.g.*, Flexas et al., 2015), and possibly along its entire extension around the continent (Stewart et al., 2019). Its variability is also known to be sensitive to large-scale wind forcing associated with climate modes such as the Southern Annular Mode (*e.g.*, Armitage et al., 2018; Thompson et al., 2018). Therefore, in a changing climate, modified large-scale wind patterns may produce regional differences in these heat exchanges, to the degree that they control the circulation in the ACM. Another important circulation feature is the Antarctic Coastal Current, which flows westward hugging the coast in some sectors of the ACM, such as the Western Antarctic Peninsula, where it is usually called the Antarctic Peninsula Coastal Current (*e.g.*, Moffat and Meredith, 2018). In this study, we focus on the localization and temporal variability of the vorticity balances that drive meridional flow through the planetary vorticity advection term (βV), partly contributing to cross-isobath transport across the continental shelf and slope of the ACM, rather than on the dynamics of a particular circulation feature, such as the ASC or the Antarctic Coastal Current.

The purpose of this study is to investigate the dynamics of the cross-slope transport in the geostrophic interior along the ACM through the lens of a vorticity budget. Specifically, we aim to test the hypothesis that a simplified Sverdrup-like vorticity balance accounts for some of the meridional mass and heat transports (both down-slope and up-slope), in an eddy-permitting global ocean model. Although transports within the surface and bottom Ekman layers may not be negligible around the entire continental margin (*e.g.*, Thompson et al., 2014; Silvano et al., 2016), the water mass that makes the largest contribution to the on-shelf heat transport (CDW) occupies the geostrophic interior of the water column, with a core typically at $\sim$300 m-600 m depth along the continental slope (*e.g.*, Schmidtko et al., 2014; Thompson et al., 2018). Although a large fraction of this transport is due to eddies (Stewart and Thompson, 2015c; Palóczy et al., 2018; Stewart et al., 2018, 2019), part of the time-mean component of the meridional, cross-slope transport (both onshore and offshore, Goddard et al., 2017; Palóczy et al., 2018) should be captured by a local Sverdrup-like balance.

The remainder of the paper is organized as follows. We begin by explaining the methodology used to diagnose the vorticity budget from our numerical simulation in Section 3.2. We then present the results of the analyses of the time-averaged (Section 3.3) and time-varying (Section 3.4) vorticity budgets, and discuss our findings and conclusions in Section 3.5.

3.2 Formulation of the vorticity diagnostics

We use a 0.1°-resolution global simulation with 42 vertical levels that couples the Los Alamos Parallel Ocean Program 2 (POP2, *e.g.*, Smith et al., 2010) with the Los Alamos Community Ice CodE 4 (CICE4, *e.g.*, Hunke et al., 2010) in the Community Earth System Model 1.2 (CESM 1.2) framework to diagnose the vorticity budget along the ACM. The vertical resolution varies from 10 m near the surface to 500 m near the bottom. The simulation was forced by interanually-varying Coordinated Ocean-Ice Reference Experiment 2 (CORE-II, Large and Yeager, 2009) surface fluxes. The simulation used biharmonic horizontal viscosity and diffusivity operators, with a viscosity coefficient of -2.7×10^{10} m^4 s^{-1} and a diffusivity coefficient of -0.3×10^{10} m^4 s^{-1} at the equator, changing proportionally to the cube of the grid cell size. The values of the viscosity/diffusivity coefficients are based on Smith et al. (2000), but with the diffusivity coefficient decreased by a factor of 3. Nonlocal vertical mixing of temperature and salinity was implemented with the K-Profile Parameterization (KPP, Large et al., 1994). The simulation was run for the 1948-2009 period, during which output fields were saved as monthly averages. The terms in the momentum equations (from which we calculate the vorticity budget) are available as daily averages over the period 2005-2009. The simulation is described in further detail by Palóczy et al. (2018) and by McClean et al. (2018).

We first write the depth-integrated absolute vorticity equation with biharmonic lateral viscosity as

$$\underbrace{\partial_t\overline{\zeta} \;=\; \overbrace{\overbrace{-\beta\overline{v} \;+\; \boldsymbol{\nabla}\times\boldsymbol{\tau_s}}^{\text{SB}} \;-\; f w_b}^{\text{TSB}}}_{\text{tTSB}} \;-\; \boldsymbol{\nabla}\times\boldsymbol{\tau_b} \;-\; \overline{\boldsymbol{\nabla}\times\left(\boldsymbol{u}\cdot\boldsymbol{\nabla}\boldsymbol{u}\right)} \;+\; \overline{A_H\boldsymbol{\nabla}^4\zeta}, \tag{3.1}$$

where overbars indicate vertical integrals, f and β are the planetary vorticity and its gradient, v is the meridional velocity, w_b and $\boldsymbol{\tau_b}$ are, respectively, the vertical velocity and horizontal kinematic stress at the bottom, $\boldsymbol{\tau_s}$ is the total surface kinematic stress (due to relative sea ice motion and wind), $\boldsymbol{u} \equiv \hat{\boldsymbol{x}}u + \hat{\boldsymbol{y}}v$ is the horizontal velocity vector, ζ is the vertical component of the relative vorticity vector and A_H is the (spatially varying) lateral viscosity coefficient. The acronyms SB, TSB and tTSB stand for Sverdrup Balance, Topographic Sverdrup Balance and transient Topographic Sverdrup balance, respectively.

Diagnosing the depth-integrated vorticity budget in a z-coordinate model such as POP introduces a technical difficulty that must be overcome in order to interpret its terms analogously to those in Eq. 3.1. The fact that each cell has a flat bottom means that the effects of topography are masked if the terms are integrated over the full depth. However, approximate equivalence with the continuous vorticity equation can be obtained if the vertical integration is performed from the surface down to the deepest grid cell with no sidewalls, rather than to the bottom cell (Bell, 1999; Yeager, 2013). The result is a vertically separated vorticity budget where the terms integrated over the interior cells (*i.e.*, away from sidewalls) may be interpreted in analogy with Eq. 3.1 (see the Appendix for the steps between Equations 3.1 and 3.2).

The vorticity budget terms are calculated from the model outputs by applying the discrete curl operator directly to the momentum budget terms, thus ensuring that the budget is numerically closed. The time-dependent term is calculated as a residual. Following Yeager (2013), we rewrite the depth-integrated vorticity budget in analogy with the momentum budget terms as

$$\mathrm{RES}_{\xi} = -\mathrm{NONL}_{\xi} - \beta V - f w_I + \mathrm{ERRCOR} + \mathrm{PGRD}_{\xi} + \mathrm{VVIS}_{\xi} + \mathrm{HVIS}_{\xi}, \tag{3.2}$$

where the ξ subscript indicates the curl operator and the terms are, from left to right, the residual (tendency + truncation error), minus the total nonlinear term (vortex tilting and twisting + relative vorticity advection), minus the planetary vorticity advection, minus the bottom vortex stretching, an error term associated with decomposing the curl of the Coriolis term (at least an order of magnitude smaller than the next-largest terms), the pressure gradient torque (negligible away from sidewalls), the vertical viscous torque and the horizontal viscous torque. The vertical velocity at the deepest interior cell (at $z = z_I$) is w_I, and V is the vertically-integrated (from $z = z_I$ to $z = 0$) meridional velocity. The continuous analog of VVIS_{ξ} is the total frictional torque in the geostrophic interior, *i.e.*, $\boldsymbol{\nabla} \times (\boldsymbol{\tau_s} - \boldsymbol{\tau_b})$ in Eq. 3.1.

3.3 The time-averaged vorticity budget

We examine the regional variability of the vorticity budget by dividing the Antarctic continental slope in six segments: Ross, Amundsen-Bellingshausen (A-B), Western Antarctic Peninsula (WAP), Weddell, Western East Antarctica (W-EA) and Eastern East Antarctica (E-EA), shown in Figure 3.1. Figure 3.2 shows that the sign of the surface stress curl ($\boldsymbol{\nabla} \times \boldsymbol{\tau_s}$ in Equation 3.1) forcing the system is mostly negative, suggesting a poleward depth-integrated motion if a simple Sverdrup Balance were to hold (SB in Equation 3.1). In the following, we describe the vorticity balance and its time-averaged spatial structure in the Amundsen-Bellingshausen segment, as this segment will be shown to have its vorticity budget best approximated by a three-way balance between VVIS_ξ, $-\beta V$, and $-fw_I$.

Figure 3.3 shows the spatial structure of the depth-integrated vorticity budget terms in the Amundsen-Bellingshausen segment, with the associated depth-averaged velocity field overlaid in panel (c). The vertical frictional torque term is generally negative across this region, except close to the coast, where the westward Antarctic Coastal Current jet is found. The spatial scales of the other terms are smaller. The magnitude of the residual and βV terms is largest beyond the continental slope, resembling the structure of the vigorous eddy field of the Antarctic Circumpolar Current (ACC) farther north. The vortex stretching, lateral viscous torque and nonlinear torque have the smallest spatial scales and are qualitatively similar, suggesting a two- or three-way balance at leading order.

The top panel of Figure 3.4 shows the 2005-2009 averages of the terms in Eq. 3.2, area-averaged within the circumpolar control volume delimited by the 800 m and 2500 m isobaths (Figure 3.1). ERRCOR and PGRD_ξ are omitted, as they are at least two orders of magnitude smaller than the other terms (Figure 3.3). The leading-order balance in the circumpolar average is between the lateral viscous torque HVIS_ξ and the bottom vortex stretching $-fw_I$. The nonlinear torque, the vertical frictional torque, and the $-\beta V$ terms are smaller in magnitude and comparable amongst themselves. However, the spatial averages taken over some of the segments are found to deviate from this circumpolar average pattern (Figure 3.4, bottom three rows). For instance, the magnitude of the nonlinear term is largest in the WAP, Weddell, Ross and W-EA segments, suggesting that eddies or interactions between topography and slope currents may be playing a more important role there than in the other three segments. The $-fw_I$ and nonlinear terms have the same sign in the W-EA segment and seem to balance HVIS_ξ. The negative sign of the VVIS_ξ term (except in the WAP and Ross segments) reflects the spatially broad cyclonic vorticity imparted at the surface by the wind and the sea ice year-round (Figure 3.2 and left column of Figure 3.5). It is also interesting to note that in the Amundsen-Bellingshausen, Weddell and E-EA segments the $-fw_I$ term is positive and the VVIS_ξ term is negative, which is qualitatively consistent with an upward surface Ekman velocity being equilibrated by an upward near-bottom velocity (due perhaps to up-slope motion). The time-averaged residual term, containing the relative vorticity tendency ζ_t, is negligible in all segments in the 2005-2009 average.

The ubiquity and persistence of the cyclonic vorticity forcing at the surface seen in Figure 3.2 prompts an investigation of the seasonal variability of the water column. Figure 3.5 shows seasonal averages for the Amundsen-Bellingshausen segment of the net vertical frictional torque VVIS_ξ and the sum $\mathrm{stretch}_{\mathrm{res}} \equiv -fw_I + \mathrm{HVIS}_\xi - \mathrm{NONL}_\xi - \mathrm{RES}_\xi$. We interpret $\mathrm{stretch}_{\mathrm{res}}$ as the portion of the bottom vortex stretching term that does not balance the combination of the other three terms (the lateral frictional torque, the nonlinear torque and the vorticity tendency), and may therefore be balancing the net vertical frictional torque. As Figure 3.2 suggests, the surface stress curl is mostly negative, especially in summer, under ice-free conditions (compare Figures 3.2 and 3.5). The Antarctic Coastal Current is seen flowing westward, potentially contributing to the net vertical stress curl VVIS_ξ. The year-round similarity between the spatial structures of VVIS_ξ and $\mathrm{stretch}_{\mathrm{res}}$ is apparent in Figure 3.5, which is physically consistent with the interpretation that part of the frictional torque that is introduced in the system forces meridional motion via conservation of planetary potential vorticity, and that part of this transport is blocked by the motion normal to the topography (see Section 3.5 and Figure 3.10).

3.4 The time–varying vorticity budget and TSB residual

Based on the description of the time-mean vorticity budget presented in the previous section and in agreement with the results of Hughes and de Cuevas (2001) and Wunsch (2011), it is clear that a classic Sverdrup Balance is not a good model for the ACM, and that other terms in

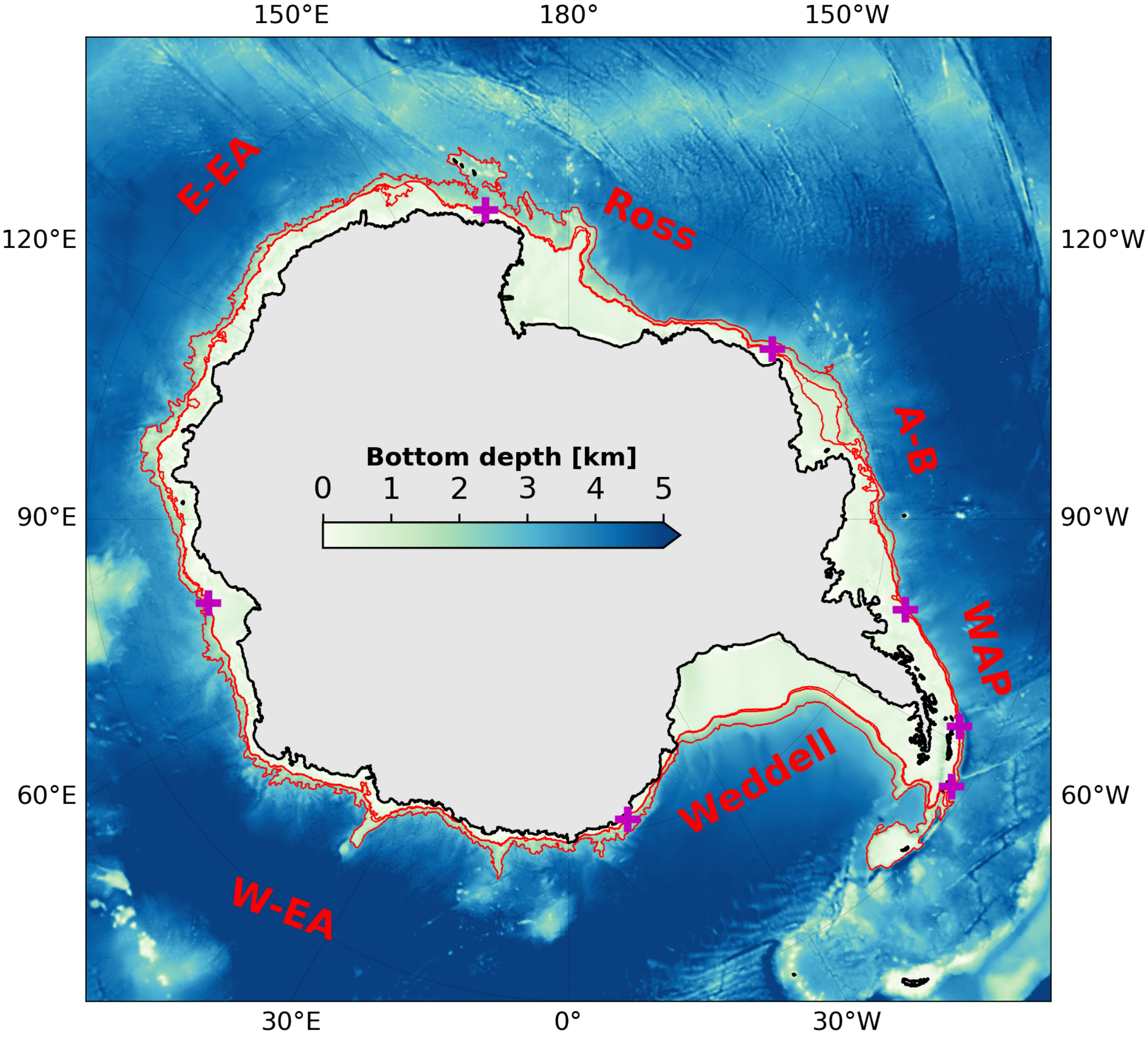

Figure 3.1: Map of the model topography. The red lines are the 800 m, 1000 m and 2500 m isobaths. The magenta crosses on the isobaths mark the zonal limits of the segments whose names are indicated in red text. The model control volume for a number of calculations described in the text is delimited by the 800 m and 2500 m isobaths. A-B = Amundsen-Bellingshausen, WAP = Western Antarctic Peninsula, W-EA = Western East Antarctica and E-EA = Eastern East Antarctica.

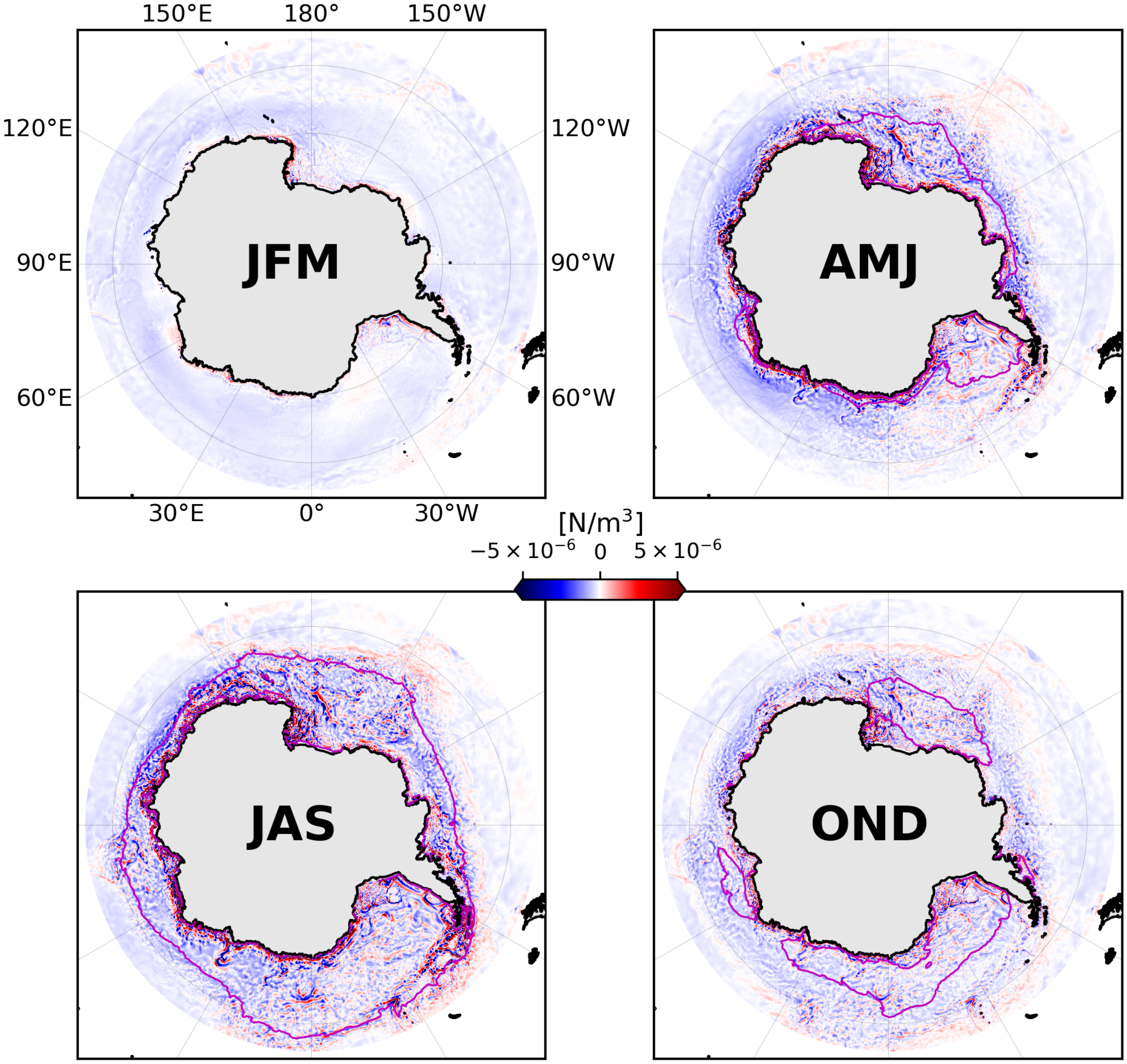

Figure 3.2: Seasonal variability of the time-averaged (2005-2009) total (wind + sea ice) surface stress curl (color shading) and sea ice edge (magenta line), defined as the 85% sea ice concentration contour. JFM, AMJ, JAS and OND indicate austral summer, autumn, winter and spring, respectively. Note that the surface stress curl is persistently cyclonic, suggesting an upward Ekman velocity and associated southward large-scale flow via conservation of planetary potential vorticity if a classic Sverdrup Balance (SB in Equation 3.1) were to hold.

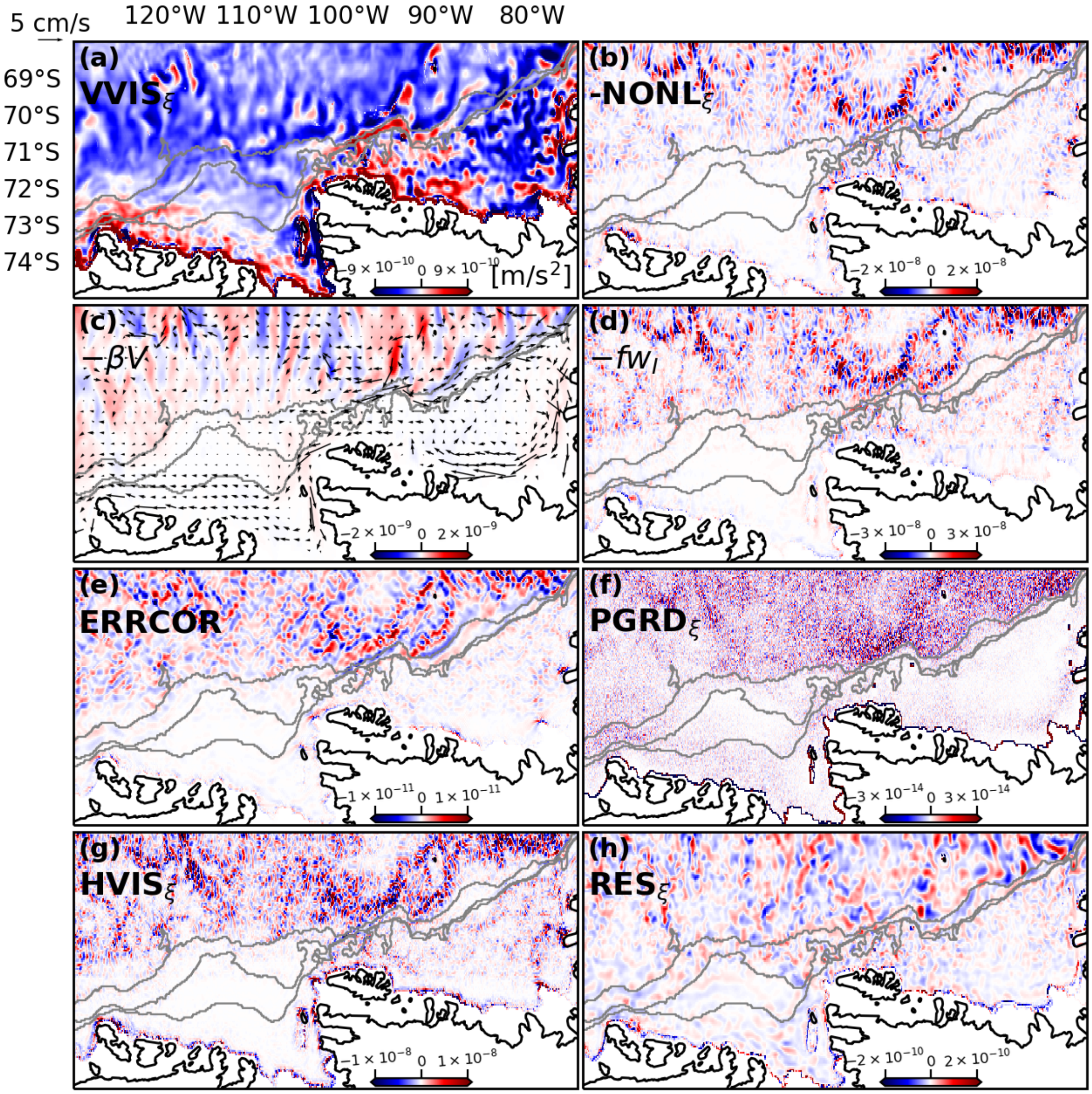

Figure 3.3: Maps of the 2005-2009 average of vertically-integrated vorticity budget terms (Equation 3.2) in the Amundsen-Bellingshausen segment. (a) Net vertical frictional torque, VVIS$_\xi$; (b) nonlinear term, -NONL$_\xi$; (c) planetary vorticity advection, $-\beta V$; (d) bottom vortex stretching, $-fw_I$; (e) Coriolis error term, ERRCOR; (f) Curl of the pressure gradient force, PGRD$_\xi$; (g) Lateral frictional torque, HVIS$_\xi$ and (h) Residual (truncation error + relative vorticity tendency), RES$_\xi$. The black arrows on (c) are the depth-averaged velocity field, and the gray lines are the 800 m, 1000 m and 2500 m isobaths. Note the difference in the color scales.

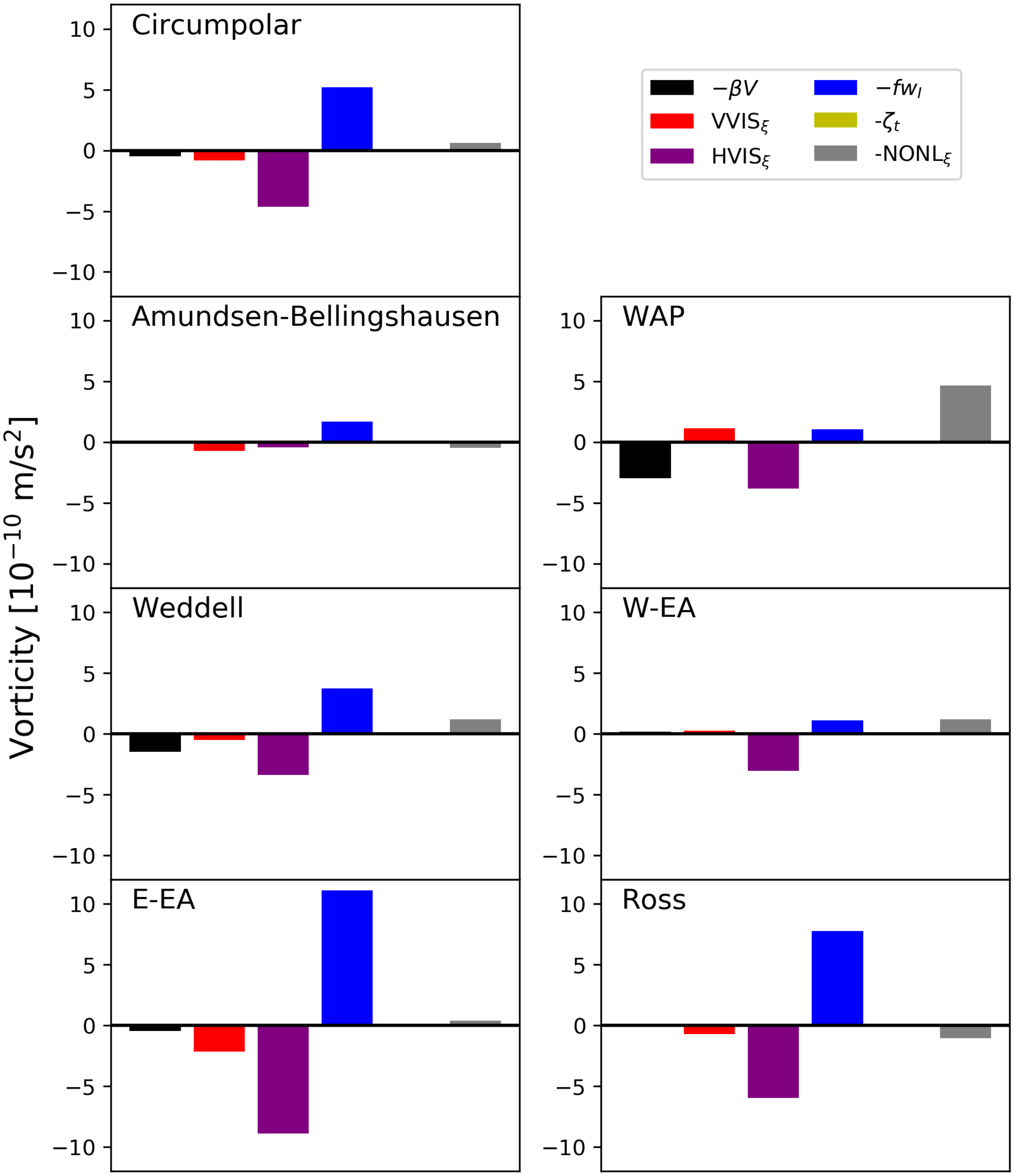

Figure 3.4: The 2005-2009 average of vertically-integrated vorticity budget terms averaged over the strip bounded by the 800 m and 2500 m isobaths. Top panel: Circumpolar average. Other panels: Averages taken over segments of the circumpolar strip.

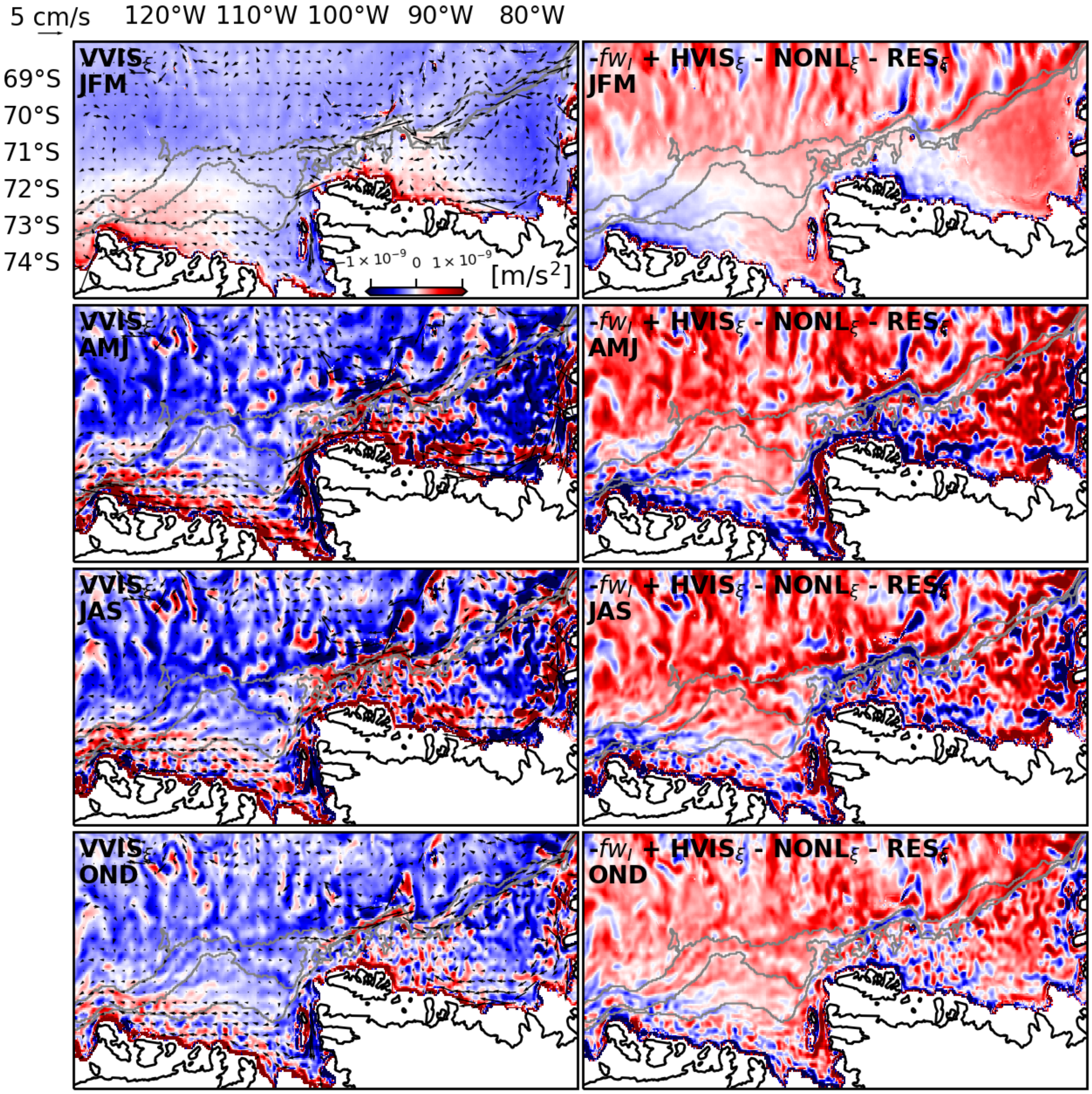

Figure 3.5: Maps of the 2005-2009 seasonal averages (JFM, AMJ, JAS and OND, rows) of the vertical frictional torque term, VVIS_ξ (left column), and the bottom vortex stretching residual, $-fw_I + \text{HVIS}_\xi - \text{NONL}_\xi - \text{RES}_\xi$ (right column), in the Amundsen-Bellingshausen segment. The gray lines are the 800 m, 1000 m and 2500 m isobaths. The black arrows on the left column are the depth-averaged velocity field. The color scale is the same for all panels.

Eq. 3.1 must be considered to balance the cyclonic surface stress forcing. We thus investigate whether the Topographic Sverdrup Balance (TSB) or the time-dependent TSB (tTSB) are valid diagnostic frameworks for the cross-slope flow in the ACM. We pursue this with correlation and coherence analyses between the time series of a subset of the vorticity terms in Eq. 3.2 averaged within the 800 m and 2500 m isobaths in each of the six segments (Figure 3.1) and over the full extent of the ACM.

3.4.1 Forcing-Response correlations

The top panel of Figure 3.6 shows the time series of the area averages of the vorticity terms over the entire continental slope. Consistent with the time-averaged fields in Figure 3.5, VVIS_ξ is mostly negative, and is balanced by the sum $-fw_I + \mathrm{HVIS}_\xi - \mathrm{NONL}_\xi - \mathrm{RES}_\xi$. The βV term is almost always positive (except for episodic reversals in the A-B, W-EA and Ross segments) and one order of magnitude smaller than the others, indicating that, most of the time, the TSB acts to produce a net northward, offshore transport. The same cancellation between VVIS_ξ and the four large terms is seen in all segments (Figure 3.6, bottom three rows). An annual cycle is most evident in the W-EA segment, although it appears to exist in the other segments as well. An estimate of the segment-integrated meridional transport associated with the βV term is given in Figure 3.6 for the A-B, Ross, W-EA and E-EA segments. Caution is required in interpreting these estimates however, as they are O(10 Sv) and do not isolate the cross-isobath transport, but are instead a combination of cross-isobath and along-isobath transports (see discussion in Section 3.5).

At this point, we have established that the spatial and temporal variability of the vorticity budget is, to leading order, a cancellation of large terms (primarily $-fw_I$ and HVIS_ξ, Figures 3.4, 3.5 and 3.6). We are now in a position to test the hypothesized vorticity balances (TSB and tTSB). The reason why we do not include HVIS_ξ in the balances is that $-fw_I$ and HVIS_ξ do not fully cancel out everywhere, but rather, $-fw_I$ tends to be slightly larger or much larger than HVIS_ξ, leaving a residual that may be balanced by other terms (Figure 3.4). However, the confirmation of this conjecture requires a correlation analysis, which will be presented next.

We begin by defining the forcing $F \equiv \mathrm{VVIS}_\xi$ and the response $R_1 \equiv \beta V + f w_I$ (for the TSB) or $R_2 \equiv \beta V + f w_I + \mathrm{RES}_\xi$ (for the tTSB), where the $-\beta V$ and $-f w_I$ terms are now grouped on the left-hand side of Eq. 3.2 and have therefore switched signs. We plot their time series in Figure 3.7. In both the TSB and tTSB cases, the response tracks the forcing for most of the time series, with some departures in the latter halves of 2006, 2007 and 2008. Regionally, the TSB seems to be a good approximation for the Amundsen-Bellingshausen, Weddell and W-EA segments (Figure 3.7, bottom three rows). The episodic departures seen in the tTSB for the circumpolar average (Figure 3.7, top panel) are most evident in the W-EA and E-EA segments.

The time series presentation is useful to reveal persistent correlations between the forcing (F) and different responses (R_1 and R_2); however it is based on spatial averages. We therefore examine the spatial extent of these correlations. Figure 3.8 shows the 2005-2009 mean geographic distribution of the TSB residual, defined as

$$\mathrm{TSB}_{\mathrm{res}} \equiv F - R_1 = \mathrm{VVIS}_\xi - \beta V - f w_I. \tag{3.3}$$

It can be seen that the WAP and the East Antarctica segments have relatively larger residuals, while areas of relatively smaller $\mathrm{TSB}_{\mathrm{res}}$ are found in the Amundsen and Weddell Seas, and to a lesser extent, in the Ross Sea. The areas of local spatial minima of $\mathrm{TSB}_{\mathrm{res}}$ extend over large spans of the ACM, notably over the entire broad continental shelves of the Amundsen and Weddell Seas.

Even in the regions of local minima found in Figure 3.8, the $\mathrm{TSB}_{\mathrm{res}}$ is often of the same size as the other terms in the vorticity budget. So are F and R_1 or R_2 quantitatively correlated? Table 3.1 shows the zero-lag correlation coefficients for the two hypothesized balances (TSB and tTSB), where the estimate of effective degrees of freedom for the minimum significant correlation coefficient was calculated based on an integral timescale of 5 days, computed as

Table 3.1: Zero-lag correlation coefficients (columns) between forcing (F) and response (R_1 or R_2) functions. $F = VVIS_\xi$ for both rows, $R_1 = \beta V + fw_I$ for the Topographic Sverdrup Balance (TSB, first row) and $R_2 = \beta V + fw_I + \mathrm{RES}_\xi$ for the transient Topographic Sverdrup Balance (tTSB, second row). The minimum statistically significant correlation coefficient at the 99% confidence level is 0.14, assuming a conservative integral timescale of 5 days for F, R_1 and R_2.

	A-B	WAP	Weddell	W-EA	E-EA	Ross	Circumpolar average
TSB	0.54	0.18	0.36	0.36	0.26	0.19	0.40
tTSB	0.94	0.11	0.74	0.52	0.63	0.48	0.61

the maximum between the integral timescales of either the F and R_1 or F and R_2. One might expect the correlations to be maximum at nonzero lags due to frictional effects (Gille et al., 2001). However, the correlations are all maximum at zero lag or lags of few days (not shown). This result suggests that F and either R_1 or R_2 generally balance directly. Intuitively, correlations are highest for the tTSB (*i.e.*, F with R_2 rather than F with R_1) in all segments (except for the WAP segment). Consistent with the spatial patterns seen in Figure 3.8, the highest-correlation segment for TSB is the Amundsen-Bellingshausen.

3.4.2 Forcing-response coherence spectra

While tTSB appears to offer a better representation than TSB of the dominant dynamics, there is no guarantee that this is true over all time scales. We use coherence analysis between the time series of F and either R_1 or R_2 (Figure 3.9) to assess the frequency dependence of the balance. In agreement with Table 3.1, the tTSB holds well for all segments at high frequencies (with the exception of the WAP segment), with squared coherences nearing 1. The higher coherences for the TSB at low frequencies in the Amundsen-Bellingshausen lends further support to the results of the correlation analyses (Table 3.1) and to the spatial minimum in the residual of the TSB (Figure 3.8). The W-EA segment also displays relatively high coherences for the TSB at low frequencies, although Figure 3.8 shows no conspicuous local minima in $\mathrm{TSB}_{\mathrm{res}}$ there, meaning that the terms have substantial covariance despite having a large mean residual. The

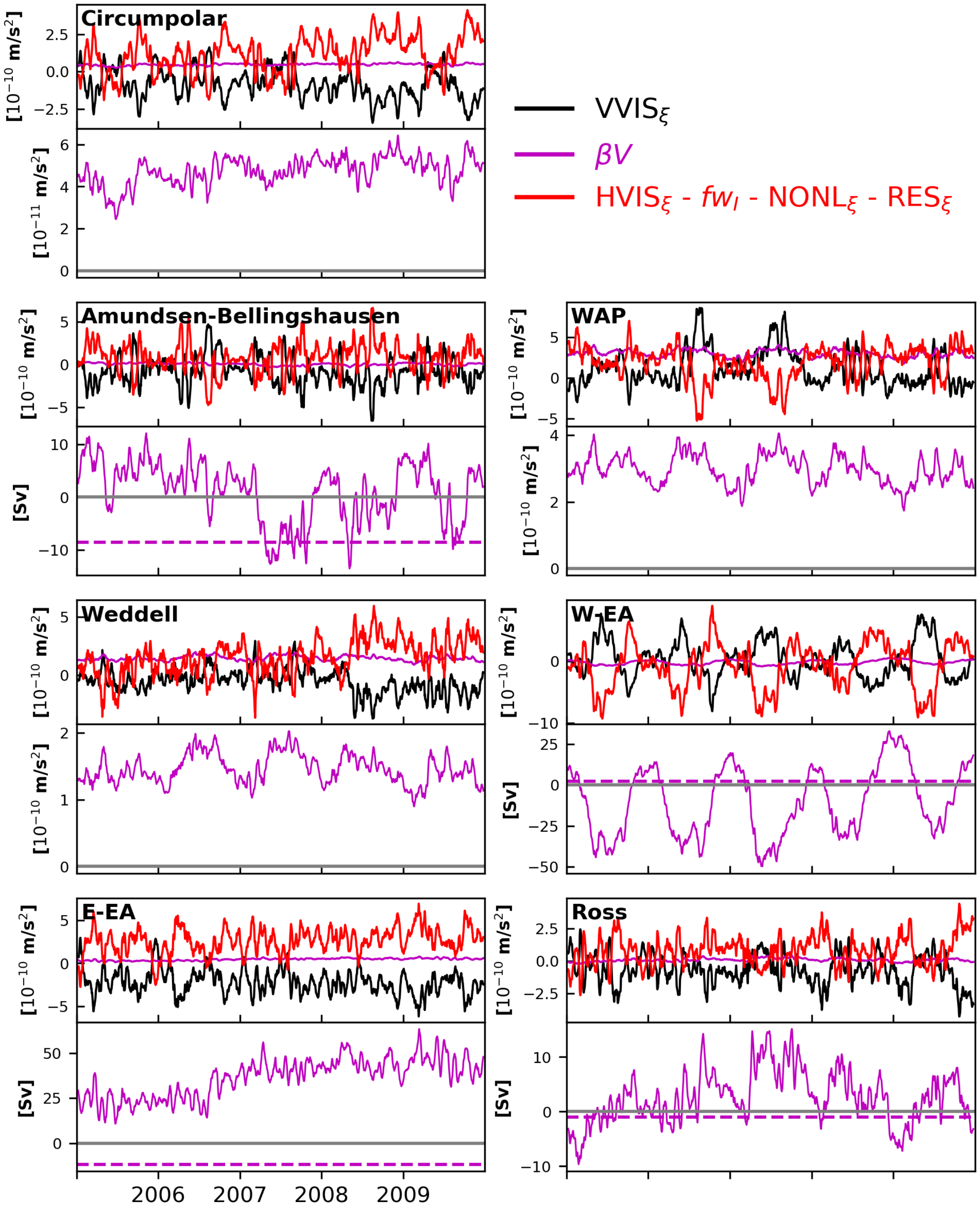

Figure 3.6: Balance of leading-order terms in the area-averaged vorticity budget. Top sub-panels: VVIS$_\xi$ (forcing), HVIS$_\xi$ - fw_I - NONL$_\xi$ - RES$_\xi$ (bottom vortex stretching residual) and βV. bottom sub-panels: Only the βV term. The βV term is a small residual of the cancellation of large terms. Top panel: Circumpolar average. Other panels: Averages taken over segments of the circumpolar strip. For segments with a predominant zonal orientation (A-B, W-EA, E-EA and Ross, see Figure 3.1), βV is given in units of volume transport (*i.e.*, βV multiplied by L/β, where L is the length of the 800 m isobath in the segment) in the lower subpanels. The horizontal magenta lines indicate the transport values estimated in Table 3.2. All time series were smoothed with a 15-day running mean window. Note the different y scales.

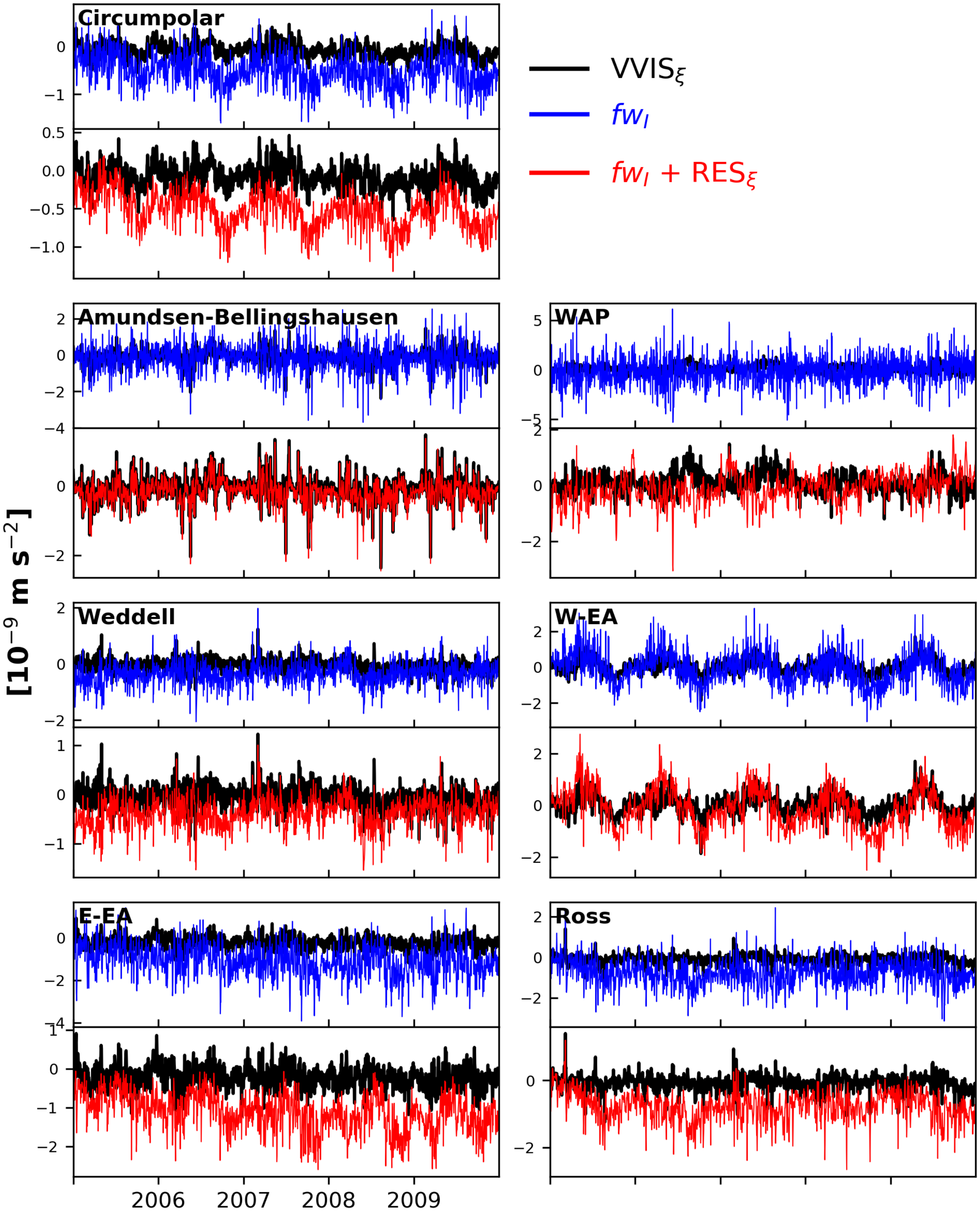

Figure 3.7: Time series of the forcing term $F = \mathrm{VVIS}_\xi$ and two simplified vorticity balances assumed as a response term R for the area-averaged budget. Upper subpanels: Topographic Sverdrup Balance (TSB, $R_1 = \beta V + fw_I$). Lower subpanels: Transient Topographic Sverdrup Balance (tTSB, $R_2 = \beta V + fw_I + \mathrm{RES}_\xi$). Top panel: Circumpolar average. Other panels: Averages taken over segments of the circumpolar strip. The βV term is smaller and has been omitted for simplicity.

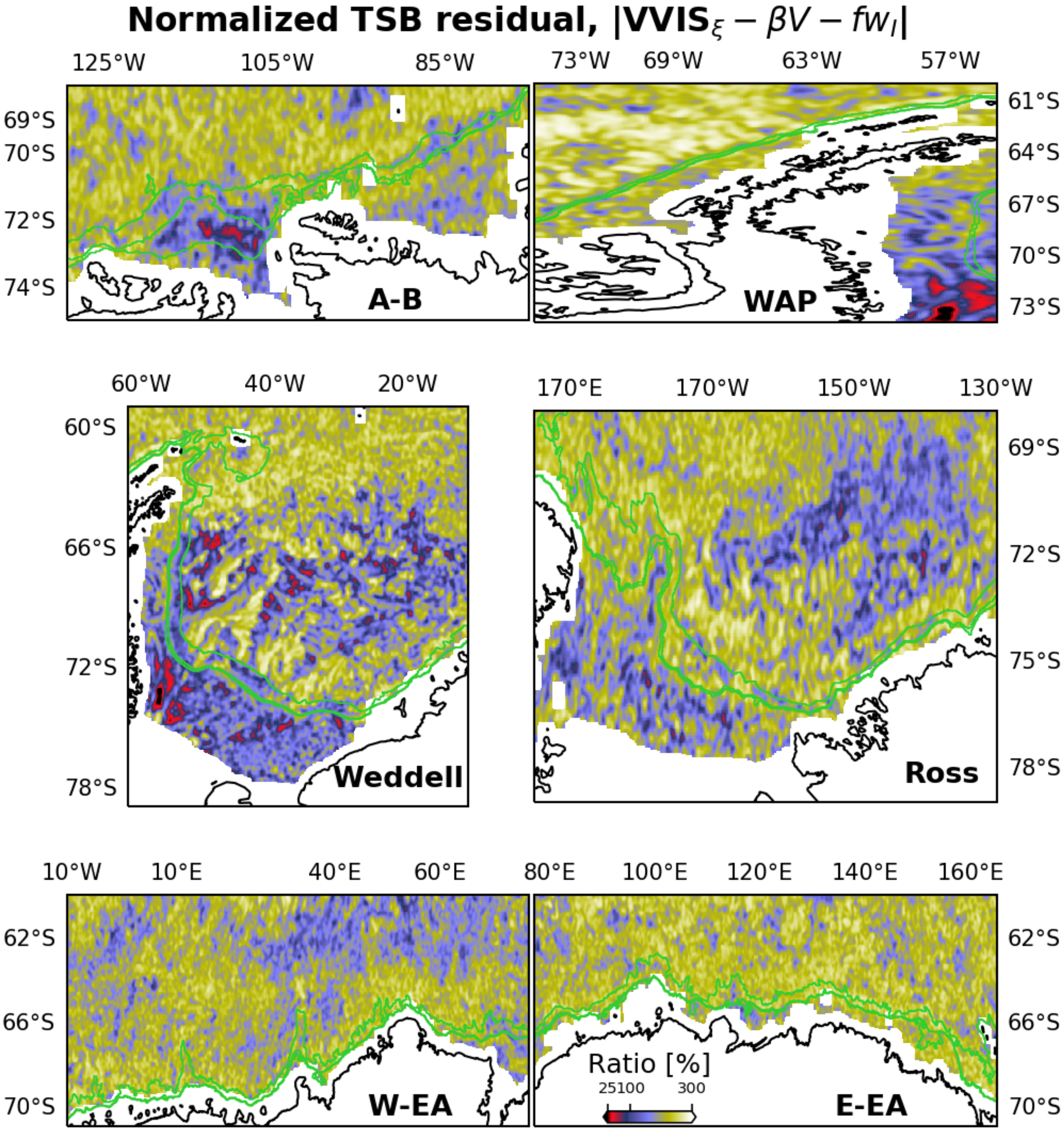

Figure 3.8: Maps of the 2005-2009 average of the residual of the Topographic Sverdrup Balance (TSB), $R_{Sv} \equiv \mathrm{VVIS}_\xi - \beta V - f w_I$ for each of the six segments. The green lines are the 800 m, 1000 m and 2500 m isobaths. The color scale is the same for all panels and indicates the ratio of the absolute value of R_{Sv} to the mean of the absolute values of all terms, at each grid cell. The fields have been smoothed with a two-dimensional Gaussian filter.

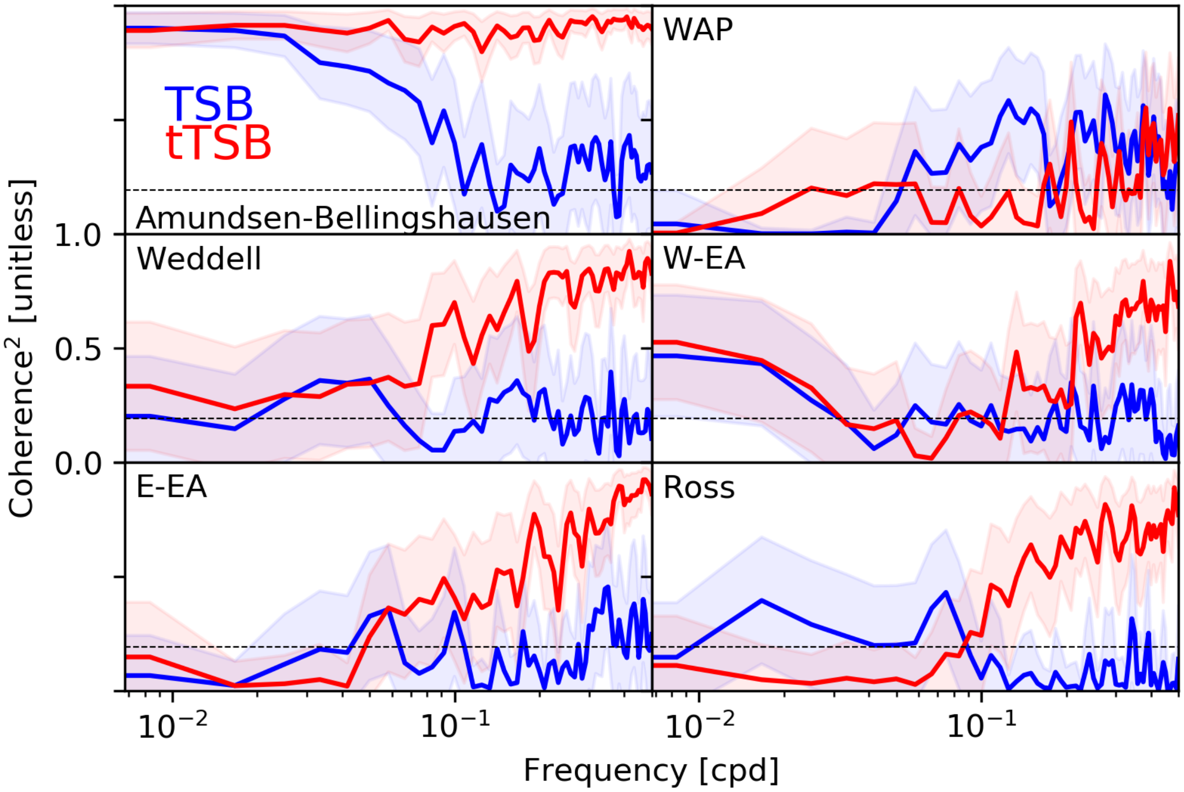

Figure 3.9: Coherence amplitude spectra between forcing $F \equiv \mathrm{VVIS}_\xi$ and response R functions, estimated with 80 degrees of freedom. For the Topographic Sverdrup Balance (TSB) time series (blue lines), $R_1 \equiv \beta V + f w_I$. For the transient Topographic Sverdrup Balance (tTSB) time series (red lines), $R_2 \equiv \beta V + f w_I + \mathrm{RES}_\xi$. The shading indicates the 95% confidence intervals of the coherence estimates. The dashed lines are the level of no significance at the 95% confidence level.

tTSB holds exceptionally well for the Amundsen-Bellingshausen segment at all frequencies, while it is marginally significant at low frequencies in the Weddell segment.

3.5 Discussion and conclusions

We have diagnosed the circumpolar-averaged and regional vorticity budgets in a global, eddy-permitting ocean/sea-ice simulation and have shown that, in some regions of the Antarctic Continental Margin (ACM), the flow follows a simplified time-dependent Sverdrup-like balance (tTSB, Equation 3.1). The Amundsen and Weddell Seas (and to a lesser extent, the W-EA segment) emerge as regions where an even simpler, steady, Topographic Sverdrup Balance (TSB, Equation 3.1) is found in the 2005-2009 average. Figure 3.10 gives a physical interpretation of these two diagnostic results. In the TSB, there is a steady-state equilibration between the surface vortex stretching/squashing imparted by the surface Ekman pumping and the bottom vortex squashing/stretching imparted by cross-slope motion. In the tTSB, relative vorticity fluctuations are important and can be understood as the manifestation of forced topographically-trapped waves, which displace water columns up- and down-slope while propagating westward.

Quantitatively, how important is the TSB for the cross-slope transport of volume and heat? We present in Table 3.2 rough estimates for the approximately zonally-oriented segments (A-B, W-EA, E-EA and Ross) based on the time-averaged (2005-2009) forcing $F \equiv \text{VVIS}_{\xi}$ scaled by $r^2 L/\beta$, where r is the TSB forcing-response correlation coefficient (Table 3.1) and L is the length of the segment. The rationale for this estimate is that each term in Equations 3.1 and 3.2 may be interpreted as a meridional transport per unit length (if these equations are divided through by β), and therefore the fraction of $R_1/\beta = V + f w_I/\beta$ that covaries with the forcing VVIS/β (this fraction is obtained by scaling VVIS/β by r^2) is an estimate of the net meridional transport associated with the two response terms in the TSB. The associated heat transports are obtained by multiplying the volume transports by $\rho C_p \Delta T$ where $\rho = 1027$ kg m^{-3} is the density, $C_p = 4000$ J kg^{-1} K^{-1} is the specific heat capacity and $\Delta T = 0.5$ K is an approximate estimate of the temperature of seawater above the freezing point. The A-B and E-EA are the segments with the largest onshore TSB-related volume and heat transports, while The Ross and W-EA have smaller transports. Note that the heat transports may be larger in segments where warmer branches of CDW (larger ΔT) are present on the continental slope.

We emphasize that caution is required in interpreting the transport estimates in Table 3.2, as well as those in Figure 3.6. The O(10 Sv) total transport derived from the βV term (Figure 3.6) is much larger than the O(0.1 Sv) estimates of the cross-slope overturning circulation, either in the geostrophic interior or in the surface and bottom Ekman layers (*e.g.*, Wåhlin et al., 2012; Stewart and Thompson, 2015c; Palóczy et al., 2018). Since it is the meridional transport (not the cross-isobath transport) that appears in the vorticity equation (Equations 3.1 and 3.2), and the ACM is not perfectly zonally-oriented (Figures 3.1 and 3.8), one should not expect the TSB and the tTSB to isolate only the cross-isobath transport, hence leading to the discrepancy between the transport estimates in Figure 3.6 and Table 3.2. We hypothesize that our vorticity-based dynamical argument can explain only a fraction of the onshore or offshore transport, and that this fraction varies regionally along the ACM.

The potential implications of these dynamics are greatest for the Amundsen Sea, where warm Circumpolar Deep Water has access to the ice shelves that buttress most of the West Antarctic Ice Sheet (*e.g.*, Schmidtko et al., 2014; Silvano et al., 2016). We note that measurements have shown that the surface-stress curl (from wind and sea ice) at the shelf break correlates with bottom temperature in Dotson Trough, located in the central Amundsen Sea (Kim et al., 2017). This provides observational support for our hypothesis that the surface-stress curl might play an important role in the cross-isobath transport of heat (both onshore and offshore) via a Sverdrup-like vorticity balance, and it also agrees with Rodriguez et al. (2016)'s model results where a net onshore transport linked to the wind stress curl was found.

Dotto et al. (2019) have shown the importance of two different mechanisms in different regions of the Amundsen Sea. The first one is change in water mass properties (along the same isopycnal) entering the continental shelf, and the second one is isopycnal heaving without change in the water mass properties. They related the variations in the water mass properties to wind-driven variations in the speed of an eastward undercurrent on the continental slope (a baroclinic feature also observed by Walker et al., 2013), and interpreted the isopycnal heaving as due to locally-induced vertical velocities associated with Ekman pumping. We argue that the TSB mechanism discussed in this study may play a role in these processes by meridionally transporting different water mass classes towards or away from the slope undercurrent in the water mass property change mechanism, and by locally inducing meridional transport associated with the isopycnal heaving mechanism (due to conservation of planetary potential vorticity).

In analyses of the depth-integrated vorticity budget in global models, areas with smoother bottom topography in the interior of tropical and subtropical basins have been found to be closer to classic Sverdrup Balance ($\beta V \approx \nabla \times \boldsymbol{\tau_s}$ in Eq. 3.1, see Wunsch, 2011), while the rough Southern Ocean and steep continental margins have been dominated by bottom pressure torques (Hughes and de Cuevas, 2001; Lu and Stammer, 2004; Yeager, 2013, 2015). The fact that the influence of remote wind perturbations communicated via barotropic Kelvin waves have been suggested to be strongest in steep regions like the WAP (Spence et al., 2017; Webb et al., 2019) is consistent with the fact that this segment has the poorest correlations and coherence magnitudes for the tTSB (Table 3.1, Figures 3.7, 3.9), and has also the narrowest and steepest continental slope (Figure 3.1). A physical interpretation of this is that relative vorticity fluctuations in the WAP are not being forced by the local surface-stress curl as in a tTSB (Figure 3.10a), but rather by remotely-generated topographically-trapped waves propagating through the region, or by nonlinear effects associated with the impingement of offshore currents. We also note that in an eddy-permitting simulation such as the one we consider here, non-topographic effects such as convergence of eddy vorticity fluxes (*e.g.*, Williams et al., 2007; Delman et al., 2015) are likely to play a role, although such effects are beyond the scope of our study. Eddy vorticity forcing in the ACC and ASC might help explain the large vertical velocities in the W-EA and E-EA segments (not shown).

The picture discussed in this study is likely robust at large scales and low frequencies. However, we remind the reader of the limitations of our analyses. The model resolution is not sufficient to fully resolve eddies in the ACM (Stewart and Thompson, 2015c), and the lack of ice shelf cavities, tides, and realistic continental freshwater sources also limits the realism of the simulation, especially on the continental shelf. The lack of tidal momentum flux convergences around the shelf break is expected to impact the structure of the ASC (Flexas et al., 2015; Stewart et al., 2019), which might modify the cross-slope transport of heat and other properties at tidal and supertidal frequencies (Stewart et al., 2018, 2019).

An interesting and important related question that could be addressed in future work is whether averaging the vorticity balance over even longer timescales would expand the areas over which the depth-integrated flow is in approximate TSB. A similar question was asked by Wunsch (2011) for the classic Sverdrup Balance based on the analysis of a 16-year average global state estimate. We are limited by the five years (2005-2009) over which model output necessary to close the vorticity budget is available, although it may be possible to test correlations between approximations to the vorticity budget terms reconstructed from the velocity and surface-stress curl fields in the monthly-averaged output of the simulation.

In summary, we have presented evidence for the existence of an approximate topographic Sverdrup balance in some areas of the ACM in a global eddy-permitting simulation. Because sea ice extent and winds change unevenly in the Southern Ocean, sectors of the ACM are expected to be exposed in different ways to low-frequency wind- and ice-stress curl. For example, the effects of poleward shifting easterlies on the heat content of the Antarctic continental shelf, as studied in global climate models by Spence et al. (2014, 2017); Goddard et al. (2017); Palóczy et al. (2018), Webb et al. (2019) and others, might be expected to affect the cross-slope transport of heat in the Amundsen, Bellingshausen and Weddell Seas and in parts of East Antarctica more strongly than elsewhere in the ACM.

Acknowledgments

A.P., J.L.M and S.T.G. gratefully acknowledge support from the US Department of Energy (DOE, grants DE-SC0014440 and DE-SC0020073) and high-performance computing support from Yellowstone (ark:/85065/d7wd3xhc) provided by NCAR's Climate Simulation Laboratory (CSL), sponsored by the National Science Foundation (NSF) and other agencies.

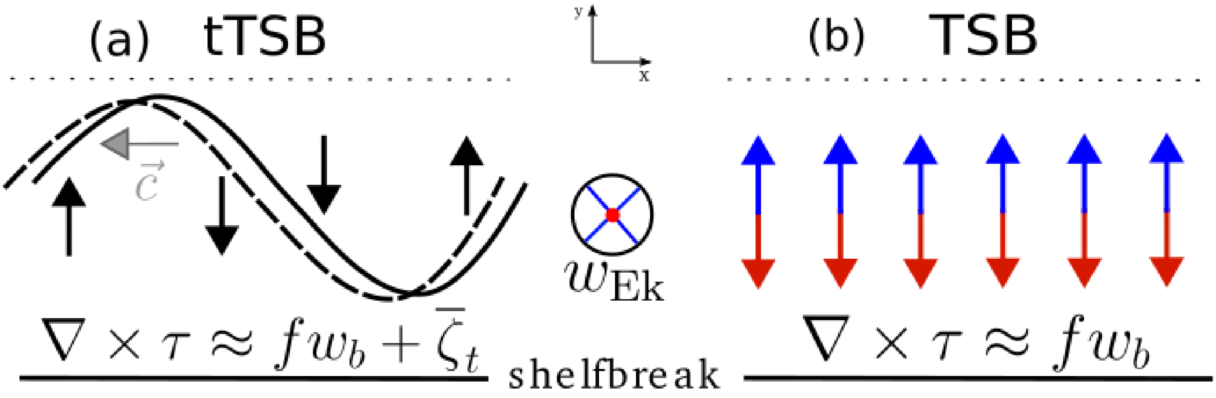

Figure 3.10: Cartoon illustrating a physical interpretation of the cross-slope transport in the time-varying Topographic Sverdrup Balance (a) and in the steady Topographic Sverdrup Balance (b) over a zonally-oriented continental margin. The βV term has been omitted for simplicity because it is usually an order of magnitude smaller than the other terms (Figure 3.6). Here, $\boldsymbol{\tau} \equiv \boldsymbol{\tau_s} - \boldsymbol{\tau_b}$ is the net kinematic stress vector, and other terms follow Equation 3.1. In (a), the gray arrow indicates the direction of propagation of the topographically-trapped waves associated with the tTSB, and the black arrows indicate the associated instantaneous meridional, cross-slope flow. The black curves illustrate the displacement of a waveform (from solid to dashed). In (b), the red arrows indicate onshore transport associated with upward Ekman pumping ($w_{\mathrm{Ek}} > 0$, directed out of the page), while the blue arrows indicate offshore transport associated with downward Ekman pumping ($w_{\mathrm{Ek}} < 0$, directed into the page).

Table 3.2: Rough estimates of volume and heat transports associated with the Topographic Sverdrup Balance (TSB). The volume transports are obtained by multiplying the time-averaged forcing (VVIS_ξ) by r^2L/β, where r is the TSB correlation coefficient (Table 3.1) and L is the length of the segment. The heat transports are obtained by multiplying the volume transports by $\rho C_p \Delta T$, where ρ, C_p and ΔT are typical values for the density, the specific heat capacity and the temperature above the freezing point.

	A-B	W-EA	E-EA	Ross
TSB volume transport [Sv]	-8.5	2.1	-11.8	-1.0
TSB heat transport [TW]	-17.4	4.2	-24.3	-2.0

J.L.M. was supported by an earlier U.S. DOE Office of Science grant entitled “Ultra-High Resolution Global Climate Simulation” via a Los Alamos National Laboratory subcontract to carry out the POP/CICE simulation; both Caroline Papadopoulos (SIO/UCSD) and Elena Yulaeva (UCSD) participated in its production. S.T.G. also acknowledges NSF awards PLR-1425989 and OCE 1658001. The analyses of the model output performed in this study were enabled by computing resources provided by Oak Ridge Leadership Computing Facility (OLCF). We are also grateful to Andrew Stewart (University of California Los Angeles) and Matt Mazloff (SIO/UCSD), for insightful exchanges and Steve Yeager (National Center for Atmospheric Research, NCAR) for the additional POP code needed to archive non-standard terms for the budget as well as an NCAR Command Language (NCL) vorticity budget code that provided a starting place for our expanded Fortran-based budget code used in this study. Thoughtful critiques and comments from two anonymous reviewers substantially improved the quality of the manuscript. Reduced datasets and code necessary to reproduce the results are available at https://github.com/apaloczy/AntarcticaVorticityBudget.

Chapter 3, in full, reprints material as it appears in Palóczy, A., McClean, J. L., Gille, S. T. & Wang, H. (2020). The large-scale vorticity balance of the Antarctic continental margin in a fine-resolution global simulation. Journal of Physical Oceanography, 50(8), 2173-2188. DOI: 10.1175/JPO-D-19-0307.1. The dissertation’s author was the primary investigator and author of

this paper.

Appendix: Discretization of the depth-integrated vorticity equation

To arrive at the discrete form of the depth-integrated vorticity equation (Equation 3.2), we begin with the continuous depth-dependent momentum equation,

$$\boldsymbol{u}_t + \boldsymbol{u} \cdot \boldsymbol{\nabla} \boldsymbol{u} + \boldsymbol{f} \times \boldsymbol{u} = -\boldsymbol{\nabla} p + A_H \boldsymbol{\nabla}^4 \boldsymbol{u} + (A_v \boldsymbol{u}_z)_z, \tag{3.4}$$

where $\boldsymbol{f} \equiv \hat{\boldsymbol{z}} f$, p is pressure, A_v is the vertical viscosity coefficient and $\boldsymbol{\nabla}^4$ is the horizontal biharmonic operator. Taking the discrete curl of 3.4 gives

$$\zeta_t + \boldsymbol{\nabla} \times \left(\boldsymbol{u} \cdot \boldsymbol{\nabla} \boldsymbol{u}\right) + \boldsymbol{\nabla} \times \left(\boldsymbol{f} \times \boldsymbol{u}\right) = -\boldsymbol{\nabla} \times (\boldsymbol{\nabla} p) + A_H \boldsymbol{\nabla}^4 \zeta + \boldsymbol{\nabla} \times \left[(A_v \boldsymbol{u}_z)_z\right], \tag{3.5}$$

where the curl of the pressure gradient term vanishes at interior grid cells only in the case of uniform grid spacing (Bell, 1999, although we find it to be negligible, figure 3.3f), but is large at grid cells with sidewalls (Yeager, 2013), which we do not include in the vertical integrals. Applying the discrete curl operator to the Coriolis term on a B-grid gives

$$\boldsymbol{\nabla} \times \left(\boldsymbol{f} \times \boldsymbol{u}\right) = -f w_z + \beta v - \mathrm{ERRCOR}, \tag{3.6}$$

where ERRCOR is a numerical artifact of the discretization (see Bell, 1999; Yeager, 2013, for details). Vertically integrating 3.5 using 3.6 gives

$$\begin{aligned}\partial_t\overline{\zeta} = -\beta\overline{v} + f\left[w(0) - w(z_I)\right] - \overline{\boldsymbol{\nabla}\times\left(\boldsymbol{u}\cdot\boldsymbol{\nabla}\boldsymbol{u}\right)} - \overline{\boldsymbol{\nabla}\times(\boldsymbol{\nabla}p)} + \overline{A_H\boldsymbol{\nabla}^4\zeta} + \cdots \\ \cdots\overline{\boldsymbol{\nabla}\times\left[(A_v\boldsymbol{u}_z)_z\right]} + \overline{\mathrm{ERRCOR}},\end{aligned} \tag{3.7}$$

where overbars indicate vertical integrals from $z = z_I$ to $z = 0$, and $z_I(x,y)$ is determined from the minimum of the vertical indices of the bottom cells of the four surrounding U-points in the model's B-grid, minus one vertical cell index. This places the lower limit of integration at a grid cell that has no sidewalls (Bell, 1999). By approximating $w(z=0) \approx 0$, defining $V \equiv \overline{v}$, $\overline{\mathrm{RES}_\xi} \equiv \partial_t\overline{\zeta}$, $\overline{\mathrm{NONL}_\xi} \equiv \overline{\boldsymbol{\nabla}\times\left(\boldsymbol{u}\cdot\boldsymbol{\nabla}\boldsymbol{u}\right)}$, $\overline{\mathrm{PGRD}_\xi} \equiv -\overline{\boldsymbol{\nabla}\times(\boldsymbol{\nabla}p)}$, $\overline{\mathrm{HVIS}_\xi} \equiv \overline{A_H\boldsymbol{\nabla}^4\zeta}$, $\overline{\mathrm{VVIS}_\xi} \equiv \overline{\boldsymbol{\nabla}\times\left[(A_v\boldsymbol{u}_z)_z\right]}$, $w(z_I) \equiv w_I$, absorbing the numerical truncation error into the residual term $\overline{\mathrm{RES}_\xi}$ and dropping overbars results in Equation 3.2.

Chapter 4

Subtidal to supertidal variability of Reynolds stresses in a mid-latitude stratified inner-shelf

4.1 Introduction

Turbulent processes in the coastal ocean are important players in the transport and mixing of chemical tracers, plankton and other biological material, heat, salt and momentum (*e.g.*, Burchard et al., 2008). Turbulence is particularly important in the shallow region of the continental shelf where surface and bottom boundary layers overlap, usually defined as the inner shelf. Here, the momentum balance is complicated, with important contributions from surface gravity waves, bottom stress, wind stress both in the along-shelf and cross-shelf directions, and pressure gradients. This situation contrasts with the mid-shelf, where boundary layers are separated by a geostrophic interior, and the momentum imparted by the wind stress is not directly transported to the bottom (*e.g.*, Lentz et al., 1999; Lentz and Fewings, 2012).

Dynamically, turbulent processes enter the momentum balance in the Reynolds-averaged equations via divergences of time-averaged covariances between velocity components (*e.g.*, Cushman-Roisin and Beckers, 2011; Kirincich, 2013), often called Reynolds stresses (RSs). Turbulence also mixes temperature and salinity, modifying the density stratification and indirectly feeding back into the momentum equation by producing or modifying pressure gradients. RSs can be directly measured in the field using high-frequency Acoustic Doppler Velocimeters (ADV's, *e.g.*, Feddersen and Williams, 2007; Guerra and Thomson, 2017; Trowbridge et al., 2018), however each ADV measures only a single point in the water column. Alternatively, a vertical profile of RS can be derived from raw Acoustic Doppler Current Profiler (ADCP) velocity measurements logged in beam coordinates using the Variance Technique (*e.g.*, Lohrmann et al., 1990; Stacey et al., 1999), described in Section 5.24.2.2.

Turbulence can be generated by a number of processes, for example surface stress due to the wind, bottom stress due to currents and surface gravity waves interacting with the bottom. Other turbulent processes include internal and surface gravity wave breaking and shear instabilities associated with the ambient shear produced by subtidal along-shelf flow, internal tides or near-inertial internal waves (*e.g.*, MacKinnon and Gregg, 2003, 2005; Rippeth, 2005; Burchard et al., 2008; Walter et al., 2012; Lamb, 2014). In particular, turbulence caused by internal tides can take a variety of forms, such as internal tidal bores, solitary wave packets or hybrids between the two (*e.g.*, Lamb, 2014). These processes might be associated with substantial RSs. However, most observational studies of RSs in the ocean using ADCPs have concentrated on tidally-dominated flows (*e.g.*, Lu and Lueck, 1999; Stacey et al., 1999; Rippeth et al., 2003; Williams and Simpson, 2004; Guerra and Thomson, 2017) or on the bottom boundary layer in deeper regions (Lohrmann et al., 1990; van Haren et al., 1994), where contamination by surface gravity waves is not a concern. However, on the continental shelf, shoaling surface gravity waves complicate the picture by adding spurious contributions to the observed stresses, and various techniques to remove these contributions have been developed (Whipple et al., 2006; Rosman et al., 2008; Kirincich et al., 2010; Kirincich and Rosman, 2011).

In terms of the subtidal circulation, the observed RS profile at the 12 m isobath off Martha's Vineyard/Massachusetts has been shown to be well correlated with the local wind stress near the surface and to be consistent with simplified theoretical models of inner shelf dynamics, when conditionally-averaged over different wind, wave and stratification settings (Kirincich, 2013). At 30 m depth, poor correlations between the local wind stress and the near-surface RSs in the Outer Cape Coastal Current have been observed (Kirincich and Gawarkiewicz, 2016). At both locations, the RS profiles showed significant vertical divergence, suggesting a departure from a purely frictional momentum balance where the bottom stress balances the wind stress directly (Kirincich, 2013; Kirincich and Gawarkiewicz, 2016). This contrasts with the constant-stress profile observed just offshore of the surfzone (Feddersen and Williams, 2007).

Other studies concentrating on linking observations of RSs to different inner shelf physical processes appear to be lacking, especially in the superinertial band. The current understanding of inner shelf dynamics is that the subinertial circulation (particularly in the along-shelf direction) is sensitive to the vertical structure of the eddy viscosity $A_v = \overline{v'w'}/S$, where $\overline{v'w'}$ is the along-shelf stress and S is the vertical shear of the along-shelf velocity (Lentz, 1995; Lentz et al., 2008). Direct observations of turbulent stresses are therefore pointed out as an important knowledge gap (Lentz and Fewings, 2012; Kirincich, 2013). The sensitivity of the inner shelf's subtidal circulation to the vertical structure and magnitude of the RSs implies that transports driven by along-shelf winds, cross-shelf winds and along-shelf pressure gradients have different stress signatures (Kirincich, 2013, his Figure 2). Therefore, understanding the observed variability of subtidal RSs is relevant for processes involved in cross-shelf exchange and in the way turbulence is represented in Reynolds-averaged coastal regional models.

This approach of linking $\overline{v'w'}$ to S through an eddy viscosity assumes a flux gradient relationship, *i.e.*, that the vertical flux of mean momentum is down-gradient. While this aspect of subtidal dynamics is a knowledge gap in its own right, it is also unclear whether the use of an eddy viscosity hypothesis is valid at supertidal frequencies. As discussed above, RSs can also be generated by high-frequency turbulent processes, most of which are highly nonlinear and have complex shear and stress signatures, transporting momentum with them often independently from the background sheared flow. We will show that processes such as internal bores and nonlinear internal wave packets often have shear and stress signals that depart from such a simplified eddy viscosity relationship.

The central aim of this study is to describe the vertical structure, temporal and spatial variability of observed Reynolds stresses in a stratified, mid-latitude (35^oN) continental shelf (25-40 m), linking this variability to some of the turbulent processes mentioned above and to the momentum balance in the inner-/mid-shelf. We first describe the dataset and the techniques used to derive turbulent stresses corrected for the bias introduced by surface gravity waves (Section 5.2). We then describe the oceanographic setting, the variability of the observed stresses and their role in the momentum balance in Section 4.3. Finally, we summarize the results and present our conclusions in Section 4.4.

4.2 Data and methods

In this section, we first describe the datasets used in the analyses and the pre-processing steps. Next, we explain the method used for estimating Reynolds stresses (RSs) with reduced influence from the surface gravity waves' orbital velocity.

4.2.1 Dataset

We analyze a subset of the moored data from the Inner Shelf Dynamics Departmental Research Initiative's (ISDRI, Lerczak et al., 2019) primary field component, which was carried out in 9-10/2017 in the vicinities of Pt. Sal, off Central California (Figure 4.1a). The ISDRI was funded by the Office of Naval Research (ONR), and had the overarching objective of advancing the understanding of the dynamics of the region of the coastal ocean inshore of the 50 m isobath, including phenomena such as surface and internal gravity waves, wind-driven currents, headland eddies and rip currents. Our focus is on part of the Oceano Array (Figure 4.1b), wherein a group of five upward-looking, five-beam Acoustic Doppler Current Profilers (ADCPs) were deployed. The moored ADCPs were all Teledyne-RD Instruments (TRDI) Sentinel V's logging at 1 Hz (OC40S, OC40N, OC25SA and OC25SB), with the exception of OC25M, which was a Nortek Signature1000 logging at 8 Hz (Figure 4.1b). The vertical resolution of the instruments at the 25 m and 40 m isobaths was 0.45 m and 0.90 m, respectively, and the near-surface blanking distance due to sidelobe contamination was 2.3 m and 3.8 m, respectively. All ADCPs had associated thermistor chains nearby (see McSweeney et al., 2020, for details).

All velocity data were quality-controlled and rotated to an across-shelf/along-shelf coordinate system based on the local along-isobath direction (approximately -6^o at 40 m and -17^o at 25 m). OC25M's vertical beam was set to high-resolution mode, which decreased its range to about 5 m above the bottom, while the Janus beams retained their near-full-depth range. OC40N failed after 10/06/2017 and OC25SB data are usable only for the final ten days of the deployment (10/20-31/2017). The wind stress and RS profiles were rotated to the same across-shelf/along-shelf coordinate system.

Wind stress data are derived from anemometers installed on a land-based meteorological tower in Oceano Beach (APL meteorological station, magenta square in Figure 4.1) and in a meteorological buoy deployed south of Pt. Sal (SIO meteorological station, magenta diamond in Figure 4.1a). Wind velocity was converted to wind stress using the Large and Pond (1982) bulk formula modified for light winds as in Trenberth et al. (1990), and rotated to the same across-shelf/along-shelf coordinate system as the 25 m moorings. Wave data are derived from a Sofar Spotter wave buoy located on the 20 m isobath off of Oceano Beach (magenta cross in Figure 4.1). Sea level data are taken from the adjacent NOAA station (ID: 9412110) located in San Luis Obispo Bay.

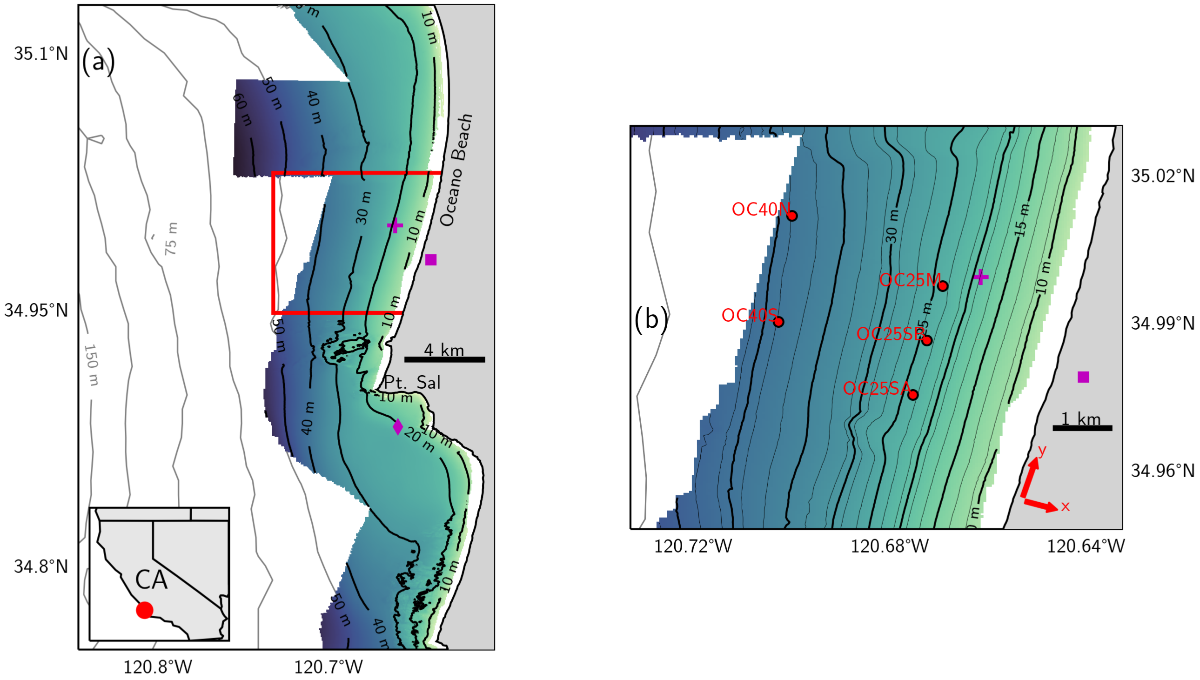

Figure 4.1: Map of the ISDRI experiment site. The dot on the inset in (a) indicates the location of the experiment site on the central California coast, and the red rectangle demarcates the area shown in (b). The red dots in (b) are the locations of the moored ADCPs used in the analysis, a subset of the Oceano Array (see McSweeney et al., 2020). The magenta cross and square are the locations of the Sofar Spotter wave buoy and APL meteorological station, respectively. The magenta diamond indicates the location of the SIO meteorological buoy. The color shading and black contours indicate high-resolution shipboard-measured topography, while gray contours indicate topography from the global 30 arcsecond Smith and Sandwell (1997) updated product. The (cross-shelf/along-shelf) coordinate system is indicated by the red arrows in (b).

4.2.2 Estimation of Reynolds stresses and wave bias removal

We estimate the $\overline{u'w'}$ (hereafter the cross-shelf stress) and $\overline{v'w'}$ (hereafter the along-shelf stress) components of the Reynolds stress tensor using the Variance Technique, which consists of using the velocity variances measured by opposing ADCP beams and assuming horizontal homogeneity of the stress tensor components across the beam separation (*e.g.*, Lohrmann et al., 1990; Stacey et al., 1999; Lu and Lueck, 1999; Whipple et al., 2006). We employ the five-beam expressions for $\overline{u'w'}$ and $\overline{v'w'}$ with full tilt corrections (Dewey and Stringer, 2020, unpublished manuscript):

$$\overline{u'w'} = \frac{-1}{4S^6C^2}\left[S^5C\left(\overline{b_2'^2} - \overline{b_1'^2}\right) + 2S^4C^2\overline{\phi_3\left(b_2'^2 + b_1'^2\right)} - 4S^4C^2\overline{\phi_3 b_5'^2} - 4S^6C^2\overline{\phi_2 u'v'}\right] \tag{4.1}$$

and

$$\overline{v'w'} = \frac{-1}{4S^6C^2}\left[S^5C\left(\overline{b_4'^2} - \overline{b_3'^2}\right) - 2S^4C^2\overline{\phi_3\left(b_4'^2 + b_3'^2\right)} + 4S^4C^4\overline{\phi_3 b_5'^2} + 4S^6C^2\overline{\phi_2 b_5'^2} + 4S^6C^2\overline{\phi_3 u'v'}\right] \tag{4.2}$$

where $b_n'^2$ is the n-th beam's variance, $\theta = 25^\circ$ is the Janus beams' angle with the vertical axis, $S \equiv \sin\theta$, $C \equiv \cos\theta$ and ϕ_2, ϕ_3, u' and v' are respectively the pitch and roll angles, and the instrument-coordinate horizontal velocity anomalies. Overbars indicate ensemble time averages. Biases in Equations 4.1 and 4.2 introduced by instrument noise are corrected (Appendix A). We use RS estimates from all valid ensembles for calculating mean RS profiles and spectral estimates. However, for interpretation of the stress signature of individual events, we mask out RSs that are smaller than the noise threshold, $\mathrm{RS}_{\mathrm{min}}$, based on a conservative single-ping standard deviation of $\sigma_{\mathrm{sp}} = 0.07$ m/s, *i.e.* (Williams and Simpson, 2004),

$$\mathrm{RS}_{\mathrm{min}} = \frac{\sigma_{\mathrm{sp}}^2}{\sqrt{M}\sin 2\theta}, \tag{4.3}$$

where M is the number of pings in the ensemble.

There are several challenges in calculating accurate turbulent RS. Removing the effect of surface wave orbital velocities is the main difficulty in the coastal ocean, and a number of wave bias correction methods exist in the literature. The applicability of these methods depends, among other factors, on the characteristics of the surface wave field. The surface wave climate during the experiment was characterized by long waves (peak periods of up to 20 s, Section 4.3.1 and Figure 4.3b,c). Additionally, the ratio between the root-mean-square velocities and the ensemble-averaged velocity ($u_{rms}/|\boldsymbol{U}|$) had medians of 2.2 or higher for the 25 m moorings (OC25SA, OC25SB and OC25M), indicating that less than 50% of the ensembles are possible candidates for the Cospectra-Fit Method (Kirincich et al., 2010), one of the wave bias removal methods. We therefore apply corrections for the bias introduced by the surface gravity waves' orbital velocities using the Adaptive Filtering Method as described by Rosman et al. (2008). Briefly, the Adaptive Filtering Method uses windowed segments of the velocity record at one of the ADCP's bins to fit a linear function to the velocity record at an overlying bin separated by a specified number of bins. The result is then subtracted from the first bin. By assuming that this vertically-coherent part of the velocity is dominated by the orbital velocities of surface gravity waves, this technique enables turbulent RS estimates with reduced surface gravity wave bias. We also estimate the RS from the low-pass filtered (cut-off period at 100 s) along-beam velocities. This eliminates the high-frequency signal both due to surface waves and stress-carrying turbulent eddies, leaving only lower-frequency, larger-scale stresses which we interpret as being due to internal wave velocities (see van Haren et al., 1994).

Figure 4.2 exemplifies the effect of the Adaptive Filtering Method on the along-beam velocities. A 5 min record from one of OC25M's beams reveals the clearly resolved signal of surface gravity wave orbital velocities, with periods around 10 s (Figure 4.2a). After application of the Adaptive Filtering Method, the orbital velocity signal has been mostly removed, presumably leaving the velocity due to turbulent eddies and instrumental noise (Figure 4.2b). We point out that the method also decreases the spectral levels of lower-frequency motions, such as nonlinear internal wave trains and along-shelf subtidal flows, as a side-effect (Figure 4.2d). The median of the Ozmidov scale (the upper bound of the vertical scale of three-dimensional turbulent eddies) estimated from the nearby thermistor chain and OC25M's vertical beam (in high-resolution, low-noise pulse-coherent mode) from turbulent kinetic energy dissipation rates independently derived from a modified structure function method (Scannell et al., 2017, not shown) is $\approx$4 m, compatible with the vertical scale of the velocity structure in Figure 4.2b. The effect of the filtering on the RS can be seen by comparing time series of filtered and unfiltered $\rho\overline{v'w'}$ (where ρ is the water density, Figure 4.2c). The raw (wave-contaminated) stress is systematically larger than its de-waved counterpart. The associated depth-averaged frequency spectra show a substantial reduction in the variance contained in the surface gravity wave band after filtering (Figure 4.2d). The noise floor is seen to be at $\approx 1 \times 10^{-5}$ (m/s)^2/cpmin, which translates into a single-ping standard deviation of $\approx$4.9 cm/s. By conservatively assuming $\sigma_{\mathrm{sp}} = 7$ cm/s in Equation 4.3, we obtain a minimum detectable RS of 0.07 Pa for OC25M (8 Hz sampling) and 0.20 Pa for the other four moorings (1 Hz sampling) if an ensemble-averaging period of 20 min is used, as in Figures 4.6, 4.7 and 4.8.

4.3 Results

We begin this section by setting the stage for our detailed examination of the observed Reynolds stress (RS) variability using the five mooring records (Figure 4.1). We first describe the general characteristics of the winds, waves and the vertical stratification throughout the experimental period (Subsection 4.3.1). Next, we examine typical flow patterns and the cross-shelf/along-shelf partitioning of horizontal kinetic energy and vertical shear (Subsection 4.3.2). Having identified the primary physical processes associated with these signals and their potential

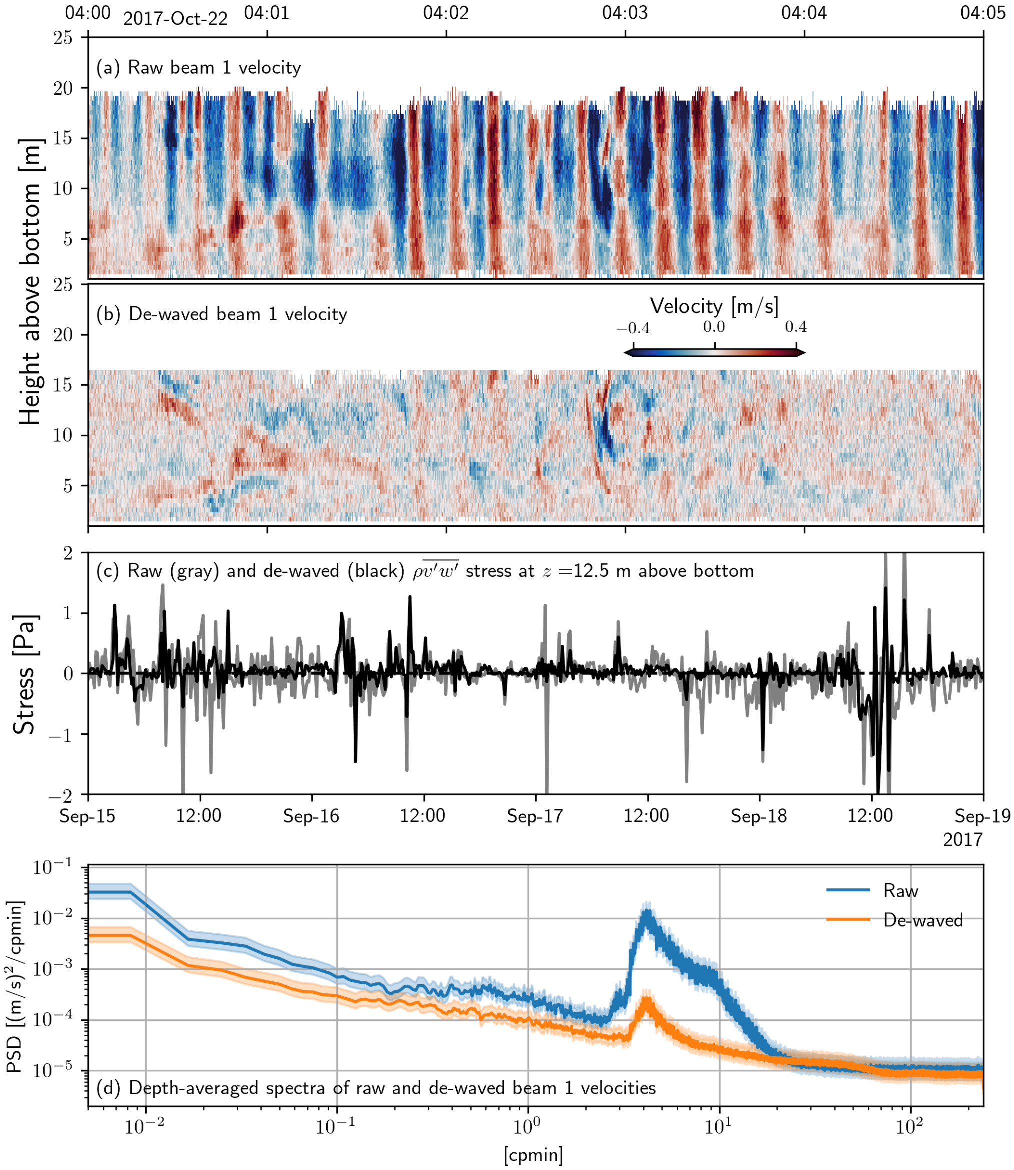

Figure 4.2: Example of the vertical Adaptive Filtering Method for removal of surface gravity wave bias in ADCP along-beam velocities. (a) Raw velocities from OC25M's beam 1 (positive towards instrument) over a 5 minute period starting at 09/12/2017 0 h. (b) As in (a), but after application of the Adaptive Filtering Method with vertical separation of 4 bins (about 2 m) and a 1 s-long window. (c) Mid-depth along-shelf Reynolds stress derived from 10 minute-ensembles of raw and de-waved along-beam velocities over a four-day period starting at 09/15/2017 00:00 h. (d) Depth-averaged frequency spectra (calculated for a 24 h period centered at 10/22 04:00 h) of along-beam velocities prior to and after application of the Adaptive Filtering Method, with shadings indicating the 95% confidence intervals about each spectrum. The color scale is the same for panels (a) and (b).

for generating turbulence, we then describe the temporal variability of the RS across different time scales (from subtidal to supertidal) and associate them with various physical processes (Subsection 4.3.3). We then examine the vertical structure of the time-averaged RSs at each mooring (Subsection 4.3.4) and the uncertainties involved (Subsection 4.3.5). Finally, we perform a dynamical analysis of the data in the cross-shelf and along-shelf momentum budgets (Subsection 4.3.6).

4.3.1 Wind, waves and stratification

The wind, wave and vertical stratification conditions during the experiment are shown in Figure 4.3. The low-frequency (low-pass filtered with cut-off period of 30 h) wind stress was mostly onshore with a typical magnitude of up to 0.05 Pa, with both the cross-shelf and the along-shelf components having similar magnitudes. Significant wave heights (H_s) fluctuated between 1 m and 3 m, and peak periods between 5 s and 25 s. The incoming wave direction remained fairly constant in the northwest quadrant, approximately between 270° and 300°. The time-mean stratification was linear and similar at all moorings (Figure 4.3d). Temperature is used here as a proxy for density because it dominated the density variability throughout the experiment (McSweeney et al., 2020). The time-mean buoyancy frequency, estimated as $N = \sqrt{g\alpha T_z}$, where g, α and T_z are respectively the gravitational acceleration, the thermal expansion coefficient of seawater and the vertical temperature gradient (estimated from a linear fit to the T profiles) was 1.44×10^{-2} s^{-1} at the 25 m isobath (from OC25M, OC25SA and OC25SB) and 1.23×10^{-2} s^{-1} at the 40 m isobath (from OC40S and OC40N). From shipboard data measured in the area of our moorings, the fractional difference between N calculated from temperature only and N calculated from both temperature and salinity was 2%. The stratification was stronger in the beginning of the experiment, and gradually eroded throughout September (Figure 4.3e).

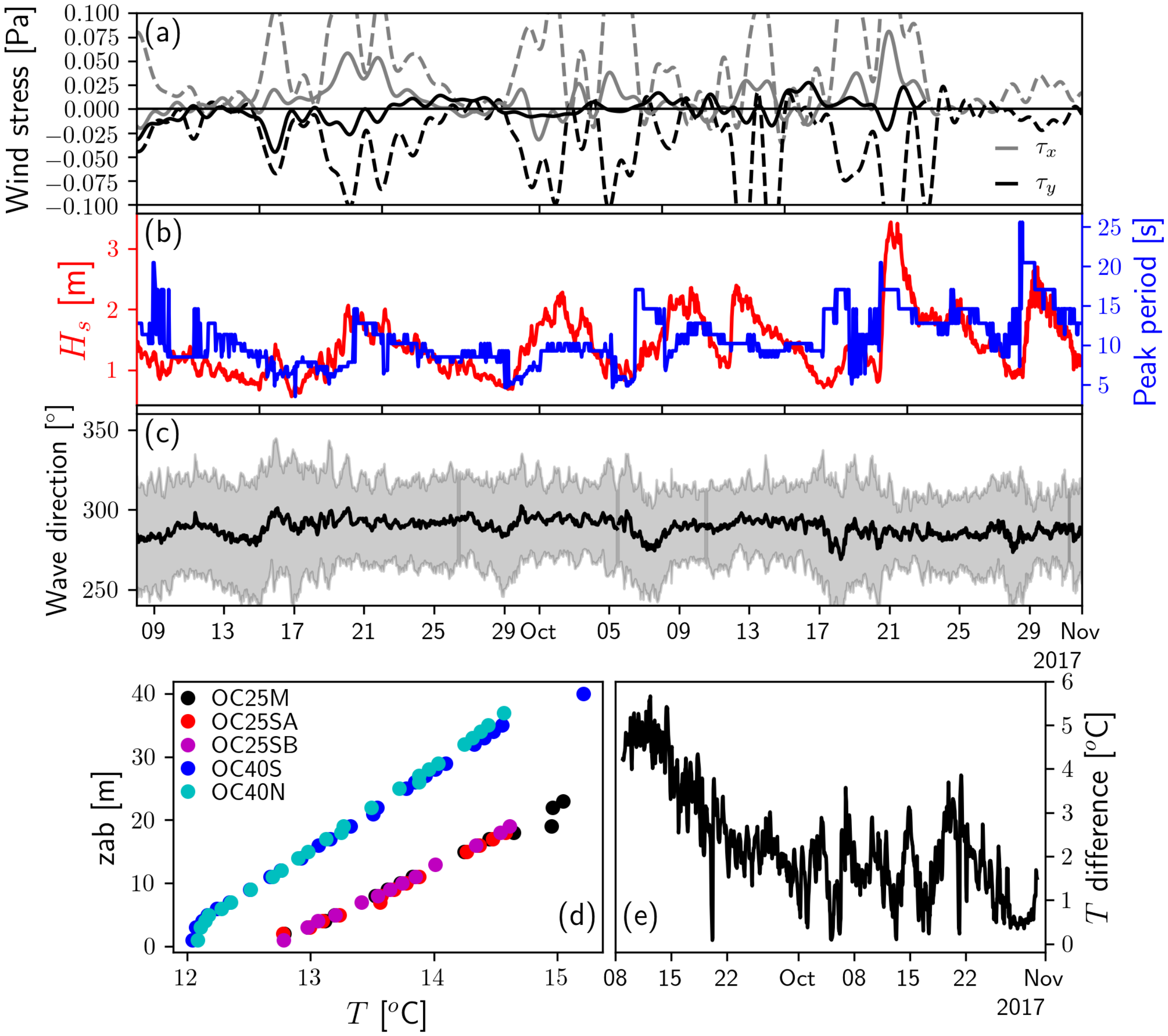

Figure 4.3: Wind, wave and vertical stratification conditions during the experiment. (a) Cross-shelf (τ_x) and along-shelf (τ_y) components of the wind stress vector estimated from the meteorological stations' wind measurements and low-pass filtered (cutoff period of 30 h). Solid and dashed lines in (a) correspond to APL and SIO meteorological stations, respectively. (b) Significant wave height (H_s) and peak period. (c) Mean wave direction (black line) and directional spread (gray shading). The locations of the two meteorological stations and Sofar Spotter wave buoy are indicated in Figure 4.1. (d) Time-averaged temperature profiles at each mooring, with temperature inversions (biased instruments) removed. (e) Time series of bulk stratification (defined as the difference between the top and bottom thermistors) at OC25M, which was representative of the time evolution of the stratification at all moorings.

4.3.2 Flow patterns, kinetic energy and shear variance

In preparation for our discussion of the temporal variability of RSs and the associated physical processes, we first examine an example of typical flow patterns in this region, and the associated temporal variability and spectral content of the horizontal kinetic energy and vertical shear variance (Figure 4.4). The baroclinic velocities exhibit an intermittent two-layer structure in the along-shelf direction and a relatively more complicated vertical structure in the cross-shelf direction, although both components have similar magnitudes ($\approx$15 cm/s, Figure 4.4a,b), except in the events of sustained along-shelf jets. The barotropic (*i.e.*, vertically-averaged) velocities are stronger in the along-shelf direction, and have typical magnitudes of 10-30 cm/s, with episodic jets that last for a few days (Figure 4.4c). These jets are associated with pulses of elevated along-shelf depth-averaged kinetic energy with duration of about a day, while the cross-shelf velocity is associated with comparatively weaker pulses of cross-shelf kinetic energy, such that the total kinetic energy is often dominated by the along-shelf component (Figure 4.4d). Shear variance, on the other hand, has a more complicated partitioning, with both cross-shelf and along-shelf components being comparable in magnitude (Figure 4.4e). Kinetic energy is slightly higher in the cross-shelf direction at high (supertidal) frequencies and in the along-shelf component at low frequencies (Figure 4.4f), consistent with the superposition of supertidal motions such as internal waves projecting preferentially on the cross-shelf velocity and subtidal wind-driven flows projecting on the along-shelf velocity. In contrast, cross-shelf and along-shelf shear variances are indistinguishable within error bounds (Figure 4.4g). The diurnal and semidiurnal tidal peaks, as well as their higher-order harmonics, are visible in both the kinetic energy and in the shear. These results show that physical processes at all frequency bands (supertidal, tidal and subtidal) are energetic and produce shear that may lead to turbulence and therefore contribute to the RS variability.

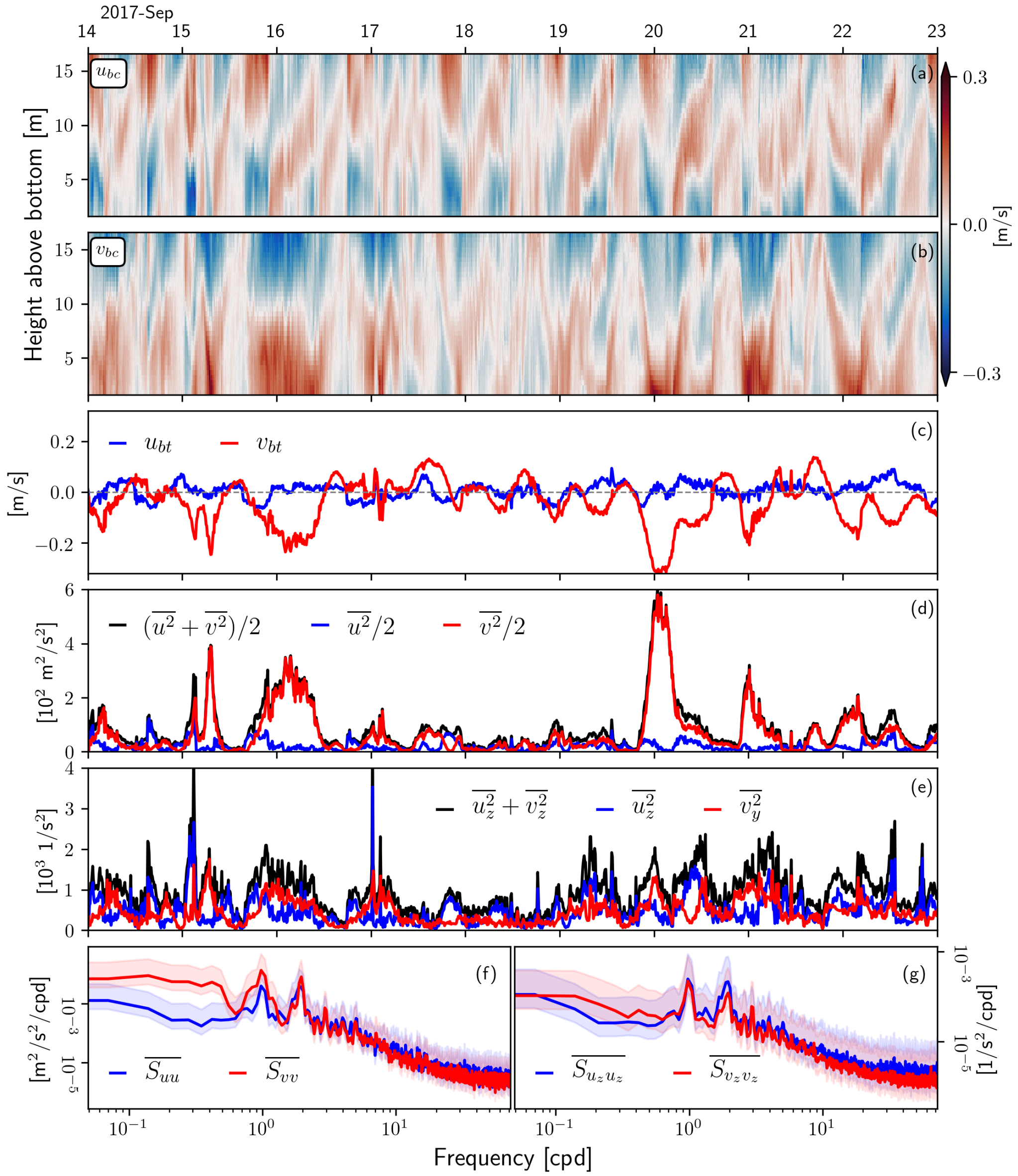

Figure 4.4: Example of baroclinic and barotropic velocities, horizontal kinetic energy and shear variance during a subset of OC25SA's deployment. (a,b) Baroclinic (total minus vertical average) cross-shelf (u_{bc}, a) and along-shelf (v_{bc}, b) velocities. (c) Time series of barotropic (vertically-averaged) cross-shelf (u_{bt}) and along-shelf (v_{bt}) velocities. (d) Time series of depth-averaged cross-shelf, along-shelf and total kinetic energies. (e) Time series of depth-averaged cross-shelf, along-shelf and total shear variance. (f) Depth-averaged frequency spectra of cross-shelf and along-shelf kinetic energies. (g) Depth-averaged frequency spectra of cross-shelf and along-shelf shear variances. The shaded areas in panels (f,g) indicate the 95% confidence intervals about each spectrum.

4.3.3 Temporal variability of Reynolds stresses

In this subsection, we describe the temporal variability of the observed RSs at different frequency bands, discussing its link with several physical processes. We begin with a qualitative overview and a description of the spectral content of the RSs at all moorings and then focus on different physical processes, namely internal bores, wind-driven along-shelf currents, nonlinear internal wave trains and subtidal currents.

Spectral content and qualitative overview

The depth-averaged frequency spectra of the cross-shelf $\overline{u'w'}$ and along-shelf $\overline{v'w'}$ stresses reveal peaks at the diurnal and semidiurnal tidal frequencies, as well as higher harmonics (Figure 4.5). All moorings exhibit similar variance levels for the RSs in both directions, especially at supertidal frequencies, and their discrepancies at tidal and subtidal frequencies are largely indistinguishable to within error bounds.

General features present in all mooring records can be identified in Figure 4.6, a representative example from OC40S's second deployment (October/2017). Wind reversals occur multiple times throughout the record, and the spring-neap cycle is clearly seen in the barotropic tide. Stratification weakens toward the fall, in agreement with Figure 4.3e. The tidal signal is most visible in u and T, which also track the sharp-edged internal bores described by McSweeney et al. (2020), especially in T. The vertical shear in u has a consistent two-layer structure, which appears to erode with the stratification. One striking feature of all events is the rich vertical structure in the shear that tracks the tidal signal (Figure 4.6b,e,h). The along-shelf shear is partly associated with the internal tide and with longer-lasting, possibly wind-driven and geostrophically-balanced, along-shelf flows, specifically the northward and southward jets around 10/17 and 10/22, respectively (Figure 4.6h). Background RSs are O(0.01 Pa), often indistinguishable from instrumental noise (Equation 4.3) and similar to the wind stress (Figures 4.3a and 4.6a,f,i). Semi-regular pulses of O(0.1-1 Pa) in the RS are conspicuous (vertical stripes on Figure 4.6f,i).

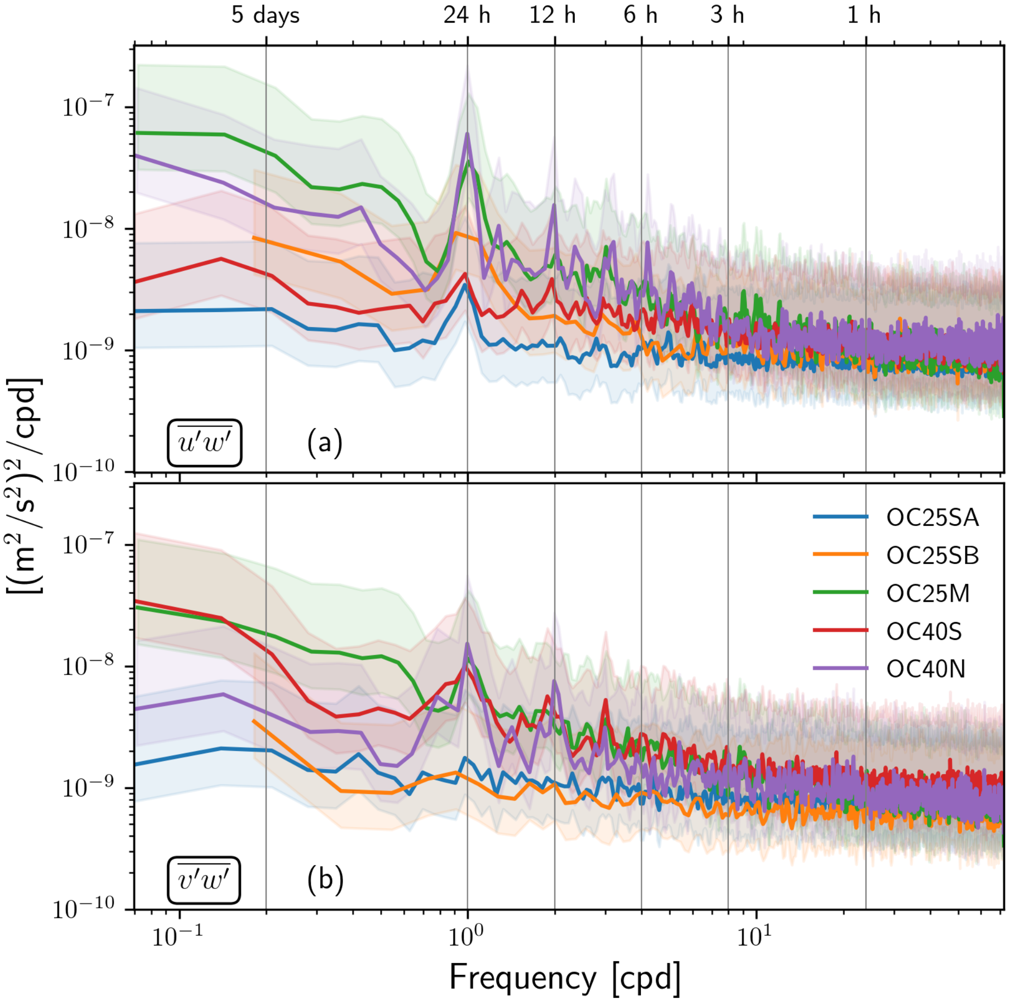

Figure 4.5: Depth-averaged frequency spectra of across-shelf ($\overline{u'w'}$, a) and along-shelf ($\overline{v'w'}$, b) stresses at each mooring. Each curve is the depth average of the spectra of $\overline{u'w'}$ or $\overline{v'w'}$ at each depth. The shaded areas indicate the 95% confidence intervals about each spectrum.

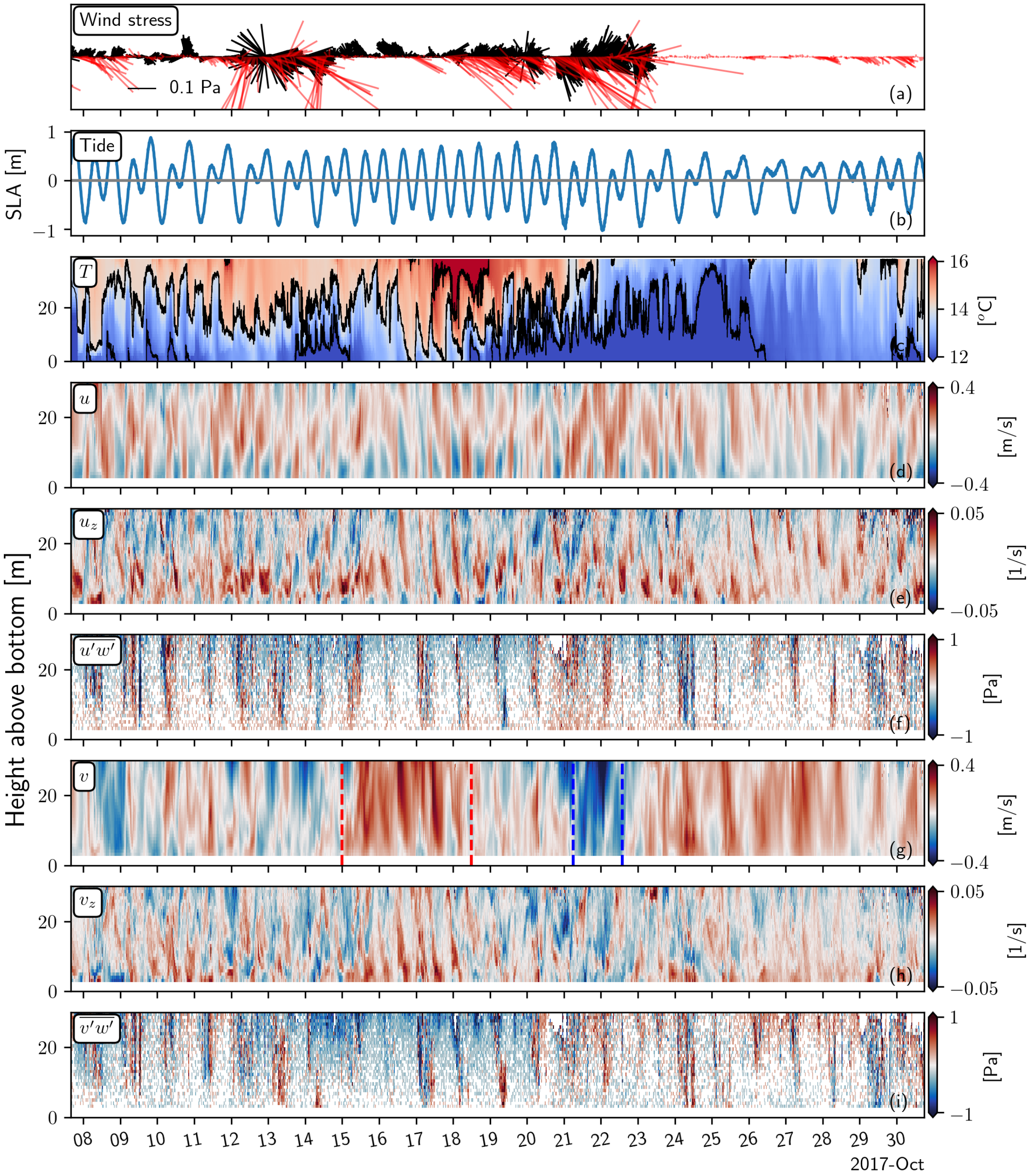

Figure 4.6: Example of the flow and vertical Reynolds stresses during a subset of OC40S's deployment. (a) Wind stress vector (the y-axis is aligned with the along-shelf direction) from the APL (black) and SIO (red) meteorological stations; (b) Sea level anomaly; (c) Temperature T; (d) Cross-shelf velocity u; (e) Cross-shelf shear u_z; (f) Cross-shelf stress $\overline{u'w'}$; (g) Along-shelf velocity v; (h) Along-shelf shear v_z and (i) Along-shelf stress $\overline{v'w'}$. The vertical dashed lines on panel (g) indicate the time spans of Figure 4.7 (red lines) and Figure 4.8 (blue lines). Panels d-i are 20 min averages. Reynolds stress values smaller than the noise threshold (Equation 4.3) are masked out on panels f,i.

Internal bores and along-shelf jets

Examples of the semi-regular elevated RS events are seen in October 15, 16, 17 and 18 around 06:00 AM (Figure 4.7f,i). These events are likely associated with the arrival of internal bores (Figure 4.7c), which share similarities with the bores observed in Monterey Bay by Walter et al. (2012). In this type of bore, there is an initial "surging" period where the near-bottom temperature drops over several hours, followed by the arrival of an abrupt warm front, which partially restores the stratification to its prior state before the next bore arrives and the cycle repeats. Interestingly, however, the other bores (*i.e.*, those occuring between the stress-laden bores) hardly display any measurable stress signature. At OC40S, McSweeney et al. (2020) identify a total of 149 bores during the experimental period (an average of 2.91 bores per day), which arrive on average every 7.93 h, with a standard deviation of 3.60 h (their Table 1). McSweeney et al. (2020) also observe that the bore type alternates between sharp-edged bores (which cause more mixing) and more rarefied bores that trail the sharp-edged ones, affected by the change in the stratification waveguide caused by the prior sharp-edged bore. Figure 4.7c,f,i suggests that, out of all the bores observed in this time period, only one per day (approximately from 00:00 h to 12:00 h daily, vertical dashed lines on Figure 4.7f,i) contains a substantial stress signature, both in $\overline{u'w'}$ and in $\overline{v'w'}$. This bore-to-bore cyclic variability may be able to explain the semi-regular, approximately diurnal elevated stress events seen in Figures 4.6f,i and 4.7f,i.

Do the prolonged along-shelf flows seen in Figure 4.6 have important RS signatures? The internal bore events described in the previous paragraph are superimposed on a period of persistent northward flow associated with a downwelling-favorable wind event centered around 10/17 (Figure 4.7a,g). Onshore velocity and its vertical shear display a semidiurnal pattern, with vertically-propagating signals in the shear (Figure 4.7d,e). The RS structure seems to lack a persistent surface-to-bottom negative signal associated with the northward jet (*i.e.*, evidence of down-gradient momentum flux), with the elevated stress signature of the stress-laden daily bore events described above being the dominant feature in the RS (Figure 4.7f,i). In contrast, a sustained southward jet associated with a mild upwelling event (Figure 4.8a,c) does exhibit a period of intense down-gradient momentum flux in both the cross-shelf and along-shelf directions (opposite signs in the shear and the associated stress, Figure 4.8e,f,h,i, around 10/22 03:00 h). In both cases, turbulence linked to processes that project their shear mostly in one direction (*i.e.*, bores in the cross-shelf direction and along-shelf sheared flows in the along-shelf direction) tends to produce elevated patches of both $\rho\overline{u'w'}$ and $\rho\overline{v'w'}$, vertically mixing both cross-shelf momentum and along-shelf momentum.

A question that naturally arises from this analysis is whether these elevated RS events linked to different physical phenomena have a net effect on driving the circulation, *i.e.*, do they contribute to the local force balance in a time-mean sense? Figure 4.9 shows the mean $\rho\overline{u'w'}$ and $\rho\overline{v'w'}$ RS profiles averaged during different time periods. The solid curves are the average profiles during the entire northward (red) and southward (blue) flow periods depicted in Figures 4.7 and 4.8, respectively. Their minimum significant RS (Equation 4.3) are 0.012 Pa and 0.019 Pa, respectively. The associated dashed curves are weighted averages over the subset of those time periods when there is elevated RS due to bores (for the northward flow case, red dashed curves) and elevated RS due to along-shelf sheared flow (for the southward flow case, blue dashed curves). The northward along-shelf current case is clearly dominated by the internal bore events, both in $\rho\overline{u'w'}$ and $\rho\overline{v'w'}$. Quantitatively, the conditionally-averaged profiles for the bore arrivals contain 94% and 91% of the total variance in the $\rho\overline{u'w'}$ and $\rho\overline{v'w'}$ profiles, respectively. This is evidence that the bulk of the stress during this northward along-shelf flow period is found during these semi-regular daily bore arrival events, but curiously, not during all bore events. It also appears that the "sharpness" of the bores is not clearly related to the presence or absence of stress (for example, the very sharp bore-like feature seen at around 10/16 06:00 h has a weaker RS signature than the other three less-sharp bores, Figure 4.7c,f,i). The southward along-shelf current case, on the other hand, is not dominated by internal bore arrivals. The main RS signal in this period is right after the peak of southward velocity (Figure 4.8f,g,i). The average $\rho\overline{u'w'}$ and $\rho\overline{v'w'}$

profiles for this period depart significantly from the profiles averaged only within the elevated stress period. In particular, the positive $\rho\overline{v'w'}$ maximum at $\approx$15 m above the bottom (Figure 4.9b, blue dashed line), is the mean signature of the red patch in $\rho\overline{u'w'}$ and $\rho\overline{v'w'}$ at around 10/22 03:00 h (Figure 4.8f,i), and the conditionally-averaged profiles for the elevated southward shear period contain only 66% and 52% of the total variance in the $\rho\overline{u'w'}$ and $\rho\overline{v'w'}$ profiles, respectively.

Nonlinear internal wave trains

While internal bores are one of a host of internal tide-related processes, another typically observed form of internal tidal signal in the mooring records are Nonlinear Internal Wave (NLIW) packets such as depicted in Figure 4.10. The along-beam velocities have been corrected for the phase differences of the NLIWs across the ADCP beam separation following a simplified form of the Scotti et al. (2005) method. The signature of a NLIW train is seen in the cross-shelf velocity u_e, the instantaneous low-pass filtered (cut-off period of 100 s) cross-shelf stress (*i.e.*, the unaveraged $\rho u'w'$ quantity derived from along-beam velocities) and the instantaneous vertical transport of cross-shelf momentum *i.e.*, the unaveraged $\rho u_e w_e$ product derived from Earth-coordinate velocities, where w_e is the vertical velocity (similar to van Haren et al., 1994). The arrival of the NLIW packet produces a similar banded signal with alternating negative and positive values in both the turbulent stress $\rho u'w'$ and the advective transport $\rho u_e w_e$, but the amplitude of the latter is a factor of $\approx$2 larger than the former. Importantly, both $\rho u_e w_e$ and the covariances independently derived from the low-pass filtered (cut-off period of 100 s) along-beam velocities are in good agreement. This suggests that there is also a substantial covariance of cross-shelf and vertical velocities at scales larger than the turbulent eddies and the ADCP's beam separation. We interpret these stresses as due to the orbital velocities of the NLIWs, whose covariance produces a net vertical transport of cross-shelf momentum in a manner analogous to the radiation stresses associated with surface gravity waves (Longuet-Higgins and Stewart, 1964). This momentum transport might be part of the manifestation of the radiation stress due to internal wave shoaling

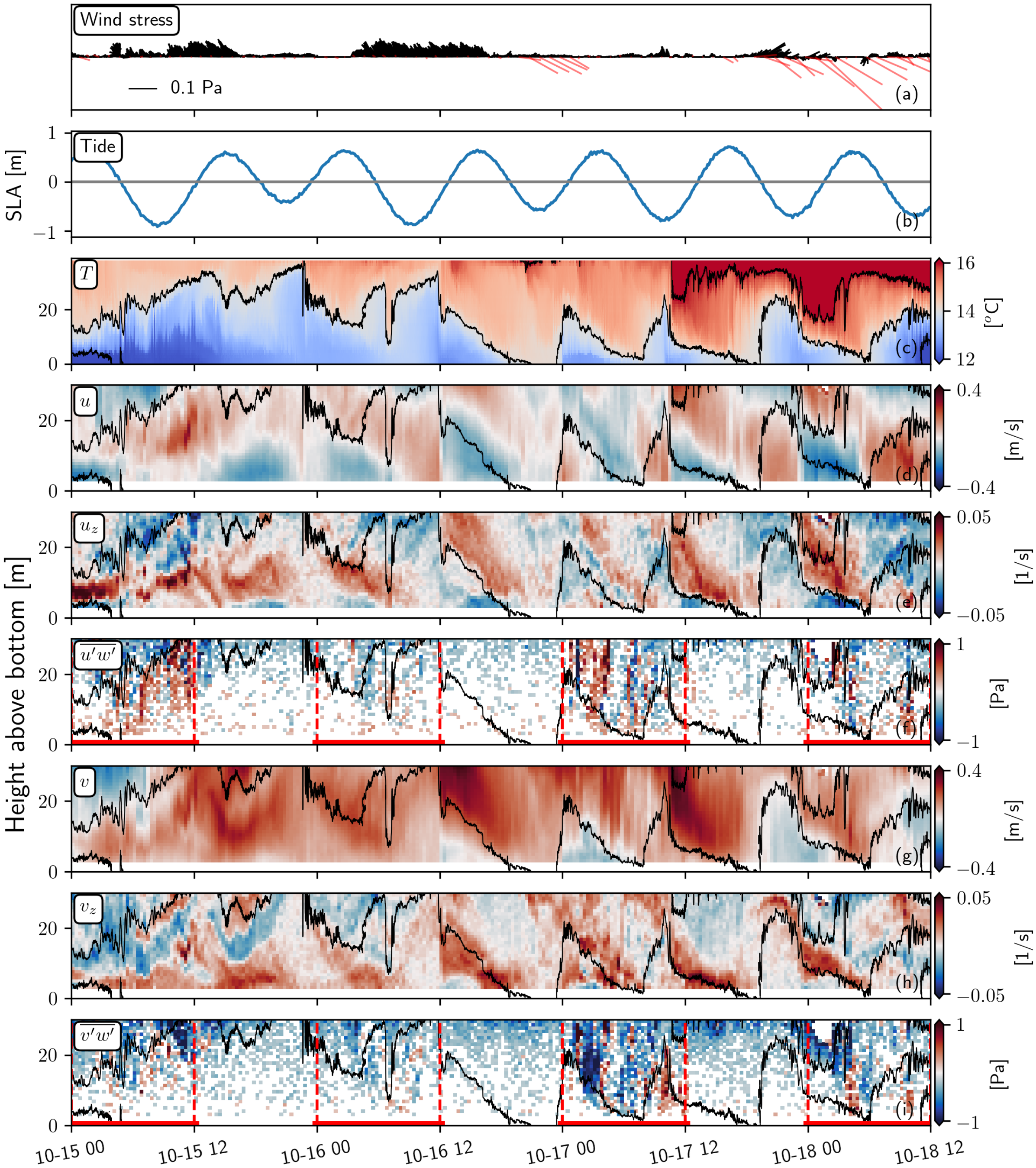

Figure 4.7: As in Figure 4.6, but zooming in on an event of persistent northward flow associated with downwelling-favorable winds. Panels d-i are 20 min averages. Reynolds stress values smaller than the noise threshold (Equation 4.3) are masked out on panels f,i. The horizontal bars and vertical dashed lines on panels f,i delimit the enhanced bore turbulence periods used for the averages in Figure 4.9 (red dashed curves).

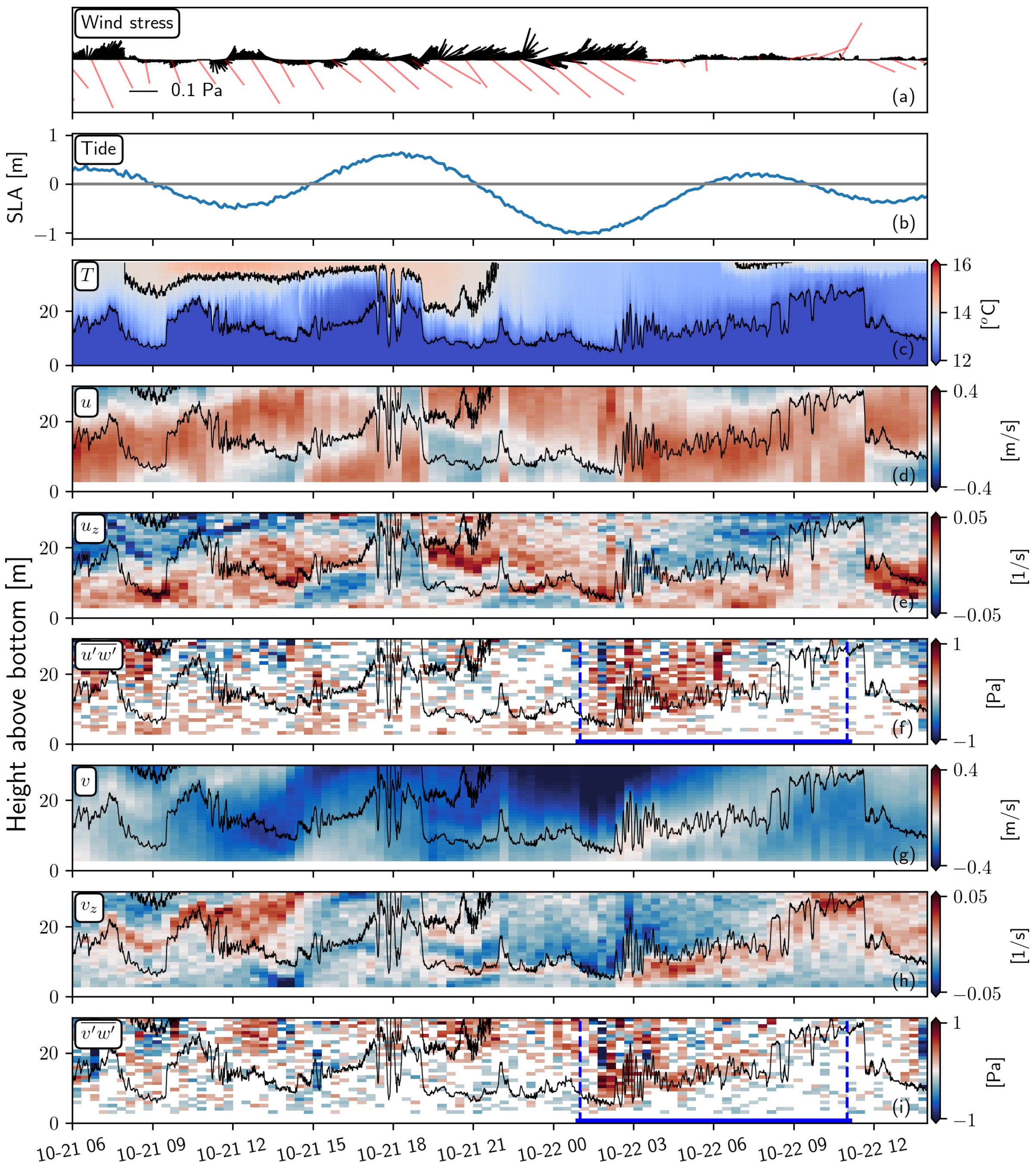

Figure 4.8: As in Figure 4.6, but zooming in on an event of persistent southward flow associated with mildly upwelling-favorable winds. Panels d-i are 20 min averages. Reynolds stress values smaller than the noise threshold (Equation 4.3) are masked out on panels f,i. The horizontal bars and vertical dashed lines on panels f,i delimit the enhanced shear-driven turbulence period used for the averages in Figure 4.9 (blue dashed curves).

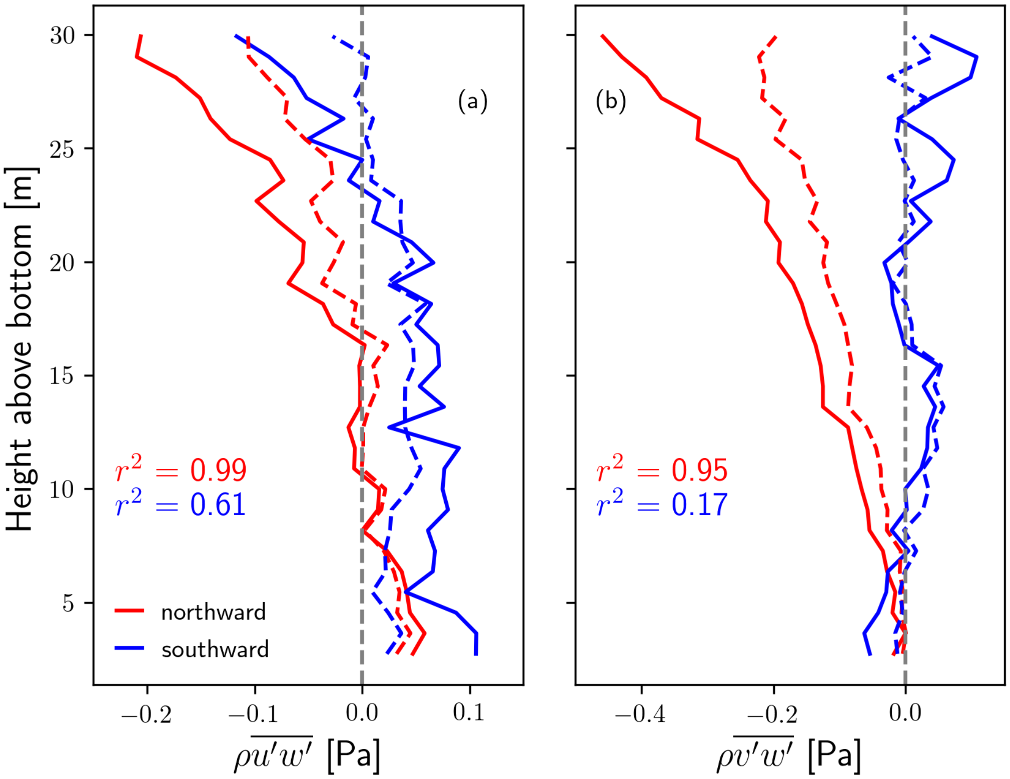

Figure 4.9: Time-averaged cross-shelf ($\rho\overline{u'w'}$, a) and along-shelf ($\rho\overline{v'w'}$, b) stress profiles for the northward jet event (red solid lines, Figure 4.7) and for the southward jet event (blue solid lines, Figure 4.8). The minimum significant RS (Equation 4.3) is 0.012 Pa for the northward jet event average and 0.019 Pa for the southward jet event average. The red dashed lines are time averages over the sub-periods of significant internal bore activity (in the case of the northward jet event). The blue dashed lines are time averages over the sub-period of significant along-shelf shear activity (in the case of the southward jet event). The dashed profiles have been weighted by the ratio of the time interval over which they were averaged to the time interval of the solid lines. The squared correlation coefficients between the solid and dashed profiles are indicated.

and breaking (Hogg, 1971; Thorpe, 1999; Zikanov and Slinn, 2001), in an analogous way to the processes undergone by surface gravity waves as they propagate onshore.

Figure 4.10e shows that the time integral of the depth-averaged vertical convergence of $\rho u_e w_e$ does not cancel out after the passage of the NLIW train, showing a net accumulation of onshore momentum in the water column (the net onshore force is sufficient to accelerate the depth-averaged flow 20 cm/s in less than an hour, solid green line in Figure 4.10e). This momentum deposition is likely balanced by other forces, as an acceleration of such magnitude is not observed (Figure 4.10a). This suggests that incoming NLIW trains in the inner shelf might be an important source of momentum in the depth-averaged equations of motion. This is a significant result, since NLIWs have not typically been considered important players in inner shelf dynamics. In contrast to the putative internal radiation stresses ($\rho u_e w_e$), the vertical divergence of the turbulent RS ($\rho u' w'$) is associated with a much smaller net momentum deposition (dashed lines in Figure 4.10e).

Examination of the time-averaged vertical profiles of $\rho u_e w_e$ and $\rho u' w'$ shows that deposition of cross-shelf momentum by this NLIW train takes place mainly via vertical divergence of the non-turbulent momentum transport (the potential internal radiation stress discussed in the previous paragraph), and not via vertical divergence of the turbulent RS (Figure 4.11), consistent with Figure 4.10e. The time-mean vertical structure of $\rho u' w'$ shows barely significant values of RS in the lower 10 m of the water column and a positive slope in the upper water column, indicating vertical divergence of onshore momentum (or convergence of offshore momentum) and an offshore-directed force. Conversely, the time-mean $\rho u_e w_e$ vertical profile shows a two-layer structure, with an offshore force at depth and an onshore force in the upper water column, with the net depth-averaged force being onshore. The fact that the net cross-shelf acceleration due to this NLIW event is onshore means that the combined effect of NLIW trains and tidal bores (also associated with net onshore acceleration, negative-sloping red lines in Figure 4.9a) may lead to a substantial time-averaged deposition of onshore momentum at tidal frequencies. This might have important implications for the cross-shelf momentum balance in this region (as we will discuss in Subsection 4.3.6), and perhaps also in other shelves with energetic internal tides.

Finally, we note that NLIWs have been observed to cause substantial cross-shelf mass transports (*e.g.*, Shroyer et al., 2010), and that may be related to the advective (*i.e.*, non-turbulent) transport of horizontal momentum. Due to the bottom slope, an onshore depth-averaged mass transport is associated with an upward velocity, and, consequently, with a positive $u_e w_e$ product. The vertical structure of this product would then lead to a nonzero vertical divergence of u_e transport, and therefore to a net deposition or removal of onshore momentum in the water column. Other motions, such as internal bores and the time-mean cross-shelf circulation, may similarly be associated with momentum deposition via nonzero vertical gradients of $u_e w_e$.

Subtidal flow

At this point, both tidal and supertidal processes have been shown to contribute to RS variability. Similarly, how do subtidal flows influence the RS variability on the inner shelf? The cross-shelf and along-shelf velocities and stresses measured at the 25 m isobath (OC25SA, Figure 4.12) show significant subtidal variability, consistent with the spectra in Figures 4.4f and 4.5. The subtidal cross-shelf velocity exhibits significant fluctuations with a mode-1 shape. The cross-shelf stress is consistently positive near the bottom and negative near the surface, and is systematically larger than the along-shelf stress.

A striking feature of Figure 4.12 is the persistence of the cross-shelf stress ($\rho\overline{u'w'}$) structure. Considering our previous finding that the $\rho\overline{u'w'}$ profile at tidal/supertidal timescales is mainly shaped by incoming internal bores (Figures 4.7f,i and 4.9a), this may be interpreted as a rectified subtidal signal linked to the semi-regular bore arrivals. We will return to this point in Subsection 4.3.6 and show that a baroclinic cross-shelf pressure gradient may be able to balance the momentum input from this subtidal vertical divergence of $\rho\overline{u'w'}$. In the along-shelf direction, evidence for sustained periods of down-gradient momentum flux can be seen in the stress during

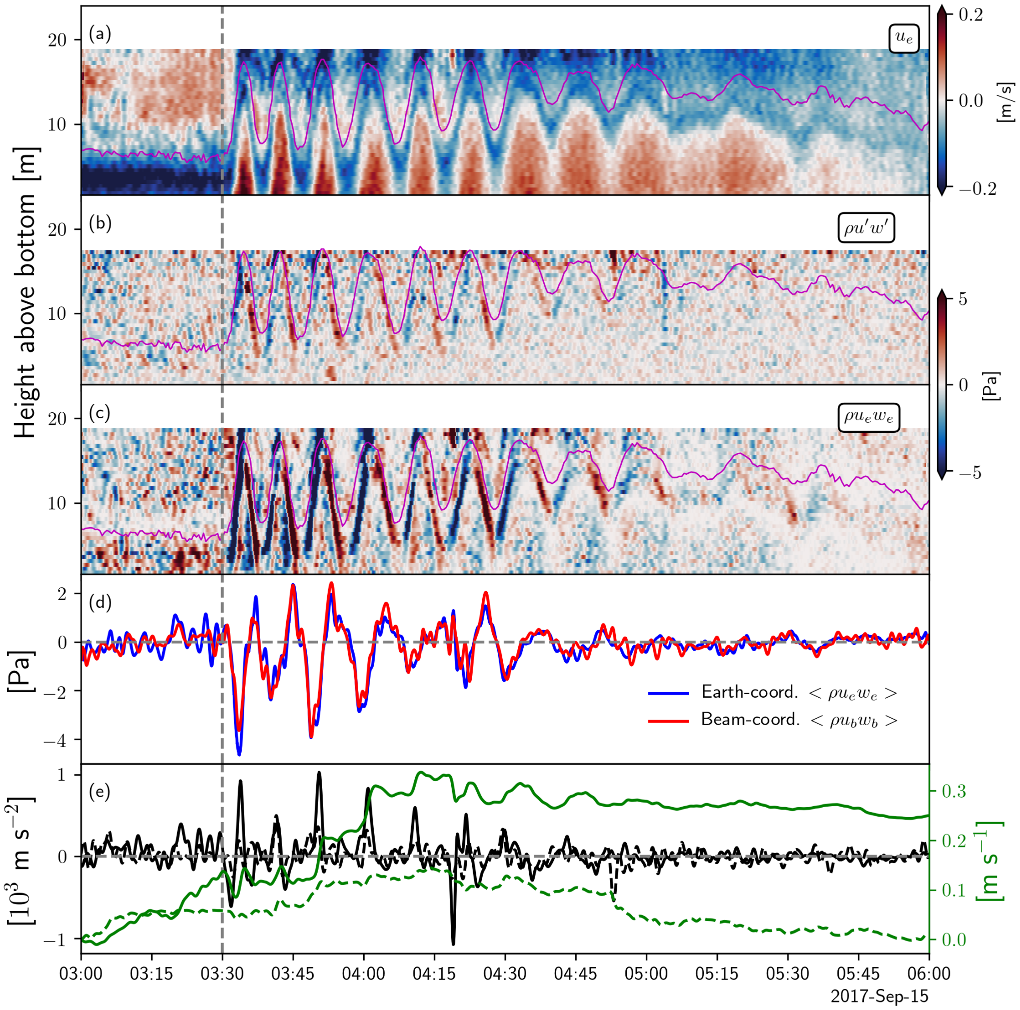

Figure 4.10: Example of the stress signature of an incoming Nonlinear Internal Wave (NLIW) train, from a subset of OC25SA's deployment. (a) Cross-shelf velocity, u_e. (b) Low-passed (cut-off period of 100 s) instantaneous (unaveraged) cross-shelf stress $\rho u'w'$. (c) Instantaneous vertical transport of cross-shelf momentum $\rho u_e w_e$, derived from Earth-referenced velocities. (d) Instantaneous depth-averaged $\rho u_e w_e$ and its beam-coordinate equivalent $\rho u_b w_b$, derived from low-passed (cut-off period of 100 s) along-beam velocities. (e) Time series of depth-averaged vertical convergence of $\rho u_e w_e$ and its time integral (solid lines) and time series of depth-averaged vertical convergence of the turbulent stress, $\rho u'w'$ (dashed lines), showing a net accumulation of onshore cross-shelf momentum in the water column after the passage of the NLIW train. The magenta contours overlain in (a,b,c) are the 16°C isotherm derived from the adjacent thermistor chain, offset by 2.5 min to account for the distance (≈ 100 m) between the ADCP and the thermistor chain. The vertical dashed lines indicate the time of arrival of the NLIW train.

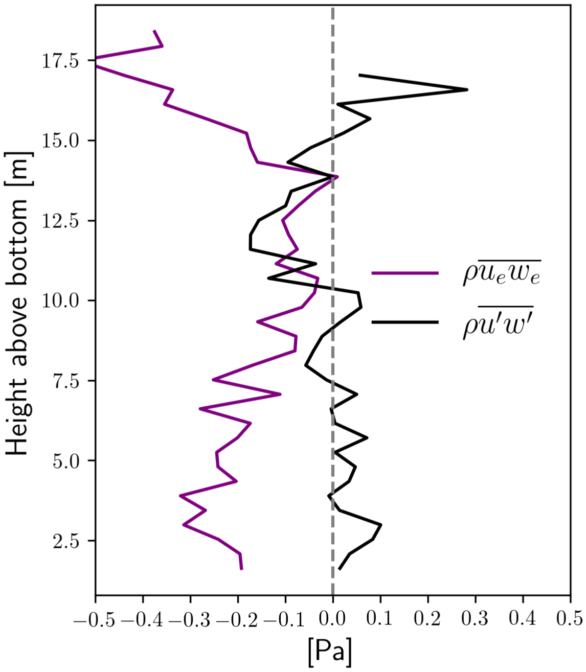

Figure 4.11: Time-averaged profiles of vertical transport of cross-shelf momentum $u_e w_e$ and cross-shelf turbulent Reynolds stress $u'w'$ during the passage of the nonlinear internal wave train depicted in Figure 4.10 (September/15 03:30-06:00 h). The minimum detectable Reynolds stress (Equation 4.3) for this averaging period is 0.07 Pa.

the northward and southward along-shelf jets around October/17-25 (see discussion on the second paragraph of Subsection 4.3.3).

Correlations between the subtidal near-surface (averaged over the top few meters) stresses and the subtidal wind stress components are weakly significant. No mooring presented significant correlations beyond the 72% confidence level. This suggests a physical situation similar to that found by Kirincich and Gawarkiewicz (2016), where a local along-shelf pressure gradient unrelated to the wind stress is found to be an important and perhaps dominant driver of the observed RSs. The near-surface gap jointly caused by the sidelobe contamination cap and the Adaptive Filtering Method's constraints can partly explain this discrepancy, since the bulk of the stress that can be expected to correlate with the wind stress might have been missed. However, we will also show in Subsection 4.3.6 that pressure gradient forces are indeed important in both the cross-shelf and along-shelf directions.

4.3.4 Spatial structure of time-averaged Reynolds stresses

Having described the temporal variability of the RSs across different frequency bands and the associated physical processes, we are now in a better position to discuss the time-averaged vertical structure of the RSs and whether any insight on the spatial variability of the RS can be gained from them. We focus on the total conditionally-averaged profiles of u, v, $\rho\overline{u'w'}$ and $\rho\overline{v'w'}$ (qualitatively similar to the subtidally-filtered velocities and stresses, not shown) for all five moorings (OC25SA, OC25SB, OC25M, OC40S and OC40N, Figure 4.1) during periods of northward along-shelf flow ($v \geq 1$ cm/s) and southward along-shelf flow ($v \leq -1$ cm/s). The conditional averages are performed to better isolate the effects of high shears, instead of averaging the entire record of mutually-cancelling signals. The mean northward and southward v profiles have positive and negative vertical shears, respectively, while the u profiles have a two- and sometimes three-layer structure (Figure 4.13a-e,k-o). The cross-shelf velocity is consistently offshore in the bottom 5-10 m, and has an onshore maximum at mid-depth (both for northward and

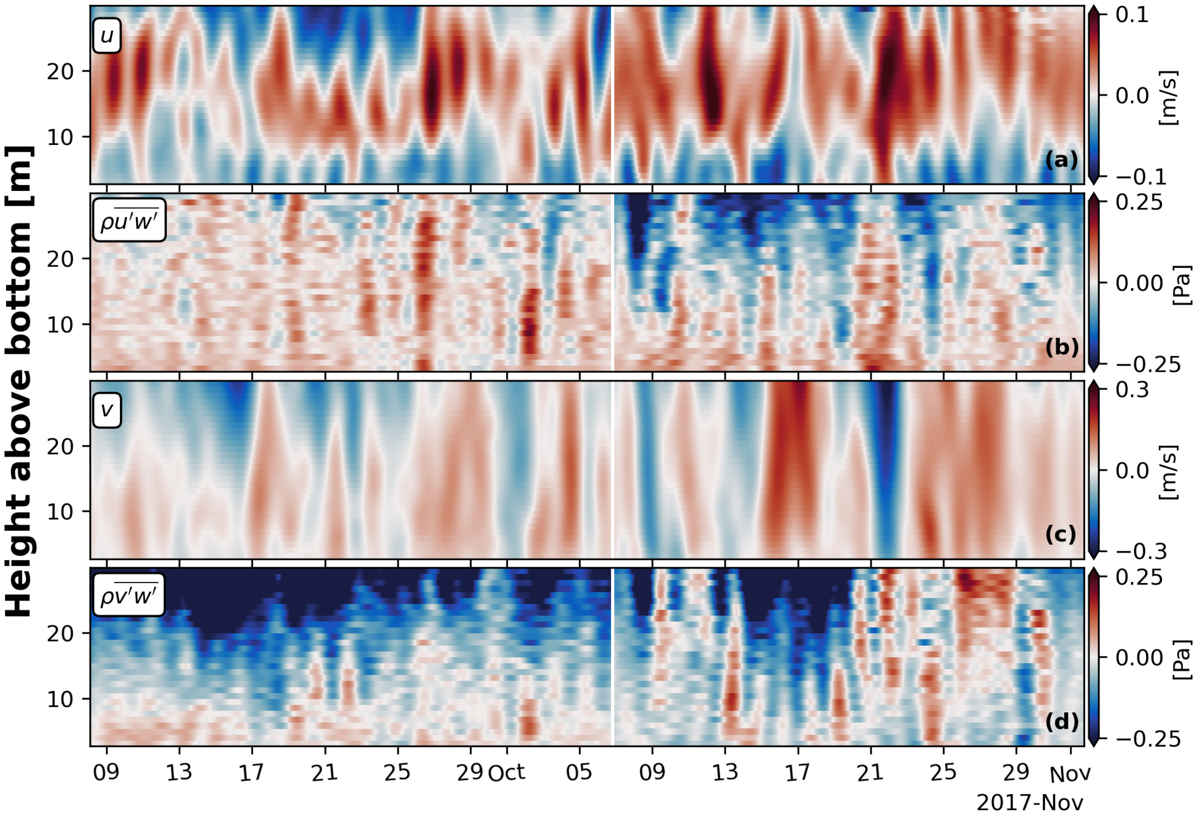

Figure 4.12: Subtidal low-pass filtered (cut-off period of 30 h) cross-shelf velocity (*u*, a), cross-shelf stress ($\rho\overline{u'w'}$, b), along-shelf velocity (*v*, c) and along-shelf stress ($\rho\overline{v'w'}$, d) for OC40S. Note the different color scales on panels (a) and (c).

southward currents), with a third offshore-flowing near-surface layer for the southward-flowing mean at the 40 m moorings (Figure 4.13n,o). This cross-shelf velocity profile resembles that observed in the late upwelling relaxation season off the Washington coast as a result of the combination of wind-driven cross-shelf transport, coastally-trapped waves and the large-scale along-shelf pressure gradient (McCabe et al., 2015).

The RS vertical structure is relatively consistent across moorings (especially in the cross-shelf direction), and is remarkably persistent in time at any given mooring, both for periods of northward and southward currents (Figure 4.13f-j,p-t). This suggests that the bulk of the RS is not associated with the time-mean along-shelf flow, and that only some events of elevated vertical shear (such as the one in Figure 4.8 and Figure 4.9 [blue lines]) cause an expected RS signature. The cross-shelf RS has a negative slope, tends to be more positive near the bottom and more negative near the surface (in agreement with Figure 4.12b). The along-shelf RS is more variable across moorings, often being single-signed throughout the water column (with the exception of OC40N, Figure 4.13j,t). This vertically-sloping structure of the RSs clearly indicates a departure from a classical inner-shelf frictional regime (*e.g.*, Lentz and Fewings, 2012) at the 25 m isobath and also (unsurprisingly) at the 40 m isobath. Interestingly, there is no consistent evidence for down-gradient momentum flux in the along-shelf direction across all moorings, but rather only at OC25SA, OC25SB, OC40S and OC40N for northward flow (Figure 4.13a,f,b,g,d,i,e,j) and OC25M for southward flow (Figure 4.13m,r).

4.3.5 Reynolds stress uncertainty

Before proceeding with the dynamical analysis of the RSs, we note the main implications of the RS uncertainties for the results in the previous subsections. Firstly, the minimum significant RS for the subtidal (Figure 4.12) and time-averaged (Figure 4.13) RSs is much smaller than the 0.2 Pa for 20 min averages. For example, for a 30 day average (like most of the profiles in Figure 4.13), Equation 4.3 gives a minimum detectable RS of 0.004 Pa. For the 30 h low-pass filtered

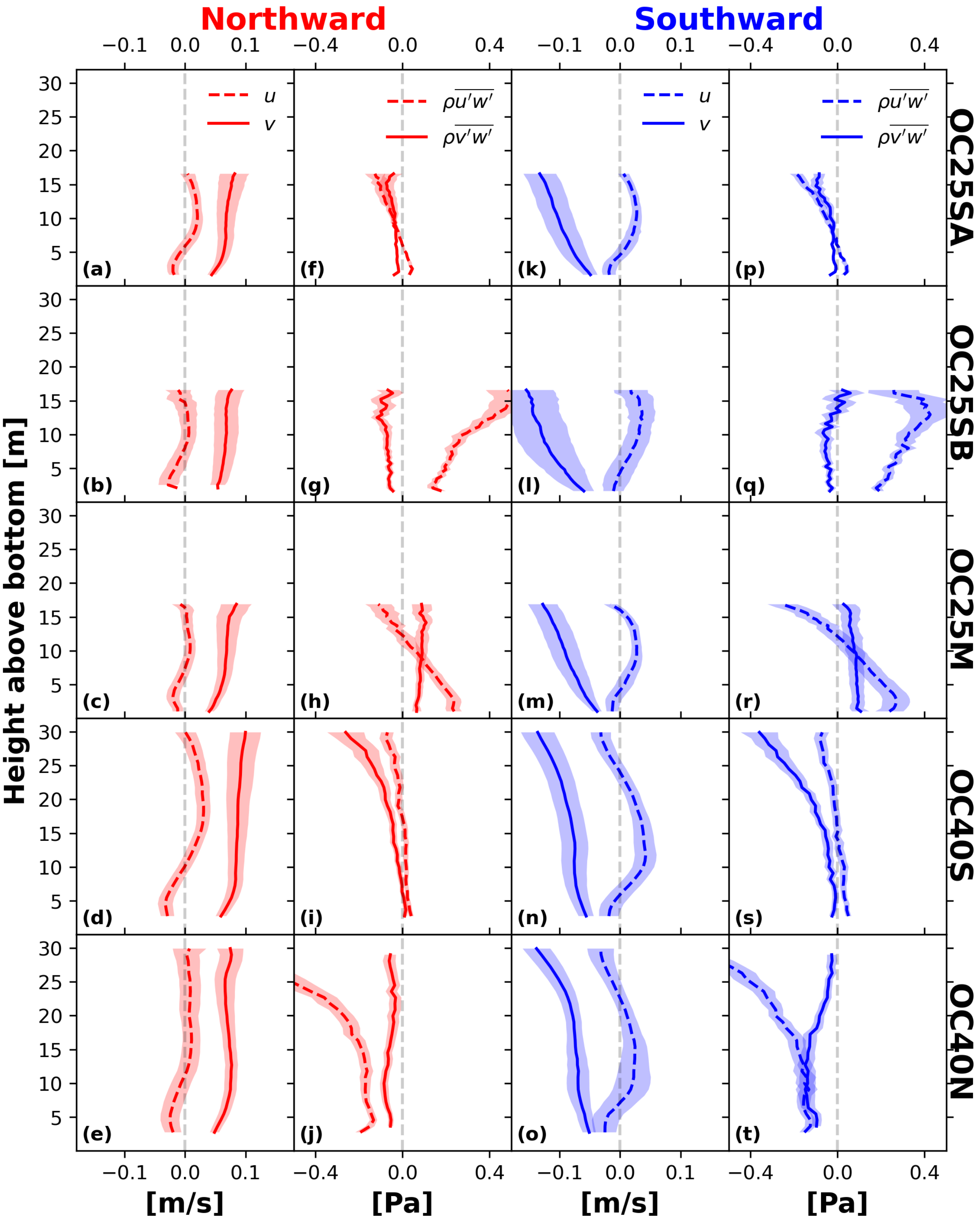

Figure 4.13: Cross-shelf and along-shelf velocities *u* and *v* (a-e, k-o) and associated stresses $\rho\overline{u'w'}$ and $\rho\overline{v'w'}$ (f-j, p-t) conditionally-averaged over periods of northward flow ($v \geq 1$ cm/s, red, a-j) and southward flow ($v \leq -1$ cm/s, blue, k-t). Each row corresponds to one mooring record. The shaded envelopes indicate the 95% confidence intervals (twice the standard errors).

data (Figure 4.12), integrating the noise floor in Figure 4.2d up to 30 h gives a noise standard deviation of 0.01 cm/s, which translates into 0.004 Pa through Equation 4.3.

4.3.6 Reynolds stress variability and the momentum balance

In this section, we seek to put some of the conclusions of the previous subsections into a broader context for inner shelf dynamics, in terms of the momentum balance. What force or forces balance the vertical divergence of the Reynolds stresses? The surface wave-free, depth-averaged, cross-shelf momentum equation can be written as

$$\partial_t \langle u \rangle + \langle \partial_x u^2 \rangle + \langle \partial_y uv \rangle + \langle \partial_z wu \rangle - f \langle v \rangle = -\rho_0^{-1} \langle \partial_x p \rangle - \langle \partial_z \overline{u'w'} \rangle, \tag{4.4}$$

and the analogous along-shelf momentum equation can be written as

$$\partial_t \langle v \rangle + \langle \partial_x uv \rangle + \langle \partial_y v^2 \rangle + \langle \partial_z wv \rangle + f \langle u \rangle = -\rho_0^{-1} \langle \partial_y p \rangle - \langle \partial_z \overline{v'w'} \rangle, \tag{4.5}$$

where $\boldsymbol{u} \equiv \hat{\boldsymbol{x}}u + \hat{\boldsymbol{y}}v + \hat{\boldsymbol{z}}w$ is the velocity vector, f is the Coriolis parameter, ρ_0 is the Boussinesq reference density (1024 kg/m^3), p is the pressure and $\langle \bullet \rangle \equiv h^{-1} \int_{-h}^{0} (\bullet)\, dz$ indicates a vertical average, where h is the water depth. All terms are derived from 10 min ensemble averages (see Appendix B for details).

Figure 4.14a,b shows time series of the terms in Equation 4.4 estimated for the OC25SA location (Figure 4.1) during the September deployment. The leading-order terms are the vertical divergence of cross-shelf stress, $\partial(\overline{u'w'})/\partial z$, the vertical divergence of the vertical advection of mean cross-shelf momentum, $\partial(uw)/\partial z$, the Coriolis term and the baroclinic pressure gradient force. The Coriolis term and the baroclinic pressure gradient force balance each other to some degree (correlation coefficient $r = 0.34$, significant at the 99% confidence level), consistent with geostrophic balance (only the baroclinic component of the cross-shelf pressure gradient force could be estimated). At second order, the lateral momentum transport terms ($\partial u^2/\partial x$ and $\partial uv/\partial y$)

and the acceleration term appear. The spectra of most terms show diurnal and semidiurnal peaks, with different variance levels for each term (Figure 4.14c,d). At high (supertidal) frequencies, $\partial(\overline{u'w'})/\partial z$ and $\partial(wu)/\partial z$ have similar spectral levels, while at subtidal frequencies, the spectral levels of all four leading-order terms are the same to within error bounds, suggesting a turbulent thermal wind-like balance (*i.e.*, geostrophy combined with turbulent friction, *e.g.*, McWilliams, 2016) with the mean momentum advection term $\partial(wu)/\partial z$ added.

In the along-shelf direction, the frictional term $\partial(\overline{v'w'})/\partial z$ is smaller than its cross-shelf counterpart, and combines with other terms to balance $\partial(wv)/\partial z$, primarily the barotropic pressure gradient force $-\partial p_{bt}/\partial y$ and the acceleration term (Figure 4.15a-d). The baroclinic pressure gradient force $-\partial p_{bc}/\partial y$ appears at second order, along with the Coriolis, acceleration and lateral momentum transport terms (Figure 4.15b,d). As in the cross-shelf direction, the diurnal and semidiurnal peaks are evident in the frequency spectra (Figure 4.15c,d). Unlike the cross-shelf momentum balance, however, in the low-frequency limit, there is a balance between the barotropic pressure gradient force and the vertical advection of along-shelf momentum, and the vertical divergence of the along-shelf stress has a much lower spectral level, comparable to the other second-order terms.

It must be noted that the terms have very low correlations with each other, with the highest correlation being that between $-fv$ and the cross-shelf pressure gradient, indicating geostrophic balance in the cross-shelf direction. Although this measurement-derived momentum budget does not close, the analysis does suggest that the vertical divergence of the cross-shelf stress is higher in the cross-shelf direction (consistent with the larger slope of $\rho\overline{u'w'}$ compared to $\rho\overline{v'w'}$, Figure 4.13f-j,p-t) and that the divergence of $\rho\overline{v'w'}$ plays a more second-order role at subtidal frequencies compared to the divergence of $\rho\overline{u'w'}$. At subtidal frequencies, the momentum balance in the along-shelf direction appears to be more complex than in the cross-shelf direction. We are unable to draw conclusions on the mechanisms involved in cross-shelf exchange (for example) from this analysis alone, since it is unclear which term or terms balance the fu term, hence driving the cross-shelf circulation. It might be the case that the term that balances the vertical divergences of the Reynolds stresses cannot be captured by the present analysis and other unmeasured gradients of covariances are important, as evidenced by the lack of correlations between $-\partial(\overline{u'w'})/\partial z$, $-\partial(\overline{v'w'})/\partial z$ and other terms in Equations 4.4 and 4.5.

4.4 Summary and conclusions

In this study, we described the observed variability of Reynolds stresses (RSs) across different frequency bands in a mid-latitude inner-/mid-shelf system (25 m-40 m depth) with an energetic internal wave climate, using Acoustic Doppler Current Profiler (ADCP) measurements of along-beam velocity variances. Emphasis is given to the RS signature of supertidal processes (nonlinear internal waves and internal bores), and subtidal along-shelf jets and the potential importance of some of these physical processes for inner shelf dynamics through vertical mixing of horizontal (cross-shelf and along-shelf) momentum.

We have presented evidence suggesting that cross-shelf momentum deposition by internal bores and Nonlinear Internal Wave (NLIW) trains can be important in the inner shelf (Figures 4.9a, 4.11). For bores, this deposition seems to be turbulent, occuring via vertical divergence of the cross-shelf RS. On the other hand, NLIWs seem to cause accumulation of cross-shelf momentum via their orbital velocities (Figures 4.10, 4.11), which we hypothesize to be the expression of radiation stress-like forces linked to the shoaling process of the NLIW trains (Hogg, 1971; Thorpe, 1999; Zikanov and Slinn, 2001).

In the along-shelf direction, the vertical divergence of momentum transport is also chiefly associated with turbulent bores (Figure 4.9b) and NLIW trains (not shown), but is modified (likely by shear instabilities) by along-shelf subtidal flows (Figures 4.8i, 4.9b). Bores account for more than 95% of the vertical structure of the $\rho\overline{u'w'}$ and $\rho\overline{v'w'}$ profiles in a four-day period (Figure 4.9). These RS features project onto the total time-averaged RS profiles (Figure 4.13), which also show

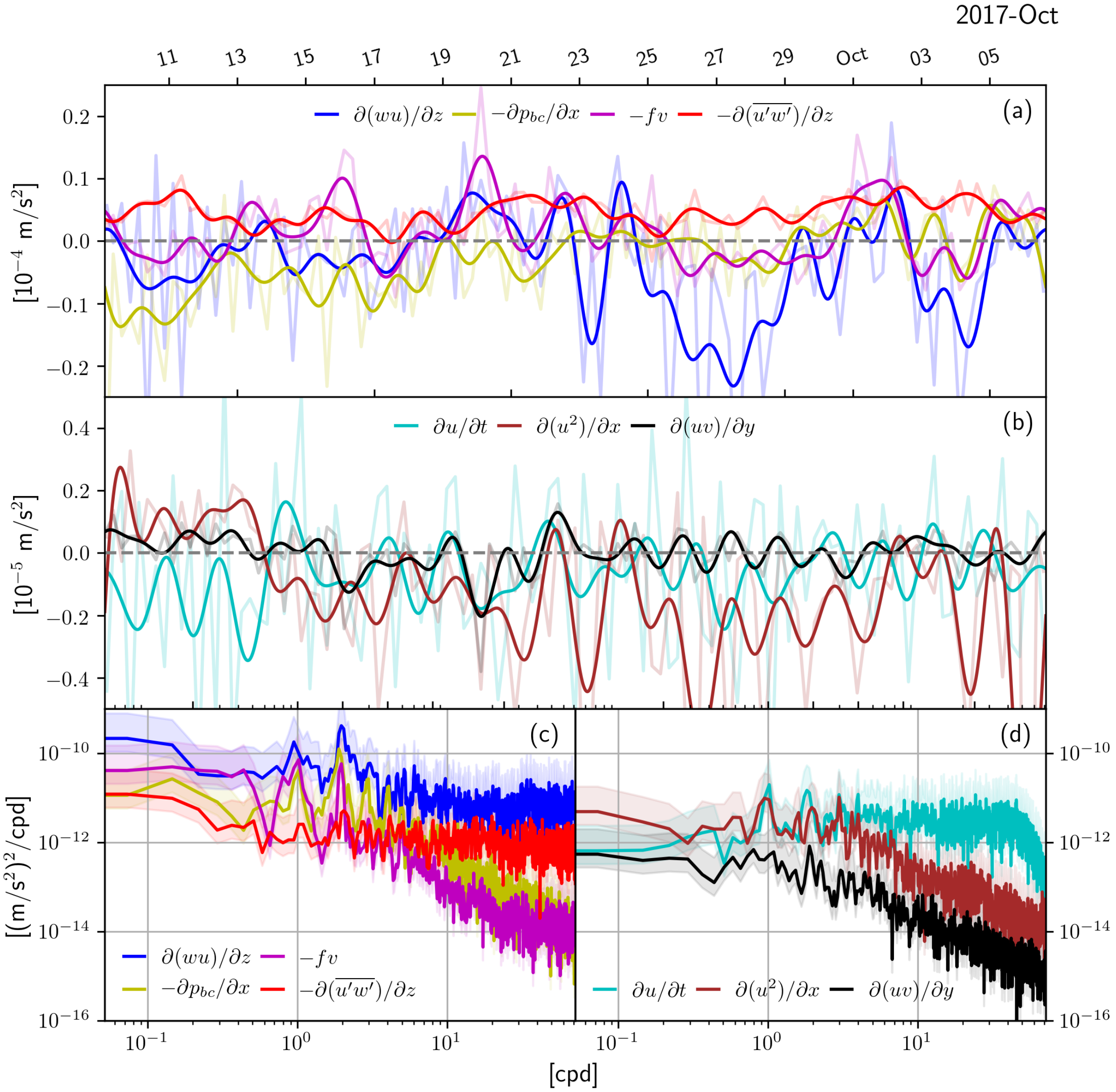

Figure 4.14: Terms in the depth-averaged cross-shelf momentum balance (Equation 4.4, angled brackets are dropped in the figure legend) For a subset of OC25SA's deployment. (a) Time series of the leading-order terms. (b) Time series of the second-order terms. The faint lines in (a,b) are 6 h averages of each term, while the heavy lines are low-pass-filtered (with a cut-off period of 30 h) versions of the 10 min ensemble averages. (c) Power spectra of the leading-order terms. (d) Power spectra of the second-order terms. The shaded areas in (c,d) indicate the 95% confidence intervals about each spectrum.

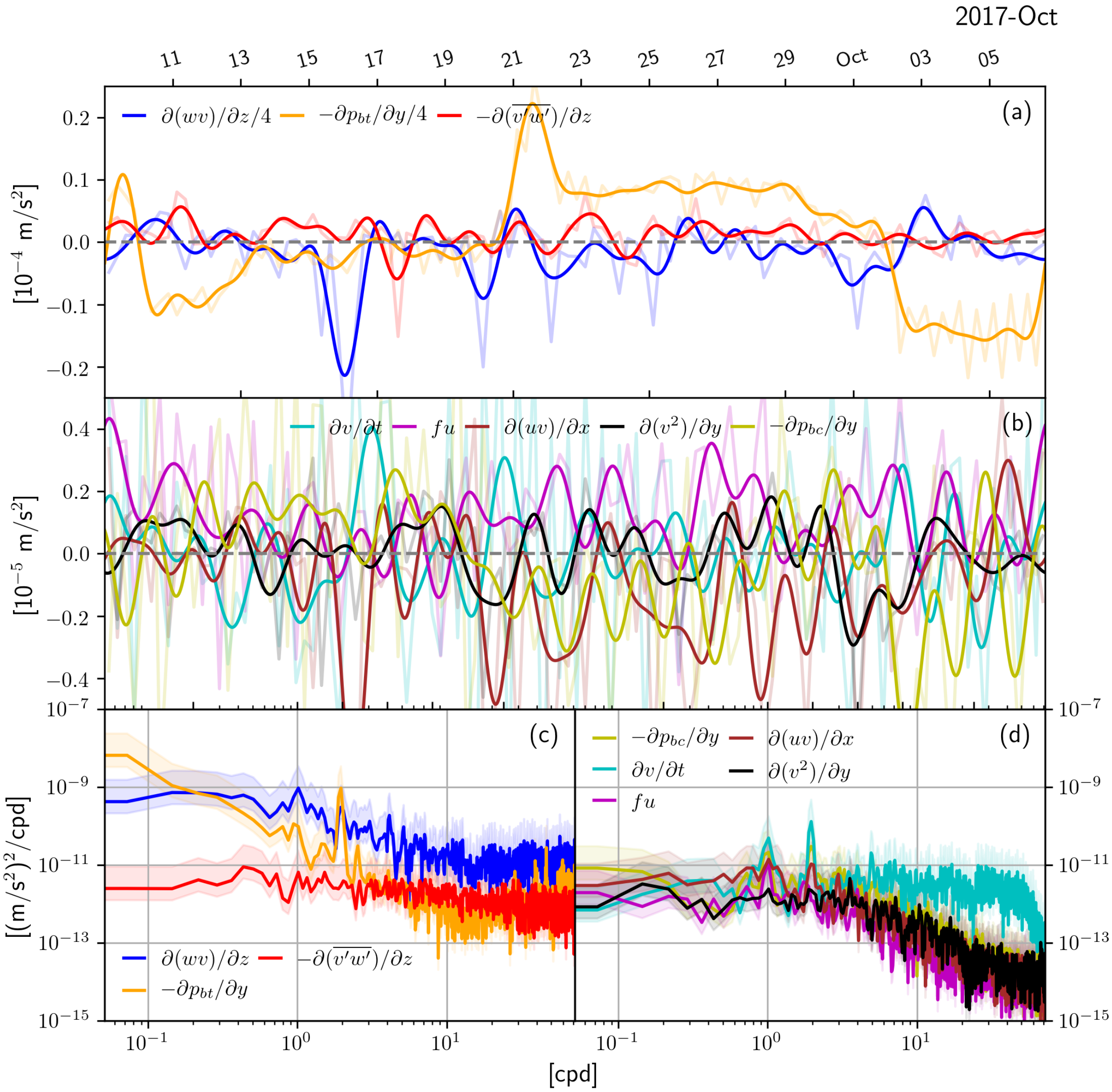

Figure 4.15: As in Figure 4.14, but for the terms in the along-shelf momentum balance (Equation 4.5).

a rather laterally-coherent vertical structure of RS across the mooring array. There is evidence for down-gradient flow of momentum (*e.g.*, Figure 4.12c,d and Figure 4.13a,f,b,g,d,i,e,j,m,r), but in some cases the signs of the shear and RS suggests up-gradient momentum flux (*e.g.*, Figure 4.13). We hypothesize that part of this up-gradient momentum flux is due to the inherently complex nature of the turbulence carried by the internal bores, which may not conform to a simple flux-gradient relationship typically employed in the Reynolds-averaged formalism.

An estimate of the momentum balance terms in the cross-shelf direction (Equation 4.4, Figure 4.14) reveals a persistent vertical convergence of onshore momentum, which we interpret as the rectification of the turbulent deposition mostly caused by internal bore arrivals. This imparts a leading-order onshore force to the water column, which coexists with the vertical divergence of non-turbulent vertical transport of cross-shelf momentum (either by NLIWs or by the mean cross-shelf circulation) and geostrophic balance. The momentum balance in the along-shelf direction (Equation 4.5, Figure 4.15) suggests a different picture, where a barotropic along-shelf pressure gradient coexists with vertical divergence of non-turbulent vertical transport of along-shelf momentum at leading-order. Turbulent deposition of along-shelf momentum is a second-order term, and changes sign with the along-shelf flow, likely modulated by elevated along-shelf shear events such as that seen in Figure 4.8g,h,i.

In both the across-shelf and along-shelf directions, the emerging picture implies a novel (to our knowledge) paradigm where internal waves can be leading-order drivers of inner shelf circulation, in addition to their known roles in mixing of scalar properties and energy dissipation. Most inner-shelf studies to date have focused on wind- and surface gravity wave-driven subtidal dynamics (*e.g.,* Mitchum and Clarke, 1986; Lentz, 1995; Lentz et al., 1999, 2008; Austin and Lentz, 2002; Pringle and Riser, 2003; Fewings et al., 2008, 2015; Lentz and Fewings, 2012; Kirincich, 2013; Horwitz and Lentz, 2014, 2016; Kirincich and Gawarkiewicz, 2016). While some of our conclusions involve subtidal processes, we believe that the most important implications of our study are that the system we examine may represent a different class of inner-shelf, where the dynamics departs from a canonical wind-driven frictional regime (*e.g.,* Lentz and Fewings, 2012). To summarize, the main specific conclusions of this study are:

- Several inner-shelf physical processes, namely internal bores, nonlinear internal wave trains and subtidal along-shelf wind-driven currents all have measurable turbulent Reynolds stress signatures;
- Internal bores and high-frequency nonlinear internal waves induce a substantial vertical divergence of vertical transport (either turbulent or advective) of cross-shelf and along-shelf momentum, hence being potentially important players in inner-shelf dynamics;
- During the experimental period, the conditionally-averaged Reynolds stresses displayed significant vertical divergence in both the cross-shelf and along-shelf directions, indicating a clear departure from a purely frictional regime where the wind stress balances the bottom stress directly and
- The vertical divergences of the cross-shelf and along-shelf Reynolds stresses are leading-order terms in the momentum balance.

We also highlight the limitations of our analyses. As discussed in Subsection 4.3.5, the fact that the top few meters of the water column are not observed due to a combination of limitations of the Adaptive Filtering Method (two vertically-separated bins are needed) and the range cap applied to eliminate sidelobe contamination can be a source of bias. Additionally, being based on point measurements, lateral gradients such as the horizontal advection terms in the momentum equations only represent gradients at the scale of the mooring separation. Finally, the low correlations in the momentum balance analysis leave a knowledge gap regarding what force or forces might balance the vertical divergence of the Reynolds stresses, which may be a good avenue for further research.

Acknowledgments

The authors gratefully acknowledge funding from the Office of Naval Research (ONR), grants N00014-15-1-2885 and N00014-15-1-2633. Input from two anonymous reviewers substantially improved the manuscript. Thanks to Stephen Monismith, Jack McSweeney, Johannes Becherer, Jim Lerczak and Anthony Kirincich for helpful discussions during the writing of this manuscript, and to Johanna Rosman for helpful discussions and assistance in implementing the Adaptive Filtering Method. We thank Pieter Smit and Tim Janssen of Sofar Technologies for providing the wave data, and Jim Thomson and Merrick Haller for providing the land-based meteorological data. Thanks also to Eric Terrill and the technical team at the Coastal Observing R&D Center at Scripps Insitution of Oceanography for providing the marine meteorological observations (miniMET buoy). We also thank the Captain and crew of the R/V *Sally Ride*, Christian McDonald and Brett Pickering for successfully deploying and recovering the moorings used in this study. Codes and reduced datasets required to reproduce the results are available at https://github.com/apaloczy/InnerShelfReynoldsStresses.

Chapter 4, in full, consists of material that has been submitted for publication in the Journal of Physical Oceanography: Palóczy, A., MacKinnon, J. A. & Waterhouse, A. F. Subtidal to supertidal variability of Reynolds stresses in a mid-latitude stratified inner-shelf. The dissertation's author was the primary investigator and author of this paper.

Appendix A: Instrument noise biases in five-beam Reynolds stress estimates

The five-beam expressions for $\overline{u'w'}$ and $\overline{v'w'}$ with full tilt corrections (Equations 4.1 and 4.2) show that the terms proportional to the tilts are time-averaged covariances between tilts and along-beam velocity variances. The measured beam-coordinate variances $\overline{b_i'^2}$ are related to the true variances $\overline{B_i'^2}$ by Stacey et al. (1999):

$$\overline{b_i'^2} = \overline{B_i'^2} + \mathrm{var}(N_b), \tag{4.6}$$

where N_b is the instrument velocity noise (single-ping standard deviation), assumed to be the same for the Janus beams (N_J) but different for the vertical beam (N_5). For each instrument, N_J is set to the average of the noise levels of the four Janus beams. The measured pitch (ϕ_2) and roll (ϕ_3) angles are related to the true pitch (Φ_2) and true roll (Φ_3) angles by

$$\phi_{2,3} = \Phi_{2,3} + N_\phi, \tag{4.7}$$

Using Equations 4.6 and 4.7 in Equation 4.1 and assuming that the signals are uncorrelated with the noises gives

$$\overline{u'w'} = \frac{-1}{4S^6C^2}\Big[S^5C\big(\overline{B_2'^2} + \mathrm{var}(N_J) - \overline{B_1'^2} - \mathrm{var}(N_J)\big) + 2S^4C^2\overline{(\Phi_3 + N_\phi)\big(B_2'^2 + B_1'^2 + 2\mathrm{var}(N_J)\big)} + \cdots \tag{4.8}$$
$$\cdots - 4S^4C^2\overline{(\Phi_3 + N_\phi)(B_5'^2 + \mathrm{var}(N_5))} - 4S^6C^2\overline{(\Phi_2 + N_\phi)[\mathrm{cov}(B_2 + N_2 - B_1 - N_1, B_4 + N_4 - B_3 - N_3)}S^2/4]\Big]$$

or

$$\overline{u'w'} = \frac{-1}{4S^6C^2}\Big[S^5C\big(\overline{B_2'^2} - \overline{B_1'^2}\big) + 2S^4C^2\overline{\Phi_3\big(B_2'^2 + B_1'^2\big)} + 4S^4C^2\overline{\Phi_3}\mathrm{var}(N_J) + \cdots \tag{4.9}$$
$$\cdots - 4S^4C^2\overline{\Phi_3 B_5'^2} - 4S^4C^2\overline{\Phi_3}\mathrm{var}(N_5) - 4S^6C^2\overline{\Phi_2 u'v'}\Big]$$

which simplifies to

$$\overline{u'w'} = \frac{-1}{4S^6C^2}\left[S^5C\left(\overline{B_2'^2}-\overline{B_1'^2}\right)+2S^4C^2\overline{\Phi_3\left(B_2'^2+B_1'^2\right)}-4S^4C^2\overline{\Phi_3 B_5'^2}-4S^6C^2\overline{\Phi_2 u'v'}\right]\cdots(4.10)$$

$$\cdots+\frac{\overline{\Phi_3}}{S^2}\left[\mathrm{var}(N_5)-\mathrm{var}(N_J)\right].(4.11)$$

Analogously, using Equations 4.6 and 4.7 in Equation 4.2 gives

$$\overline{v'w'} = \frac{-1}{4S^6C^2}\left[S^5C\left(\overline{B_4'^2}-\overline{B_3'^2}\right)-2S^4C^2\overline{\Phi_3\left(B_4'^2+B_3'^2\right)}-4S^4C^2\overline{\Phi_3}\mathrm{var}(N_J)+4S^4C^4\overline{\Phi_3 B_5'^2}\cdot\cdot(4.12)\right.$$

$$\left.\cdots+4S^4C^4\overline{\Phi_3}\mathrm{var}(N_5)+4S^6C^2\overline{\Phi_2 B_5'^2}+4S^6C^2\overline{\Phi_2}\mathrm{var}(N_5)+4S^6C^2\overline{\Phi_3 u'v'}\right],$$

which simplifies to

$$\overline{v'w'} = \frac{-1}{4S^6C^2}\left[S^5C\left(\overline{B_4'^2}-\overline{B_3'^2}\right)-2S^4C^2\overline{\Phi_3\left(B_4'^2+B_3'^2\right)}+4S^4C^4\overline{\Phi_3 B_5'^2}+4S^6C^2\overline{\Phi_2 B_5'^2}+4S^6C^2\overline{\Phi_3 u'v'}\right]\cdot(4.13)$$

$$\cdots+\frac{\overline{\Phi_3}}{S^2}\left[\mathrm{var}(N_J)-C^2\mathrm{var}(N_5)\right]-\overline{\Phi_2}\mathrm{var}(N_5).$$

Equations 4.10 and 4.13 show that the biases (red terms) are proportional to the pitch and roll angles averaged within each ensemble, and are therefore time-dependent.

Appendix B: Estimation of the momentum balance terms

The linear terms (except for the vertical stress divergence) in Equations 4.4 and 4.5 are estimated for mooring OC25SA (Figure 4.1) following Lentz et al. (1999). Vertical averages are calculated as vertical medians to decrease the effect of the frequently noisy vertical structure of the momentum balance terms. The vertical integrals of the vertical divergence terms ($\partial wu/\partial z$, $\partial wv/\partial z$, $\partial\overline{u'w'}/\partial z$ and $\partial\overline{v'w'}/\partial z$) are calculated by taking the difference between the near-surface and near-bottom values of the quantities in the derivatives (averaged within the top and bottom 5 m of the ADCP record, respectively).

The depth-averaged pressure gradient force is estimated by combining the near-bottom pressure p_b measured by the ADCPs with the density ρ derived from the adjacent thermistor chains, and using an expression obtained from vertically integrating the hydrostatic equation, taking its lateral derivative and depth-averaging the result. In the cross-shelf direction, the depth-averaged pressure gradient force is

$$-\langle \partial_x p \rangle = -\partial_x p_b + g\partial_x \int_{-h(x)}^{0} \rho \, dz' - g \int_{-h(x)}^{0} \partial_x \rho \, dz' - \frac{g}{h} \int_{-h(x)}^{0} z' \partial_x \rho \, dz', \tag{4.14}$$

where $g = 9.81$ m s^{-2} is gravity, $\rho = \rho_0[1 + \alpha(T - T_0)]$, $T_0 = 21^o$C is the reference temperature, $\alpha = 2.65 \times 10^{-4}$ K^{-1} is the thermal expansion coefficient and T is the temperature measured by the thermistors. In the along-shelf direction, the depth-averaged pressure gradient force is simpler:

$$-\langle \partial_y p \rangle = -\partial_y p_b - \frac{g}{h} \int_{-h(x)}^{0} z' \partial_y \rho \, dz'. \tag{4.15}$$

The vertical advection term is estimated using the vertical velocity measured by the ADCP's vertical beam. Gradients in the along-shelf ($\hat{\boldsymbol{y}}$) direction are calculated as finite differences between OC25M and OC25SA, and gradients in the cross-shelf ($\hat{\boldsymbol{x}}$) direction are calculated as finite differences between OC25SA and OC40S (Figure 4.1). For gradients in the $\hat{\boldsymbol{y}}$ direction, the time-mean of the relevant quantity is removed at OC25M and OC25SA, since small misalignments in the cross-shelf direction are expected to dominate the mean signal.

Chapter 5

Balanced to unbalanced transition in the coastal ocean: Insights from simulations and an along-isobath survey

5.1 Introduction

The scale and dynamical nature of the transition from geostrophically-balanced, larger-scale motions to unbalanced, smaller-scale motions in the upper water column of the deep ocean has gained considerable attention over the past decade (*e.g.*, Callies and Ferrari, 2013; Bühler et al., 2014, 2017; Balwada et al., 2016; Rocha et al., 2016; Qiu et al., 2017, 2018; Chereskin et al., 2019; Sukhatme et al., 2020). Analysis of a global high-resolution numerical simulation has placed the transition scale at 40 km-200 km in the upper water column of the deep ocean and at scales smaller than 40 km for western boundary currents (Qiu et al., 2018). In the Southern California Current System, Chereskin et al. (2019) find a transition scale of 70 km from shipboard Acoustic Doppler Current Profiler (ADCP) data. Knowledge of the balanced-to-unbalanced transition, its spatial distribution and temporal variability is important for understanding the ocean's energy budget, assessing the representation of different physical processes in numerical models and interpreting signals from the upcoming Surface Water Ocean Topography (SWOT) satellite altimetry mission and from other altimetry datasets (see Vignudelli et al., 2019, for a recent review of developments in coastal altimetry). In the coastal ocean, high-frequency radar-derived velocity observations have enabled a detailed examination of the surface velocity field's dynamics (*e.g.*, Soh and Kim, 2018; Yoo et al., 2018), and some insight has stemmed from comparisons of observed spectral slopes with theoretical predictions for geophysical turbulence. For example, Quasigeostrophic theory predicts spectral slopes of $k^{-5/3}$ and k^{-3} for inverse and forward cascades, respectively, where k is the wavenumber (*e.g.*, Yoo et al., 2018).

The region examined in this study is located in the central California Bight (Figure 5.2a). In this region, "relaxation events" are reversals of the along-shelf flow, related to synoptic events of weakening or cessation of the generally upwelling-favorable winds and a resulting poleward transport of warm water from the Santa Barbara Channel (*e.g.*, Washburn et al., 2011; Fewings et al., 2015, Figure 5.1a,d,e). In this work, we contribute to the study of the transition from balanced to unbalanced motions on the continental shelf of this region by quantifying the scale of this transition and its cross-shelf dependence for the first time. We begin with an overview of the shipboard data and numerical simulation outputs in Section 5.2. We then describe the observed and modeled energy distributions in Section 5.3, and summarize and discuss our findings in Section 5.4.

5.2 Data

In this section, we present a general description of the balanced and unbalanced motions present in the observed and simulated fields, in preparation for the analysis of the energy density dependence on along-isobath scale performed in Section 5.3.

5.2.1 Shipboard isobath-following measurements

We analyze temperature and velocity data from an isobath-following cruise carried out in 09/17-18/2017 on the R/V *R. G. Sproul* off central California, from Oceano Beach to Santa Barbara (Figure 5.1). The dataset is comprised of underway ADCP and Conductivity, Temperature, Depth (CTD) data. The ADCP data were processed in a single-ping fashion using the Common Ocean Data Access System (CODAS) framework (*e.g.*, Firing and Hummon, 2010), averaged over 30 s intervals (approximately 38 m resolution in the along-track direction) and rotated to an isobath-following coordinate system, where the cross-isobath velocity u is positive onshore and the along-isobath velocity v is positive poleward. The ADCP velocities were further averaged in 5 min blocks (approximately 380 m resolution) for the spectral analyses performed in Section 5.3 to decrease the spectral noise level. Temperature data were derived from a profiling RBR Concerto that was deployed on a fishing reel and provided vertical profiles spaced on average 175 m in the along-track direction.

To define the differences in the along- and cross-isobath energy levels, each component of the kinetic energy is calculated. In this region, flow is predominantly along-isobath, poleward, likely the signature of a wind relaxation event (Figure 5.1a,d, *e.g.*, Washburn et al., 2011). The depth-averaged flow is mainly along-isobath. Notably, the cross-isobath velocity u has smaller scales than the along-isobath velocity v, both components likely bearing the signal of a combination of processes, including mesoscale eddies, internal tides and coastally-trapped waves (Figure 5.1c,d). We define the total kinetic energy density in the cross-isobath ($\hat{\boldsymbol{x}}$) and along-isobath ($\hat{\boldsymbol{y}}$) directions as

$$\mathrm{KE}_x = \frac{\overline{u^2}}{2}, \quad \mathrm{KE}_y = \frac{\overline{v^2}}{2}, \tag{5.1}$$

and the eddy kinetic energy densities as

$$\mathrm{EKE}_x = \mathrm{KE}_x - \frac{\overline{u}^2}{2}, \quad \mathrm{EKE}_y = \mathrm{KE}_y - \frac{\overline{v}^2}{2}, \tag{5.2}$$

where the $\overline{\bullet}$ operator indicates an along-isobath average. Profiles of the four quantities in Equations 5.1 and 5.2 show that almost all of the variance in u is associated with the eddy component (depth-averaged $\mathrm{EKE}_x/\mathrm{KE}_x$ ratio of 93%), while v also has a large mean component (depth-averaged $\mathrm{EKE}_y/\mathrm{KE}_y$ ratio of 57%, Figure 5.1b). That is consistent with a weak mean cross-isobath flow at all depths, where onshore transport is compensated by offshore transport in the along-isobath average. The temperature structure (Figure 5.1e) shows the warmer water in the Santa Barbara Channel (roughly the second half of the section between PC and SB) being advected poleward.

5.2.2 Model output

In order to extrapolate conclusions drawn from the observations to larger scales and to other isobaths, we analyze output from twin Regional Ocean Modeling System (ROMS) simulations with and without tides, part of the modeling component of the Inner Shelf Dynamics Experiment (ISDE, Lerczak et al., 2019). ROMS solves the rotating Reynolds-Averaged Navier-Stokes equations under the Boussinesq and hydrostatic approximations (*e.g.*, Shchepetkin and McWilliams, 2005). The simulations have a horizontal resolution of 600 m and 42 vertical levels, and are part of a sequence of multiply-nested grids in an offline scheme. We also analyze a simulation on these simulations' child grid (200 m horizontal resolution, with tides) in Section 5.3. The simulations were run for 143 days starting on 07/01/2017, and snapshots were saved hourly. The coefficients for vertical viscosity and diffusivity are solved for using a Generic Length Scale (GLS) scheme with $k-\omega$ coefficients. Horizontal viscosity and diffusivity are implemented with Laplacian operators with a viscosity/diffusivity coefficient of 1 m^2/s. For the simulation with tides, the barotropic tides are prescribed along the grid's open boundaries as surface elevation and

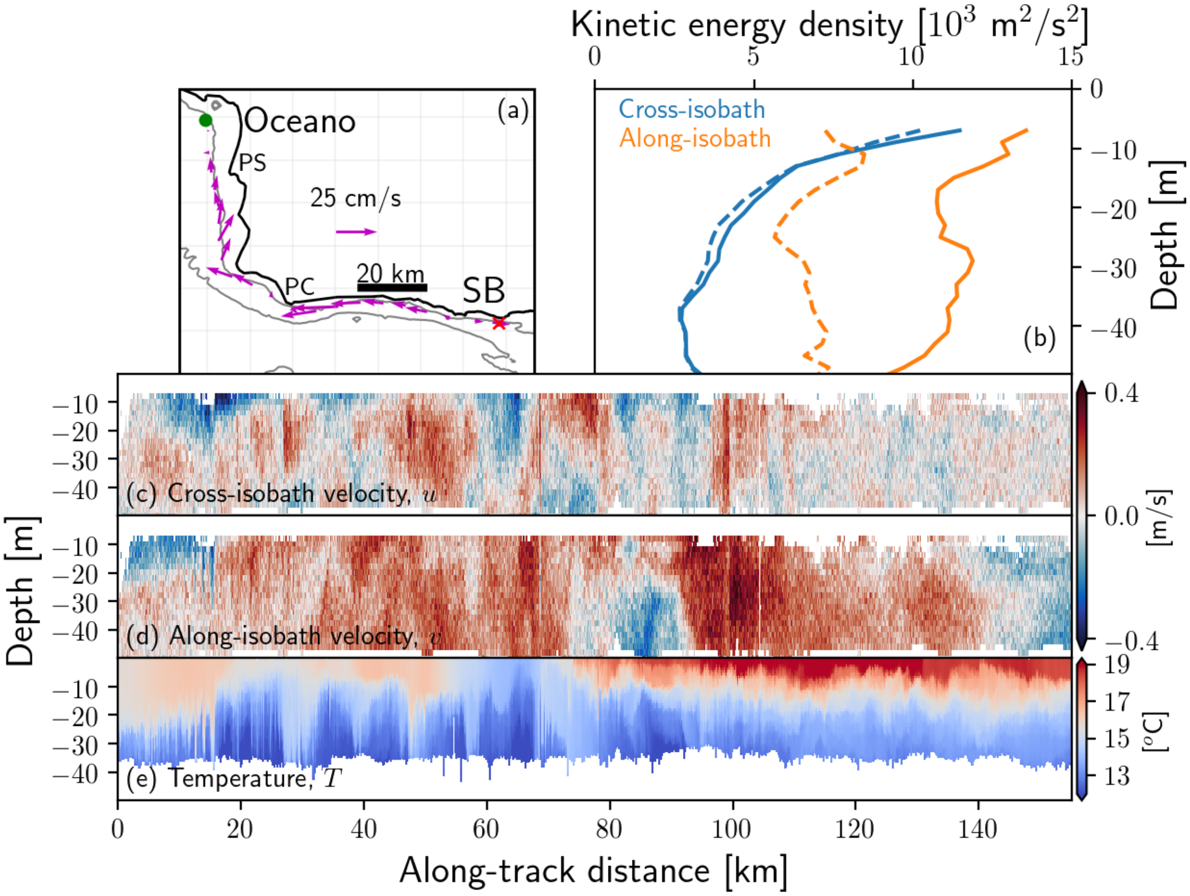

Figure 5.1: Shipboard survey along the 50 m isobath off the central California coast. (a) Map of the survey site with the green dot marking the start and the red “x” the end of the ship track. The magenta arrows are depth-averaged velocities (block-averaged in the along-track coordinate to facilitate visualization), and the gray lines are the 50 m and 200 m isobaths from an updated version of the Smith and Sandwell (1997) product. (b) Along-track averaged kinetic energy density (KE) profiles, where the solid lines are total KE and the dashed lines are eddy KE (see text for definitions). (c-e) Along-track sections of cross-isobath velocity (c, positive onshore), along-isobath velocity (d, positive from Santa Barbara to Oceano) and temperature (e). PS = Point Sal, PC = Point Conception, SB = Santa Barbara.

depth-averaged velocities for the astronomical tidal constituents K_2, S_2, M_2, N_2, K_1, P_1, Q_1, and N_1 and overtides M_4 and M_6 from a barotropic tidal model, along with baroclinic forcing from a parent coarser grid (≈1 km horizontal resolution). The simulations and the nesting scheme are discussed in further detail by Kumar et al. (2019) and by Suanda et al. (2016).

To obtain a horizontal two-dimensional view of the circulation, Figure 5.2 shows the model domain and a snapshot of depth-averaged vertical vorticity normalized by the Coriolis parameter ζ/f as an example of the simulated fields. Both simulations have an active eddy field, with eddies with radii of ≈10-20 km all over the domain offshore of the 200 m isobath. Inshore of the 200 m isobath, smaller-scale structures such as headland eddies (off PS) and an along-shelf relaxation jet (flowing from SB to PC) can be seen (Figure 5.2c,d). The simulation with tides has finer-scale structures elongated in the along-shelf direction (likely the expression of secondary flows linked to shoaling internal tides, for example off of Oceano) that are not present in the simulation without tides (Figure 5.2c,d).

5.3 Wavenumber spectra

A widely used approach for studying the balanced-to-unbalanced transition in the ocean is the Helmholtz and wave-vortex decompositions of one-dimensional along-track shipboard measurements developed by Bühler et al. (2014) and Lindborg (2015), when their underlying assumptions hold. The u-v cross-spectrum $\hat{C}^{uv}$ is a helpful observational test of the applicability of the Helmholtz decomposition technique (Bühler et al., 2017). If $\hat{C}^{uv}$ has a non-negligible imaginary part (as in our shipboard dataset and model outputs, not shown), the divergent and rotational parts of the flow are correlated, and neither the isotropic nor the anisotropic versions of the Helmholtz decomposition are applicable (Bühler et al., 2017). Indeed, Chereskin et al. (2019) point out that the assumptions of homogeneity and isotropy do have some observational support in the Southern California Current System; however the rotational and divergent components

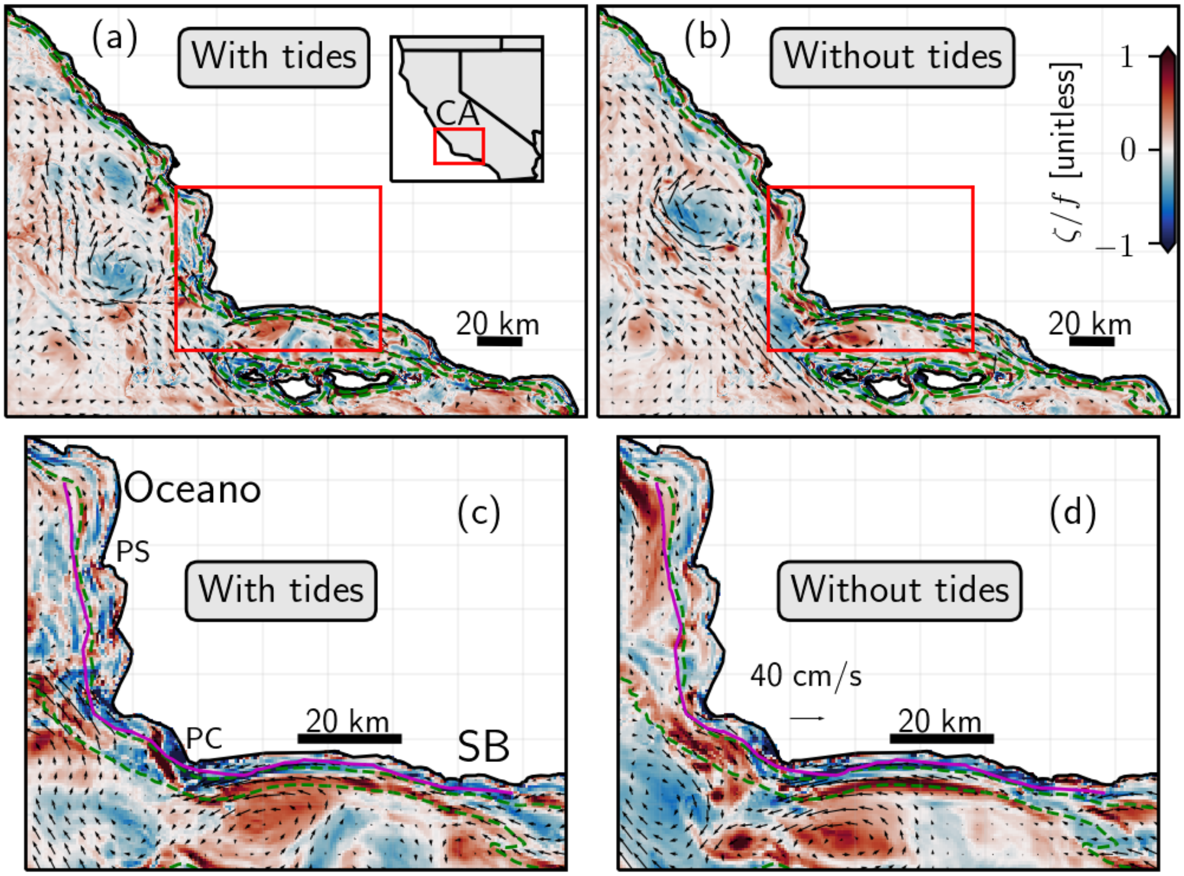

Figure 5.2: A snapshot of depth-averaged vertical vorticity ζ normalized by the Coriolis parameter f in the twin ROMS simulations with/without tides on 2017/09/17, 20 h. The arrows represent depth-averaged velocities. The green dashed lines mark the 50 m and 200 m model isobaths. The magenta lines in (c) and (d) mark the isobath-following ship track (Figure 5.1). The red rectangle on the map inset in (a) indicates the geographic bounding box of the domain depicted in (a) and (b), while the red rectangle in (a) and (b) indicates the domain depicted in (c) and (d). The color and arrow scales are the same for all panels. PS = Point Sal, PC = Point Conception, SB = Santa Barbara.

of the motion are likely to be correlated, and Soh and Kim (2018) note that the assumptions of stationarity, homogeneity and isotropy are unlikely to be true for the surface currents off of San Diego. However, on the continental shelf, balanced motions are expected to project mainly on the along-shelf velocity v, while unbalanced motions project mainly on the cross-isobath velocity u (Brink, 2016b; Brink and Seo, 2016). We thus limit ourselves to analyzing the spectral content of u and v in the isobath-following shipboard survey and in realistic primitive-equation numerical simulations described in the previous section. It must be emphasized, however, that u and v do not, respectively, contain only unbalanced and balanced kinetic energy, and that we take their ratio only as an approximation of such a decomposition.

Interpreting wavenumber spectra from non-synoptic observations such as shipboard data implies a fast-tow assumption (as made by, *e.g.*, Callies and Ferrari, 2013; Rocha et al., 2016; Chereskin et al., 2019; Sukhatme et al., 2020), *i.e.*, that the sampling time scale of each spectral realization is much shorter than that of the signal's propagation speed. For the data proposed here (assuming a range of underway speeds $\sim$1.15-2.5 m/s) the ship travels 4-9 km in 1 h, thus resolving *e.g.*, high-frequency, small scale internal waves and $\sim$5-20 km mesoscale eddies with translational time scales of days, but not tides, which will be aliased. In addition, nonlinear effects become increasingly important as the internal waves shoal. Comparison with truly synoptic model-derived wavenumber spectra (as well as the tides/no tides twin simulations) allows us to evaluate the validity of the fast-tow assumption and the effects of tides (*e.g.*, Rocha et al., 2016; Chereskin et al., 2019). To minimize the effect of internal waves, we derive the wavenumber spectra from the depth-averaged velocities u, v and buoyancy $b \equiv -g\rho/\rho_0$ (where g is the acceleration due to gravity, ρ is the density and ρ_0 is the Boussinesq reference density). We analyze along-track (longitudinal, along-isobath) and cross-track (transverse, cross-isobath) kinetic energy density spectra and the potential energy density $b^2/\overline{N}^2$ (where N is the buoyancy frequency) spectrum derived from the shipboard ADCP and towed CTD and from the ROMS simulations. The hourly snapshots of model u, v and $b/\overline{N}$ data are first depth-averaged, concatenated with 50% overlap for the last 40 days of model output, windowed with a Hanning window and then Fourier-transformed and averaged. The model wavenumber spectra sample the entire extension of the model isobaths (Figures 5.2a,b for the 600 m grid and 5.4d for the 200 m grid). The ship-derived spectra are calculated in a similar manner, but the single ship track (Figures 5.2c,d and 5.1a) is broken up in 3 segments prior to windowing, Fourier-transforming and averaging. The choice of 3 segments is a compromise between narrowing the confidence intervals of the spectral estimates and resolving L_t in the low-wavenumber end of the observed spectra.

We look for evidence of change in spectral slopes in the model and observed energy density spectra (Figure 5.3). Perhaps the most salient feature is the difference between the cross-isobath ($\hat{C}^u/2$) and along-isobath ($\hat{C}^v/2$) kinetic energy density spectra at low wavenumbers, specifically the drop-off in cross-isobath kinetic energy in the low-wavenumber end in the model-derived spectra (Figure 5.3a,c), which is not well resolved by the observations. The $\hat{C}^u/2$ energy levels at wavenumbers O(0.1 cpkm) are higher in the observations than in the simulation with tides, although the difference might be within the error estimates. A plausible explanation for the low $\hat{C}^u/2$ model values at high wavenumbers is the absence of remote baroclinic forcing, which has been shown to be important for the representation of high-wavenumber baroclinic kinetic energy in regional models in this area (Mazloff et al., 2020), while spurious signals generated at the southern open boundary propagating poleward as coastally-trapped waves might explain the elevated $\hat{C}^v/2$ model values at high wavenumbers. The potential energy density spectrum ($\hat{C}^b/2$) follows $\hat{C}^v/2$ both in the model and in the observations (Figure 5.3a,c), consistent with an along-isobath flow that is mostly geostrophically-balanced and larger-scale than the more ageostropic cross-isobath flow. The energy levels in the simulation with tides are, as expected, higher than in the simulation without tides, and the difference appears mostly in $\hat{C}^u/2$ (Figure 5.3c). The transition scale L_t, defined here as the largest wavelength at which the ratio between along-isobath and cross-isobath kinetic energy densities ($\hat{C}^v/\hat{C}^u$) is unity, is at 12 km in both simulations (Figure 5.3d), and is at $\approx$19 km in the observations (Figure 5.3b), although conclusive evidence would require more measured spectral realizations. L_t^{obs} varies between 17-22 km depending on the number of segments chosen for the spectral averaging, and the 95% confidence intervals almost overlap at wavenumbers smaller than L_t^{obs} (Figure 5.3a); therefore this result should be viewed only as suggestive. The observed spectra have a high noise level, but there is a $\approx k^{-2}$ spectral slope both in the model and in the observations in the 0.01-0.1 cpkm (10-100 km) range. The model energy spectra display a shallower, $\approx k^{-1}$ roll-off at scales shorter than L_t and a higher energy level in $\hat{C}^v/2$ than in $\hat{C}^u/2$ that is not found in the observations (Figure 5.3a,c). Plotting model spectra along the 50 m isobath for the overlapping segments of the 600 m and 200 m grids (not shown) suggests that these features at high wavenumbers are indeed numerical artifacts present in both grids. Both the total kinetic energy spectrum (Figure 5.3e) and the enstrophy spectrum (Figure 5.3f) show a change in the slope at around the same wavenumber, which further supports the existence of a model injection scale at $L_{t600m}^{mod} = 12$ km. The fact that the observed and model energy spectra have an $\approx k^{-2}$ slope and overlap over a wide wavenumber range gives confidence in the model analysis as an extrapolation of the observations.

We have so far examined L_t along the 50 m isobath only. What is the spatial dependence of L_t, and in particular, how does it change with local depth H? Figure 5.4 shows $\hat{C}^u/2$, $\hat{C}^v/2$ and $\hat{C}^b/2$ spectra for a ROMS simulation with 200 m horizontal resolution and tides (the child simulation to the twin runs shown in Figure 5.2). As one moves from the 200 m isobath towards the coast (along the contours plotted in Figure 5.4d), the energy density distribution across along-isobath scales changes markedly. First, $\hat{C}^u/2$ decreases at low wavenumbers (especially inshore of the 50 m isobath), partly because of the coastal boundary condition (Figure 5.4a). Second, the $\hat{C}^b/2$ energy level steadily increases, as does the $\hat{C}^v/2$ energy level (except at very low wavenumbers, Figure 5.4b,c). The model transition scale L_{t200m}^{mod} in this 200 m grid simulation is close to 17 km at the 50 m isobath, similar to the observed value ($L_t^{obs} = 17$-22 km), and slightly larger than the 600 m grid value ($L_{t600m}^{mod} = 12$ km, Figure 5.3b,d). The peaks in $\hat{C}^u/2$ and $\hat{C}^v/2$ appear at the scale of a sequence of canyons present in the southwest corner of the 200 m grid, for isobaths deeper than about 100 m (Figure 5.4a-d). Topographically-influenced currents inertially overshooting isobaths may explain these peaks, as they tend to imprint the spatial scales of the topography on the energy spectra.

Based on linear stability arguments, it may be intuitively hypothesized that L_t would scale proportionally to the internal deformation radius NH/f, and therefore with H if N varies slowly in the cross-isobath direction (at a fixed latitude). However, for a developed, finite-amplitude eddy field, Brink (2016b) has shown that in an idealized wind-driven along-shelf uniform model where baroclinic instability is the dominant eddy-generating process, an inertial scale

$$L_i = av^*/f = a\mathrm{EKE}_M^{\frac{1}{2}}/f \tag{5.3}$$

based on an eddy swirl velocity v^* derived from the time-maximum eddy kinetic energy EKE_M and a scaling constant a is more accurate than NH/f in predicting the injection scale's dependence on cross-shelf location (as evidenced by the mean wavelength of the eddies along a fixed isobath). The model transition scale L_t^{mod} and inertial scale L_i^{mod} between the 20 m and 90 m isobaths reveal similar dependence on the local depth (correlation coefficient of 0.61). Between the 100 m and 200 m isobaths, L_{i200m}^{mod} no longer tracks L_{t200m}^{mod}, likely due to the dominance of topographic effects associated with the sharp canyons in the southwest corner of the grid, which occupy an along-isobath segment ≈10 km long in the 100 m-200 m isobath range (Figure 5.4d,f).

5.4 Summary and discussion

We have presented an analysis of the scale-dependent energy distribution off the central California coast to investigate the scales of transition between geostrophically-balanced and unbalanced motions. This is, to our knowledge, the first such analysis performed on an isobath-following shipboard survey and realistic model output.

Results show that the transition from geostrophically-balanced to unbalanced motions, as

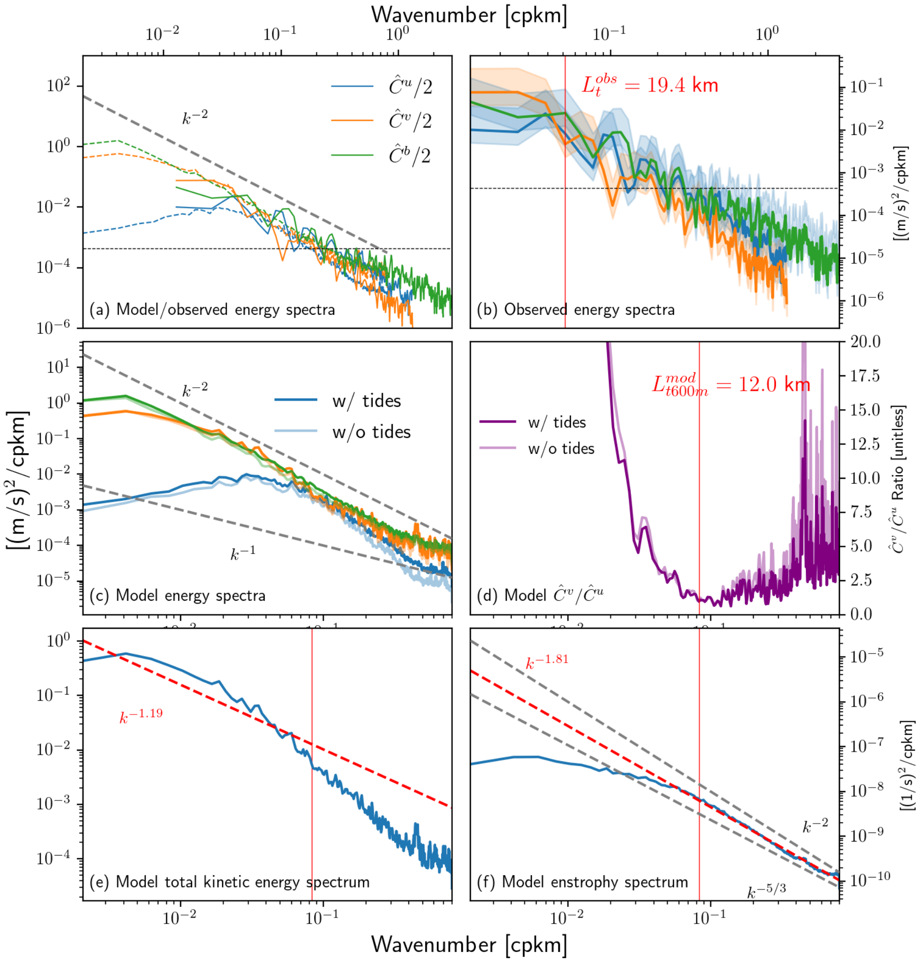

Figure 5.3: Model and observed wavenumber spectra of depth-averaged quantities along the 50 m isobath. (a) Model-derived (dashed lines) and ship-derived (solid lines) wavenumber energy spectra. (b) Ship-derived wavenumber energy spectra. (c) Model wavenumber energy spectra for the simulations with tides (solid lines) and without tides (faint lines). (d) $\hat{C}^v/\hat{C}^u$ ratio for the simulations with/without tides, serving as a proxy for the balanced/unbalanced energy ratio. The transition wavelength L_t where $\hat{C}^v/\hat{C}^u$ is unity is annotated. The color-coding is the same for panels (a-c). The symbols $\hat{C}^u/2$, $\hat{C}^v/2$ and $\hat{C}^b/2$ represent the cross-isobath kinetic energy spectrum, the along-isobath kinetic energy spectrum and the potential energy spectrum. The shadings about the ship-derived spectra in (b) are 95% confidence intervals, and are omitted in (a) for clarity. Formal error estimates for the model spectra are insignificant and are therefore omitted. The vertical red line in (b) marks the observed transition wavenumber $1/L_t^{obs}$, while the vertical red lines in (d-f) mark the model transition wavenumber on the 600 m model grid $1/L_{t600m}^{mod}$. The horizontal dashed black lines in (a) and (b) mark the spectral noise level of the observational kinetic energy density estimates. Gray dashed lines in (a), (c) and (f) are exact power-law slopes for reference. Red dashed lines in (e) and (f) are least-squares fits to the total kinetic energy and enstrophy spectra in the inverse cascade and forward cascade wavenumber ranges, respectively.

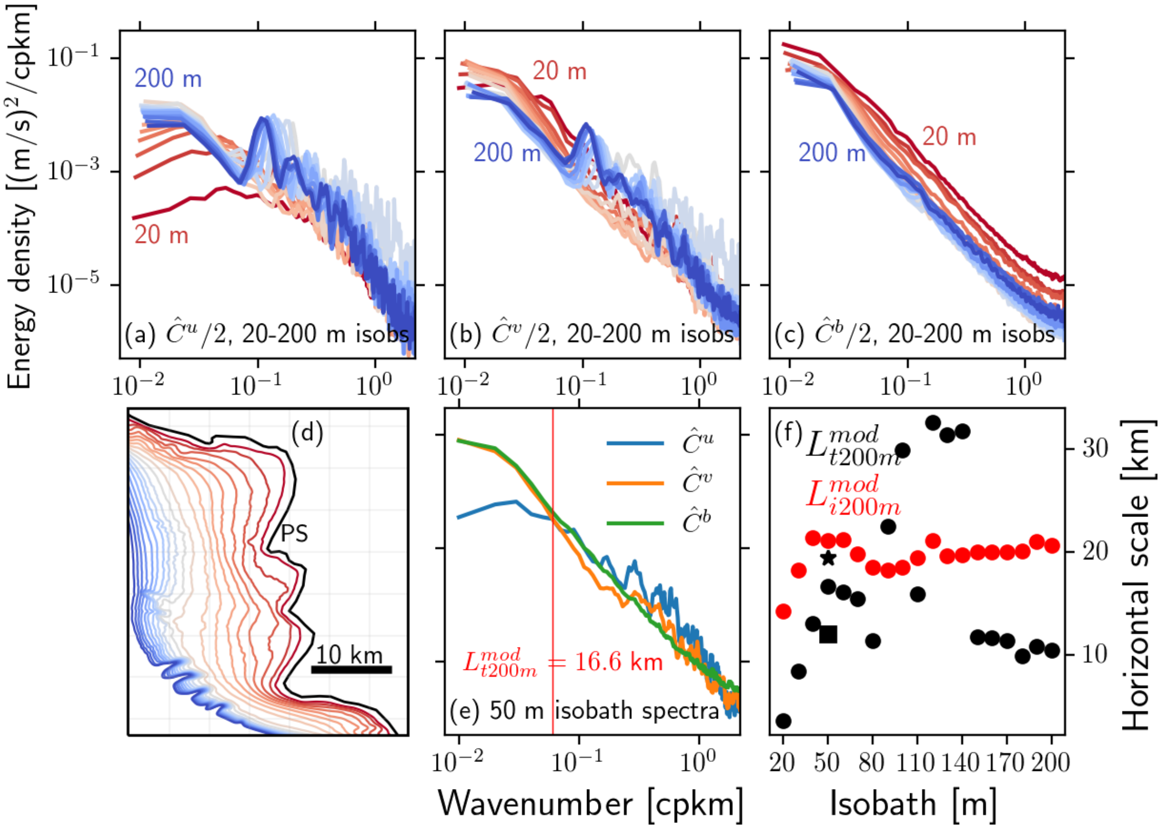

Figure 5.4: Dependence of model wavenumber energy spectra and balanced/unbalanced transition scale L_t^{mod} on isobath. (a-c) Model wavenumber energy spectra sampled along a range of isobaths (20-200 m), color-coded by the isobath (reddish lines are from shallower isobaths and blueish lines are from deeper isobaths). (a) Cross-isobath kinetic energy spectra, $\hat{C}^u/2$. (b) Along-isobath kinetic energy spectra, $\hat{C}^v/2$. (c) Potential energy spectra, $\hat{C}^b/2$. (d) The 200 m grid model domain with the 20, 30, 40... 190 and 200 m model isobaths color-coded as in (a-c). (e) $\hat{C}^u/2$, $\hat{C}^v/2$ and $\hat{C}^b/2$ for the model 50 m isobath. (f) Model transition scale L_t^{mod} (inverse wavenumber at which $\hat{C}^u/2$ and $\hat{C}^v/2$ exchange dominance) and inertial scale ($L_i = a\mathrm{EKE}_M^{\frac{1}{2}}/f$, with $a = 10$) as a function of isobath. The black square indicates L_{t600m}^{mod} at the 50 m isobath and the black star indicates L_t^{obs} at the 50 m isobath. The axes of panels (a), (b), (c) and (e) are the same. PS = Point Sal.

evidenced by the exchange in dominance between the cross-isobath and along-isobath kinetic energy components, happens at 12-22 km, which is considerably shorter than the 70 km found from ADCP data by Chereskin et al. (2019) for the offshore Southern California Current System region. The transition scale L_t increases from 3 km to 30 km between the 20 m and 100 m isobaths, presumably approaching a more spatially slowly-varying value offshore, as predicted by Qiu et al. (2018)'s model diagnostic maps of L_t (their Figure 4). The cross-shelf dependence of L_t in the smooth topography segment of the shelf is well predicted by an inertial length scale proportional to the eddy kinetic energy (Equation 5.3 and Brink, 2016b). The finding that the presence of tides does not affect L_t (Figure 5.3c,d) further suggests that other types of unbalanced motion are important players.

The observed and simulated spectral slopes give some insight on the potential dynamical regimes. In a coastal setting, wavenumber spectra of surface currents with slopes between $k^{-5/3}$ and k^{-3} have been observed in different wavenumber bands (Soh and Kim, 2018; Yoo et al., 2018). The $\approx k^{-2}$ spectral slope could be the signature, for example, of secondary ageostrophic motions generated by frontal circulations or nonlinear interactions between near-inertial inertia-gravity waves (*e.g.*, Callies and Ferrari, 2013). At 50 m, the slope of the enstrophy spectrum in the forward cascade wavenumber range ($k > 1/L_t$) is close to $k^{-5/3}$ and the slope of the kinetic energy spectrum in the inverse cascade wavenumber range ($k < 1/L_t$) is shallower, closer to k^{-1}. These slopes might indicate a Surface Quasigeostrophic regime (SQG), but the flattening of the kinetic energy spectrum in low wavenumbers might also indicate energy dissipation by bottom friction (*e.g.*, Yoo et al., 2018, their Table 1).

Although the inference of dynamical regimes from spectral slopes alone can be ambiguous, a transition in spectral slope at an intermediate wavenumber is a result that indicates the injection scale, *i.e.*, the scale at which energy and enstrophy are introduced in the system and are expected to follow inverse and forward cascades, respectively (*e.g.*, Vallis, 2019). The flattening of $\hat{C}^u/2$ at wavenumbers smaller than $1/L_t$, taken together with the change in the slope of the spectrum of depth-averaged vorticity at a similar wavenumber (Figure 5.3) and the fact that Brink (2016b)'s predictions for the cross-shelf dependence of the injection scale (his Figure 11) match the cross-shelf dependence of L_t up to $\approx$100 m (where topographic effects likely become dominant, Figure 5.4) suggests that the injection scale is around L_t, and that baroclinic instability of the wind-driven along-shelf subtidal flow controls L_t in the part of this region's shelf with smooth isobaths. We also point out that the sharp drop-off in the $\hat{C}^u/2$ (the cross-track component) spectra and the lack of a ratio of $\hat{C}^v/\hat{C}^u = 2$ (due to the k^{-2} spectral slope for $\hat{C}^v/2$ and $\hat{C}^b/2$) in the balanced wavenumber range are inconsistent with the theoretical predictions for isotropic interior geostrophic turbulence (*e.g.*, Charney, 1971; Callies and Ferrari, 2013), as may be expected for a system dominated by anisotropy such as the continental shelf and slope (Soh and Kim, 2018).

In closing, we note that our results also bring up an interesting implication for coastal altimetry, namely that along-track sea surface height data might be used to accurately derive cross-track geostrophic (balanced) velocities farther inshore, where L_t is smaller. In addition, the fact that so much of the kinetic energy in the coastal ocean often lies in the barotropic mode (*e.g.*, Clarke and Brink, 1985) could render the combination of land-based high-frequency radar observing systems and coastal altimetry (such as SWOT and other modern altimetry missions and reprocessed datasets, Vignudelli et al., 2019) a powerful tool for deriving geostrophic and ageostrophic velocities on the continental shelf.

Acknowledgments

APF, JAM and AFW gratefully acknowledge support from the Office of Naval Research, grant # N00014-15-1-2633. The authors also acknowledge helpful discussions with Sarah Gille and Ken Brink, which significantly improved this manuscript. The collection of the shipboard dataset used in this study was enabled by the UC Ship Funds Program, and we are indebted to the captain and crew of the R/V *R. G. Sproul* for their professionalism and navigation skills in such

an unusual form of shipboard survey. We also thank Nirnimesh Kumar for giving us access to the ROMS model output used in this study. The reduced datasets and codes necessary to reproduce the results are available at https://github.com/apaloczy/InnerShelfWavenumberSpectra. This work is dedicated to the memory of Nirni Kumar.

Chapter 5, in full, consists of material that is being prepared for submission for publication in Geophysical Research Letters: Palóczy, A., MacKinnon, J. A. & Waterhouse, A. F. Balanced to unbalanced transition in the coastal ocean: Insights from simulations and an along-isobath survey. The dissertation's author was the primary investigator and author of this paper.

Bibliography

Armitage, T. W. K., Kwok, R., Thompson, A. F., and Cunningham, G. (2018). Dynamic topography and sea level anomalies of the Southern Ocean: Variability and teleconnections. *J. Geophys. Res.-Oceans*.

Assmann, K. M., Jenkins, A., Shoosmith, D. R., Walker, D. P., Jacobs, S. S., and Nicholls, K. W. (2013). Variability of Circumpolar Deep Water transport onto the Amundsen Sea continental shelf through a shelf break trough. *J. Geophys. Res.-Oceans*, 118(12):6603–6620.

Austin, J. A. and Lentz, S. J. (2002). The Inner Shelf Response to Wind-Driven Upwelling and Downwelling. *J. Phys. Oceanogr.*, 32(7):2171–2193.

Balwada, D., LaCasce, J. H., and Speer, K. G. (2016). Scale-dependent distribution of kinetic energy from surface drifters in the Gulf of Mexico. *Geophys. Res. Lett.*, 43(20):10,856–10,863.

Bell, M. J. (1999). Vortex stretching and bottom torques in the Bryan-Cox ocean circulation model. *J. Geophys. Res. Ocean.*, 104(C10):23545–23563.

Brink, K. (2016a). Cross-Shelf Exchange. *Annu. Rev. Mar. Sci.*, 8(1):59–78.

Brink, K. H. (2016b). Continental Shelf Baroclinic Instability. Part I: Relaxation from Upwelling or Downwelling. *J. Phys. Oceanogr.*, 46(2):551–568.

Brink, K. H. and Seo, H. (2016). Continental Shelf Baroclinic Instability. Part II: Oscillating Wind Forcing. *J. Phys. Oceanogr.*, 46(2):569–582.

Bühler, O., Callies, J., and Ferrari, R. (2014). Wave–vortex decomposition of one-dimensional ship-track data. *J. Fluid Mech.*, 756:1007–1026.

Bühler, O., Kuang, M., and Tabak, E. G. (2017). Anisotropic Helmholtz and wave–vortex decomposition of one-dimensional spectra. *J. Fluid Mech.*, 815:361–387.

Burchard, H., Craig, P. D., Gemmrich, J. R., van Haren, H., Mathieu, P.-P., Meier, H. M., Smith, W. A. M. N., Prandke, H., Rippeth, T. P., Skyllingstad, E. D., Smyth, W. D., Welsh, D. J., and Wijesekera, H. W. (2008). Observational and numerical modeling methods for quantifying coastal ocean turbulence and mixing. 76(4):399–442.

Callies, J. and Ferrari, R. (2013). Interpreting Energy and Tracer Spectra of Upper-Ocean Turbulence in the Submesoscale Range (1–200 km). *J. Phys. Oceanogr.*, 43(11):2456–2474.

Castagno, P., Falco, P., Dinniman, M. S., Spezie, G., and Budillon, G. (2017). Temporal variability of the Circumpolar Deep Water inflow onto the Ross Sea continental shelf. *J. Mar. Syst.*, 166:37–49.

Charney, J. G. (1971). Geostrophic Turbulence. *J. Atmos. Sci.*, 28(6):1087–1095.

Chavanne, C. P., Heywood, K. J., Nicholls, K. W., and Fer, I. (2010). Observations of the Antarctic Slope Undercurrent in the southeastern Weddell Sea. *Geophys. Res. Lett.*, 37(13).

Chereskin, T. K., Rocha, C. B., Gille, S. T., Menemenlis, D., and Passaro, M. (2019). Characterizing the Transition From Balanced to Unbalanced Motions in the Southern California Current. *J. Geophys. Res.*, 124(3):2088–2109.

Clarke, A. J. and Brink, K. H. (1985). The Response of Stratified, Frictional Flow of Shelf and Slope Waters to Fluctuating Large-Scale, Low-Frequency Wind Forcing. *J. Phys. Oceanogr.*, 15(4):439–453.

Cook, A. J., Holland, P. R., Meredith, M. P., Murray, T., Luckman, A., and Vaughan, D. G. (2016). Ocean forcing of glacier retreat in the western Antarctic Peninsula. *Science*, 353(6296):283–286.

Couto, N., Martinson, D. G., Kohut, J., and Schofield, O. (2017). Distribution of Upper Circumpolar Deep Water on the warming continental shelf of the West Antarctic Peninsula. *J. Geophys. Res. Ocean.*, 122(7):5306–5315.

Cushman-Roisin, B. and Beckers, J.-M. (2011). *Introduction to Geophysical Fluid Dynamics: Physical and Numerical Aspects*. Academic press.

Delman, A. S., McClean, J. L., Sprintall, J., Talley, L. D., Yulaeva, E., and Jayne, S. R. (2015). Effects of Eddy Vorticity Forcing on the Mean State of the Kuroshio Extension. *J. Phys. Oceanogr.*, 45(5):1356–1375.

Depoorter, M. A., Bamber, J. L., Griggs, J. A., Lenaerts, J. T. M., Ligtenberg, S. R. M., van den Broeke, M. R., and Moholdt, G. (2013). Calving fluxes and basal melt rates of Antarctic ice shelves. *Nature*, 502(7469):89–92.

Dewey, R. K. and Stringer, S. (2020). Reynolds Stresses and Turbulent Kinetic Energy Estimates from Various ADCP Beam Configurations: Theory. *Unpublished, updated version of manuscript available at https://www.researchgate.net/publication/280100811_Reynolds_Stresses_and_Turbulent_Kinetic_Energy_Estimates_from_Various_ADCP_Beam_Configurations_Theory*.

Dinniman, M., Asay-Davis, X., Galton-Fenzi, B., Holland, P., Jenkins, A., and Timmermann, R. (2016). Modeling ice shelf/ocean interaction in Antarctica: A review. *Oceanography*, 29(4):144–153.

Dinniman, M. S. and Klinck, J. M. (2004). A model study of circulation and cross-shelf exchange on the West Antarctic Peninsula continental shelf. *Deep. Res. Part II Top. Stud. Oceanogr.*, 51(17-19):2003–2022.

Dinniman, M. S., Klinck, J. M., Bai, L. S., Bromwich, D. H., Hines, K. M., and Holland, D. M. (2015). The effect of atmospheric forcing resolution on delivery of ocean heat to the Antarctic floating ice shelves. *J. Climate*, 28(15):6067–6085.

Dinniman, M. S., Klinck, J. M., and Smith, W. O. (2011). A model study of Circumpolar Deep Water on the West Antarctic Peninsula and Ross Sea continental shelves. *Deep. Res. Part II Top. Stud. Oceanogr.*, 58:1508–1523.

Dotto, T. S., Naveira Garabato, A. C., Bacon, S., Holland, P. R., Kimura, S., Firing, Y. L., Tsamados, M., Wåhlin, A. K., and Jenkins, A. (2019). Wind-Driven Processes Controlling Oceanic Heat Delivery to the Amundsen Sea, Antarctica. *J. Phys. Oceanogr.*, 49(11):2829–2849.

Downes, S. M., Farneti, R., Uotila, P., Griffies, S. M., Marsland, S. J., Bailey, D., Behrens, E., Bentsen, M., Bi, D., Biastoch, A., Böning, C., Bozec, A., Canuto, V. M., Chassignet, E., Danabasoglu, G., Danilov, S., Diansky, N., Drange, H., Fogli, P. G., Gusev, A., Howard, A., Ilicak, M., Jung, T., Kelley, M., Large, W. G., Leboissetier, A., Long, M., Lu, J., Masina, S., Mishra, A., Navarra, A., Nurser, A. G., Patara, L., Samuels, B. L., Sidorenko, D., Spence, P., Tsujino, H., Wang, Q., and Yeager, S. G. (2015). An assessment of Southern Ocean water masses and sea ice during 1988–2007 in a suite of interannual CORE-II simulations. *Ocean Model.*, 94:67 – 94.

Feddersen, F. and Williams, A. J. (2007). Direct Estimation of the Reynolds Stress Vertical Structure in the Nearshore. *J. Atmos. Oceanic Technol.*, 24(1):102–116.

Fewings, M. R., Lentz, S. J., and Fredericks, J. (2008). Observations of Cross-Shelf Flow Driven by Cross-Shelf Winds on the Inner Continental Shelf. *J. Phys. Oceanogr.*, 38(11):2358–2378.

Fewings, M. R., Washburn, L., and Ohlmann, J. C. (2015). Coastal water circulation patterns around the Northern Channel Islands and Point Conception, California. 138:283–304.

Firing, E. and Hummon, J. M. (2010). Shipboard ADCP Measurements.

Flexas, M. M., Schodlok, M. P., Padman, L., Menemenlis, D., and Orsi, A. H. (2015). Role of tides on the formation of the Antarctic Slope Front at the Weddell-Scotia Confluence. *J. Geophys. Res. Ocean.*, 120(5):3658–3680.

Fogt, R. L., Bromwich, D. H., and Hines, K. M. (2011). Understanding the SAM influence on the South Pacific ENSO teleconnection. *Clim. Dyn.*, 36(7-8):1555–1576.

Foppert, A., Rintoul, S. R., and England, M. H. (2019). Along-Slope Variability of Cross-Slope Eddy Transport in East Antarctica. *Geophys. Res. Lett.*, 46(14):8224–8233.

Gent, P. R. and McWilliams, J. C. (1990). Isopycnal Mixing in Ocean Circulation Models. *J. Phys. Oceanogr.*, 20(1):150–155.

Gille, S. T., McKee, D. C., and Martinson, D. G. (2016). Temporal Changes in the Antarctic Circumpolar Current: Implications for the Antarctic continental shelves. *Oceanography*, 29.

Gille, S. T., Stevens, D. P., Tokmakian, R. T., and Heywood, K. J. (2001). Antarctic Circumpolar Current response to zonally averaged winds. *J. Geophys. Res.*, 106(C2):2743–2759.

Goddard, P. B., Dufour, C. O., Yin, J., Griffies, S. M., and Winton, M. (2017). CO_2-induced ocean warming of the Antarctic continental shelf in an eddying global climate model. *J. Geophys. Res.-Oceans*, 122(10):8079–8101.

Graham, J. A., Dinniman, M. S., and Klinck, J. M. (2016). Impact of model resolution for on-shelf heat transport along the West Antarctic Peninsula. *J. Geophys. Res.-Oceans*, 121(10):7880–7897.

Greenbaum, J. S., Blankenship, D. D., Young, D. A., Richter, T. G., Roberts, J. L., Aitken, A. R. A., Legresy, B., Schroeder, D. M., Warner, R. C., Van Ommen, T. D., and Siegert, M. J. (2015). Ocean access to a cavity beneath Totten Glacier in East Antarctica. *Nat. Geosci.*, 8(4):294–298.

Guerra, M. and Thomson, J. (2017). Turbulence Measurements from Five-Beam Acoustic Doppler Current Profilers. *J. Atmos. Oceanic Technol.*, 34(6):1267–1284.

Gunn, K. L., White, N. J., Larter, R. D., and Caulfield, C. P. (2018). Calibrated Seismic Imaging of Eddy-Dominated Warm-Water Transport Across the Bellingshausen Sea, Southern Ocean. *J. Geophys. Res. Ocean.*, 123(4):3072–3099.

Ha, H. K., Wåhlin, A. K., Kim, T. W., Lee, S. H., Lee, J. H., Lee, H. J., Hong, C. S., Arneborg, L., Björk, G., and Kalén, O. (2014). Circulation and modification of warm deep water on the central Amundsen shelf. *J. Phys. Oceanogr.*, 44(5):1493–1501.

Hammond, M. D. and Jones, D. C. (2016). Freshwater flux from ice sheet melting and iceberg calving in the Southern Ocean. *Geoscience Data Journal*, 3(2):60–62.

Hauer, M. E., Fussell, E., Mueller, V., Burkett, M., Call, M., Abel, K., McLeman, R., and Wrathall, D. (2019). Sea-level rise and human migration. *Nat. Rev. Earth Environ.*, pages 1–12.

Hogg, N. G. (1971). Longshore current generation by obliquely incident internal waves. 2(1):361–376.

Holland, W. R. (1973). Baroclinic and topographic influences on the transport in western boundary currents. *Geophys. Fluid Dyn.*, 4(1):187–210.

Holloway, G. (2008). Observing global ocean topostrophy. *J. Geophys. Res.*, 113(C7):C07054.

Horwitz, R. M. and Lentz, S. J. (2014). Inner-Shelf Response to Cross-Shelf Wind Stress: The

Importance of the Cross-Shelf Density Gradient in an Idealized Numerical Model and Field Observations. *J. Phys. Oceanogr.*, 44(1):86–103.

Horwitz, R. M. and Lentz, S. J. (2016). The effect of wind direction on cross-shelf transport on an initially stratified inner shelf. *J. Mar. Res.*, 74(4):201–227.

Hughes, C. W. and de Cuevas, B. A. (2001). Why western boundary currents in realistic oceans are inviscid: A link between form stress and bottom pressure torques. *J. Phys. Oceanogr.*, 31(10):2871–2885.

Hunke, E. C., Lipscomb, W. H., Turner, A. K., Jeffery, N., and Elliott, S. (2010). CICE: the Los Alamos Sea Ice Model documentation and software user's manual version 4.1 LA-CC-06-012. Technical report, T-3 Fluid Dynamics Group, Los Alamos National Laboratory.

Jacobs, S. S., Jenkins, A., Giulivi, C. F., and Dutrieux, P. (2011). Stronger ocean circulation and increased melting under Pine Island Glacier ice shelf. *Nat. Geosci.*, 4(8):519–523.

Jenkins, A., Dutrieux, P., Jacobs, S., Steig, E. J., Gudmundsson, G. H., and Smith, J. (2016). Decadal ocean forcing and Antarctic ice sheet response: Lessons from the Amundsen Sea. *Oceanography*, 29(4):106–117.

Jourdain, N. C., Mathiot, P., Merino, N., Durand, G., Le Sommer, J., Spence, P., Dutrieux, P., and Madec, G. (2017). Ocean circulation and sea-ice thinning induced by melting ice shelves in the Amundsen Sea. *J. Geophys. Res.-Oceans*, 122(3):2550–2573.

Kalén, O., Assmann, K. M., Wåhlin, A. K., Ha, H. K., Kim, T. W., and Lee, S. H. (2015). Is the oceanic heat flux on the central Amundsen Sea shelf caused by barotropic or baroclinic currents? *Deep. Res. Part II Top. Stud. Oceanogr.*, 123:7–15.

Kim, T., Ha, H., Wåhlin, A., Lee, S., Kim, C., Lee, J., and Cho, Y. (2017). Is Ekman pumping responsible for the seasonal variation of warm circumpolar deep water in the Amundsen Sea? *Cont. Shelf Res.*, 132:38–48.

Kirincich, A. R. (2013). Long-Term Observations of Turbulent Reynolds Stresses over the Inner Continental Shelf. *J. Phys. Oceanogr.*, 43(12):2752–2771.

Kirincich, A. R. and Gawarkiewicz, G. G. (2016). Drivers of spring and summer variability in the coastal ocean offshore of Cape Cod, MA. *J. Geophys. Res.*, 121(3):1789–1805.

Kirincich, A. R., Lentz, S. J., and Gerbi, G. P. (2010). Calculating Reynolds Stresses from ADCP Measurements in the Presence of Surface Gravity Waves Using the Cospectra-Fit Method. *J. Atmos. Oceanic Technol.*, 27(5):889–907.

Kirincich, A. R. and Rosman, J. H. (2011). A Comparison of Methods for Estimating Reynolds Stress from ADCP Measurements in Wavy Environments. *J. Atmos. Oceanic Technol.*, 28(11):1539–1553.

Kumar, N., Suanda, S. H., Colosi, J. A., Haas, K., Di Lorenzo, E., Miller, A. J., and Edwards, C. A. (2019). Coastal Semidiurnal Internal Tidal Incoherence in the Santa Maria Basin, California: Observations and Model Simulations. *J. Geophys. Res.*, page 2018JC014891.

Kusahara, K. and Ohshima, K. I. (2009). Dynamics of the wind-driven sea level variation around Antarctica. *J. Phys. Oceanogr.*, 39(3):658–674.

Kusahara, K. and Ohshima, K. I. (2014). Kelvin Waves around Antarctica. *J. Phys. Oceanogr.*, 44(11):2909–2920.

Lamb, K. G. (2014). Internal Wave Breaking and Dissipation Mechanisms on the Continental Slope/Shelf. *Annu. Rev. Fluid Mech.*, 46(1):231–254.

Large, W. and Pond, S. (1982). Sensible and latent heat flux measurements over the ocean. *J. Phys. Oceanogr.*, 12(5):464–482.

Large, W. G., McWilliams, J. C., and Doney, S. C. (1994). Oceanic vertical mixing: A review and a model with a nonlocal boundary layer parameterization. *Reviews of Geophysics*, 32(4):363–403.

Large, W. G. and Yeager, S. G. (2009). The global climatology of an interannually varying air–sea flux data set. 33(2):341–364.

Lentz, S. J. (1995). Sensitivity of the Inner-Shelf Circulation to the Form of the Eddy Viscosity Profile. *J. Phys. Oceanogr.*, 25(1):19–28.

Lentz, S. J., Fewings, M., Howd, P., Fredericks, J., and Hathaway, K. (2008). Observations and a Model of Undertow over the Inner Continental Shelf. *J. Phys. Oceanogr.*, 38(11):2341–2357.

Lentz, S. J. and Fewings, M. R. (2012). The Wind- and Wave-Driven Inner-Shelf Circulation. *Annu. Rev. Mar. Sci.*, 4(1):317–343.

Lentz, S. J., Guza, R. T., Elgar, S., Feddersen, F., and Herbers, T. H. C. (1999). Momentum balances on the North Carolina inner shelf. *J. Geophys. Res.*, 104(C8):18205–18226.

Lerczak, J., Barth, J. A., Celona, S., Chickadel, C., Colosi, J., Feddersen, F., Haller, M., Haney, S., Lenain, L., MacKinnon, J., MacMahan, J., Melville, K., O'Dea, A., Smit, P., Waterhouse, A., and Xu, T. (2019). Untangling a web of interactions where surf meets coastal ocean. *Eos*, (100). Published on 02 May 2019.

Lindborg, E. (2015). A Helmholtz decomposition of structure functions and spectra calculated from aircraft data. *J. Fluid Mech.*, 762(1).

Liu, Y., Moore, J. C., Cheng, X., Gladstone, R. M., Bassis, J. N., Liu, H., Wen, J., and Hui, F. (2015). Ocean-driven thinning enhances iceberg calving and retreat of Antarctic ice shelves. *Proc. Natl. Acad. Sci.*, 112(11):3263–3268.

Lohrmann, A., Hackett, B., and Røed, L. P. (1990). High Resolution Measurements of Turbulence, Velocity and Stress Using a Pulse-to-Pulse Coherent Sonar. *J. Atmos. Oceanic Technol.*, 7(1):19–37.

Longuet-Higgins, M. and Stewart, R. (1964). Radiation stresses in water waves; a physical discussion, with applications. 11(4):529–562.

Lu, Y. and Lueck, R. G. (1999). Using a Broadband ADCP in a Tidal Channel. Part II: Turbulence. *J. Atmos. Oceanic Technol.*, 16(11):1568–1579.

Lu, Y. and Stammer, D. (2004). Vorticity Balance in Coarse–Resolution Global Ocean Simulations. *J. Phys. Oceanogr.*, 34(3):605–622.

MacKinnon, J. A. and Gregg, M. C. (2003). Mixing on the Late-Summer New England Shelf—Solibores, Shear, and Stratification. *J. Phys. Oceanogr.*, 33(7):1476–1492.

MacKinnon, J. A. and Gregg, M. C. (2005). Spring Mixing: Turbulence and Internal Waves during Restratification on the New England Shelf. *J. Phys. Oceanogr.*, 35(12):2425–2443.

Mallett, H. K. W., Boehme, L., Fedak, M., Heywood, K. J., Stevens, D. P., and Roquet, F. (2018). Variation in the distribution and properties of Circumpolar Deep Water in the Eastern Amundsen Sea, on seasonal timescales, using seal-borne tags. *Geophys. Res. Lett.*

Martinson, D. G. and McKee, D. C. (2012). Transport of warm Upper Circumpolar Deep Water onto the Western Antarctic Peninsula continental shelf. *Ocean Sci.*, 8(4):433–442.

Martinson, D. G., Stammerjohn, S. E., Iannuzzi, R. A., Smith, R. C., and Vernet, M. (2008). Western Antarctic Peninsula physical oceanography and spatio–temporal variability. *Deep Sea Res. Part II Top. Stud. Oceanogr.*, 55(18-19):1964–1987.

Mazloff, M. R., Cornuelle, B., Gille, S. T., and Wang, J. (2020). The Importance of Remote Forcing for Regional Modeling of Internal Waves. *J. Geophys. Res.*, 125(2):1–15.

McCabe, R. M., Hickey, B. M., Dever, E. P., and MacCready, P. (2015). Seasonal Cross-Shelf Flow Structure, Upwelling Relaxation, and the Alongshelf Pressure Gradient in the Northern California Current System. *J. Phys. Oceanogr.*, 45(1):209–227.

McClean, J. L., Bader, D. C., Maltrud, M. E., Evans, K. J., Taylor, M., Tang, Q., Ivanova, D., Veneziani, C., Ritchie, J., Branstetter, M. L., and Mahajan, S. (2018). High-resolution fully-coupled ACME v0.1 approximate present day transient climate simulations. Ocean Sciences Meeting 2018, 12-16/February, Portland/OR. Abstract ID: OM44C-2143.

McSweeney, J. M., Lerczak, J. A., Barth, J. A., Becherer, J., Colosi, J. A., MacKinnon, J. A., MacMahan, J. H., Moum, J. N., Pierce, S. D., and Waterhouse, A. F. (2020). Observations of Shoaling Nonlinear Internal Bores across the Central California Inner Shelf. *J. Phys. Oceanogr.*, 50(1):111–132.

McWilliams, J. C. (2016). Submesoscale currents in the ocean. *P. Roy. Soc. A-Math. Phy.*, 472(2189):20160117.

Mertz, G. and Wright, D. G. (1992). Interpretations of the JEBAR Term. *J. Phys. Oceanogr.*, 22(3):301–305.

Mitchum, G. T. and Clarke, A. J. (1986). The Frictional Nearshore Response to Forcing by Synoptic Scale Winds. *J. Phys. Oceanogr.*, 16(5):934–946.

Moffat, C. and Meredith, M. (2018). Shelf–ocean exchange and hydrography west of the Antarctic Peninsula: a review. *Philos. Trans. R. Soc. A Math. Phys. Eng. Sci.*, 376(2122):20170164.

Moffat, C., Owens, B., and Beardsley, R. C. (2009). On the characteristics of Circumpolar Deep Water intrusions to the West Antarctic Peninsula continental shelf. *J. Geophys. Res.-Oceans*, 114(5):1–16.

Nakayama, Y., Schröder, M., and Hellmer, H. H. (2013). From circumpolar deep water to the glacial meltwater plume on the eastern Amundsen Shelf. *Deep. Res. Part I Oceanogr. Res. Pap.*, 77:50–62.

Nerem, R. S., Beckley, B. D., Fasullo, J. T., Hamlington, B. D., Masters, D., and Mitchum, G. T. (2018). Climate-change–driven accelerated sea-level rise detected in the altimeter era. *Proc. Natl. Acad. Sci.*, 115(9):2022–2025.

Nøst, O. A., Biuw, M., Tverberg, V., Lydersen, C., Hattermann, T., Zhou, Q., Smedsrud, L. H., and Kovacs, K. M. (2011). Eddy overturning of the Antarctic Slope Front controls glacial melting in the Eastern Weddell Sea. *J. Geophys. Res.-Oceans*, 116(C11):C11014.

Pacanowski, R. C. and Gnanadesikan, A. (1998). Transient response in a z-level ocean model that resolves topography with partial cells. *Monthly Weather Review*, 126(12):3248–3270.

Palóczy, A., Gille, S. T., and McClean, J. L. (2018). Oceanic Heat Delivery to the Antarctic Continental Shelf: Large-Scale, Low-Frequency Variability. *J. Geophys. Res. Ocean.*, 123(11):7678–7701.

Paolo, F. S., Fricker, H. A., and Padman, L. (2015). Volume loss from Antarctic ice shelves is accelerating. *Science*, 348(6232):327–331.

Paolo, F. S., Padman, L., Fricker, H. A., Adusumilli, S., Howard, S., and Siegfried, M. R. (2018). Response of Pacific-sector Antarctic ice shelves to the El Niño / Southern Oscillation. *Nat. Geosci.*, 11(February).

Peña-Molino, B., McCartney, M. S., and Rintoul, S. R. (2016). Direct observations of the Antarctic Slope Current transport at 113°E. *J. Geophys. Res.-Oceans*, 121(10):7390–7407.

Pringle, J. M. and Riser, K. (2003). Remotely forced nearshore upwelling in Southern California. *J. Geophys. Res.*, 108(C4):3131.

Qiu, B., Chen, S., Klein, P., Wang, J., Torres, H., Fu, L.-L., and Menemenlis, D. (2018). Seasonality in Transition Scale from Balanced to Unbalanced Motions in the World Ocean. *J. Phys. Oceanogr.*, 48(3):591–605.

Qiu, B., Nakano, T., Chen, S., and Klein, P. (2017). Submesoscale transition from geostrophic flows to internal waves in the northwestern Pacific upper ocean. *Nat. Commun.*, 8(1):14055.

Rignot, E., Jacobs, S., Mouginot, J., and Scheuchl, B. (2013). Ice-shelf melting around Antarctica. *Science*, 341(6143):266–270.

Rintoul, S. R., Silvano, A., Peña-Molino, B., van Wijk, E., Rosenberg, M., Greenbaum, J. S., and Blankenship, D. D. (2016). Ocean heat drives rapid basal melt of the Totten Ice Shelf. 2(12):e1601610–e1601610.

Rippeth, T. P. (2005). Mixing in seasonally stratified shelf seas: a shifting paradigm. *Philos. Trans. R. Soc. A*, 363(1837):2837–2854.

Rippeth, T. P., Simpson, J. H., Williams, E., and Inall, M. E. (2003). Measurement of the Rates of Production and Dissipation of Turbulent Kinetic Energy in an Energetic Tidal Flow: Red Wharf Bay Revisited. *J. Phys. Oceanogr.*, 33(9):1889–1901.

Rocha, C. B., Chereskin, T. K., Gille, S. T., and Menemenlis, D. (2016). Mesoscale to Submesoscale Wavenumber Spectra in Drake Passage. *J. Phys. Oceanogr.*, 46(2):601–620.

Rodriguez, A. R., Mazloff, M. R., and Gille, S. T. (2016). An oceanic heat transport pathway to the Amundsen Sea Embayment. *J. Geophys. Res.-Oceans*, pages 1–14.

Roquet, F., Charrassin, J.-B., Marchand, S., Boehme, L., Fedak, M., Reverdin, G., and Guinet, C. (2011). Delayed-mode calibration of hydrographic data obtained from animal-borne satellite relay data loggers. *J. Atmos. Oc. Tech.*, 28(6):787–801.

Roquet, F. et al. (2014). A Southern Indian Ocean database of hydrographic profiles obtained with instrumented elephant seals. *Sci. Data*, 1(40028).

Rosman, J. H., Hench, J. L., Koseff, J. R., and Monismith, S. G. (2008). Extracting Reynolds Stresses from Acoustic Doppler Current Profiler Measurements in Wave-Dominated Environments. *J. Atmos. Oceanic Technol.*, 25(2):286–306.

Ruan, X., Thompson, A. F., Flexas, M. M., and Sprintall, J. (2017). Contribution of topographically generated submesoscale turbulence to Southern Ocean overturning. *Nat. Geosci.*, 10(11):840–845.

Ryan, S., Hattermann, T., Darelius, E., and Schröder, M. (2017). Seasonal cycle of hydrography on the eastern shelf of the Filchner Trough, Weddell Sea, Antarctica. *J. Geophys. Res.-Oceans*, 122(8):6437–6453.

Scannell, B. D., Rippeth, T. P., Simpson, J. H., Polton, J. A., and Hopkins, J. E. (2017). Correcting Surface Wave Bias in Structure Function Estimates of Turbulent Kinetic Energy Dissipation Rate. *J. Atmos. Oceanic Technol.*, 34(10):2257–2273.

Schmidtko, S., Heywood, K. J., Thompson, A. F., and Aoki, S. (2014). Multidecadal warming of Antarctic waters. *Science*, 346(6214):1227–1231.

Scotti, A., Butman, B., Beardsley, R. C., Alexander, P. S., and Anderson, S. (2005). A Modified Beam-to-Earth Transformation to Measure Short-Wavelength Internal Waves with an Acoustic Doppler Current Profiler. *J. Atmos. Oceanic Technol.*, 22(5):583–591.

Shchepetkin, A. F. and McWilliams, J. C. (2005). The regional oceanic modeling system (roms): a split-explicit, free-surface, topography-following-coordinate oceanic model. 9(4):347–404.

Shepherd, A., Ivins, E., Rignot, E., Smith, B., van den Broeke, M., Velicogna, I., Whitehouse, P., Briggs, K., Joughin, I., Krinner, G., Nowicki, S., Payne, T., Scambos, T., Schlegel, N., A, G., Agosta, C., Ahlstrøm, A., Babonis, G., Barletta, V., Blazquez, A., Bonin, J., Csatho, B., Cullather, R., Felikson, D., Fettweis, X., Forsberg, R., Gallee, H., Gardner, A., Gilbert, L., Groh, A., Gunter, B., Hanna, E., Harig, C., Helm, V., Horvath, A., Horwath, M., Khan, S., Kjeldsen, K. K., Konrad, H., Langen, P., Lecavalier, B., Loomis, B., Luthcke, S., McMillan, M., Melini, D., Mernild, S., Mohajerani, Y., Moore, P., Mouginot, J., Moyano, G., Muir, A., Nagler, T., Nield, G., Nilsson, J., Noel, B., Otosaka, I., Pattle, M. E., Peltier, W. R., Pie, N., Rietbroek, R., Rott, H., Sandberg-Sørensen, L., Sasgen, I., Save, H., Scheuchl, B., Schrama, E., Schröder, L., Seo, K.-W., Simonsen, S., Slater, T., Spada, G., Sutterley, T., Talpe, M., Tarasov, L., van de Berg, W. J., van der Wal, W., van Wessem, M., Vishwakarma, B. D., Wiese, D., and Wouters, B. (2018). Mass balance of the Antarctic Ice Sheet from 1992 to 2017. *Nature*, 558(7709):219–222.

Shroyer, E. L., Moum, J. N., and Nash, J. D. (2010). Vertical heat flux and lateral mass transport in nonlinear internal waves. *Geophys. Res. Lett.*, 37(8):1–5.

Silvano, A., Rintoul, S. R., and Herraiz-Borreguero, L. (2016). Ocean-ice shelf interaction in East Antarctica. *Oceanography*, 29(4):130–143.

Silvano, A., Rintoul, S. R., Peña-Molino, B., and Williams, G. D. (2017). Distribution of water masses and meltwater on the continental shelf near the Totten and Moscow University ice shelves. *J. Geophys. Res.-Oceans*, 122:2050–2068.

Smith, R., Jones, P., Briegleb, B., Bryan, F., Danabasoglu, G., Dennis, J., Dukowicz, J., Eden, C., Fox-Kemper, B., Gent, P., et al. (2010). The Parallel Ocean Program (POP) reference manual ocean component of the Community Climate System Model (CCSM) and Community Earth System Model (CESM). *Rep. LAUR-01853*, 141:1–140.

Smith, R. D., Maltrud, M. E., Bryan, F. O., and Hecht, M. W. (2000). Numerical simulation of the north atlantic ocean at 1/10°. *J. Phys. Oceanogr.*, 30(7):1532–1561.

Smith, W. H. and Sandwell, D. T. (1997). Global sea floor topography from satellite altimetry and ship depth soundings. *Science*, 277(5334):1956–1962.

Snow, K., Sloyan, B. M., and Rintoul, S. R. (2016). Controls on circulation , cross-shelf exchange and dense water formation in an Antarctic polynya. *Geophys. Res. Lett.*, (May):1–24.

Soh, H. S. and Kim, S. Y. (2018). Diagnostic Characteristics of Submesoscale Coastal Surface Currents. *J. Geophys. Res.*, 123(3):1838–1859.

Spence, P., Griffies, S., England, M., Hogg, A., Saenko, O. A., and Jourdain, N. C. (2014). Rapid subsurface warming and circulation changes of Antarctic coastal waters by poleward shifting winds. *Geophys. Res. Lett.*, pages 4601–4610.

Spence, P., Holmes, R. M., Hogg, A. M., Griffies, S. M., Stewart, K. D., and England, M. H. (2017). Localized rapid warming of West Antarctic subsurface waters by remote winds. *Nat. Clim. Chang.*, (July):1–10.

St-Laurent, P., Klinck, J. M., and Dinniman, M. S. (2013). On the role of coastal troughs in the circulation of warm Circumpolar Deep Water on Antarctic shelves. *J. Phys. Oceanogr.*, 43(1):51–64.

Stacey, M. T., Monismith, S. G., and Burau, J. R. (1999). Measurements of Reynolds stress profiles in unstratified tidal flow. *J. Geophys. Res.*, 104(C5):10933–10949.

Steig, E., Ding, Q., Battisti, D., and Jenkins, A. (2012). Tropical forcing of Circumpolar Deep Water inflow and outlet glacier thinning in the Amundsen Sea Embayment, West Antarctica. *Ann. Glaciol.*, 53(60):19–28.

Stewart, A. and Thompson, A. (2015a). The Neutral Density Temporal Residual Mean overturning circulation. *Ocean Model.*, 90:44–56.

Stewart, A. L., Klocker, A., and Menemenlis, D. (2018). Circum-Antarctic shoreward heat transport derived from an eddy- and tide-resolving simulation. *Geophys. Res. Lett.*, 45.

Stewart, A. L., Klocker, A., and Menemenlis, D. (2019). Acceleration and Overturning of the Antarctic Slope Current by Winds, Eddies, and Tides. *J. Phys. Oceanogr.*, 49(8):2043–2074.

Stewart, A. L. and Thompson, A. F. (2013). Connecting Antarctic cross-slope exchange with Southern Ocean overturning. *J. Phys. Oceanogr.*, 43(7):1453–1471.

Stewart, A. L. and Thompson, A. F. (2015b). Eddy-mediated transport of warm Circumpolar Deep Water across the Antarctic shelf break. *Geophys. Res. Lett.*, 42(2):432–440.

Stewart, A. L. and Thompson, A. F. (2015c). Eddy-mediated transport of warm Circumpolar Deep Water across the Antarctic Shelf Break. *Geophys. Res. Lett.*, 42(2):432–440.

Stewart, A. L. and Thompson, A. F. (2016). Eddy generation and jet formation via dense water outflows across the Antarctic continental slope. *J. Phys. Oceanogr.*, 46(12):3729–3750.

Suanda, S. H., Kumar, N., Miller, A. J., Di Lorenzo, E., Haas, K., Cai, D., Edwards, C. A., Washburn, L., Fewings, M. R., Torres, R., and Feddersen, F. (2016). Wind relaxation and a coastal buoyant plume north of Pt. Conception, CA: Observations, simulations, and scalings. *Journal of Geophysical Research: Oceans*, 121(10):7455–7475.

Sukhatme, J., Chaudhuri, D., MacKinnon, J., Shivaprasad, S., and Sengupta, D. (2020). Near-surface ocean kinetic energy spectra and small scale intermittency from ship based ADCP data in the Bay of Bengal. *J. Phys. Oceanogr.*

Thoma, M., Jenkins, A., Holland, D., and Jacobs, S. (2008). Modelling Circumpolar Deep Water intrusions on the Amundsen Sea continental shelf, Antarctica. *Geophys. Res. Lett.*, 35(18):L18602.

Thompson, A. F., Heywood, K. J., Schmidtko, S., and Stewart, A. L. (2014). Eddy transport as a key component of the Antarctic overturning circulation. *Nat. Geosci.*, 7(12):879–884.

Thompson, A. F., Stewart, A. L., Spence, P., and Heywood, K. J. (2018). The Antarctic Slope Current in a Changing Climate. *Rev. Geophys.*, 56(4):741–770.

Thorpe, S. (2004). Recent Developments in the Study of Ocean Turbulence. *Annu. Rev. Earth Planet. Sci.*, 32(1):91–109.

Thorpe, S. A. (1999). The generation of alongslope currents by breaking internal waves. *J. Phys. Oceanogr.*, 29(1):29–38.

Trenberth, K. E., Large, W. G., and Olson, J. G. (1990). The mean annual cycle in global ocean wind stress. *J. Phys. Oceanogr.*, 20(11):1742–1760.

Trowbridge, J., Scully, M., and Sherwood, C. R. (2018). The Cospectrum of Stress-Carrying Turbulence in the Presence of Surface Gravity Waves. *J. Phys. Oceanogr.*, 48(1):29–44.

Vallis, G. K. (2019). *Essentials of Atmospheric and Oceanic Dynamics*. Cambridge University Press.

van Haren, H., Oakey, N., and Garrett, C. (1994). Measurements of internal wave band eddy fluxes above a sloping bottom. *J. Mar. Res.*, 52(5):909–946.

Vignudelli, S., Birol, F., Benveniste, J., Fu, L.-L., Picot, N., Raynal, M., and Roinard, H. (2019). Satellite Altimetry Measurements of Sea Level in the Coastal Zone. *Surv. Geophys.*, 40(6):1319–1349.

Wåhlin, A. K., Kalén, O., Arneborg, L., Björk, G., Carvajal, G. K., Ha, H. K., Kim, T. W., Lee, S. H., Lee, J. H., and Stranne, C. (2013). Variability of Warm Deep Water inflow in a submarine trough on the Amundsen Sea shelf. *J. Phys. Oceanogr.*, 43(10):2054–2070.

Wåhlin, A. K., Kalén, O., Assmann, K. M., Darelius, E., Ha, H. K., Kim, T. W., and Lee, S. H. (2016). Subinertial Oscillations on the Amundsen Sea Shelf, Antarctica. *J. Phys. Oceanogr.*, 46(9):2573–2582.

Wåhlin, A. K., Muench, R. D., Arneborg, L., Björk, G., Ha, H. K., Lee, S. H., and Alsén, H. (2012). Some implications of Ekman layer dynamics for cross-shelf exchange in the Amundsen Sea. *J. Phys. Oceanogr.*, 42:1461–1474.

Walker, D. P., Brandon, M. A., Jenkins, A., Allen, J. T., Dowdeswell, J. A., and Evans, J. (2007). Oceanic heat transport onto the Amundsen Sea shelf through a submarine glacial trough. *Geophys. Res. Lett.*, 34(2):L02602.

Walker, D. P., Jenkins, A., Assmann, K. M., Shoosmith, D. R., and Brandon, M. A. (2013). Oceanographic observations at the shelf break of the Amundsen Sea, Antarctica. *J. Geophys. Res.-Oceans*, 118(6):2906–2918.

Walter, R. K., Brock Woodson, C., Arthur, R. S., Fringer, O. B., and Monismith, S. G. (2012). Nearshore internal bores and turbulent mixing in southern Monterey Bay. *J. Geophys. Res.*, 117(7):1–13.

Washburn, L., Fewings, M. R., Melton, C., and Gotschalk, C. (2011). The propagating response of coastal circulation due to wind relaxations along the central California coast. *J. Geophys. Res.*, 116(C12).

Webb, D. J., Holmes, R. M., Spence, P., and England, M. H. (2019). Barotropic Kelvin Wave-Induced Bottom Boundary Layer Warming Along the West Antarctic Peninsula. *J. Geophys. Res.*, 124(3):1595–1615.

Whipple, A. C., Luettich, R. A., and Seim, H. E. (2006). Measurements of Reynolds stress in a wind-driven lagoonal estuary. 56(3-4):169–185.

Williams, E. and Simpson, J. H. (2004). Uncertainties in Estimates of Reynolds Stress and TKE Production Rate Using the ADCP Variance Method. *J. Atmos. Oceanic Technol.*, 21(2):347–357.

Williams, R. G., Wilson, C., and Hughes, C. W. (2007). Ocean and Atmosphere Storm Tracks: The Role of Eddy Vorticity Forcing. *J. Phys. Oceanogr.*, 37(9):2267–2289.

Wunsch, C. (2011). The decadal mean ocean circulation and Sverdrup balance. *J. Mar. Res.*, 69(2):417–434.

Yeager, S. (2013). *Understanding and predicting changes in North Atlantic sea surface temperature*. PhD thesis, University of Colorado. 176 pp.

Yeager, S. (2015). Topographic Coupling of the Atlantic Overturning and Gyre Circulations. *J. Phys. Oceanogr.*, 45(5):1258–1284.

Yoo, J. G., Kim, S. Y., and Kim, H. S. (2018). Spectral Descriptions of Submesoscale Surface Circulation in a Coastal Region. *J. Geophys. Res.*, 123(6):4224–4249.

Zhang, X., Thompson, A. F., Flexas, M. M., Roquet, F., and Bornemann, H. (2016). Circulation and meltwater distribution in the Bellingshausen Sea: From shelf break to coast. *Geophys. Res. Lett.*, 43(12):6402–6409.

Zikanov, O. and Slinn, D. N. (2001). Along-slope current generation by obliquely incident internal waves. *J. Fluid Mech.*, 445:235–261.